

Modelling and numerical simulation of viscous sintering

Citation for published version (APA):

Vorst, van de, G. A. L. (1994). *Modelling and numerical simulation of viscous sintering*. [Phd Thesis 1 (Research TU/e / Graduation TU/e), Mathematics and Computer Science]. Technische Universiteit Eindhoven.
<https://doi.org/10.6100/IR410008>

DOI:

[10.6100/IR410008](https://doi.org/10.6100/IR410008)

Document status and date:

Published: 01/01/1994

Document Version:

Publisher's PDF, also known as Version of Record (includes final page, issue and volume numbers)

Please check the document version of this publication:

- A submitted manuscript is the version of the article upon submission and before peer-review. There can be important differences between the submitted version and the official published version of record. People interested in the research are advised to contact the author for the final version of the publication, or visit the DOI to the publisher's website.
- The final author version and the galley proof are versions of the publication after peer review.
- The final published version features the final layout of the paper including the volume, issue and page numbers.

[Link to publication](#)

General rights

Copyright and moral rights for the publications made accessible in the public portal are retained by the authors and/or other copyright owners and it is a condition of accessing publications that users recognise and abide by the legal requirements associated with these rights.

- Users may download and print one copy of any publication from the public portal for the purpose of private study or research.
- You may not further distribute the material or use it for any profit-making activity or commercial gain
- You may freely distribute the URL identifying the publication in the public portal.

If the publication is distributed under the terms of Article 25fa of the Dutch Copyright Act, indicated by the "Taverne" license above, please follow below link for the End User Agreement:

www.tue.nl/taverne

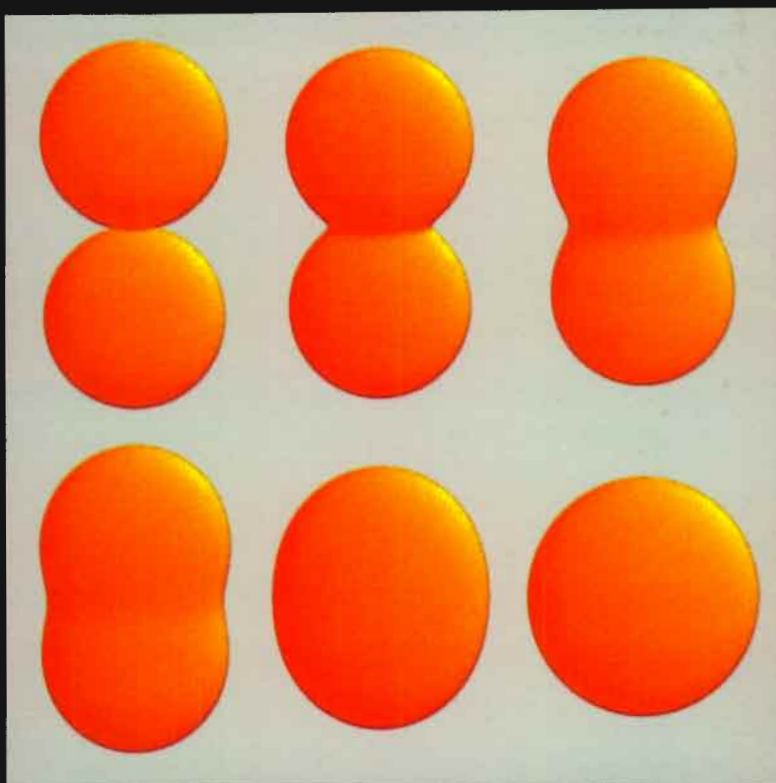
Take down policy

If you believe that this document breaches copyright please contact us at:

openaccess@tue.nl

providing details and we will investigate your claim.

MODELLING AND NUMERICAL SIMULATION OF VISCOUS SINTERING



G.A.L. VAN DE VORST

**MODELLING AND
NUMERICAL SIMULATION
OF VISCOUS SINTERING**

MODELLING AND NUMERICAL SIMULATION OF VISCOUS SINTERING

PROEFSCHRIFT

ter verkrijging van de graad van doctor aan de Technische Universiteit Eindhoven, op gezag van de Rector Magnificus, prof. dr. J.H. van Lint, voor een commissie aangewezen door het College van Dekanen in het openbaar te verdedigen op vrijdag 21 januari 1994 te 16.00 uur

door

GODEFRIDUS ALEXIUS LAMBERTUS VAN DE VORST

Geboren te Steensel (NBr)

Dit proefschrift is goedgekeurd door de promotoren
prof.dr. R.M.M. Mattheij
en
prof.dr.ir. H.K. Kuiken

cover: The coalescence of two equal spheres into one sphere occupying the same amount of fluid at subsequent time steps.

CIP-DATA KONINKLIJKE BIBLIOTHEEK, DEN HAAG

Vorst, Godefridus Alexius Lambertus van de

Modelling and numerical simulation of viscous sintering /
Godefridus Alexius Lambertus van de Vorst. – Eindhoven:
Eindhoven University of Technology
Thesis Eindhoven. – With ref.
ISBN 90-386-0083-6
Subject headings: viscous sintering; numerical simulation

Copyright ©1994 by G.A.L. van de Vorst, Eindhoven, The Netherlands
Printed by Febodruk – Enschede, The Netherlands

Aan mijn ouders

PREFACE

The main objective of this thesis is to develop reliable numerical methods to predict the deformation of an incompressible Newtonian viscous fluid region driven by surface tension. In particular this mathematical model describes the physical processes that appear when a compact of glassy particles is heated to such a high temperature that the glass becomes a viscous creeping fluid. As a result, the particles are joining together so that the cohesion of the compact is increasing with time. This phenomenon is usually called *viscous sintering* and e.g. appears in the production of high-quality glasses by means of what is known as the sol-gel technique: ideally, one wants to produce a dense and homogeneous glass, free from voids and impurities at this way. From the methods developed in this thesis, theoretical insights can be obtained about the densification kinetics of such a sintering compact. A numerical simulation program is presented to calculate the deformation of a representative unit cell of the compact.

At this place, I would like to express my gratitude to a couple of people who have contributed directly or indirectly to the work presented in this thesis. First, I would like to thank Prof.dr. R.M.M. Mattheij for the pleasant cooperation, the fruitful discussions, the improvement of my English writing and the support I received in all the things I have being done the last four years. Prof.dr.ir. H.K. Kuiken render thanks for encouraging me in both attending conferences and writing to other researchers who were working in similar research fields. Moreover, I want to honour him for the vision that the viscous sintering problem as presented in this thesis was an ideally suited subject for a PhD-thesis. Prof.dr. G. de With of both Philips Research Laboratory and the University of Technology Eindhoven is thanked for the stimulating discussions, the suggestions about interesting aspects to study and checking the chemical and physical contents of this thesis. I would like to thank him also for providing me with some experimental data. Prof.dr.ir. J. de Graaf owes my gratitude for providing me insights in solving a moving Stokes flow by using a conformal mapping technique and for checking the contents in this thesis of this particular subject. Dr.ir. S.J.L. van Eijndhoven render thanks for his valuable comments concerning the contents of chapter 1 and section 4.1.

Dr.ir. J.K.M. Jansen owes thanks for always having the time for me to arrange things in all kinds of fields when I made an appeal to him. Furthermore, I would like to express my gratitude to all the members of the STW-utilization committee concerning this research for their valuable comments and discussions the last four years. Besides the people who are mentioned above, I should mention in particular Dr.ir. H. Schippers of the National Aerospace Laboratory NLR and Ir. M. Engels, Drs. P. de Jong both of Royal Sphinx. I would also like to thank the students whose master thesis contributed directly or indirectly to this work, i.e. Jeroen van de Spek and Nico Helmes.

The foreign contacts with people who showed interest in my work is greatly appreciated. Within this context I should mention Prof. D.B. Ingham of the University of Leeds (U.K.) for the possibility to visit him and to discuss my work. Dr. R.W. Hopper of the Lawrence Livermore National Laboratory (U.S.A.) renders thanks for giving me the opportunity to visit him. The discussion we had about the method he uses and the suggestion on other interesting aspect to consider, appeared to be very useful and worthwhile. His arrangement of my stay and his hospitality are very much appreciated.

Finally, all colleagues of the group *Toegepaste Analyse* render thanks for the pleasant work atmosphere during this four years. Moreover, I would like to thank my family and friends for their interests and encouragements during these years.

This research was supported by the Technology Foundation (Stichting voor de Technische Wetenschappen (STW)), project EW199.1753 (modelleren en numeriek simuleren van systemen voor het viskeuze sinteren). Furthermore, the financial support obtained from Philips Research Laboratories Eindhoven is much appreciated.

Alfred van de Vorst

Eindhoven, January 1994

CONTENTS

Preface	vii
1 Introduction	1
1.1 Viscous Sintering and its Applications	1
1.2 State of the Art	7
1.2.1 Analytical Approaches to Viscous Sintering	7
1.2.2 Numerical Solutions of Viscous Sintering	9
1.2.3 Integral Method and Numerical Solution for Stokes Flows with Moving Boundaries	11
1.3 The Contents of this Thesis	13
1.4 Outlook on Further Developments and Applications	16
2 Problem Description and Mathematical Formulation	19
2.1 The Mathematical Model	20
2.2 Integral Formulation for a Simply Connected Domain	26
2.3 Equations for a Multiply Connected Domain	33
3 Two-Dimensional Analytical Solution Method for Stokes Flow	39
3.1 Analytical Solution	39
3.2 The Coalescence of Two Equal Cylinders	44
3.3 The Coalescence of a Cylinder on a Half Space	48
3.4 Discussion of Results	53
4 Numerical Solution of the Stokes Problem	59
4.1 Solving a Fredholm Integral Equation of the Second Kind	59
4.2 Implementing the BEM for the Stokes Problem	63
4.3 Problems with the Approximation of the Curvature	67

4.4	Mesh Redistribution and Verification	71
4.5	Algorithmic Considerations of the Mesh Redistribution	75
4.6	Discussion of Mesh Redistribution Results	78
5	Time Integration	83
5.1	Stiffness	83
5.2	Approximation of the Jacobian	87
5.3	Restart of Integration after a Node Redistribution	93
5.4	Numerical Experiments and Discussion	96
6	Sensitivity Analysis	103
6.1	Perturbation Analysis of Two Coalescing Cylinders	103
6.1.1	Perturbation of the initial radius	104
6.1.2	The Evolution of the Neck Region	107
6.2	Implications for the Numerical Solution	109
7	The Sintering of Two-Dimensional Shapes	111
7.1	Shrinkage Models Compared to Numerical Simulations	111
7.2	The Sintering of Cylindrical Packings	119
7.3	A Few Mesocell Densification Simulations	128
7.4	Conclusion	136
8	The Sintering of Axisymmetric Shapes	137
8.1	Axisymmetric Integral Formulation	137
8.2	Numerical Solution	140
8.3	Numerical Results and Discussion	142
8.4	Conclusion	154
A	Analytical Solution Method for Moving Stokes Flow	155
A.1	The Stokes Equation in the Complex Plane	155
A.2	The Kinematic Relation	157
A.3	Hopper's Evolution Equation	158
	Bibliography	163
	Index	172
	Summary	175
	Samenvatting	177
	Curriculum Vitae	181

INTRODUCTION

The process of *viscous sintering* occurs in a number of industrial applications. The main motivation to write this thesis is the need to obtain a better theoretical understanding of this phenomenon. The mathematical model of this physical process is investigated both analytically and numerically though the numerical simulation is the main subject of this thesis.

In this introductory chapter we start with a brief outline describing the sintering process and physical principles that are involved. We restrict ourselves to sintering that occurs by a viscous volume flow, which is particularly applicable for glasses. Moreover, we describe the production and application of high-quality glasses by means of sol-gel processing which has led to a renewed interest in the study of viscous sintering. The goal of these investigations will be discussed and an overview of the studies on this subject is given thereafter. Finally, we outline the structure of this thesis and discuss other possible applications of the methods developed.

1.1 VISCOUS SINTERING AND ITS APPLICATIONS

Sintering, in general, is the process in which a granular compact of metals, ionic crystals or glasses, consisting of many particles, is heated to such a high temperature that sufficient mobility is present to release the excess free energy of the surface of the compact, thereby joining the particles together. As a result, the cohesion of the compact increases with time. The sintering process may be divided into three types, viz. without a liquid phase (solid-state sintering), with a limited ($< 10\%$) liquid phase (liquid-phase sintering) or as a liquid phase only (e.g. viscous sintering). Moreover, one can apply pressure (hot-pressing), carry out chemical reactions (reactive sintering) or both together during sintering.

An example of a sintering phenomenon occurring in nature is the formation of rock strata from sandy sediments under the influence of high pressures exerted by later deposits. One of the oldest applications of sintering by humans is the production of

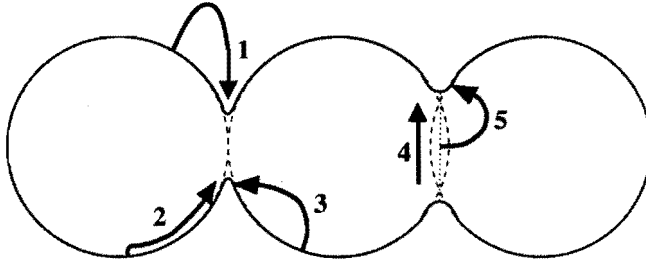


Figure 1.1 The transport mechanisms that can be involved in the case of solid-state sintering. The mechanisms (1)-(3) causes only a particle growth, while (4)-(5) leads also to shrinkage (of the compact). Only in the latter case material is removed from the contact area so that the centres of the spheres approach each other.

earthenware from clay, which dates back to before 5000 B.C. Nowadays, besides the more traditional products (e.g. bricks, tiles, sanitary ware, porcelain), ceramic materials have a wide range of technical application in industry and their significance is still increasing because of the useful physical properties of these materials. We mention their height of melting point, their stiffness and compression strength, their hardness and corrosion resistance. Their weak mechanical properties, such as brittleness, but also the difficulties arising in the ceramic production process are still important topics of material research. This research contains also the sintering stage of the process. However, progress in this respect is being made only slowly. Therefore there is a need for theoretical models and numerical simulations to improve the homogeneity of the microstructure of the ceramic material, the prediction of the shrinkage rate and the reduction of the firing stage of the process. For a general overview on ceramic processing we refer to Reed [88]; comprehensive reviews about sintering phenomena can be found in Exner [23] and Sōmiya and Moriyoshi [97].

In order to illustrate the complexity of the physical principles involved, we give a rough description of solid-state sintering. In this type of sintering, one usually distinguishes between five main transport mechanisms which can occur simultaneously, cf. figure 1.1. Three mechanisms cause particle growth only and do not lead to shrinkage and reduction of porosity; they are (1) transport of material through the gaseous phase by evaporation from areas with large radii of curvature and condensation on those with small radii, flow of material (2) by surface diffusion and (3) by volume diffusion of vacancies in the atomic structure starting from the surface. Two mechanism cause densification of the compact, i.e. (4) grain boundary diffusion and (5) volume diffusion starting at the grain boundary.

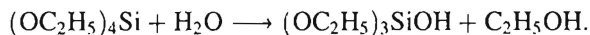
In viscous sintering the material transport is caused by a volume flow driven by surface tension. In this type of sintering there are no grain boundaries between two coalescing particles since we consider fluids. When in the sequel the term *viscous sintering* is used, we refer to a viscous sintering process where the volume flow is taken to be Newtonian and incompressible. Sintering processes of this type occur in the sintering of amorphous materials such as glasses; at sintering temperature glasses appear to behave like incompressible Newtonian fluids reasonably well (cf. De With and

Corbijn [113]).

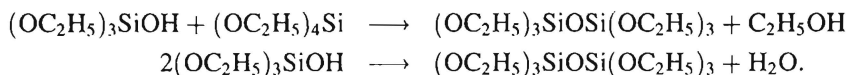
A recent technological application in which viscous sintering occurs, is the production of high-quality glasses (monoliths) which cannot be manufactured in a traditional way. For example, glasses with a component preferentially evaporating at high temperatures, have to be produced at temperatures lower than the temperatures at which glasses are produced normally, and so sintering must be applied in their manufacturing. One of the characteristics of sintering is that it occurs at a relatively low temperature; the particles are already coalescing at one-half to two-third of the melting temperature. In this way, also glasses with an extremely high melting temperature can be produced by applying the sintering technique at a substantially reduced temperature. In the traditional manufacturing of glass contamination of the glass melt occurs by corrosion of the melting crucible. Since this happens more easily at higher temperatures, sintering can be applied in the production of glasses free of such crucible contaminants which are particularly important for the manufacturing of some high technology materials.

One method to make a monolith is the viscous sintering of a glassy compact that is produced in a controlled manner by the so-called *sol-gel* technique. In sol-gel processing, colloidal particles in a suspension, a *sol*, is heated or mixed with a liquid (acid or basic). This causes the particles to aggregate or polymerize and form a giant aggregate or molecule that extends completely throughout the sol; the substance is said to be a *gel*. The fundamental importance of this technique is the ability to tailor the microstructure on molecular length scales. For example, a wide range of gel structures can be obtained by varying the pH of the liquid. Sol-gel techniques and their applications are extensively discussed in the books of Brinker and Scherer [12], Klein [56] and Paul [76].

There are two kinds of sol-gel techniques: dispersion of colloidal particles from ionic species in an aqueous medium (water) and the more commonly applied technique of the hydrolysis and polymerization of alkoxides in an organic solvent (normally an alcohol). Here we briefly discuss the latter technique to show the typical chemical reactions involved to produce such a sol-gel. More specifically, we consider the forming of a silica gel by hydrolysis and polymerization of the alkoxide tetra-ethoxy-silane, $(\text{OC}_2\text{H}_5)_4\text{Si}$, in an alcohol solution (cf. Klein [56] p.84). The adding of water under acid or basic conditions catalyzes the hydrolysis of the alkoxide into hydroxyl groups. This can be represented by the following reaction



The by-product $\text{C}_2\text{H}_5\text{OH}$ can readily be removed by volatilization. Subsequent condensation reactions of the hydroxyl groups produces net-works composed of inorganic oxide linkages (polymerization) plus the by-products water and alcohol. This *gelling* is described by the following two reactions



As polymerization proceeds, the viscosity of the sol slowly rises until the so-called *gel point* is reached. Then the gel is composed of continuous solid and liquid phases, the

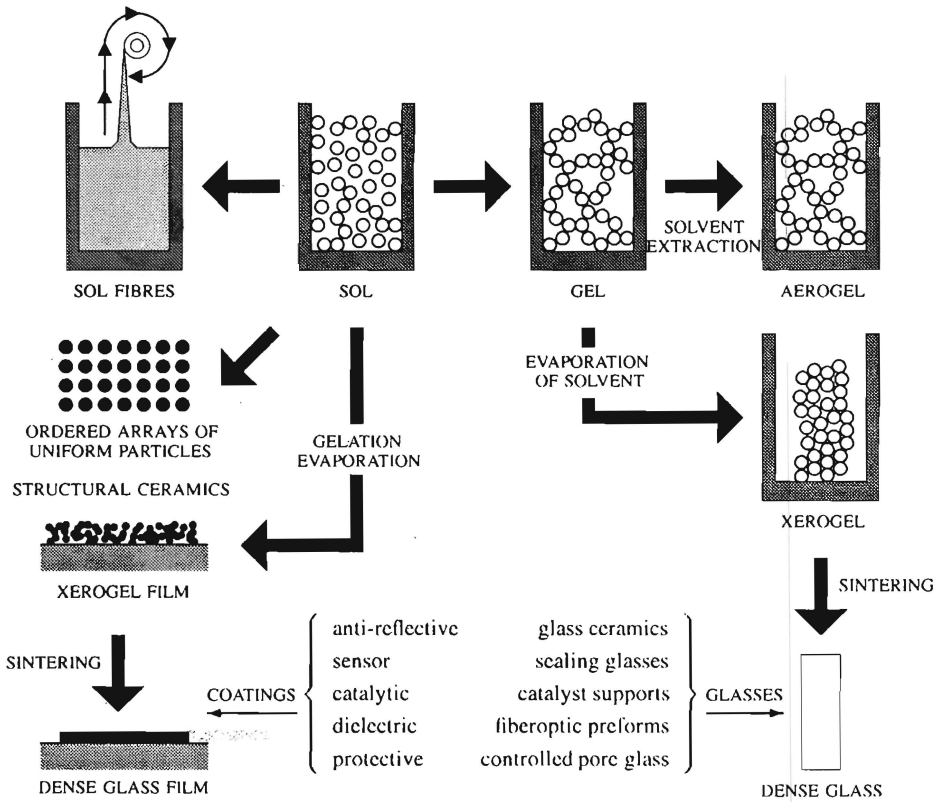


Figure 1.2 A schematic overview of sol-gel processing for ceramics which includes powder forming, monoliths, fibres and thin film coatings (after Brinker [11]).

solid phase prevents the liquid from escaping and the liquid phase prevents the solids from collapsing (Brinker [11]).

A schematic overview of sol-gel processing is given in figure 1.2 which includes powder forming, monoliths, fibres and thin film coatings (obtained from Brinker [11]). Here we will briefly dwell on the production of the latter two applications, i.e. fibres and thin films. Monolithic applications were discussed already.

There are two main methods of making fibres by sol-gel processing. The first method consists of pulling fibres from the solution during an appropriate viscosity period (cf. Klein [56] p.142). In the second method, a monolith is formed, dried and sintered and then the fibre is drawn; it is possible to dry the gel in a conventional way by removing the remaining liquid phase (alcohols and water) at ambient or moderate temperature ($< 100^{\circ}\text{C}$) and during this drying stage considerable shrinking of the gel network occurs. But because of the relatively large structure of the gel compared to the pore sizes (1-50 nm), the drying has to be performed extremely slow to avoid cracking of the gel. For example, the drying of even small monolithic pieces can last a period from a few days to even months. Finally, one obtains what is called a *xerogel*.

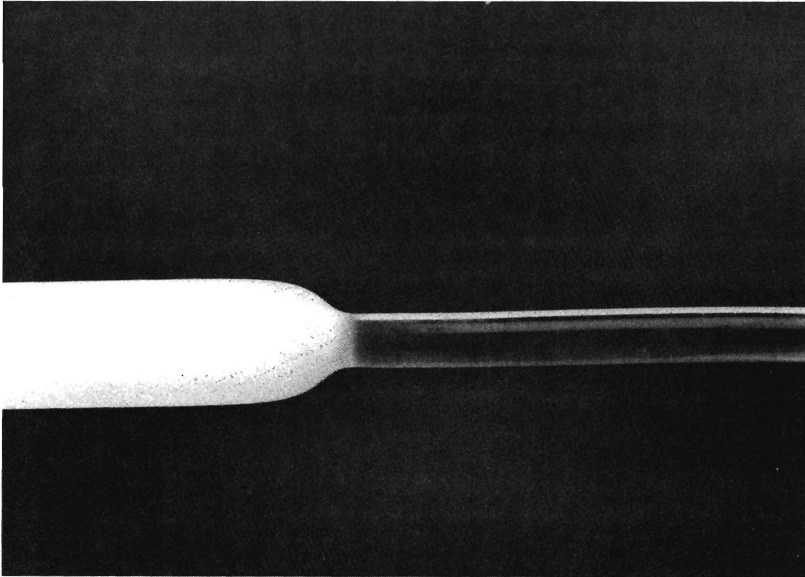


Figure 1.3 A partially densified aerogel into glass, which is obtained by moving the aerogel through a hot zone.

A much faster method without shrinking the gel is hypercritical drying. This is achieved by heating up the gel above the critical temperature in an autoclave with excess solvent. This excessive liquid evaporates and produces a high pressure on the gel preventing premature drying of the gel. When the system has exceeded these critical conditions, the pressure is released by keeping the temperature above the critical point. Then an extremely light material is obtained from which most of its volume is taken up by air: this is normally called an *aerogel*. A popular description of such an aerogel has been given by Fricke [26]. When the aerogel is heated to a sufficiently high temperature, the viscosity of the glass becomes low enough for surface tension acting on the interior surface of the gel to cause the gel to collapse into a *hopefully* dense and homogeneous glass from which the fibres can be drawn. This technique has been used in the production of glass fibres for the telecommunications industry. In figure 1.3 an example of a partially densified aerogel is plotted which is obtained by moving the aerogel through a hot zone (from Mulder *et al.* [71]).

Sol-gel processing can be applied also to make thin film coatings. Techniques that are used for producing such a thin film out of a sol-gel solution include: spraying processes, dipping processes in which the surface to be coated is withdrawn from the solution and spinning processes spreading the liquid from the centre of a rotating substrate. Since the obtained layers are only a few hundreds nanometers thick, the solvent evaporates readily and one obtains a xerogel film which is sintered thereafter. Applications for these sol-gel coatings can be found in optics (especially anti-reflective coatings for silicon solar cells, glasses and plastics), in electronic and sensor devices, in corrosion resistance and in

strengthening (see also figure 1.2).

As we observed already, the sintering process is the final step of the gel-to-glass transition, when the dry gel is converted into a densified glass. We may distinguish two stages. The first stage of this heat treatment process is performed at moderate temperatures but higher than the one used for drying (up to ca. 500°C); the second stage is performed at temperatures higher than 700°C. During the first stage, the residual alkoxy and hydroxy groups are removed by the condensation reactions previously mentioned, which amounts in only negligible densification of the gel compact. In the second stage, depending on the heating rate, the pores will gradually disappear which yields shrinkage of the gel. Even higher temperatures are needed to make larger pores collapse. However, the closing of the pores may trap residual volatiles such as water, organic residues and carbon. Trapped impurities can lead to bloating, swelling and foaming as heating progresses. Finally, assuming these problems can be avoided, the sintering process has to be completed before significant crystallization of the glass starts to occur. The rate of sintering and of crystallization increases and the viscosity of glass decreases as the temperature rises. This is an extra difficulty that one has to take into account. More about the gel to glass transition can be found in the reviews of both James [51] and Orgaz [75].

Most studies on viscous sintering aim at better insights in the densification kinetics of such a gel (compact). In particular, one is interested in the shrinkage rate as a function of the important variables involved such as viscosity and particle size, thus reflecting how time, temperature and microstructure influence the development of the densification process. One wants to know what kind of structural configuration leads to a higher free energy of the gel and hence to a higher densification rate. Moreover, one is interested to find controlling factors that influence besides the processing time and temperature, the bubbles and properties of the finally obtained densified glass.

Clearly, a deterministic description of the viscous flow of a structure as complicated as a dried gel (xerogel or aerogel) is out of the question, even when restricting to a simple Newtonian constitutive model. The structure is simply too stochastic for such an attempt to be successful. Hence, the first attempts describing sintering phenomena dealt with the behaviour of simple systems only, like the coalescing of two spheres, or the sintering of a sphere onto a flat surface, hoping to recover the phenomenological behaviour for macroscopic systems by this. An overview of such studies will be given in the next section.

In later attempts one tried to determine a representative unit cell within such a gel and to simulate the sintering of that particular cell. This unit cell is representative in the sense that it reflects the sintering of the gel as a whole. Such a unit cell may consist of a number of particles, depending on the structure of the compact, this cell is also referred to as a *meso-cell* (De With [112]).

The ultimate goal of the present research, reported in this thesis, is the development of numerical algorithms that are able to simulate the sintering of such a meso-cell. Point of departure is the simulation of simple unit problems. However, the applicability of the software developed is not restricted to such viscous sintering problems only. It turns out that these algorithms can be applied to all kind of problems which involve a curvature

driven Stokes flow.

1.2 STATE OF THE ART

This section consists of two parts: firstly, we give a review of the general approaches that have been applied to formulate the kinetics of viscous sintering both analytically and numerically. Secondly, we review the numerical methods applied to solve the creeping flow problems involved.

1.2.1 Analytical Approaches to Viscous Sintering

Most mathematical models of viscous sintering to date are based on an empirical rule first introduced by Frenkel [25] back in 1945. This rule states that the work done by surface tension in decreasing the total surface area is equal to the total energy produced by dissipation of the flow. So in applying this energy balance one has to know beforehand both the shape deformation and the description of the governing flow field during sintering. Generally, this shape and flow field evolution are unknown and approximate descriptions are used which only allow to predict rough estimates of the sintering kinetics. Frenkel's method for analyzing viscous sintering has been used for example by Mackenzie and Shuttleworth [70] and Scherer [92]-[93] subsequently.

Frenkel applied this energy balance to describe the early stage of the coalescence of two equal spherical particles. Therefore, he assumed a uniform uniaxial flow of fluid towards the surface of contact between the spheres, usually called the *neck*. Moreover, he assumed a shape transformation by letting the centres of the spheres approaching to one another, forming a sharp neck at the contact. In order to preserve the volume of the spheres, Frenkel also made the assumption that the spherical radii grow as coalescence proceeds. It appears that these assumptions are reasonably valid during the early stage of the coalescence. The equation that follows from his model shows that the neck develops proportionally to the square root of the sintering time. Other models to describe the shape deformation of such coalescing spheres have been developed by Nishitani *et al.* [74], Kingery and Berg [55] and Exner and Petzow [22]. The latter two are referred to as *tangent circle models* and can be used to estimate the neck curvature and to describe the rate of approach of the centres of both spheres (shrinkage) during the initial stage.

Experimentally the derived shrinkage rate depends linearly on the sintering time, cf. Kuczynski [61] and Kingery and Berg [55]. Their experiments show that this shrinkage rate applies for even later stages also. However, Exner and Petzow [22] pointed out that the shrinkage rate is also influenced considerably by asymmetric neck growth, particle rearrangement and the formation of new contacts that occur during sintering. This makes the applicability of the linear shrinkage behaviour as a quantitative description of the shrinking of irregularly packed particles dubious.

The model of Mackenzie and Shuttleworth [70] (MS-model) is generally accepted for the late-stage viscous sintering. In this model, the densification results from the shrinkage of uniform spherical pores distributed throughout the compact. Hence the

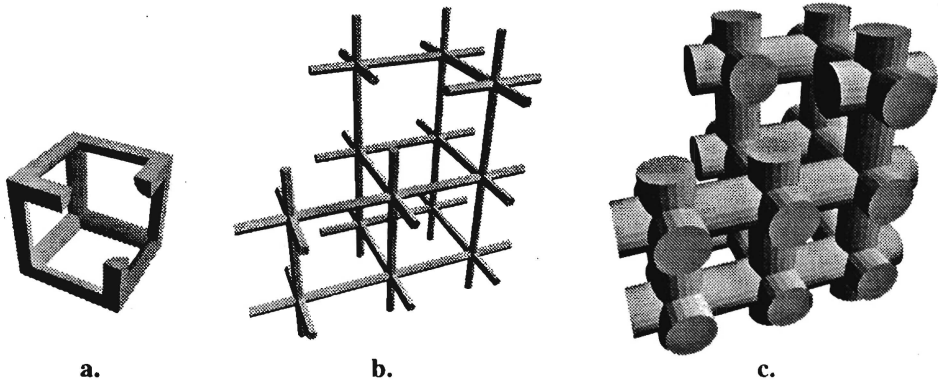


Figure 1.4 Microstructural model of a gel developed by Scherer [92] consisting of liquid cylinders in a cubic array: (a) is the unit cell of the microstructure, (b) and (c) are a low and a high density gel structure respectively.

MS-model is also referred to as the *closed pores model*. Different from the previous mentioned descriptions, the flow field of an individual spherical pore can be calculated analytically because of the simple geometrical deformation. After applying Frenkel's empirical rule, the MS-model leads to an equation for the sintering time necessary to reach a particular density of the compact.

Scherer [92] developed the so-called *open pores model* that assumes the gel to be a regular three dimensional array of interconnected liquid cylinders and considered its shrinkage. This model was used by Scherer to analyze the early and intermediate stage of the sintering of gels. For the unit cell that represents this structure, Scherer took a cubic array that consists of intersecting cylinders on all the edges from which the total surface was calculated (see also figure 1.4). After applying Frenkel's energy balance, he obtained an analytical relationship between the relative density and the time. However, the model breaks down when the pore is trapped in each cell, in the late sintering stage. Scherer's main result is a figure showing the density of the gel as a function of time which is very close to the predicted densification rate of the MS-model. In [93], Scherer extended his model to bimodal pore-sizes distributions. In [94], Scherer and Garino present analyses for the sintering kinetics of porous glass layer on a rigid substrate (i.e. thin film). A review of experimental studies to verify the above presented densification models for the case of gels is given by Orgaz [75].

Starting from the surface curvature driven Stokes's flow equations, without any assumption on the shape deformation and flow field, Hopper [41]-[44] solved two unit viscous sintering problems analytically, viz. the coalescence of two equal cylinders (Hopper [41],[42]) and the coalescence of a cylinder on a half-space (Hopper [44]). He applied a conformal mapping technique to solve the Stokes equations in which the time evolution of the shape was described in terms of an equation of motion involving the mapping function (see also chapter 3). In Hopper [42], the method is demonstrated for a number of regions which are bounded by a simple smooth closed curve. Moreover, Hopper was able to solve some problems for semi-infinite regions also. However, the

examples in the referred papers show that his method depends on *guessing* a mapping function which, initially, has a built-in behaviour that describes the time evolution of the shape. The difficulty of finding such a mapping is illustrated in Hopper [43]: the only doubly connected domain he could solve this way was a circular disk with circular hole centred at the origin. This problem can also be solved easily with the use of cylindrical coordinates.

Some mathematical and physical details of Hopper's solution method, in particular the kinematical aspects, are discussed by De Graaf [29]. Richardson [89] was able to solve the unit problem of the coalescence of two unequal cylinders by applying Hopper's method. Antanovskii [2] solved the problem of a two-dimensional deformable bubble in a viscous flow by applying a similar conformal mapping technique. He suggested that his solution might be applied to investigate the densification of pores. Scherer [95] used the geometric evolution function that describes the coalescence of two equal cylinders as an approximation for the evolution of two sintering spheres. He tried to estimate the coalescing rate of those spheres by applying Frenkel's energy balance. Therefore, the flow field has to be calculated or guessed in which he did not yet succeed.

An experimental verification of Hopper's solution for two equal coalescing cylinders has been performed by Korwin *et al.* [57]-[58]. They considered the sintering of two fibres of initial diameter 0.25 mm and obtained a reasonably good agreement between the measured values and the analytically values (i.e. the deviation was ranging from 10 to 15%). Recently, De With and Corbijn [113] studied experimentally the sintering of a cylinder on a half space by considering the relaxation of glass fibres, with diameters of approximately 50, 130 and 190 μm , on a plate of similar glass. They observed an excellent agreement between the shapes obtained experimentally and the theoretical predictions of Hopper [44]. Moreover, the *maximum* relative difference for the neck diameter between the experimental and theoretical values was 5%. In this paper, a method is also outlined for the determination of the surface tension of glass at relatively low temperatures (600° C) by using the fiber-on-plate experimental results together with Hopper's analytical solution.

1.2.2 Numerical Solutions of Viscous Sintering

Application of computational methods by which the viscous sintering process is simulated, is relatively recent. Generally, these numerical simulations are carried out by successively solving the Stokes problem for the present level geometry, and employing a time step (usually Forward Euler) to predict the next level geometry.

The first attempt to simulate a unit problem of viscous sintering numerically was performed by Cosgrove *et al.* [18]. They considered the sintering of an infinite line of cylinders by employing a partly analytical and numerical technique based on Fourier series. In order to solve the equations involved, it was necessary to assume that the surface was locally planar. Hence, their solution was restricted to the late sintering stage. Hrma and Carter [45] used a similar method to simulate the late stage of the coalescence of two equal spheres and the relaxation of some other axisymmetric shapes with smooth curves (nearly spherical). They described this boundary curve as a series

of Legendre polynomials. From this an expression for the boundary velocity in terms of a similar series was obtained. For their solution, it was required that the boundary consists of planar parts too.

The first genuine numerical simulation of a unit problem of viscous sintering was carried out by Ross *et al.* [90]-[91]. Like Cosgrove *et al.*, they considered the sintering of an infinite line of equal cylinders and performed their simulation by employing a Finite Element Method (FEM) to solve the Stokes problem. Unfortunately, they kept the center to center distance between those cylinders fixed (no shrinkage) which makes their study of less interest to our case. Jagota and Dawson [48]-[50] were the first who could simulate some realistic unit viscous sintering problems. They applied the FEM to two axisymmetric problems, i.e. the coalescence of two equal spheres and of an infinite line of equal spheres. In Jagota and Dawson [49], the calculated behaviour of the two coalescing spheres is used to simulate the densification of a powder compact. In that paper, the particle packing is modelled as a framework of links between any pair of touching spheres and the growth of those links is described by considering the behaviour of each pair of coalescing spheres separately.

The difficulty in applying a FEM lies in the motion of the mesh since the error of the approximate solution depends on both the regularity of the triangulation and the angles of such a single triangle. These angle may not become too small. Especially in the neighbourhood of the neck region, a distortion of the triangulation occurs as time proceeds. Those difficulties regarding a moving mesh occur also in a recent study of Helmes [37] who applied the FEM for the sintering of arbitrary two-dimensional fluid domains. Jagota and Dawson [50] solved this problem by dividing the FEM mesh in a number of subregions and after each time step, they regenerated only the triangulation of the neck region. The whole mesh was regenerated after a few hundred of time steps.

Kuiken [62]-[63] simulated viscous sintering problems for domains with moderately curved shapes; he used an integral representation in terms of the stream and vorticity function. A Boundary Element Method (BEM) was employed to solve the resulting equations, i.e. a collocation method. In summary, this method consist of discretizing the boundary into a sequence of nodal points and both the curve and unknowns are approximated by element-wise truncated polynomial expansions (basis functions). Kuiken was inspired by the work of Ingham and Kelmanson [47] who applied this approach to solve a number of potential and biharmonic problems in which a free boundary was involved. Since the only interest is the motion of the total fluid domain, the sintering problem is suited ideally to be solved by the BEM. Another advantage of the BEM is that the dimensionality of the problem is reduced by one, i.e. the two-dimensional mesh is replaced by a discretized boundary curve which makes the redistribution of collocation points easier in some way. However, Kuiken's approach shows serious numerical problems when simulating a geometry that shows a more extreme curvature. Those problems are due to inaccuracies in computing the derivative of the curvature, required in the chosen integral formulation (driving force). Therefore, the method can only be applied to simulate rather smoothly shaped domains.

Another integral formulation of the Stokes problem is based on boundary distributions of hydrodynamical single- and double-layer potentials where the velocity and

surface tension are the primary variables. This representation will be referred to as the *SDLP-formulation* here. In essence, this integral formulation was obtained by Lorentz [69] back in 1896. In the next subsection we point at a number of numerical studies to simulate the deformation of the interfaces between two different fluids and the corresponding motion at each fluid medium based on this formulation. Examples of the phenomena considered are the flow of a suspension of bubbles, drops, biological cells, etc.

On Kuiken's suggestion, Van de Spek [98] studied the applicability of this integral formulation to the sintering problem. As already mentioned, the sintering problem requires the determination of the boundary velocity field only. Hence the *SDLP-formulation* appears to be the best choice in determining this unknown velocity field, since it has the nice property that those unknowns are obtained without any overhead of useless information. This formulation will be solved numerically by applying a BEM.

1.2.3 Integral Method and Numerical Solution for Stokes Flows with Moving Boundaries

This subsection reviews the application of the *SDLP-formulation* based on hydrodynamical single- and double-layer potentials to Stokes flows with moving boundaries. The movement of the boundary is described by a kinematic constraint that relates the change of the boundary curve to the velocity at the curve, i.e. a *quasi-static* approach is employed. The *SDLP-formulation* appears to be a Fredholm integral equation of the second kind. It can be deduced by applying a fundamental singular solution of the Stokes differential equations for the free-space into the so-called Green's integral identity. More precisely, that fundamental solution is used that represents the velocity field in the free-space induced by a force in a fixed point. This solution is also referred to as the flow due to a *Stokeslet*. A proof of the existence of solution is given in Ladyzhenskaya [64]. Fundamental solutions for geometries other than the free-space, like a rigid plane wall, can be found in Pozrikidis [82].

In the middle of the seventies, Youngren and Acrivos [115] were the first to apply this representation for the simulation of viscous fluids. They presented calculations for exterior flow past three dimensional rigid particles of arbitrary shape using a single layer potential formulation. Shortly thereafter, Rallison and Acrivos [86] extended the method to study axisymmetric flow past deformable drops and Lee and Leal [67] considered the motion of rigid spheres near deformable interfaces. At the moment, most work is done on axisymmetric and two-dimensional flow problems which ranges from the study of rising (deformable) drops towards an interface (see, for instance, Geller *et al.* [28], Chi and Leal [16] and Pozrikidis [79],[83],[84]), to problems as the deformation of a blood cell (Pozrikidis [80]), the deformation of a liquid film along a wall (Pozrikidis [78], Pozrikidis and Thoroddsen [81]) and the gas-liquid drainage in a capillary cavity (Lasseux [65]). Moreover, a generalization of the *SDLP-formulation*, i.e. the complete double layer integral representation developed by Power and Miranda [77], is used to solve the problem of multiple particle interactions (microhydrodynamical problems) that occur in

filtration, floatation, aggregation and deposition processes (Kim and Karrila [54]). To be able to handle a large number of particles, they developed efficient parallel computing algorithms which enabled them to consider of over a thousand particles (Karrila *et al.* [53]). Studies of three dimensional arbitrarily shaped surface deformations are still in their early stages and only modest distortions have been computed.

In early numerical approaches to solve this integral formulation for viscous flow problems, BEM techniques were used in which the velocity and tension are taken constant over each boundary element, i.e. the so-called constant boundary element method. Later approaches use a higher order local piecewise polynomial interpolation or global interpolations involving all nodal points by applying spline functions (Cabral *et al.* [14]-[15]). Thereafter, the discretized integral equation is enforced on all the collocation points to produce a square full rank system of linear algebraic equations for the unknown variables (i.e. usually the velocity field). The resulting completely filled square matrix equation may be solved by a direct method like Gaussian elimination with partial pivoting. However, when dealing with a large system of equations, Kim and Karrila [54] and Pozrikidis [82] claimed that it may be more efficient to use an iterative solution method from a computational point of view. For the initial guess of such an iterative method generally the solution of the previous time step is taken. Monographs that outline the numerical implementation of the BEM are, among others, Jawson and Symm [52], Brebbia *et al.* [8]-[9] and Becker [7].

Having calculated the boundary velocity field at a fixed time by the BEM, a time step has to be performed to obtain the boundary deformation at the next time level. The difficulties that have to be taken care of during the evolution of such a fluid domain are the following: (1) the boundary condition involves the computation of the curvature in order to describe surface tension effects which requires an accurate evaluation at the boundary. Furthermore, the boundary may undergo large distortions during the deformation; this causes (2) that the collocation points become unevenly distributed. This will lead to numerical inaccuracies in computing the boundary conditions as well as the unknowns to be calculated. Moreover, (3) non-analytic cusp-like curves may evolve and (4) the connectivity of the domain can change by breaking up or touching of boundaries.

As mentioned before, the boundary movement is modelled by a kinematical constraint. Generally, three kinds of constraints are distinguished, i.e. the so-called Eulerian, Lagrangian or the mixed Eulerian-Lagrangian point of view.

In the Eulerian viewpoint, the collocation points on the boundary move in the direction normal to the boundary and so the normal component of the boundary velocity field is used. An advantage of this approach is that the nodal points tend to remain evenly distributed for a smooth boundary. However, in the neighbourhood of cusp-like regions the collocation points need to be redistributed since otherwise these nodes come too close to each other leading to numerical instabilities. A disadvantage of this approach is the difficulty of the implementation of higher order time integration schemes for the governing kinematic constraint. Therefore, only a simple Forward Euler method is employed to obtain the next time level geometry.

In the Lagrangian viewpoint, the nodes are considered to be material points and

moved according to the actual boundary velocity, i.e. the characteristic curves are followed. Actually, one obtains a system of nonlinear ordinary differential equations (ODEs) which can be solved easily by employing a multistep integrator. However, in literature, generally the Forward Euler scheme is applied to solve these ODEs. Yet, some higher order explicit time integrators were implemented by Longuet-Higgins and Cokelet [68], Haack *et al.* [32], for example. Both applied an Adams-Bashforth-Moulton method. A Runge Kutta scheme was applied by Ramsden and Holloway [87]. When the system of ODEs appears to be stiff such explicit methods will not be very efficient, however. The disadvantage of the Lagrangian description is the tendency to sweep nodal points tangent to the boundary even if only small deformations occur. Hence, the collocation points have to be redistributed frequently.

In the mixed Eulerian-Lagrangian viewpoint the path line of a fluid particle is followed by using a higher order Taylor expansion in terms of the material time derivative. This explicit time stepping method has not been applied yet in the case of Stokes flows. However, it has been used successfully in the simulation of water waves when the velocity field can be modelled by Laplace's equation, e.g. see for instance, Grilli *et al.* [31] and Cooker *et al.* [17]. In order to obtain the coefficients of the Taylor expansion in the latter problem, one has to solve a successive number of Laplace problems for the velocity potential and its time derivatives (depending on the number of terms that is applied).

In this thesis the SDLP-formulation is solved by applying linear or quadratic boundary elements. As kinematic constraint is used the Lagrangian viewpoint, since this enables the applicability of higher order time integration schemes. In order to accomplish that the nodal points are kept evenly distributed, an efficient node redistribution scheme is developed.

More about recent numerical techniques for the solution of Stokes flows can be found in a general review of Weinbaum *et al.* [110]. Tanzosh *et al.* [100] reviewed the numerical solution of free creeping Stokes flows in which the integral formulations of single- and/or double-layer potentials are applied. The recent books of both Kim and Karrila [54] and Pozrikidis [82] extensively outline the theoretical derivation and the practical application of such formulations. A review on the present state-of-the-art of numerical solution methods that can be used for viscous flows with moving boundaries are to be found in Floryan and Rasmussen [24].

1.3 THE CONTENTS OF THIS THESIS

This thesis is a further elaboration of earlier work of the author *et al.* [102]-[107] with respect to viscous sintering phenomena. We outline briefly the contents of each chapter of this thesis.

In chapter 2 we describe the derivation of the mathematical formulation that is applied to model viscous sintering. Basically, this physical process can be modelled by the full-scale Navier-Stokes equations which describe the motion of a fluid in general. Assuming the fluid to be Newtonian and incompressible, making the Navier-Stokes equations

dimensionless and assessing the parameters of the involved physical quantities, we arrive at the Stokes (creeping) flow equations. From thermodynamical considerations, it follows that on the fluid boundary the tension in the outer normal direction has to be proportional to the mean surface curvature. With this boundary condition, the flow equations can be solved for a fixed fluid domain up to an arbitrary rigid-body motion of the domain in principle. Since the time-dependency does not appear in the governing Stokes equations explicitly, we have to define a kinematic constraint that describes the movement of the fluid region. For this kinematic equation of motion we apply the Lagrangian description of the boundary velocity field. Furthermore, we show that an arbitrary sintering domain is evolving to a spherical shape as time proceeds, since a sphere minimizes the surface of a shape that occupies a particular amount of matter. As we already discussed in the previous section, the viscous sintering problem is suited ideally to be solved numerically by the BEM. Therefore, the creeping flow equations are transformed into an equivalent system of integral equations, i.e. the SDLP-formulation. First we consider the derivation of this formulation for a simply connected domain. It appears that the rigid-body motion functions span the null space of the involved integral operator: the double layer potential. In order to make the formulation uniquely determined, this double layer potential is “deflated” with respect to the rigid-body motions. Secondly, we outline the extension of the SDLP-formulation to a multiply connected domain. Note that in all simulations mentioned in section 1.2, the sintering problem was considered for simply connected domains only. It turns out that besides the deflation of the rigid-body motions, we have to apply an deflation of the outer normal which appears to be a eigenfunction of the adjoint of the double-layer potential. The latter deflation has to be performed in order to obtain a formulation that is capable to describe the shrinkage and expansion of the holes inside the fluid domain correctly.

The objective of chapter 3 is to deduce simple expressions approximating the exact analytic solution of some unit problems in viscous sintering. These exact solutions are obtained by applying Hopper’s solution method [41]-[44] for the two-dimensional Stokes problem driven by surface tension on the free boundary. The analytic solutions corresponding to the coalescence of two cylinders with arbitrary initial radii and a cylinder on a half space are briefly described; they appear to be fairly complicated. However, these solutions are very useful for finding simple approximate expressions relating sintering-time, neck curvature and shrinkage rate to the coalescence rate, both in the case of the two equal coalescing cylinders and in the case of a cylinder coalescing on a half-space. These problems may be considered as special limit situations of the coalescence of two unequal sintering cylinders. A comparison is made between the obtained approximations here and the approximations that can be found in literature and which were derived by modelling the coalescence in a very simple way. This comparison shows that especially the neck curvature and the time dependence of the neck growth differ from earlier descriptions.

In chapter 4 we consider in more detail the numerical solution of the SDLP-formulation by the application of the BEM. This results into a full rank system of linear algebraic equations for the unknown boundary velocity field at a fixed time. Moreover, we pay special attention to problems that can occur from numerically approximating the

curvature, especially when at a certain point of the boundary a cusp arises. The curvature at this cusp point may become very large; as a consequence the approximation error may be large due to numerical cancellation since collocation points become very close to each other in such a region. In order to handle this problem, we propose an algorithm for a fairly optimal grid (re)distribution based on equidistributing the curvature of the boundary. The algorithm treats cusp regions in such a way that the curvature of this particular region is preserved after redistribution and thus (numerical) oscillations in the computed velocity field are avoided. Another objective of the algorithm is a nearly optimal number and position of the discretization points, which is important for a minimal of the computational cost per time step.

Chapter 5 deals with the numerical solution of the motion of the fluid domain in time. Substituting the Lagrangian representation for the velocity of the collocation points into the system of algebraic equations derived by the BEM, we obtain a system of non-linear Ordinary Differential Equations (ODEs). In this chapter we consider the numerical integration of this system of ODEs. It turns out that for most of the geometrical shapes under consideration, the system of ODEs is *stiff*. Because of this, the time step will be carried out by a more sophisticated time integrator: a variable step, variable order Backward Differences Formulae (BDF) scheme. Thus, opposite to all earlier mentioned studies, we will use an *implicit* multistep method. The numerical implementation of this integration method will be outlined. In particular we will high light some important features like the approximation of the Jacobian matrix and the continuation of integration after a mesh redistribution.

The subject of chapter 6 is the question of the conditioning of the sintering problem with respect to the evolution of sharply curved domains based on a simple but typical example, viz. the evolution of the coalescence of two equal cylinders. This example demonstrates the main features of the cusp evolution of the sintering phenomenon very well. Moreover, the exact analytical solution is available. By using this analytical solution we are able to give a fairly quantitative sensitivity analysis; i.e. we can investigate the influence of a perturbation of the initial cylindrical radius, the measure of contact and the neck curvature on the shape and curvature of the region where those cylinders are touching. From this analysis we will draw conclusions about the conditioning of the coalescence as an evolutionary problem and as a boundary value problem at each time step as well. As a result, we can explain that both the exact and the numerically obtained neck curvature differ quite a bit in the early stage of the coalescence while this difference does not show any noticeable effect on the numerically obtained coalescence rate between both cylinders.

In chapter 7 the numerical results obtained by simulating a number of two-dimensional sintering geometries is presented in order to demonstrate both the typical evolution properties and the developed numerical code. In particular a few analytic densification models are compared with the results obtained by the simulation of two-dimensional shapes, which give some quantitative insights in the applicability of those models. Also the sintering of cylindrical packings is considered. It is shown that the unit problem of two equal coalescing cylinders can be used to describe the sintering behaviour of a regular and equally sized particle packing. In the case of an irregular packing, effects

are shown that occur due to these irregularities.

Finally, in chapter 8, we extend the numerical solution method to axisymmetric domains, i.e. domains formed by rotating a two-dimensional plane about a given axis. Because of this axial symmetry, a three-dimensional sintering problem can be reduced to a two-dimensional one since the motion is unknown in the axial and radial direction only. Hence the developed node redistribution algorithm and the time integration method also apply to these problems. In this chapter we briefly outline the derivation of the governing integral formulation used to simulate axial symmetric domains without inside holes in the fluid. Moreover, we discuss some numerical aspects of the solution of this integral equation by the BEM-BDF method as described earlier. Finally, these algorithms are applied to simulate some typical axial symmetric sintering geometries.

1.4 OUTLOOK ON FURTHER DEVELOPMENTS AND APPLICATIONS

The sintering simulations shown in the chapters 7 and 8, demonstrate the present capabilities and limitations of the designed numerical code. As a limitation we mention that we cannot yet handle the touching of boundaries which occur in some of the two-dimensional and axisymmetric example shape evolutions. Hence, it is clear that a further improvement of the simulation capabilities may be achieved by the design of a detect and handle algorithm for the case of such touching boundaries.

This problem is not quite straightforward, since it requires a measure that indicates when two boundaries are coalescing. Of course, this measure has to depend on the discretization error too. After the coalescence, the surface curvature of the coalescing region has to be prescribed. The most sensible value for this curvature may be taken to be the neck curvature obtained from the unit problem of the sintering of two cylinders or spheres. The initial radii of these cylinders (spheres) should then be chosen such that they mimic the both parts of the coalescing surface locally quite well. And of course, experimental verification has to be carried out, to justify this choice. Starting in two-dimensions, such experiments could concern the sintering of a packing of well-controlled glass fibres. Thereafter, the results of these experiments can be compared with the numerical simulation of that particular packing. A question that should be answered is the occurrence of other forces (like van der Waals forces) during such a stage.

Dealing with a more complicated geometry, like a meso-cell, brings along the problem of the rapid increase of the number of unknowns. The scale-up of the code requires extra effort with respect to the data structures and indeed the computation as such. It seems that the use of a super computer may be needed eventually. Because of this, research has to be devoted to parallelizing the computations. Other research activities may be concentrated on both the development of a faster solver for the system of equations and a cheaper approximation of the Jacobian matrix required for the time integration scheme when the fluid domain contains a large number of holes.

A further extension is the introduction of solid particles in the viscous flow. One of the problems in simulating such a flow will be to model the contact between a liquid and a solid interface. However, naturally, there will be an overlap with the simulation of two touching glass boundaries. Then can be investigated the behaviour of lumps in a sintering gel. Another application of this extension is in the study of two-phase sintering, i.e. processes in which both a liquid phase (glass) and a solid phase exist. Two phase sintering phenomena occur during the vitrification of sanitary ware and ceramic tiles, for example. Yet in order to understand and - if necessary - to improve this process both for the glass and the ceramic body, it is important to study the sintering on a microscale, i.e. the actual process of coalescence of a small number of particles. For instance, one is interested in determining the melting activity as a function of the magnitude of the particles, which typically measure about $50 \mu\text{m}$ (with a broad distribution). Here one needs numerical simulations of what we called a meso-cell. Insight in the sintering of such meso-cells even gives clues to macroscopic properties, like porosity structures, which determine the quality of the product. Typically for ceramic floor tiles one tries to bring this porosity down to 2% and for sanitary ware to less than 1%. The temperature of the product during the processing stage is varying to take care of various processes that occur in such a multicomponent material. A temperature cycle may last from about 2 hours till about 10 hours depending on the material and the desired properties of the end product. Sometimes the vitrification may be done in two shifts.

Another possible application of the numerical code designed in this thesis is the surface deformation of viscous material, partly free and partly confined by a mould. Thus, the numerical simulation of the rheology of filling valleys in the mould under the influence of a small pressure so that surface tension effects are not negligible. This problem arises in the pressing of glasses where a specified surface morphology is required, for example the inner side of the screen of a cathode ray tube. The main question is whether full transfer of mould morphology to the glass is obtained, given a certain set of experimental parameters as time, temperature of glass and mould, and pressure. The temperature-time profile during contact of the mould is important since the viscosity is highly temperature dependent. However, a first approach to tackle this problem might be to model the fluid as a temperature independent flow. Then this simplified flow is governed by the Stokes equations basically. Moreover, this problem is ideally suited to be solved by a BEM type algorithm as presented in this thesis.

After the mould is withdrawn from the glass, the pressed morphology is smoothing out, since the viscosity of the glass is still low enough for the occurrence of a fluid flow driven by surface curvature. This effect causes that the finally obtained morphology of the glass to differ considerably from the profile of the mould. A first attempt to model this problem was recently performed by De With and Corbijn [114]. They developed a model to describe the morphological relaxation of two-dimensional glass profiles for arbitrary temperature-time schedules. In their approach, the surface profile is modelled by a Fourier expansion and for each separate term the decay is calculated in time. From experimental verification, they obtained an excellent agreement with the theoretical predicted shapes. In order to handle this problem numerically, and again assuming that the fluid is independent from the temperature, the present code may be extended easily to

simulate the evolution of a two-dimensional or axisymmetric locally given morphology on an infinite half-space of glass. This extension can also be used to investigate the smoothing of cracks on a glass surface.

PROBLEM DESCRIPTION AND MATHEMATICAL FORMULATION

Viscous sintering problems can basically be modelled by the full-scale Navier-Stokes equation which describes the motion of a fluid in general. We will assume the fluid to be Newtonian and incompressible. After non-dimensionalising these equations and assessing the parameters of the involved physical quantities, we arrive at the Stokes (creeping) flow equations. From thermodynamical considerations, it is shown that on the fluid boundary the tension in the outer normal direction has to be proportional to the mean surface curvature. Applying these (Neumann) boundary conditions, the flow is determined for a fixed domain up to an arbitrary rigid-body motion of the domain.

Since the time-dependency does not appear in the governing equations explicitly, we have to define a kinematic constraint that describes the movement of the region of fluid. For this kinematic equation of motion we apply the Lagrangian description of the boundary velocity field. Furthermore, we show that an arbitrary sintering domain is evolving to a spherical shape as time proceeds, since a sphere minimizes the surface of a shape that occupies a particular amount of matter.

From the outline above, it is clear that we are interested only in the evolution of a particular, initially prescribed, fluid domain. Hence we require the boundary flow field of the evolving shape only. Such a problem is ideally suited to be solved numerically by the Boundary Element Method, since this method obtains the boundary velocity field exclusively. To do this, we have to reformulate the problem as an integral equation over the boundary: we transform the creeping flow equations with (Neumann) boundary conditions into an equivalent set of integral equations.

We start with the derivation of this integral equation for a simply connected domain. It appears that the obtained formulation is a Fredholm integral equation of the second kind, which is expressed in terms of the so-called SDLP-formulation. We summarize some general theorems concerning these type of Fredholm integral equations. These properties are applied to make the integral equation uniquely determined by “deflating” the double layer potential with respect to the rigid-body motions since these motion functions represent the null space of the integral operator.

Finally, we outline the extension of this integral formulation to a multiply connected

domain. It appears that besides the deflation of the rigid-body motions, we have to apply an extra deflation with respect to the outer boundary normal which appears to be an eigenfunction of the adjoint of the double-layer potential. The latter deflation has to be performed in order to have a formulation that is capable to describe the shrinkage and expansion of the holes inside the fluid domain correctly.

2.1 THE MATHEMATICAL MODEL

We consider an incompressible Newtonian fluid that is characterized by the dynamic viscosity η , the surface tension γ and the magnitude of the body say through its cross-section, e.g. length ℓ . The velocity of the fluid is denoted by \mathbf{v} and the pressure by p . A simply connected region of fluid is defined by a closed curve Γ and the interior area is denoted by Ω . In the case of a multiply connected domain, the region is bounded externally by Γ_0 , internally by $\Gamma_1, \dots, \Gamma_M$: the complete boundary will be denoted by Γ . The orientation of the boundary is taken so that on progressing on Γ , the fluid region Ω lies at the *left hand side*.

The motion of the fluid is governed by the following two equations (see, among others, Aris [4], Batchelor [6] and Happel & Brenner [35]). First we require conservation of mass, i.e. the *continuity equation* applies which reduces to

$$\operatorname{div} \mathbf{v} = 0, \quad (2.1)$$

since the fluid is assumed to be incompressible; a vector field \mathbf{v} satisfying equation (2.1) is also called to be *solenoidal*. Secondly, the Navier-Stokes equation (equation of motion) holds for the flow, i.e.

$$\rho \left(\frac{\partial \mathbf{v}}{\partial t} + (\mathbf{v} \operatorname{grad}) \mathbf{v} \right) = -\operatorname{grad} p + \eta \Delta \mathbf{v} + \rho \mathbf{g}, \quad (2.2)$$

where ρ is the density of the fluid and \mathbf{g} is a body force (here we consider only a gravitational force). The latter equation expresses the *conservation of momentum*. Since we assume the fluid to be Newtonian, this yields the following constitutive equation for the *stress tensor* \mathcal{T} , with

$$\mathcal{T}_{ij} = -p\delta_{ij} + 2\eta\mathcal{E}_{ij}, \quad (2.3)$$

where δ_{ij} is the *Kronecker delta* and the rate of deformation tensor \mathcal{E} , which is equal to

$$\mathcal{E}_{ij} = \frac{1}{2} \left(\frac{\partial v_i}{\partial x_j} + \frac{\partial v_j}{\partial x_i} \right). \quad (2.4)$$

Following Kuiken [62], we can define a characteristic velocity v_c , a characteristic pressure p_c and a characteristic time t_c based on the parameters γ, η and ℓ by

$$v_c = \frac{\gamma}{\eta}, \quad p_c = \frac{\gamma}{\ell}, \quad t_c = \frac{\ell\eta}{\gamma}. \quad (2.5)$$

Using these characteristic parameters and taking ℓ as the characteristic length, we obtain for the Navier-Stokes equation the following dimensionless form

$$\text{Re} \left(\frac{\partial \mathbf{v}'}{\partial t'} + (\mathbf{v}' \text{grad}') \mathbf{v}' \right) = -\text{grad}' p' + \Delta' \mathbf{v}' + \frac{\text{Re}}{\text{Fr}} \mathbf{g}', \quad (2.6)$$

where \mathbf{v}' , p' and \mathbf{g}' are the dimensionless velocity, pressure and body force respectively. The differential operators grad' and Δ' denote these operators in the dimensionless space variables. Here Re is the Reynolds number defined by

$$\text{Re} = \frac{\rho \ell v_c}{\eta} = \frac{\rho \ell \gamma}{\eta^2},$$

and Fr is the Froude number which is equal to

$$\text{Fr} = \frac{v_c^2}{g \ell} = \frac{\gamma^2}{g \ell \eta^2},$$

where g is the acceleration of gravity.

For a typical sintering system of a glassy aerogel the magnitude of the characteristic parameters are the following: the particles are of a few micro meter in size or smaller, the density of the gel is $\rho \approx 10^2 \text{ kg m}^{-3}$ (Fricke [26]), the viscosity $\eta \approx 10^8 \text{ N s m}^{-2}$ (Reed [88] p.462) and the surface tension $\gamma \approx 10^{-1} \text{ N m}^{-1}$ (Paul [76] p.125). From these numbers it follows that the characteristic velocity v_c is of order 10^{-9} m s^{-1} which gives a Reynolds number of order 10^{-21} and a Froude number of order 10^{-13} . Hence both the convective and gravitational forces can be ignored in comparison to the viscous forces so that equation (2.6) reduces to the so-called *Stokes creeping flow* equations. In combination with the dimensionless form of the continuity equation (2.1) this yields

$$\begin{aligned} \Delta' \mathbf{v}' - \text{grad}' p' &= 0 \\ \text{div}' \mathbf{v}' &= 0, \end{aligned} \quad (2.7)$$

which has to be solved together with the dimensionless form of the constitutive relation (2.3). In the sequel we will skip the $'$ and call \mathbf{v} , p the velocity and pressure respectively.

As we already mentioned in chapter 1, the driving force of sintering is the excess free energy of the surface of the compact. Physically, a molecule in the interior of the fluid is completely surrounded by other molecules so that these molecules have an (equally) average attraction in all directions. On the other hand, a molecule at the surface will be subjected to a net inwards attraction. Therefore, the fluid surface will always tend to contract to a shape with the smallest possible surface area. The work required to decrease the area is called the *free surface energy*. The energy change can be stated by the following thermodynamical relation

$$\gamma = \left(\frac{dG}{dA} \right)_{p,T,N_i} \quad (2.8)$$

where G is the Gibbs free energy (cf. Waldram [108]) and A is the surface area. This equation expresses that the pressure (p), the temperature (T) and the number of species

(N_i) in the system remain constant during the change in surface area (Reed [88]). Here we assume a homogeneous surface tension. If a volume element dV is removed from or added to a surface with principal curvatures κ_1 and κ_2 , the energy change involved is equal to

$$\frac{dG}{dV} = \gamma \frac{dA}{dV} = \gamma(\kappa_1 + \kappa_2), \quad (2.9)$$

where we used equation (2.8). The term (dG/dV) formally corresponds to a stress. The right-hand side of equation (2.9) shows the pressure difference across a curved surface which is positive (negative) if the surface is convex (concave) as seen from the inside of the fluid. From equation (2.9) the boundary condition in the normal direction for a free fluid surface (Batchelor [6] p.150) can be found as

$$T_{ij} n_j = -\gamma(\kappa_1 + \kappa_2) n_i, \quad (2.10)$$

where a repeated index in an expression denotes a summation over all possible values of that index (Einstein summation convention). Moreover \mathbf{n} denotes the outward unit normal vector. The calculation of the principal curvatures κ_i of a surface in the three-dimensional plane can be found, for example, in Aris [4] (§9.38). Here we will denote the summed principal curvatures by κ_m , i.e.

$$\kappa_m = \kappa_1 + \kappa_2.$$

Note that the tangential component of the surface tension vector must be equal to zero since there is no fluid outside Γ that can cause a shearing force, i.e.

$$T_{ij} n_j \tau_i = \mathcal{E}_{ij} n_j \tau_i = 0,$$

where $\boldsymbol{\tau}$ is the unit tangential vector of the boundary.

In the two-dimensional case which we will consider mainly, the dimensionless form of equation (2.10) reduces to the boundary condition

$$T_{ij} n_j = -\kappa n_i = b_i \quad (2.11)$$

Here κ denotes the curvature of the boundary curve, which is taken positive for a convex boundary curve as is considered from the interior of the fluid, and the vector \mathbf{b} will be referred to as the *body force* further on. When the boundary curve is written in parametric form, say $\mathbf{x} = \mathbf{x}(s)$, we obtain for the curvature the following expression (Haantjes [33]),

$$\kappa(s) = \frac{x'_1 x''_2 - x''_1 x'_2}{((x'_1)^2 + (x'_2)^2)^{\frac{3}{2}}},$$

where $'$ denotes the derivative with respect to s .

In the case of a multiply connected region, we assume that the normal component of the stress vector is also proportional to the local curvature of the inner hole boundaries. Thus we exclude that the holes can move as a consequence of buoyancy or that there is an extra stress component due to a gas inside those holes. This is a reasonable simplification,

since we observed that the force due to gravity can be neglected. Furthermore, we assume that gas inside the interior holes vanish by diffusion into the glass which will not be included into the mathematical model.

The uniqueness of the *fixed* domain solution of the above outlined Stokes problem can be formulated by the following statement.

Theorem 2.1 *The solution of the Stokes problem (2.7), subjected to the boundary tension (2.10) is uniquely determined up to an arbitrary rigid-body motion of the domain.*

Proof. In order to prove this uniqueness of the Stokes problem up to a rigid-body motion, we use that the solution \mathbf{v} of equation (2.7) satisfies the conservation law that the rate of work done by the surface tension on the boundary is equal to the rate of dissipation of mechanical energy by viscous forces *within* the geometry. Successively using equation (2.10), the constitutive relation for the stress, the divergence theorem of Gauss, equations (2.7) and the symmetry of the tensor \mathcal{E} yields the following integral relation

$$\begin{aligned}
 \int_{\Gamma} v_i b_i d\Gamma &= \int_{\Gamma} v_i (-p \delta_{ij} + 2\mathcal{E}_{ij}) n_j d\Gamma \\
 &= \int_{\Omega} \frac{\partial}{\partial x_j} (-p v_j + 2v_i \mathcal{E}_{ij}) d\Omega \\
 &= \int_{\Omega} 2 \frac{\partial v_i}{\partial x_j} \mathcal{E}_{ij} + 2v_i \frac{\partial \mathcal{E}_{ij}}{\partial x_j} - v_j \frac{\partial^2 v_j}{\partial x_i^2} d\Omega \\
 &= 2 \int_{\Omega} \mathcal{E}_{ij} \mathcal{E}_{ij} d\Omega, \tag{2.12}
 \end{aligned}$$

Now, let us assume that \mathbf{v}^1 and \mathbf{v}^2 are both solutions of the problem defined by equations (2.7) and (2.11). Because the Stokes equations are linear, the function $\hat{\mathbf{v}} = \mathbf{v}^1 + \mathbf{v}^2$ is a solution of equation (2.7) together with *zero* tension acting on the boundary curve. Using the energy dissipation balance (2.12), it follows that

$$\hat{\mathcal{E}}_{ij} = 0,$$

which implies that $\hat{\mathbf{v}}$ has to be a rigid-body motion and the proof is completed. \square

If we were to solve the above outlined Stokes problem for a fixed domain, we would find, in general, a non-zero flow field on the boundary curve, which would mean an inflow through one part of the boundary and an outflow elsewhere. This is unphysical since we have a material boundary; hence the fluid domain is moving. The time-dependency does not appear explicitly in the Stokes equations (2.7). Because of this we define a *kinematic constraint* that describes the movement of the fluid domain. This treatment is also called a *quasi-static* approach, which requires that the inertia force is much smaller than the viscous force, i.e. from equation (2.2)

$$\frac{\partial \mathbf{v}}{\partial t} \ll \dots \nu \Delta \mathbf{v},$$

or applying a dimension analysis

$$\frac{\ell^2}{\nu} \ll t_c,$$

where ν is the *kinematic viscosity* which relates to the dynamical viscosity η as $\nu = \eta/\rho$. The time ℓ^2/ν denotes the time scale of vorticity diffusion over a length ℓ since the equality of the above differential (diffusion) equation models the vorticity of an incompressible Newtonian fluid (Aris [4] p.115). In the case of the sintering of a glassy gel we observe that ℓ^2/ν is of order 10^{-18} s and the characteristic time t_c is of order 10^3 s; hence the usage of the quasi static approach is clearly justified. Physically, this assumption means that the fluid immediately adjust to changes of the material boundary owing to rapid vorticity diffusion (Tanzosh *et al.* [100]).

As we already mentioned in subsection 1.2.3, one of the two kinematic constraints following below is used to describe the motion of the boundary of the viscous fluid domain in general. These are derived from both an Eulerian and a Lagrangian point of view respectively. We remark that in fluid mechanics a particle description is referred to as the *Lagrangian representation*, while a field description is known as the *Eulerian representation* (for example the Stokes equations (2.7)). Note that the mixed Eulerian–Lagrangian formulation will not be considered here.

The first constraint is derived from the Eulerian viewpoint and is used in for example Lee *et al.* [66]–[67], Geller *et al.* [28] and Chi *et al.* [16]. It is assumed that the material boundary can be represented by a the functional relation $f(\mathbf{x}, t) = 0$. Differentiating this function with respect to the time t yields,

$$\frac{\partial f}{\partial t} = -|\text{grad } f| v_i n_i. \quad (2.13)$$

The advantage of using the above hyperbolic equation is that marker points, which are introduced by the discretization (cf. chapter 4), tend to remain evenly distributed during the evolution. As we remarked in subsection 1.2.3, numerically it is not straight-forward to solve the above equation. Often a simple Forward Euler method is applied which requires very small time steps in order to evolve boundaries with a very sharp curvature (cusps). Therefore, this particular kinematic constraint is generally applied to simulate “smooth” shaped fluid motions.

Since the fluid regions that we consider have sharply curved boundaries, we apply the kinematic constraint which is equal to the Lagrangian representation of the movement of a *material* fluid particle, i.e.

$$\frac{d\mathbf{x}}{dt} = \mathbf{v}(\mathbf{x}) \quad (\mathbf{x} \in \Gamma). \quad (2.14)$$

The above equation expresses the trajectories of the material particles. Note that this equation also describes the *characteristic curves* of the hyperbolic equation (2.13) which is a particular strategy that can be employed to solve such a hyperbolic equation. The disadvantage of the Lagrangian representation is that nodal points do not remain uniformly distributed during the shape evolution. Hence a number of redistributions of

the collocation points has to be carried out, cf. section 4.4. From (2.14), a system of (non-linear) ordinary differential equations can be obtained which describe the trajectories of the nodal points. In chapter 5 we discuss the solution of this system of non-linear equations.

Finally, we consider the asymptotic behaviour of the quasi-static Stokes flow for proceeding time. As is shown before, the driving force for sintering arises from the excess free surface energy. Hence a viscous blob will transform itself through time into a sphere, since that shape minimizes the outer surface that occupies a certain amount of matter. This can also be demonstrated from the energy dissipation balance (2.12),

$$\int_{\Gamma} v_i b_i d\Gamma = - \int_{\Gamma} \kappa v_i n_i d\Gamma = 2 \int_{\Omega} \mathcal{E}_{ij} \mathcal{E}_{ij} d\Omega \geq 0. \quad (2.15)$$

In the case that Ω is spherical, the integral on the left hand side will vanish, which follows from the integral description of the continuity equation and the fact that κ is constant. Hence $\mathcal{E}_{ij} = 0$, and when we do not allow any rigid-body motions, this implies that $\mathbf{v} = 0$. Note that the zero-equality of equation (2.15) is also satisfied when $\kappa = 0$, i.e. Γ is a minimal surface.

Prokert [85] (§6.3) shows some limiting properties for $t \rightarrow \infty$ for the solution of the quasi-static problem. These properties are derived under the presumption that the solution does exist for any time $t \geq 0$ for a certain starting geometry. Here, we will briefly summarize one of these properties which we apply in chapter 5.

Property 2.1 *An arbitrarily sintering geometry is deforming to a steady state as time increases.*

Proof. We will only sketch the proof; for the precise mathematical derivation, we refer to the original text. Let $\Gamma_t = \Gamma(t)$ and denote the surface of the viscous blob by $A(t)$, i.e.

$$A(t) = \int_{\Gamma_t} d\Gamma_t.$$

Differentiating the above relation with respect to t together by applying equation (2.14), Prokert shows that

$$\frac{d}{dt}(A(t)) = \int_{\Gamma_t} \kappa v_i n_i d\Gamma_t.$$

Substituting the left hand side into equation (2.15), we derive that the surface of the viscous blob $A(t)$ has to be *monotonously decreasing*. Since the fluid is incompressible, this means that $A(t)$ has to be bounded from below. Hence

$$\frac{d}{dt}(A(t)) \rightarrow 0 \quad (t \rightarrow \infty),$$

and from the uniqueness of \mathbf{v} , we obtain that $\mathbf{v} = 0$ which implies that Ω has to be a sphere as is shown previously. \square

2.2 INTEGRAL FORMULATION FOR A SIMPLY CONNECTED DOMAIN

From the previous section it is clear that we are interested only in the evolution of a particular initially prescribed fluid domain. Hence we require the boundary flow field of the evolving shape only. Therefore we reformulate the problem as an integral equation over the boundary: we transform the two-dimensional creeping flow equations with boundary conditions into an equivalent set of integral equations. In this section we will deduce the formulation for a simply connected domain.

Consider Ω to be a *simply connected* domain surrounded by a closed curve Γ in the plane \mathbb{R}^2 in the following sense: let Γ be a Lyapunov surface, i.e. the normal vector is continuously varying. Many authors attribute the following analysis and the resulting integral formulation to Ladyzhenskaya [64] (1963), but actually it was Lorentz [69] who derived this formulation in essence, back in 1896. Here we will closely follow the derivation of the integral equation as can be found in Ladyzhenskaya [64].

We introduce the vector field $\mathbf{u}^k(\mathbf{x}, \mathbf{y})$ and the scalar function $q^k(\mathbf{x}, \mathbf{y})$ that satisfies the following Stokes problem

$$\begin{aligned} \Delta \mathbf{u}^k(\mathbf{x}, \mathbf{y}) - \text{grad } q^k(\mathbf{x}, \mathbf{y}) &= \delta(\mathbf{x} - \mathbf{y}) \mathbf{e}^k \\ \text{div } \mathbf{u}^k &= 0. \end{aligned} \quad (2.16)$$

Here $k = 1, 2$, $\mathbf{e}^k = (\delta_{1k}, \delta_{2k})$ is the k^{th} unit vector of an arbitrary chosen Cartesian coordinate system, \mathbf{y} is an arbitrary point in the plane \mathbb{R}^2 and $\delta(\mathbf{x} - \mathbf{y})$ is the *Dirac delta function*. Physically, these equations may be interpreted as the velocity at \mathbf{x} induced by a two-dimensional unit point force in the \mathbf{e}^k -direction concentrated at the point \mathbf{y} . This solution is also referred to as a flow due a *Stokeslet*. The problem (2.16) can be solved uniquely using the requirements

$$u_j^k(\mathbf{x}, \mathbf{y}) = \mathcal{O}(\log |\mathbf{x} - \mathbf{y}|) \quad \text{and} \quad q^k(\mathbf{x}, \mathbf{y}) = o(1), \quad (|\mathbf{x}| \rightarrow \infty),$$

and applying a Fourier transformation (cf. Van de Spek [98]). We obtain

$$\begin{aligned} u_j^k(\mathbf{x}, \mathbf{y}) &= -\frac{1}{4\pi} \left[\delta_{jk} \log \frac{1}{|\mathbf{x} - \mathbf{y}|} + \frac{(x_j - y_j)(x_k - y_k)}{|\mathbf{x} - \mathbf{y}|^2} \right] \\ q^k(\mathbf{x}, \mathbf{y}) &= -\frac{x_k - y_k}{2\pi |\mathbf{x} - \mathbf{y}|^2}. \end{aligned} \quad (2.17)$$

This solution is also called the fundamental singular solution of the Stokes problem. The functions (2.17) are also the solutions to the *adjoint system*,

$$\begin{aligned} \Delta_y \mathbf{u}^k(\mathbf{x}, \mathbf{y}) + \text{grad}_y q^k(\mathbf{x}, \mathbf{y}) &= \delta(\mathbf{x} - \mathbf{y}) \mathbf{e}^k \\ \text{div}_y \mathbf{u}^k &= 0. \end{aligned} \quad (2.18)$$

By $(\)_y$ we mean that the differentiation is carried out with respect to \mathbf{y} . Furthermore, we require the so-called *Green's formulae* corresponding to the Stokes problem.

Theorem 2.2 (Green's Formulae) *Let \mathbf{u}, \mathbf{v} be two arbitrary solenoidal vector fields and let the scalar functions p, q be sufficiently smooth. Then, the following integral identity holds for those functions,*

$$\begin{aligned} \int_{\Omega} \left[\left(\Delta v_i - \frac{\partial p}{\partial x_i} \right) u_i - \left(\Delta u_i + \frac{\partial q}{\partial x_i} \right) v_i \right] d\Omega &= \\ &= \int_{\Gamma} [T_{ij}(p, \mathbf{v})u_i n_j - T_{ij}(-q, \mathbf{u})v_i n_j] d\Gamma. \end{aligned} \quad (2.19)$$

Proof. This theorem can be verified by noting that according to equation (2.3) the stress tensor $\mathcal{T}(q, \mathbf{u})$ for this Newtonian fluid is equal to

$$\mathcal{T}_{ij}(q, \mathbf{u}) = -q\delta_{ij} + \left(\frac{\partial u_i}{\partial x_j} + \frac{\partial u_j}{\partial x_i} \right). \quad (2.20)$$

When we integrate the identity

$$\frac{\partial}{\partial x_k} [T_{ik}(q, \mathbf{u})v_i] = \frac{1}{2} \left(\frac{\partial u_i}{\partial x_k} + \frac{\partial u_k}{\partial x_i} \right) \left(\frac{\partial v_i}{\partial x_k} + \frac{\partial v_k}{\partial x_i} \right) + \left(\Delta u_i - \frac{\partial q}{\partial x_i} \right) v_i$$

over Ω and use the divergence theorem of Gauss, we obtain

$$\begin{aligned} \int_{\Omega} \left(\Delta u_i - \frac{\partial q}{\partial x_i} \right) v_i d\Omega &= -\frac{1}{2} \int_{\Omega} \left(\frac{\partial u_i}{\partial x_k} + \frac{\partial u_k}{\partial x_i} \right) \left(\frac{\partial v_i}{\partial x_k} + \frac{\partial v_k}{\partial x_i} \right) d\Omega \\ &+ \int_{\Gamma} T_{ik}(q, \mathbf{u})v_i n_k d\Gamma. \end{aligned} \quad (2.21)$$

By interchanging u_i and v_i in equation (2.21) and introducing the arbitrary smooth function p together with q , we obtain from equation (2.21) the Green's formulae corresponding to the Stokes problem, i.e. equation (2.19). \square

We replace \mathbf{u} and q in the Green's formulae with the fundamental singular solutions $\mathbf{u}^k(\mathbf{x}, \mathbf{y})$, $q^k(\mathbf{x}, \mathbf{y})$ of (2.17) and consider those as a function of \mathbf{y} , to be the solution of the adjoint system (2.18). Furthermore, we require that \mathbf{v} , p satisfy the Stokes problem outlined in the previous section. Hence we obtain the following Fredholm integral equation of the second kind (cf. Kress [59]),

$$v_k(\mathbf{x}) = \int_{\Gamma} T_{ij}(-q^k, \mathbf{u}^k)_y v_i n_j d\Gamma_y - \int_{\Gamma} T_{ij}(p, \mathbf{v})u_i^k n_j d\Gamma_y, \quad (2.22)$$

for any $\mathbf{x} \in \Omega$. Substitution of the fundamental solution (2.17) into equation (2.20) yields

$$T_{ij}(-q^k, \mathbf{u}^k)_y = -\frac{(x_i - y_i)(x_j - y_j)(x_k - y_k)}{\pi|\mathbf{x} - \mathbf{y}|^4}.$$

Note that $T_{ij}(p, \mathbf{v})n_j$ is given by the boundary condition (2.11), i.e. $\mathcal{T}(p, \mathbf{v})\mathbf{n} = \mathbf{b}$.

When we let \mathbf{x} in equation (2.22) approach the boundary and use the assumption that this boundary is "smooth", the following integral formulation can be deduced

$$c_{ij}v_j(\mathbf{x}) + \int_{\Gamma} q_{ij}(\mathbf{x}, \mathbf{y})v_j(\mathbf{y}) d\Gamma_y = \int_{\Gamma} u_{ij}(\mathbf{x}, \mathbf{y})b_j(\mathbf{y}) d\Gamma_y. \quad (2.23)$$

Here c_{ij} , q_{ij} and u_{ij} are equal to respectively:

$$c_{ij} = \begin{cases} \delta_{ij} & \mathbf{x} \in \Omega \\ \frac{1}{2}\delta_{ij} & \mathbf{x} \in \Gamma \\ 0 & \mathbf{x} \in \Omega', \end{cases} \quad q_{ij}(\mathbf{x}, \mathbf{y}) = \frac{r_i r_j}{\pi R^4} r_k n_k, \quad (2.24)$$

$$u_{ij}(\mathbf{x}, \mathbf{y}) = \frac{1}{4\pi} \left[-\delta_{ij} \log R + \frac{r_i r_j}{R^2} \right],$$

where $r_i = x_i - y_i$, $R = \sqrt{r_1^2 + r_2^2} = |\mathbf{x} - \mathbf{y}|$ and Ω' is the complementary region of $\Omega \cup \Gamma$. Note that if $\mathbf{x} \in \Omega'$ equation (2.23) is an Fredholm integral equation of the first kind (cf. Kress [59]). When $\mathbf{x} \in \Gamma$ the Cauchy principal value of the integrals is taken. The integral at the right-hand side is the so-called *single-layer hydrodynamic potential* and the other integral is called the *double-layer hydrodynamic potential*. Therefore, (2.23) is usually referred to as the integral equation of single- and double-layer potentials. Here, this formulation will be denoted as the *SDLP-formulation*.

The "jump" in the coefficient c_{ij} can be explained as follows. Considering $\mathbf{x} \in \Omega'$ and using Green's formulae, it is easy to see that c_{ij} is equal to zero. When \mathbf{x} is a boundary point, we surround this point by a piece of a small circle curve of radius ε situated in Ω' , say B_ε . By Γ_ε is denoted the intersection curve of Γ with this piece of circle. Consider the formulation (2.23) for this extended domain and take the limit for $\varepsilon \rightarrow 0$. We rearrange the single-layer potential as follows,

$$\int_{\Gamma - \Gamma_\varepsilon + B_\varepsilon} u_{ij} b_j d\Gamma_y = \int_{\Gamma - \Gamma_\varepsilon} u_{ij} b_j d\Gamma_y + \int_{B_\varepsilon} u_{ij} (b_j(\mathbf{y}) - b_j(\mathbf{x})) d\Gamma_y + b_j(\mathbf{x}) \int_{B_\varepsilon} u_{ij} d\Gamma_y.$$

The first integral on the right hand side becomes an integral on the whole boundary Γ when $\varepsilon \rightarrow 0$. The other two integrals tend to zero as $\varepsilon \rightarrow 0$, since it is assumed that \mathbf{b} is continuous along Γ , the term u_{ij} will be of order $1 + \delta_{ij} \log \varepsilon$ and the line integral produces a ε . The double layer potential can be written similar, i.e.

$$\int_{\Gamma - \Gamma_\varepsilon + B_\varepsilon} q_{ij} v_j d\Gamma_y = \int_{\Gamma - \Gamma_\varepsilon} q_{ij} v_j d\Gamma_y + \int_{B_\varepsilon} q_{ij} (v_j(\mathbf{y}) - v_j(\mathbf{x})) d\Gamma_y + v_j(\mathbf{x}) \int_{B_\varepsilon} q_{ij} d\Gamma_y.$$

Here q_{ij} is of order $1/\varepsilon$ and the line integral gives a ε . Using this and that \mathbf{v} is continuous along Γ , it follows that the second integral tend to zero when $\varepsilon \rightarrow 0$. However, the third integral will not vanish as $\varepsilon \rightarrow 0$. From the assumption that the boundary is smooth, B_ε will tend to a hemicycle when ε is sufficiently small. Using this in the third integral and carrying out the integration on this half circle curve yields,

$$v_j(\mathbf{x}) \int_{B_\varepsilon} q_{ij}(\mathbf{x}, \mathbf{y}) d\Gamma_y = -\frac{1}{2} \delta_{ij} v_j(\mathbf{x}).$$

The first integral can be written as the integral on the whole Γ , when defined in the sense of the Cauchy principal value. Note that $c_{ij} = \frac{1}{2} \delta_{ij}$ is equal to the mean value of c_{ij} on either side of Γ . The above procedure can also be followed to compute the coefficients c_{ij} for non-smooth boundaries, cf. Hartmann [36].

In the previous section, it is shown that the Stokes problem does have a unique solution up to an arbitrary rigid-body motion. The SDLP-formulation (2.23) is also showing this behaviour. Because of this, we have to prescribe or remove these degrees of freedom from the formulation in order to obtain a fully determined problem. To perform this, we will have a closer look at both hydrodynamical potentials. We denote the single layer potential operator with a continuous varying density $\phi(\mathbf{y})$ as

$$(\mathcal{G}\phi)_i = \int_{\Gamma} u_{ij}(\mathbf{x}, \mathbf{y}) \phi_j(\mathbf{y}) d\Gamma_{\mathbf{y}}. \quad (2.25)$$

The double layer potential with density $\psi(\mathbf{y})$ is defined similarly, i.e.

$$(\mathcal{H}\psi)_i = \int_{\Gamma} q_{ij}(\mathbf{x}, \mathbf{y}) \psi_j(\mathbf{y}) d\Gamma_{\mathbf{y}}. \quad (2.26)$$

The kernel of the single layer potential (2.25) is weakly singular so that \mathcal{G} is a compact operator (cf. Kress [59] p.23). It can be shown that the kernel of the double layer potential (2.26) is continuous and bounded, thus the operator \mathcal{H} is compact too. This implies that the Fredholm-Riesz-Schauder theory for compact operators applies on to both potentials. The essence of this theory is that the Fredholm equation of the second kind shares several properties with ordinary square matrices. Hence the functional operators might be viewed as the usual matrix operations used in linear algebra. The SDLP-formulation (2.23) can be represented in terms of these potentials as follows

$$(\lambda \mathcal{J} + \mathcal{H})\mathbf{v} = \mathcal{G}\mathbf{b}, \quad (2.27)$$

where \mathcal{J} is the identity operator and $\lambda = c_{11} = c_{22}$. From now on, we assume that \mathbf{x} is a point of the boundary Γ , i.e. $\lambda = \frac{1}{2}$, hence we have to solve a Fredholm integral equation of the second kind.

The functional *inner product* is defined in the usual way, i.e.

$$\langle \phi, \psi \rangle = \int_{\Gamma} \phi_i \psi_i d\Gamma, \quad (2.28)$$

and the adjoint \mathcal{A}^* of an operator \mathcal{A} is defined through

$$\langle \phi, \mathcal{A}\psi \rangle = \langle \mathcal{A}^*\phi, \psi \rangle. \quad (2.29)$$

Here the adjoint operators of (2.25) and (2.26) can be found by transposing the indices j and k and swapping the arguments \mathbf{x} and \mathbf{y} of the coefficients (2.24). In particular, it follows that

$$(\mathcal{G}^*\phi)_i = (\mathcal{G}\phi)_i, \quad \text{and} \quad (\mathcal{H}^*\psi)_i = -n_k(\mathbf{x}) \int_{\Gamma} \frac{r_i r_j r_k}{\pi R^4} \psi_j d\Gamma_{\mathbf{y}}. \quad (2.30)$$

Hence \mathcal{G} is a *self-adjoint* (symmetric) linear operator. From the Fredholm-Riesz-Schauder theory for compact linear operators, we mention the following two theorems which will be applied further on.

Theorem 2.3 (First Fredholm Theorem) *Let \mathcal{A} be a compact operator, then the null spaces of the operators $\mathcal{J} - \mathcal{A}$ and $\mathcal{J} - \mathcal{A}^*$ have the same finite dimension.*

The proof of this theorem can be found in Kress [59] p.42.

Theorem 2.4 (Second Fredholm Theorem) *Let \mathcal{A} be a compact operator, the nonhomogeneous equation*

$$\phi - \mathcal{A} \phi = \mathbf{f}$$

has a solution if and only if the condition

$$\langle \mathbf{f}, \psi \rangle = 0$$

is satisfied for all the solutions ψ of the homogeneous adjoint equation

$$\psi - \mathcal{A}^* \psi = 0.$$

Again the proof of this theorem is outlined in Kress [59] p.43 and is also called the Fredholm alternative. Note that the above theorem also holds when \mathcal{A} and \mathcal{A}^* are interchanged.

Let the three linearly independent rigid-body motions be denoted by φ^k , where

$$\varphi^k(\mathbf{x}) = \mathbf{e}^k \quad (k = 1, 2) \quad \text{and} \quad \varphi^3(\mathbf{x}) = x_2 \mathbf{e}^1 - x_1 \mathbf{e}^2. \quad (2.31)$$

For the solution to the homogeneous equation (2.27) the following theorem holds.

Theorem 2.5 *The functions $\varphi^k(\mathbf{x})$ span the null space of the operator $(\frac{1}{2}\mathcal{J} + \mathcal{H})$.*

Proof. In theorem 2.1 we observed that the functions φ^k were solutions of the Stokes equations with zero tensions on the boundary, i.e. the body force $\mathbf{b}=0$. Substituting this equality into equation (2.27), it is clear that those functions satisfy the homogeneous part of the equation. In order to prove that these functions are a basis for the null space, it is sufficient to show the validity for the adjoint $(\frac{1}{2}\mathcal{J} + \mathcal{H}^*)$, since the First Fredholm theorem 2.3 states that the null spaces of both the operators have the same finite dimension. Therefore, we suppose that ϕ satisfies

$$(\frac{1}{2}\mathcal{J} + \mathcal{H}^*)\phi = 0. \quad (2.32)$$

Define the single-layer potential (solenoidal) velocity field $\hat{\mathbf{v}}$ by

$$\hat{\mathbf{v}}(\mathbf{x}) = \mathcal{G} \phi,$$

and the single-layer potential that is associated with the pressure \hat{p} of this flow as

$$\hat{p}(\mathbf{x}) = - \int_{\Gamma} q^k(\mathbf{x}, \mathbf{y}) \phi_k(\mathbf{y}) d\Gamma_y,$$

where $\mathbf{x} \in \Omega$. Using these definitions, we obtain for this combined pressure and velocity field the following expression for the stress tensor

$$\mathcal{T}_{ij}(\hat{p}, \hat{\mathbf{v}}) = - \int_{\Gamma} \frac{r_i r_j r_k \phi_k}{\pi R^4} d\Gamma_y.$$

Taking the limit from inside the fluid towards a point \mathbf{x} of the boundary curve, we obtain for the tension in the normal direction

$$\mathcal{T}_{ij}(\hat{p}, \hat{\mathbf{v}})n_j(\mathbf{x}) = (\tfrac{1}{2}\mathcal{J} + \mathcal{H}^*)\phi = 0, \quad (2.33)$$

where this limit can be found in a similar way as the coefficients c_{ij} are deduced previously, together by applying the identity

$$\mathcal{T}_{ij}(\hat{p}, \hat{\mathbf{v}})n_j(\mathbf{x}) = (\mathcal{T}_{ij}(\hat{p}, \hat{\mathbf{v}})n_j(\mathbf{x}) + \mathcal{H}\phi) - \mathcal{H}\phi.$$

The zero equality in equation (2.33) follows from the assumption (2.32). Hence this zero boundary tension implies that $\hat{\mathbf{v}}$ has to be a rigid-body motion (cf. theorem 2.1). From this it follows that ϕ has to be a rigid-body motion too. Intuitively, the latter is clear since a rigid-body force will not change the actual flow field of the fluid domain. \square

Now, we can also prove that any solution of equation (2.27) satisfies the incompressibility condition, i.e.

Theorem 2.6 *Let \mathbf{v} be a solution of equation (2.27), then this function satisfies*

$$\langle \mathbf{v}, \mathbf{n} \rangle = 0.$$

Proof. In order to prove this theorem, we will use the following identities that apply on the potentials in relation to the outer normal, i.e.

$$(\mathcal{H}^* \mathbf{n})_i = (-n_j(\mathbf{x})\mathcal{H}e^j)_i = \begin{cases} n_i & \mathbf{x} \text{ inside } \Gamma \\ \frac{1}{2}n_i & \mathbf{x} \text{ on } \Gamma \\ 0 & \mathbf{x} \text{ outside } \Gamma. \end{cases} \quad (2.34)$$

Hence the outer normal \mathbf{n} is an eigenfunction of the adjoint operator \mathcal{H}^* . Furthermore, for the single layer potential can be found,

$$(\mathcal{G} \mathbf{n})_i = \int_{\Gamma} u_{ij}n_j d\Gamma = \int_{\Omega} \operatorname{div} \mathbf{u}^i d\Omega = 0, \quad (2.35)$$

which is derived from the application of the divergence theorem of Gauss and from noting that \mathbf{u}^i is the solution of (2.17) which satisfies the incompressibility condition. Let $\mathbf{x} \in \Gamma$, taking the inner product of equation (2.27) with respect to the outer normal, we obtain

$$\begin{aligned} \langle \mathbf{n}, (\tfrac{1}{2}\mathcal{J} + \mathcal{H})\mathbf{v} \rangle &= \langle (\tfrac{1}{2}\mathcal{J} + \mathcal{H}^*)\mathbf{n}, \mathbf{v} \rangle = \langle \mathbf{n}, \mathbf{v} \rangle \\ &= \langle \mathbf{n}, \mathcal{G}\mathbf{b} \rangle = \langle \mathcal{G}^*\mathbf{n}, \mathbf{b} \rangle = 0, \end{aligned}$$

where we used the self-adjointness of \mathcal{G} and the above mentioned identities. For $\mathbf{x} \in \Omega$ the proof is straight-forward. \square

There are mainly two approaches to make (2.27) uniquely solvable. The first method is related to the approach employed by Hsiao, Kopp and Wendland [46]. In Van de Vorst *et al.* [105], three additional variables are added to the integral equation that prescribe the

rigid-body movements. In order to achieve a full rank system, three integral constraints are included. The translation freedom is prescribed by considering the flow stationary at a reference point inside the fluid. This point is normally taken equal to the centre of mass. With regard to this point the boundary flow field is computed. Substitution of the reference point as the \mathbf{x} -argument into the integral equation yields two integral constraints which have to be satisfied. The third integral constraint is derived by taking the inner product of the velocity field and the tangential vector along the boundary curve equal to zero.

The other method is to “remove” the eigenvalue of the double-layer integral operator \mathcal{H} that causes this null space, i.e. $-\frac{1}{2}$, and construct a “deflated” operator. The advantage of deflation is that the number of unknowns does not change and that we do not have to seek extra integral constraints: it is a purely mathematical approach. For example, this approach can be achieved by *Wielandt’s deflation* (Wilkinson [111] p.596) which is extensively discussed in two recently published books by Kim and Karrila [54] and Pozrikidis [82] respectively. This method “replaces” the deflated eigenvalue by zero without affecting the other eigenvalues which is an important property in the case that when an iterative solution method is applied, cf. Kim and Karrila [54]. Furthermore, this technique can be used to make the integral equation uniquely solvable (range completion).

Before presenting the deflated equation, we require the rigid-body motions φ^k to be an orthonormal set with respect to the inner product (2.28). This can easily be accomplished by the Gram-Schmidt process (cf. Kreyszig [60] p.157). Then the following three orthonormal functions, say $\hat{\varphi}^k$, are derived,

$$\hat{\varphi}^k = \frac{\varphi^k}{\sqrt{L}} \quad k = 1, 2, \quad \hat{\varphi}^3 = \frac{(x_2 - x_2^t)\varphi^1 - (x_1 - x_1^t)\varphi^2}{\sqrt{I}}, \quad (2.36)$$

where

$$L = \int_{\Gamma} d\Gamma, \quad x_i^t = \frac{1}{L} \int_{\Gamma} x_i d\Gamma \quad \text{and} \quad I = \int_{\Gamma} (x_1 - x_1^t)^2 + (x_2 - x_2^t)^2 d\Gamma.$$

Here I is the moment of inertia about the centre of torque \mathbf{x}^t of the fluid domain. Using the functions (2.36), we define three projection operators \mathcal{P}^k by

$$\mathcal{P}^k = \hat{\varphi}^k \langle \cdot, \hat{\varphi}^k \rangle.$$

Note that these rank-one operators are self-adjoint. We introduce as deflated form for \mathcal{H} the operator

$$\mathcal{H} + \mathcal{P} := \mathcal{H} + \mathcal{P}^1 + \mathcal{P}^2 + \mathcal{P}^3.$$

Replacing the operator \mathcal{H} in equation (2.27) by the above operator yields the following deflated formulation

$$\left(\frac{1}{2}\mathcal{J} + \mathcal{H} + \mathcal{P}\right)\mathbf{v} = \mathcal{G}\mathbf{b}. \quad (2.37)$$

Now, there exists a unique solution \mathbf{v} of the above equation since the operator $(\frac{1}{2}\mathcal{J} + \mathcal{H} + \mathcal{P})$ is bijective (cf. Kress [59] p.43). Moreover, this solution also satisfies the original

equation (2.27). The latter statement requires that $\mathcal{P}\mathbf{v} = 0$, which is fulfilled since

$$\begin{aligned} \langle \mathbf{v}, \hat{\varphi}^k \rangle &= \langle \mathbf{v}, (\tfrac{1}{2}\mathcal{J} + \mathcal{H}^*)\hat{\varphi}^k \rangle + \langle \mathbf{v}, \hat{\varphi}^k \rangle \\ &= \langle (\tfrac{1}{2}\mathcal{J} + \mathcal{H})\mathbf{v}, \hat{\varphi}^k \rangle + \langle \mathbf{v}, \hat{\varphi}^i \rangle \langle \hat{\varphi}^i, \hat{\varphi}^k \rangle \\ &= \langle (\tfrac{1}{2}\mathcal{J} + \mathcal{H} + \mathcal{P})\mathbf{v}, \hat{\varphi}^k \rangle \\ &= \langle \mathcal{G}\mathbf{b}, \hat{\varphi}^k \rangle = 0, \end{aligned}$$

where the equality follows from the solvability condition of the original equation, i.e. Fredholm's second theorem 2.4. In terms of ordinary integrals, equation (2.37) can be expressed by,

$$c_{ij}v_j(\mathbf{x}) + \int_{\Gamma} q_{ij}(\mathbf{x}, \mathbf{y})v_j d\Gamma_y + \hat{\varphi}_i^k(\mathbf{x}) \int_{\Gamma} \hat{\varphi}_j^k v_j d\Gamma = \int_{\Gamma} u_{ij}(\mathbf{x}, \mathbf{y})b_j d\Gamma_y. \quad (2.38)$$

The above integral formulation will be solved in the case of a simply connected domain.

2.3 EQUATIONS FOR A MULTIPLY CONNECTED DOMAIN

The next step will be the extension to an integral formulation for a multiply connected domain. Let this domain be bounded externally by Γ_0 and internally by $\Gamma_1, \dots, \Gamma_M$. By Γ we denote the complete boundary. Note that we have chosen the orientation of the boundary so that on progressing on Γ the fluid region lies on the left hand side. This means that the outer boundary Γ_0 is considered in counter-clockwise direction and all the inner boundaries Γ_m are passed through in clockwise direction. Hence, the normal vector is always pointing to the outward of the fluid.

If we formally apply equation (2.27) on to this multiply connected domain, we find

$$\begin{aligned} \left(\tfrac{1}{2}\mathcal{J} + \mathcal{H}_0\right)\mathbf{v}^0 - \sum_{j=1}^M \mathcal{H}_j \mathbf{v}^j &= \sum_{j=0}^M \mathcal{G}_j \mathbf{b}^j \quad \mathbf{x} \in \Gamma_0 \\ \mathcal{H}_0 \mathbf{v}^0 - \sum_{j=1}^M \mathcal{H}_j \mathbf{v}^j + \tfrac{1}{2}\mathcal{J}\mathbf{v}^m &= \sum_{j=0}^M \mathcal{G}_j \mathbf{b}^j \quad \mathbf{x} \in \Gamma_m, \end{aligned} \quad (2.39)$$

where the subscript j of both potentials $\mathcal{H}_j, \mathcal{G}_j$ denotes that the integration is subjected to the boundary Γ_j which is passed through in a counter-clockwise direction (this explains the occurrence of the minus sign for the operator \mathcal{H}_j for the interior boundaries). The factor $\frac{1}{2}$ in the second equation is due to the contribution of the outer boundary. Here $\mathbf{v}^m, \mathbf{b}^m$ are the velocity, tension function respectively of the boundary Γ_m . Again, the rigid-body motion functions (2.36) are a basis for the null space of the homogeneous part of equation (2.39) which easily can be shown by inspection. Using those functions, the above double-layer potential can be deflated in a similar way as was done for the simply connected domain.

Let $\hat{\varphi}^{mk}(\mathbf{x})$ be the k -th rigid-body motion of the hole enclosed by Γ_m when $\mathbf{x} \in \Gamma_m$, otherwise this function is taken equal to zero. The projection operator \mathcal{P}_m is defined by

$$\mathcal{P}_m = \sum_{k=1}^3 \hat{\varphi}^{mk} \langle \cdot, \hat{\varphi}^{mk} \rangle_m,$$

where the inner product is considered with respect to Γ_m . Using these projection operators, the following deflated formulation of (2.39) is obtained,

$$\begin{aligned} \left(\frac{1}{2}\mathcal{J} + \mathcal{H}_0 + \mathcal{P}_0\right)\mathbf{v}^0 - \sum_{j=1}^M \mathcal{H}_j \mathbf{v}^j &= \sum_{j=0}^M \mathcal{G}_j \mathbf{b}^j \quad \mathbf{x} \in \Gamma_0 \\ \mathcal{H}_0 \mathbf{v}^0 - \sum_{j=1}^M \mathcal{H}_j \mathbf{v}^j + \left(\frac{1}{2}\mathcal{J} + \mathcal{P}_m\right)\mathbf{v}^m &= \sum_{j=0}^M \mathcal{G}_j \mathbf{b}^j \quad \mathbf{x} \in \Gamma_m. \end{aligned} \quad (2.40)$$

The integral formulation that is derived so far cannot describe the shrinkage or the expansion of the inside holes of the fluid domain. Physically, this means that the porosity changes during sintering. This can be illustrated by the following example shape, viz. a circular fluid disk with a circular hole centred at the origin. This problem can be solved analytically, cf. Van de Vorst [107], and one obtains that the interior hole of the annulus shrinks and vanishes when time proceeds. However, when we put this particular shape into the above integral formulation, the null solution is derived since the right hand side is equal to zero. This zero equality follows from the fact that the curvature is constant and hence can be taken to the outside of the operator \mathcal{G} , together by using equation (2.35).

The shrinking or expanding can be modelled as if there were *point sinks* or *sources* respectively situated inside the interior of such a hole. For an introduction to the usage of such singularity points to model such a flow behaviour, we refer to any book about fluid dynamics, see for example Batchelor [6] p.88. The reason that equation (2.40) cannot describe this behaviour is due to the fact that the outer normal is an eigenfunction of \mathcal{H}^* . As was stated in Pozrikidis [82] p.110, the double-layer potential is capable of representing a flow that contains sinks, but sometimes the adjoint double-layer potential's outer normal eigenvalue has to be removed. The method of deflating the boundary normal as described by both Kim and Karrila [54] and Pozrikidis [82] cannot be applied here straightforwardly, since they consider resistance and movement problems of solid and liquid particles in the fluid only. Therefore, we will perform a further deflation of equation (2.40) by applying an integral constraint which is presented below.

In a similar way as the integral formulation (2.23) is obtained from the fundamental solution of a point force in an infinite two-dimensional fluid, an integral equation can be obtained that represents a point source at a particular place. Again, we consider a simply connected domain bounded externally by Γ . The fundamental solution that represents a source, say $\hat{\mathbf{u}}$ and \hat{q} , satisfy the following equation,

$$\begin{aligned} \Delta \hat{\mathbf{u}} - \text{grad } \hat{q} &= 0 \\ \text{div } \hat{\mathbf{u}} &= -\delta(\mathbf{x} - \mathbf{y}). \end{aligned} \quad (2.41)$$

Physically, equation (2.41) may be interpreted as the velocity at \mathbf{x} induced by a point sink with unit force concentrated in the point \mathbf{y} , (the point \mathbf{y} is called a source point when the above Dirac delta function has a positive sign). This fundamental solution can be deduced after applying a cylindrical coordinate transformation, i.e. we obtain

$$\hat{u}_i(\mathbf{x}, \mathbf{y}) = -\frac{x_i - y_i}{2\pi|\mathbf{x} - \mathbf{y}|^2}, \quad \hat{q}(\mathbf{x}, \mathbf{y}) = 0. \quad (2.42)$$

The functions \mathbf{u} and q in the Green's formulae (2.19) are replaced by the above fundamental solution $\hat{\mathbf{u}}(\mathbf{x}, \mathbf{y})$, $\hat{q}(\mathbf{x}, \mathbf{y})$ which is also a solution of the adjoint of problem (2.41), when considered as function of \mathbf{y} . Substitution of this fundamental solution into the adjoint stress tensor (2.20) yields

$$\mathcal{T}_{ij}(-\hat{q}, \hat{\mathbf{u}})_y = \mathcal{T}_{ij}(0, \hat{\mathbf{u}})_y = -\frac{2(x_i - y_i)(x_j - y_j)}{\pi|\mathbf{x} - \mathbf{y}|^4} + \frac{\delta_{ij}}{\pi|\mathbf{x} - \mathbf{y}|^2}.$$

Requiring that \mathbf{v} , p satisfy the Stokes problem and consider \mathbf{x} to be in the inside of the fluid, we derive the following equation

$$\int_{\Gamma} \hat{q}_i(\mathbf{x}, \mathbf{y}) v_i(\mathbf{y}) d\Gamma_y = \int_{\Gamma} \hat{u}_i(\mathbf{x}, \mathbf{y}) b_i(\mathbf{y}) d\Gamma_y, \quad (2.43)$$

where

$$\hat{q}_i = \frac{1}{\pi} \left(\frac{2r_i r_j n_j}{R^4} - \frac{\delta_{ij} n_j}{R^2} \right), \quad \hat{u}_i = -\frac{r_i}{2\pi R^2}.$$

Note that when a source point is modelled, we obtain the same integral equation since the point source solution will differ only in sign with equation (2.42). From the above outline, it is easy to observe that this sign does not have any effect on the resulting integral equation. Hence this equation is suited to model both the shrinking and expansion of inner holes.

Now, we choose an *arbitrary* point in all the holes: let \mathbf{x}^m be a point in the inside of the area surrounded by Γ_m ($m=1, \dots, M$). Consider the integral (2.43) for the multiply connected domain and replace the point \mathbf{x} by the source point \mathbf{x}^m , i.e. we obtain M equations which, after summation, reduces to the following integral equation,

$$\sum_{m=0}^M \int_{\Gamma_m} \hat{q}_i(\mathbf{x}^m, \mathbf{y}) v_i^m(\mathbf{y}) d\Gamma_y = \sum_{m=0}^M \int_{\Gamma_m} \hat{u}_i(\mathbf{x}^m, \mathbf{y}) b_i^m(\mathbf{y}) d\Gamma_y, \quad (2.44)$$

where

$$\hat{q}_i = \sum_{m=1}^M \hat{q}_i(\mathbf{x}^m, \mathbf{y}), \quad \hat{u}_i = \sum_{m=1}^M \hat{u}_i(\mathbf{x}^m, \mathbf{y}).$$

The above integral is applied as a constraint on the solution of equation (2.40), i.e we seek a velocity field \mathbf{v} that both satisfies equations (2.40) and (2.44). We denote the latter equation in a similar operator notation as we employed for the potentials, i.e.

$$\mathbf{h}_0 \mathbf{v}^0 - \sum_{m=1}^M \mathbf{h}_m \mathbf{v}^m = \sum_{m=0}^M \mathbf{g}_m \mathbf{b}^m. \quad (2.45)$$

where

$$\mathbf{g}_k \phi = \int_{\Gamma_k} \bar{u}_j \phi_j d\Gamma_y, \quad \text{and} \quad \mathbf{h}_k \psi = \int_{\Gamma_k} \bar{q}_j \psi_j d\Gamma_y,$$

and Γ_k is considered in counter-clockwise direction.

This equation can be applied in order to deflate equation (2.40) with respect to the outer normal in the following way,

$$\begin{aligned} \left(\frac{1}{2}\mathcal{J} + \mathcal{K}_0 + \mathcal{P}_0 + \mathbf{n}^0 \mathbf{h}_0\right) \mathbf{v}^0 - \sum_{j=1}^M \left(\mathcal{K}_j + \mathbf{n}^0 \mathbf{h}_j\right) \mathbf{v}^j \\ = \sum_{j=0}^M \left(\mathcal{G}_j + \mathbf{n}^0 \mathbf{g}_j\right) \mathbf{b}^j, \quad \mathbf{x} \in \Gamma_0 \\ \left(\mathcal{K}_0 + \mathbf{n}^m \mathbf{h}_0\right) \mathbf{v}^0 - \sum_{j=1}^M \left(\mathcal{K}_j + \mathbf{n}^m \mathbf{h}_j\right) \mathbf{v}^j + \left(\frac{1}{2}\mathcal{J} + \mathcal{P}_m\right) \mathbf{v}^m \\ = \sum_{j=0}^M \left(\mathcal{G}_j + \mathbf{n}^m \mathbf{g}_j\right) \mathbf{b}^j, \quad \mathbf{x} \in \Gamma_m. \end{aligned} \quad (2.46)$$

The solution of the above equation satisfies the original equations (2.40) and (2.45), which requires that the following relation has to be fulfilled,

$$w := \mathbf{g}_0 \mathbf{b}^0 - \mathbf{h}_0 \mathbf{v}^0 + \sum_{m=1}^M \left(\mathbf{g}_m \mathbf{b}^m + \mathbf{h}_m \mathbf{v}^m\right) = 0. \quad (2.47)$$

This can be shown by taking the inner product of equation (2.46) with respect to the outer normal, i.e. $\langle \mathbf{n}^m, \cdot \rangle_m$. In order to perform this we note that

$$\langle \mathbf{n}^j, \mathcal{G}_m \mathbf{b}^m \rangle_j = \langle \mathcal{G}_j^* \mathbf{n}^j, \mathbf{b}^m \rangle_m = \langle \mathcal{G}_j \mathbf{n}^j, \mathbf{b}^m \rangle_m = 0, \quad (2.48)$$

which is deduced from the self-adjointness of \mathcal{G} together with equation (2.35). Furthermore, it can be found that

$$\langle \hat{\varphi}^{mk}, \mathbf{n}^m \rangle_m = 0, \quad (k = 1, 2, 3), (m = 0, \dots, M). \quad (2.49)$$

First, we take the inner product of (2.46) with respect to the outer normal of Γ_0 . Using equations (2.34), (2.48) and (2.49), it follows that

$$\begin{aligned} w \mathbf{L}_0 &= \frac{1}{2} \langle \mathbf{n}^0, \mathbf{v}^0 \rangle_0 + \langle \mathbf{n}^0, \mathcal{K}_0 \mathbf{v}^0 \rangle_0 - \sum_{j=1}^M \langle \mathbf{n}^0, \mathcal{K}_j \mathbf{v}^j \rangle_0 \\ &= \frac{1}{2} \langle \mathbf{n}^0, \mathbf{v}^0 \rangle_0 + \langle \mathcal{K}_0^* \mathbf{n}^0, \mathbf{v}^0 \rangle_0 - \sum_{j=1}^M \langle \mathcal{K}_0^* \mathbf{n}^0, \mathbf{v}^j \rangle_j \\ &= \langle \mathbf{n}^0, \mathbf{v}^0 \rangle_0 - \sum_{j=1}^M \langle \mathbf{n}^j, \mathbf{v}^j \rangle_j, \end{aligned} \quad (2.50)$$

where L_0 is the curve length of the outer boundary Γ_0 . Next, the inner product is taken of equation (2.39) with respect to the outer normal of Γ_m ($m=1, \dots, M$), we obtain

$$\begin{aligned}
 wL_m &= \langle \mathbf{n}^m, \mathcal{H}_0 \mathbf{v}^0 \rangle_m - \sum_{j=1}^M \langle \mathbf{n}^m, \mathcal{H}_j \mathbf{v}^j \rangle_m + \frac{1}{2} \langle \mathbf{n}^m, \mathbf{v}^m \rangle_m \\
 &= \langle \mathcal{H}_m^* \mathbf{n}^m, \mathbf{v}^0 \rangle_0 - \sum_{j=1}^M \langle \mathcal{H}_m^* \mathbf{n}^m, \mathbf{v}^j \rangle_j + \frac{1}{2} \langle \mathbf{n}^m, \mathbf{v}^m \rangle_m \\
 &= -\frac{1}{2} \langle \mathbf{n}^m, \mathbf{v}^m \rangle_m + \frac{1}{2} \langle \mathbf{n}^m, \mathbf{v}^m \rangle_m = 0,
 \end{aligned} \tag{2.51}$$

where L_m is defined analogically. The latter equality shows that w has to be equal to zero; hence the solution of the deflated equation (2.46) satisfies both the equations (2.40) and (2.44). Note that because of $w = 0$, the inner product (2.50) reduces to the incompressibility requirement for the flow field.

Equation (2.47) can be expressed in terms of ordinary integrals as,

$$\begin{aligned}
 \frac{1}{2} v_i^m(\mathbf{x}) + \sum_{k=0}^M \left(\int_{\Gamma_k} q_{ij}(\mathbf{x}, \mathbf{y}) v_j^k d\Gamma_y + n_i^m(\mathbf{x}) \int_{\Gamma_k} \bar{q}_j v_j^k d\Gamma \right) + \varphi_i^{ml}(\mathbf{x}) \int_{\Gamma_m} \varphi_j^{ml} v_j^m d\Gamma \\
 = \sum_{k=0}^M \left(\int_{\Gamma_k} u_{ij}(\mathbf{x}, \mathbf{y}) b_j^k d\Gamma_y + n_i^m(\mathbf{x}) \int_{\Gamma_k} \bar{u}_j b_j^k d\Gamma \right), \quad \mathbf{x} \in \Gamma_m.
 \end{aligned} \tag{2.52}$$

This integral equation is applied to simulate a Stokes flow with vanishing holes in the inside.

TWO-DIMENSIONAL ANALYTICAL SOLUTION METHOD FOR STOKES FLOW

In this chapter we review an analytical solution method for the two-dimensional Stokes problem driven by surface tension on the free boundary. The method was originally developed by Hopper [41]-[44] and it basically consists of applying a conformal mapping technique to solve the Stokes equations in which the time evolution of the shape is described in terms of an equation of motion involving the mapping function. This kinematic equation of motion appears to be an intermediate between the Eulerian and Lagrangian approach which will be called the “pseudo Lagrangian description”.

The analytic solutions for the coalescence of two cylinders with arbitrary initial radii and a cylinder on a half space are summarized. It appears that these solutions are fairly complicated. Because of this, we will only apply those solutions in order to find simple approximate expressions for obtaining sintering-time and neck curvature as a function of the coalescence rate, in the case of the coalescence of two equal cylinders and a coalescing cylinder on a half-space each. These problems are limiting coalescence problems when this is considered from the point of view of the sintering of two unequal cylinders. The latter coalescence problem will not be considered in detail, because of the rather complicated expressions for the solution, as it will turn out. Moreover, we will describe the neck curvature and shrinkage rate in terms of the coalescence rate.

Finally, a comparison is made between the obtained expressions and approximations that have been used in literature so far and which were derived by modelling the coalescence in a very simple way. The comparison shows that especially the neck curvature and the time dependence of the neck growth differ from the solutions derived in the past.

3.1 ANALYTICAL SOLUTION

We start with a brief outline of Hopper’s method to solve the time evolution of a creeping viscous incompressible flow in a two-dimensional region, bounded by a smooth closed curve and driven solely by surface tension. A detailed description of this solution technique can be found in appendix A.

The method basically consists of finding a conformal mapping function that maps the domain onto the unit circle in the complex plane. Afterwards, an evolution equation is applied to this mapping function for obtaining the deformation of the domain as time proceeds. In order to use this conformal mapping technique, the Stokes equations (2.7) and boundary conditions (2.11) are written in the complex plane (cf. Muskhelishvili [72], chapter 5). This implies that the tension and velocity can be expressed in terms of two functions $\varphi(z)$ and $\chi(z)$ which are analytic in the (complex) region of fluid. Here z denotes the complex variable which will also be written as $z = x + iy$. In the remainder of this chapter x and y will be used instead of x_1, x_2 respectively.

Let

$$z = \Omega(\zeta, t) \quad |\zeta| \leq 1,$$

be a conformal mapping of the fluid domain onto the complex unit disk. Rigid-body motions, that may also determine the choice of Ω , are ignored. Moreover, the outer boundary of the fluid is described in the complex ζ -plane by

$$\sigma = e^{i\theta} \quad 0 \leq \theta \leq 2\pi.$$

Because of the incompressibility condition, we require the area of the domain, say A , to remain constant during the evolution. Expressing this area in terms of Ω by an integral on the unit circle yields

$$\text{area} = A = \frac{1}{2i} \int_{|\sigma|=1} \overline{\Omega(\sigma, t)} \Omega'(\sigma, t) d\sigma. \quad (3.1)$$

Here the prime ' denotes the derivative with respect to the dependent complex variable and the bar denotes the complex conjugate. Hence the mapping Ω has to be chosen so that this requirement is satisfied.

The kinematic equation for motion of Ω should ensure that the unit disk in the ζ -plane remains unchanged as time proceeds. It appears that the kinematic constraint obtained this way is an intermediate between the Eulerian and Lagrangian representation in fluid dynamics; it is therefore called the *pseudo Lagrangian description* (cf. appendix A). Substituting this kinematic relation into the complex equation that expresses the equality of the boundary tension to the curvature in normal direction yields an evolution equation that explicitly describes the values of $\tilde{\chi}(\sigma, t) = \chi(\Omega(\sigma, t), t)$ on the boundary by

$$-\frac{d}{d\sigma} \left(\overline{\sigma \Omega(\sigma, t)} \Omega'(\sigma, t) \mathcal{F}(\sigma, t) \right) + \frac{d}{dt} \left(\overline{\Omega(\sigma, t)} \Omega'(\sigma, t) \right) = 2\tilde{\chi}'(\sigma, t). \quad (3.2)$$

Hopper [42], was the first to derive this result in 1990. Here the function \mathcal{F} is analytic on the unit disk and is uniquely defined by

$$\text{Re } \mathcal{F}(\sigma, t) = \frac{1}{2|\Omega'(\sigma, t)|} \quad \text{and} \quad \text{Im } \mathcal{F}(0, t) = 0,$$

A specific representation for \mathcal{F} in terms of a Taylor series is stated in appendix A. Other representations for \mathcal{F} in terms on an integral can be found in the papers of Hopper [42] and Richardson [89].

In Hopper's evolution equation (3.2), the unknowns are the functions $\tilde{\chi}$ and the derivative of Ω with respect to t (i.e. $\dot{\Omega}$). These unknowns can be determined uniquely by requiring $\tilde{\chi}(\zeta, t)$ to be a function analytic and single-valued on $|\zeta| \leq 1$ when time proceeds, by analytic continuation of equation (3.2) which is performed by replacing σ with ζ . Then the boundary values $\tilde{\chi}(\sigma, t)$ determine $\dot{\Omega}(\sigma, t)$. Hopper [42] shows that when certain conjectural parametric descriptions are chosen for the mapping function Ω , these equations will be fulfilled. In particular, Hopper also shows that polynomial mapping functions of type

$$\Omega(\zeta, t) = \sum_{n=1}^N a_n(t) \zeta^n,$$

where a_n may be both real or complex functions, satisfy Hopper's equation (3.2) when $\tilde{\chi}$ is determined so that all the singularities inside the unit disk are cancelled; i.e. all the poles have to lie in $|\zeta| > 1$. This leads to a system of N complex ODEs for the coefficients a_n . Another ansatz are the rational polynomial maps of the form

$$\Omega(\zeta, t) = \zeta \sum_{n=1}^N \frac{b_n(t)}{1 - a_n(t)\zeta},$$

where $|a_n(t)| < 1$. In the appendix A we show that this set of mapping functions yields $2N$ complex coupled ODEs. More details about the derivation of solutions for a number of geometries can be found in Hopper [42], Richardson [89] and Antanovskii [2]-[3]. Here we will summarize some solutions only.

The first example that we consider is the coalescence of two equal cylinders. The analytical solution for the evolution of this coalescence is given in Hopper [41]-[42], §4.4. In the latter paper, the equations derived are valid for the coalescence of two cylinders with initial radius $\frac{1}{2}\sqrt{2}$. Here, we follow Hopper's method to obtain the evolution equations for two cylinders with initial radius 1, in the beginning.

For the coalescence of two equal cylinders consider the mapping function

$$z = x + iy = \Omega(\zeta, t) = \frac{B\lambda\zeta}{1 - \lambda^2\zeta^2}, \quad (3.3)$$

where $|\zeta| \leq 1$, $\lambda = \lambda(t)$, $0 \leq \lambda < 1$ and $B=B(t)$. When $\lambda \rightarrow 1$, equation (3.3) gives the shape of the touching cylinders with centres $(1, 0)$ and $(-1, 0)$ each. The function B is chosen in such a way that the total area A of the interior of the mapping is *constant* in time, i.e. the incompressibility condition is satisfied. Using (3.3) in equation (3.1) yields

$$B(t) = \frac{(1 - \lambda^4)\sqrt{2}}{\lambda\sqrt{1 + \lambda^4}}. \quad (3.4)$$

Combining relations (3.3), (3.4) and considering ζ to be on the unit circle, the following shape evolution relation is derived for this problem

$$z = x + iy = \frac{(1 - \lambda^4)\sqrt{2}\sigma}{(1 - \lambda^2\sigma^2)\sqrt{1 + \lambda^4}}. \quad (3.5)$$

The time-dependence requires the determination of $\lambda(t)$ only. Hopper [42] shows that the following differential integral equation for $\lambda(t)$ applies

$$\frac{d\lambda}{dt} = - \frac{\lambda\sqrt{1+\lambda^4}K(\lambda^2)}{\pi\sqrt{2}}. \quad (3.6)$$

Here $K(k)$ is the complete elliptic integral of the first kind defined by

$$K(k) = \int_0^{\frac{\pi}{2}} \frac{d\vartheta}{\sqrt{1-k^2\sin^2\vartheta}}. \quad (3.7)$$

Integrating equation (3.6) and replacing the parameter λ by $\nu = \lambda^2$ ($0 \leq \nu < 1$), we obtain for t (as a function of ν)

$$t(\nu) = \frac{\pi}{\sqrt{2}} \int_{\nu}^1 \frac{dk}{k\sqrt{1+k^2}K(k)}. \quad (3.8)$$

The equations (3.5) and (3.8) describe the evolution of the two identical coalescing cylinders with initial radius 1.

Next, we consider the coalescence of two cylinders with arbitrarily initial radii, say R_1 and R_2 with $R_1 \leq R_2$. Richardson [89] derived the analytical solution for this coalescence problem. He applied the mapping function

$$z = \Omega(\zeta, t) = \zeta \left(\frac{C\alpha}{1-\alpha\zeta} + \frac{D\beta}{1+\beta\zeta} \right), \quad (3.9)$$

where α , β , C and D are functions of t and $0 \leq \alpha, \beta < 1$ and $C, D > 0$. It can be shown that when $\alpha = \beta$ and $C = D$ the solution for the two equal coalescing cylinders is obtained since then the mapping function (3.9) is identical to equation (3.3). Here we will summarize the results that Richardson derived by employing the above mapping function into Hopper's equation. It appears that the parameters α and β have to satisfy the following coupled system of ODEs,

$$\begin{aligned} \frac{d\alpha}{dt} &= - \frac{\alpha(1-\alpha^2)}{2\pi D} [(1+\beta^2)I_1 + 2\beta I_2] \\ \frac{d\beta}{dt} &= - \frac{\beta(1-\beta^2)}{2\pi D} [(1+\alpha^2)I_1 - 2\alpha I_2]. \end{aligned} \quad (3.10)$$

Here both I_1 , I_2 are integrals defined by

$$\begin{aligned} I_1 &= I_1(\alpha, \beta) = \int_0^{\pi} \frac{d\vartheta}{\sqrt{b_1 + b_2 \cos \vartheta + b_3 \cos 2\vartheta}} \\ I_2 &= I_2(\alpha, \beta) = \int_0^{\pi} \frac{\cos \vartheta d\vartheta}{\sqrt{b_1 + b_2 \cos \vartheta + b_3 \cos 2\vartheta}}, \end{aligned}$$

where

$$\begin{aligned}
 b_1 &= (a_1\alpha + \beta)^2 + \alpha^2\beta^2(4(a_1 - 1)^2 + (a_1\beta + \alpha)^2), \\
 b_2 &= 4\alpha\beta(a_1 - 1)(a_1\alpha(1 + \beta^2) + \beta(1 + \alpha^2)), \\
 b_3 &= 2\alpha\beta(a_1\alpha + \beta)(a_1\beta + \alpha), \\
 a_1 &= \frac{a_3(R_1^2 - R_2^2) + a_5}{2a_2R_2^2}, \quad a_2 = \frac{\alpha^2}{(1 - \alpha^2)^2}, \quad a_3 = \frac{\alpha\beta}{(1 + \alpha\beta)^2}, \\
 a_4 &= \frac{\beta^2}{(1 - \beta^2)^2}, \quad a_5 = \sqrt{a_3^2(R_1^2 - R_2^2)^2 + 4a_2a_4R_1^2R_2^2}, \\
 C &= a_1D, \quad D = \sqrt{\frac{a_3^2(R_1^2 - R_2^2) - 2a_2a_4R_2^2 + a_3a_5}{2a_4(a_3^2 - a_2a_4)}}.
 \end{aligned}$$

Because of the rather complicated expressions, we will not try to find simple approximations for the coalescence rate in the remainder of this chapter. Therefore, we consider the coalescence of a cylinder on a half-space which can be seen as a special (limiting) case of the coalescence of two cylinders with arbitrary radii. Especially, we will show that the initial stage coalescence rate of the latter problem is similar to the two equal cylinder problem. Hence we expect that the initial stage coalescence rate of the two unequal cylinders will behave similarly too.

Also Hopper [44] was able to solve the coalescence of a cylinder on a half-space analytically; however by a different mapping as considered so far, instead of the unit disk Hopper used a mapping onto the positive imaginary half-space. More precisely, he applied the following mapping function

$$z = \Omega(\zeta, t) = - \left(\zeta + \frac{Eh}{\zeta + iE} \right) \quad \text{Im}\zeta \geq 0. \quad (3.11)$$

It appears that $E = (1 - h^2)/4h$, where the parameter h specifies the degree of the coalescence. In particular h is equal to the height of the cylindrical blob. The mapping function is defined so that it represents the coalescence of a cylinder with diameter equal to 1 on a half-space which is taken equal to the area below the x -axis. The origin of the coordinate system is the point where the cylinder and half-space are touching initially. Hence the parameter h has to be decreasing from 1 to 0 if the time t proceeds. Hopper shows that the function $h(t)$ is the solution of the following ordinary differential equation

$$\frac{dh}{dt} = - \frac{4h^2\sqrt{1-h^2}}{\pi(1+h^2)\sqrt{1+3h^2}} K\left(\frac{2h}{\sqrt{1+3h^2}}\right). \quad (3.12)$$

After integration and substituting $\cos \vartheta$ for the dummy variable of the integrand, it is found that

$$t(\alpha) = \frac{4}{\pi} \int_0^\alpha \frac{(1 + \cos^2 \vartheta)\sqrt{1 + 3\cos^2 \vartheta}}{\cos^2 \vartheta K\left(2\cos \vartheta/\sqrt{1 + 3\cos^2 \vartheta}\right)} d\vartheta, \quad (3.13)$$

where $h = \cos \alpha$ and $0 \leq \alpha \leq \pi/2$. Equations (3.11) and (3.13) describe the complete evolution of this coalescence problem.

It is clear that the differential equations obtained above which describe the time dependence of the parametric variables, have to be solved numerically in order to obtain the evolution of the accompanying mapping functions. In the next section, we will apply these analytical solutions to obtain simple relations for the coalescence rate. Note, that analytical solutions for a number of other initial shapes can be found in the previously mentioned papers too.

3.2 THE COALESCENCE OF TWO EQUAL CYLINDERS

This section is built up in two parts. Firstly, we deduce some general properties concerning the coalescence of equal cylinders. In particular, we give expressions for the contact curvature and shrinkage as functions of the neck radius. Secondly, we will present asymptotic expansions for the time as function of the coalescence rate and the ranges for which those approximations are valid.

Substituting $\sigma = e^{i\theta}$ into the analytical solution (3.5) yields the following parametric equations for the shape evolution of the two equal cylinders

$$\begin{aligned} x(\theta, \nu) &= \frac{(1 - \nu^2)(1 - \nu)\sqrt{2} \cos \theta}{(1 - 2\nu \cos 2\theta + \nu^2)\sqrt{1 + \nu^2}} \\ y(\theta, \nu) &= \frac{(1 - \nu^2)(1 + \nu)\sqrt{2} \sin \theta}{(1 - 2\nu \cos 2\theta + \nu^2)\sqrt{1 + \nu^2}}. \end{aligned} \quad (3.14)$$

Note that the degree of coalescence is specified by the parameter ν , which decreases from 1 to 0 if time increases (t is going to infinity as $\nu \rightarrow 0$), and the boundary curve is specified by the parameter θ which is varying from 0 to 2π . At $t = 0$, both the cylinders are making contact at the origin.

During the evolution, the line of contact is along the y -axis, i.e. θ is equal to $\pi/2$ or $3\pi/2$. We denote by r the *neck radius* between both cylinders. From equation (3.14), we obtain for this neck radius as function of ν ,

$$r(\nu) = y\left(\frac{\pi}{2}, \nu\right) = \frac{(1 - \nu)\sqrt{2}}{\sqrt{1 + \nu^2}}. \quad (3.15)$$

From this equation we observe that when $\nu \rightarrow 0$, i.e. $t \rightarrow \infty$, then $r \rightarrow \sqrt{2}$; which is the radius of the cylinder that the shape evolution approaches as the time proceeds. By elimination for the parameter ν as function of r , we obtain from equation (3.15)

$$\nu = \nu(r) = \frac{2 - r\sqrt{4 - r^2}}{2 - r^2}. \quad (3.16)$$

For the curvature of the contact point between both cylinders, say κ_n , we can derive from the parametric equations (3.14)

$$\kappa_n(\nu) = \left. \frac{y_{\theta\theta}x_\theta - y_\theta x_{\theta\theta}}{(x_\theta^2 + y_\theta^2)^{\frac{3}{2}}} \right|_{\theta=\frac{\pi}{2}}$$

$$= \frac{(1 - 6\nu + \nu^2)\sqrt{1 + \nu^2}}{(1 - \nu)^3\sqrt{2}}. \quad (3.17)$$

Remark that as $\nu \rightarrow 0$, i.e. $t \rightarrow \infty$, then $\kappa_n \rightarrow 1/\sqrt{2}$, as assumed. The derived neck curvature (3.17) can be written as a function of the neck radius r ; from equations (3.16) and (3.17), we obtain

$$\kappa_n(r) = -\frac{4}{r^3} + \frac{3}{r}. \quad (3.18)$$

The shrinkage of the two cylinders can also be described as a function of the neck radius. Let therefore s denote the *relative shrinkage* of both cylinders, i.e. s is the displacement of the point on the boundary curve that intersects the straight line through both the centres of the cylinders. From equation (3.14) we obtain

$$s = 2 - x(0, \nu),$$

and by eliminating ν using equation (3.16), we yield for this relative shrinkage rate,

$$s = 2 - \sqrt{4 - r^2}. \quad (3.19)$$

By taking a Taylor expansion for equation (3.19) in $r = 0$ up to the first order, we find the following approximate shrinkage rate for the early stage, i.e.

$$s \simeq \frac{r^2}{4}. \quad (3.20)$$

Next, we will derive an approximate solution for the coalescence time as function of the neck radius. Therefore, we differentiate equation (3.8) with respect to ν and use equation (3.16). Hence we obtain the following ordinary differential equation which gives the relation between the time and the neck radius,

$$\frac{dr}{dt} = \frac{1}{2\pi} (4 - r^2 - r\sqrt{4 - r^2}) \mathbf{K}\left(\frac{2 - r\sqrt{4 - r^2}}{2 - r^2}\right). \quad (3.21)$$

After integration, the following analytical solution for $t(r)$ is found

$$t(r) = 2\pi \int_0^r \left[(4 - k^2 - k\sqrt{4 - k^2}) \mathbf{K}\left(\frac{2 - k\sqrt{4 - k^2}}{2 - k^2}\right) \right]^{-1} dk. \quad (3.22)$$

First, we develop an approximation for the analytical solution $t(r)$ above which is valid as long as r is small, i.e. the initial stage of the coalescence. Afterwards, we will deduce an expression which is valid for the later stage neck radius. These approximate relations are obtained by using the following asymptotic expansions for the complete elliptic integral $\mathbf{K}(k)$, i.e. equations (8.113.1) and (8.113.3) of Gradshteyn and Ryzhik [30],

$$\mathbf{K}(k) = \frac{1}{2} \log \frac{16}{1 - k^2} + \mathcal{O}\left((1 - k^2) \log(1 - k^2)\right) \quad (k \rightarrow 1) \quad (3.23)$$

$$\mathbf{K}(k) = \frac{\pi}{2} \left[1 + \frac{1}{4} k^2 + \mathcal{O}(k^4) \right] \quad (k < 1). \quad (3.24)$$

Substituting equation (3.23) into the differential equation (3.21) and applying a Taylor expansion in $r = 0$ of the right-hand side up to the second order yields

$$\frac{dt}{d\omega} \simeq -\frac{8\pi}{\log \omega} - \frac{32\pi(2 + \log \omega)}{\log^2 \omega} \omega,$$

where $\omega = r/8$. Hence after integration of the above relation between 0 and $r/8$, we get

$$t \simeq -8\pi \left(\text{li}(\omega) + 20 \text{li}(\omega^2) - \frac{8\omega^2}{\log \omega} \right). \quad (3.25)$$

Here $\text{li}(\omega)$ is the logarithmic integral which is defined by

$$\text{li}(\omega) = \int_0^\omega \frac{dk}{\log k}.$$

In Nielsen [73] the following asymptotic expansion of the logarithmic integral for small values of ω can be found,

$$\text{li}(\omega^\Theta) = \omega^\Theta \sum_{j=1}^{\infty} \frac{(j-1)!}{\Theta^j (\log \omega)^j}, \quad (\Theta > 0). \quad (3.26)$$

Substituting (3.26) into equation (3.25) and eliminating ω yields

$$t \simeq \frac{\pi r}{3 \log 2 - \log r} \left[1 + \frac{r}{4} - \frac{1}{3 \log 2 - \log r} \right], \quad (3.27)$$

which is the approximate solution of $t(r)$ when r is small. However, it appears that the much simpler expression

$$t = \frac{\pi r}{4 \log 2 - \log r}, \quad (3.28)$$

is also close to the initial stage coalescence rate.

In figure 3.1 we have plotted the absolute difference in coalescence time (δt) between the exact analytical solution and both the approximations (3.27) (solid line) and (3.28) (dashed line). The exact solution is obtained by numerical integration of the ODE (3.21). It can be observed from the figure that equation (3.28) is the most accurate approximate coalescence time in the initial stage range $0 \leq r \leq 0.65$. Moreover, we have plotted the absolute difference between both approximate solutions (dotted line) which shows to be less than 0.03. Hence we use the relation (3.28) as the approximation for the initial-stage coalescence because of the much simpler form. Note that the validity of the considered range of r will be demonstrated later.

The approximate solution of $t(r)$ for the later stage neck radius is found by substituting equation (3.24) into the differential equation (3.21) and applying a Taylor expansion in $\sqrt{2}$ (the radius of the final cylinder) of the right-hand side up to the second order, i.e.

$$\frac{dt}{dr} \simeq -\frac{\sqrt{2}}{r - \sqrt{2}} - \frac{1}{2} - \frac{r - \sqrt{2}}{\sqrt{2}} - (r - \sqrt{2})^2.$$

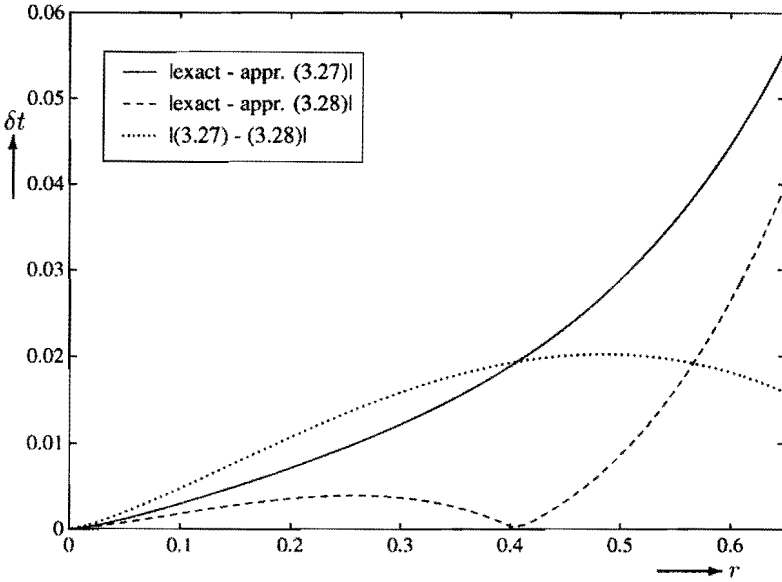


Figure 3.1 The absolute difference in coalescence time (δt) between the exact initial-stage neck solution and both the obtained approximations as the neck radius r increases. The figure shows that the latter simple approximation (3.28) is the most accurate.

Integration between r and $\sqrt{2}$ gives the following approximate solution for the late-stage neck radius,

$$\begin{aligned}
 t &\simeq -\sqrt{2} \log(\sqrt{2} - r) + \frac{1}{2}(\sqrt{2} - r) - \frac{1}{2\sqrt{2}}(\sqrt{2} - r)^2 + \frac{1}{3}(\sqrt{2} - r)^3 \\
 &= \frac{1}{6\sqrt{2}} \left[-12 \log \vartheta + 3\sqrt{2}\vartheta - 3\vartheta^2 + 2\sqrt{2}\vartheta^3 \right], \tag{3.29}
 \end{aligned}$$

where $\vartheta = \sqrt{2} - r$.

Now, we will deduce a range for the neck radius r in which both the approximate coalescence time solutions (3.28) and (3.29) are valid. In figure 3.2 we have plotted (solid line) the analytical neck radius behaviour as a function of the coalescence time, which is described implicitly by equation (3.22). This curve is obtained by numerical integration of the ODE (3.21). In the figure we have also plotted (dotted line) the approximate initial stage solution, i.e. equation (3.28). As can be observed, this approximation is valid when $0 \leq r \leq 0.65$. The dashed line of figure 3.2 represents the later-stage approximation as is given by (3.29) which shows the validity as $0.65 \leq r < \sqrt{2}$, i.e. the remaining part of the neck radius range. In section 3.4 we will apply these approximations for a comparison to the in literature usually applied coalescence relations.

The deduced initial and later stage expansions for the coalescence time as function of the contact radius can be used to obtain a relation between the coalescence time and

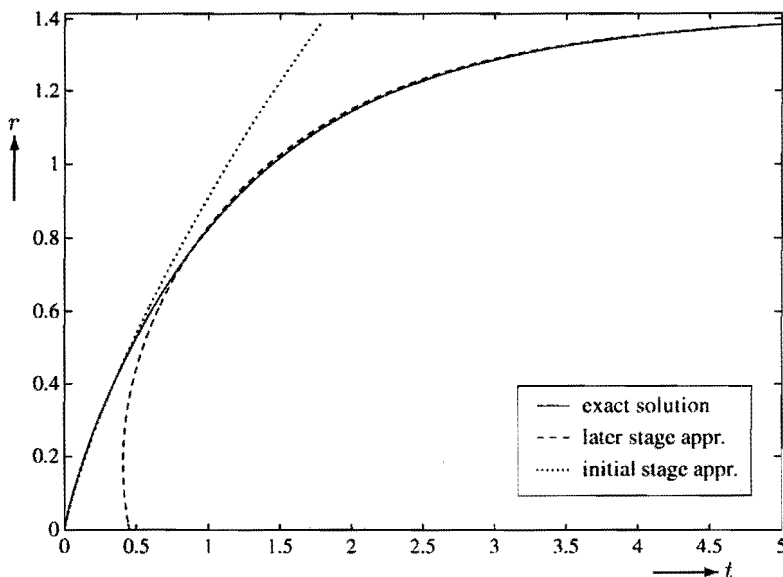


Figure 3.2 The matching of both the approximate initial radius and the later stage neck radius r compared with the exact analytical solution.

the shrinkage s . Therefore, we note that equation (3.19) can be rewritten by

$$r = \sqrt{s(4-s)}.$$

Substituting this equation in the expressions (3.28) and (3.29) yields the coalescence time as function of s . Moreover, the in this way obtained initial stage solution can be simplified by using that

$$\sqrt{s(4-s)} \simeq 2\sqrt{s},$$

when s is small.

3.3 THE COALESCENCE OF A CYLINDER ON A HALF SPACE

In this section we will derive properties from the analytical solution for the coalescing cylinder on a half-space. In particular we will derive approximate expressions for the coalescence time t as a function of the height h of the cylinder and as a function of the contact line between cylinder and half-space each. For the curvature of the coalescence point is an approximation obtained which is valid during the early stage of the deformation process.

The mapping function (3.11) that represents this shape evolution problem, reads in

parametric form

$$\begin{aligned} x(\theta, h) &= \theta \left(1 + \frac{4h^2(1-h^2)}{16\theta^2 h^2 + (1-h^2)^2} \right) \\ y(\theta, h) &= \frac{h(1-h^2)^2}{16\theta^2 h^2 + (1-h^2)^2}, \end{aligned} \quad (3.30)$$

where the boundary curve is specified by the parameter θ ($\theta \in \mathbb{R}$) and the function $h(t)$ is given by the ODE (3.12).

Similar to the previous subsection, we will denote the contact line between the cylinder and the half-space by the contact radius r . Following Hopper [44], this contact radius is defined as the distance between the y -axis and the point of the shape with vertical tangent (minimum width). This definition is only applicable for the initial stage of the coalescence; in the later stage it is not possible to define such a contact radius any more.

From the parametric form (3.30), we can describe the shape evolution as a function of the y -coordinate and the parameter h , i.e.

$$x(y, h) = \pm \frac{(1 + 4hy - h^2)\sqrt{h-y}}{4h\sqrt{y}}. \quad (3.31)$$

After differentiating this equation with respect to y and solving

$$\frac{dx}{dy} = 0,$$

we obtain for the height of the contact point, say y_c , as function of h ,

$$y_c(h) = \frac{1}{4}(h - \mu), \quad (3.32)$$

where $\mu = \sqrt{3h^2 - 2}$. Substituting the above expression into equation (3.31) yields for the contact radius

$$r(h) = \frac{(1 - h\mu)\sqrt{3h + \mu}}{4h\sqrt{h - \mu}}. \quad (3.33)$$

From two times differentiating equation (3.31) with respect to y and using relation (3.32), we derive for the curvature of the contact point, say κ_c , the following relation

$$\kappa_c(h) = -\frac{d^2x}{dy^2}(y_c) = \frac{16\mu(h\mu - 1)}{(1 - \mu)^{\frac{3}{2}}(3h + \mu)^{\frac{3}{2}}}. \quad (3.34)$$

Note that the definition of the contact radius above is applicable only when $h \geq \sqrt{2/3} \simeq 0.8165$, or after numerical integration of (3.13) one obtains $t \leq 0.5930$. Hence we observe that during the initial stage of the coalescence, the parameter h is close to 1. Because of this, we introduce a new variable $s = 1 - h$, which can also be considered as the shrinkage of the cylinder on to the half-space. After substituting s into equations

(3.33), (3.32) and (3.34) respectively, and employing an asymptotic expansion for $s \rightarrow 0$ of all these equations up to the second order, we obtain

$$r = \sqrt{2s} + \mathcal{O}(s\sqrt{s}) \quad (3.35)$$

$$y_c = \frac{s}{2} + \mathcal{O}(s^2) \quad (3.36)$$

$$\kappa_c = -\frac{1}{\sqrt{s}} \left(\frac{\sqrt{2}}{s} + \mathcal{O}(1) \right). \quad (3.37)$$

From equation (3.35) we derive for the initial stage shrinkage s of the cylinder as function of the contact radius

$$s \simeq \frac{r^2}{2}, \quad (3.38)$$

In order to compare this shrinkage rate with the shrinkage of two coalescing cylinders found in the previous section, i.e. equation (3.20), we have to multiply expression (3.38) by a factor $\frac{1}{2}$ since the initial diameter of those coalescing cylinders is two times larger than the cylinder that is considered here.

Eliminating s in (3.36) and using (3.38), yields for the height of the neck point y_c

$$y_c \simeq \frac{r^2}{4}.$$

After a similar elimination of equation (3.37), we obtain for the curvature κ_c of the coalescence point

$$\kappa_c \simeq -\frac{4}{r^3}.$$

This latter result shows that the contact curvature is depending on r in a similar order (only the constant differs, i.e. has to be multiplied by a factor 4), when compared to the case of the coalescence of two equal cylinders (cf. equation (3.18)).

Note that in the case of the coalescing cylinder on a half-space the contact point is nearly the point where the maximum value of the curvature is reached. Another definition of the contact point would be the point where the curvature has maximum magnitude. However, we were not successful in solving the equations involved for the height of the contact point analytically resulting from the latter definition. Another disadvantage is that from a practical point of view, it would be difficult to measure such a contact radius.

Next, we outline the derivation of the initial- and later-stage approximation for the coalescence time as function of the height h (or shrinkage s) and an initial-stage approximation of the contact radius each. These approximate expressions will be deduced from the analytical solution and this analysis does show similarities with the derivation of the approximate relations for the neck for the two equal cylinders case.

First, we obtain an approximation for the initial time stage. Therefore, we substitute the asymptotic expansion for the complete elliptic integral K , i.e. equation (3.23) and the parameter s into the ODE (3.12), we obtain

$$\frac{2}{\pi} \frac{dt}{ds} \simeq \frac{(2 - 2s + s^2)\sqrt{4 - 6s + 3s^2}}{(1 - s)^2\sqrt{s(2 - s)}} \log^{-1} \left[\frac{16(4 - 6s + 3s^2)}{s(2 - s)} \right].$$

If we expand the expression on the right hand side above in $s = 0$ up to the first order, we obtain

$$\frac{1}{8\pi} \frac{dt}{d\omega} \simeq -\frac{1}{\sqrt{2} \log \omega},$$

where $\omega = s/32$. After integration between 0 and ω we find

$$t \simeq -8\pi \operatorname{li}(\sqrt{\omega}). \quad (3.39)$$

Substituting the asymptotic expansion of the logarithmic integral for small values of ω (equation (3.26) with $\Theta = \frac{1}{2}$) into equation (3.39) and eliminating ω , we obtain the following initial-stage approximation for $t(s)$

$$t(s) \simeq \frac{2\pi\sqrt{2}s}{5 \log 2 - \log s} \left[1 - \frac{2}{5 \log 2 - \log s} + \frac{8}{(5 \log 2 - \log s)^2} \right]. \quad (3.40)$$

An approximation for $t(h)$, at later stages of the coalescence, was already given by Hopper [44] for a general h . Here, we substituted $h = 0.155$ which simplifies the expansion to

$$t(h) \simeq 0.90591 + \frac{\sqrt{1+3h^2}}{2h} - \frac{7h}{4\sqrt{1+3h^2}} - \frac{25h^3}{16(1+3h^2)^{\frac{3}{2}}}. \quad (3.41)$$

In order to express the asymptotic behaviour as $t \rightarrow \infty$, we substitute into the ODE (3.12) the asymptotic expansion (3.24) of the complete elliptic integral, i.e.

$$2 \frac{dt}{dh} \simeq -\frac{(1+h^2)(1+3h^2)^{\frac{3}{2}}}{h^2(1+4h^2)\sqrt{1-h^2}}.$$

For the right hand side the following asymptotic behaviour is found as $h \rightarrow 0$,

$$\frac{dt}{dh} \simeq -\frac{1}{2h^2}.$$

After integration we obtain,

$$t \simeq \frac{1}{2h}, \quad (3.42)$$

which is the asymptotic solution for $t(h)$ when $h \rightarrow 0$ and is also found in Hopper [44]. Hence this asymptotic behaviour shows that an isolated disturbance is decaying by a rate of t^{-1} . This behaviour is consistent with Kuiken's analysis of an arbitrary isolated disturbance, cf. Kuiken [62].

In figure 3.3 shows the matching of both the initial- and the later stage approximation compared with the exact solution for the change of the height h of the coalescing cylinder on a half-space for increasing time. Again, the exact solution is obtained by numerical integration of ODE (3.12). As can be observed from this figure, the initial stage approximation (3.40) matches the exact solution reasonably well as $h > 0.5$ and otherwise the later stage expression (3.41) is valid. The dashed-dotted line in this figure

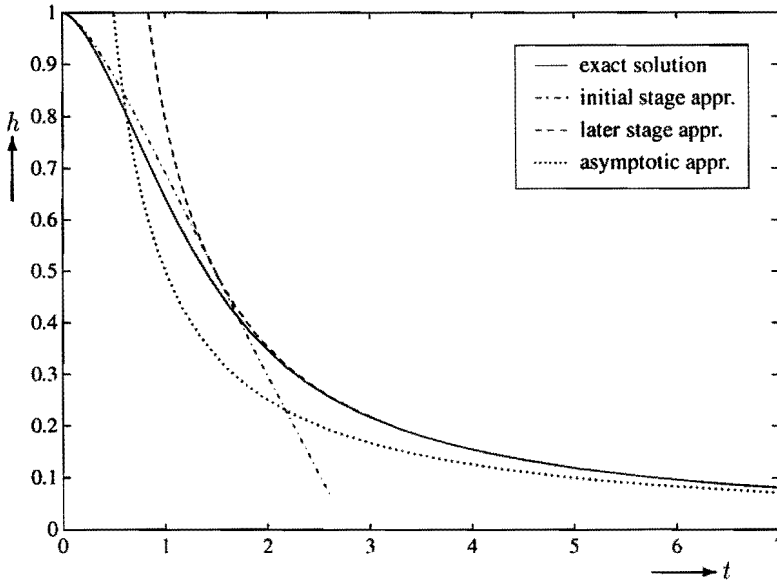


Figure 3.3 The matching of the initial- and later approximate solutions and the asymptotic behaviour of the cylindrical height (h) compared with the exact analytical solution as time increases.

is the asymptotic behaviour as is expressed by equation (3.42). From this curve plot we see that the latter asymptotic expansion is reasonably applicable when $h < 0.1$.

The approximate solution for the time as function of the contact radius can be obtained by substituting equation (3.38) into the approximate initial solution (3.40). It follows that

$$t(r) \simeq \frac{\pi r}{3 \log 2 - \log r} \left[1 - \frac{1}{3 \log 2 - \log r} + \frac{2}{(3 \log 2 - \log r)^2} \right]. \quad (3.43)$$

In figure 3.4 is plotted the exact contact radius (solid line) and the approximate solution (3.43) (dotted line) as a function of time as $t \leq 0.59$. As can be observed from this figure, the matching of both solutions is reasonably well when $r < 0.5$. In this figure we have also plotted the exact solution of the comparable coalescing equal cylinders problem (dashed line), i.e. the initial radius of those cylinders is taken equal to $\frac{1}{2}$. The plot shows that both exact solutions are matching reasonably well during the early stage of the coalescence.

This behaviour can be explained by considering both approximate solutions for the coalescence time as a function of the neck radius, i.e. equations (3.28) and (3.29). In particular, we obtain that the leading term of the approximate expression (3.43) is similar to the initial stage relation derived for the coalescence of two equal cylinders, i.e. equation (3.28) where r is replaced by $r/2$. This similar behaviour of neck growth in the early stage is something that could be expected since we deduced that the neck curvature as function of the contact radius is for both the cases of comparable magnitude.

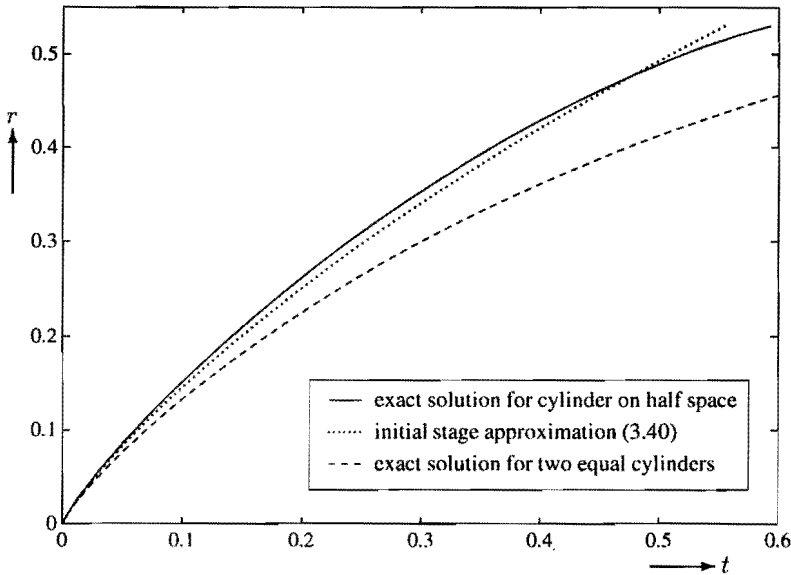


Figure 3.4 The matching of the initial approximate solution for the contact radius r compared with the exact analytical solution by increasing time. The contact radius of two equal cylinders with diameter equal to 1 is also plotted to show that the growth of the neck radius is almost the same in the early time region.

3.4 DISCUSSION OF RESULTS

In this section we will summarize some (static) models that are applied in literature to predict the coalescence rate and neck curvature development. These relations are then compared with the asymptotic results that we have derived in the previous sections. Here we will denote the dimension-full quantities by *roman symbols*.

A simplified theoretical (static) model attempting to describe the early stages of viscous sintering of two spherical particles was first formulated in 1945 by Frenkel [25]. He assumed that the energy dissipated in viscous flow is equal to the energy change resulting from the reduction in surface area. Moreover, he let the centres of the spheres approach one another and form a sharp neck at the contact. In order to preserve the volume of the spheres, Frenkel made the assumption that the spherical radii equally increased as coalescence proceeded. He limited the model to the early stage of sintering when the radii of the spheres could be approximated by the initial radii reasonably well.

Frenkel's model leads to the following equation for the neck radius (r) as function of the sintering time (t)

$$\frac{r^2}{\ell^2} = C_F \frac{\gamma t}{\ell \eta}, \quad (3.44)$$

where the characteristic length ℓ is equal to the initial radius of the coalescing spheres and C_F is a constant which depends on the system considered: C_F is equal to $3/2$ in the case of sintering spheres (Frenkel [25]) and equal to 4 when the model is applied to

the coalescence of two equal cylinders (Ross [90]). The relation above (for spherical particles) is well known in literature and Frenkel's method for analyzing viscous sintering has subsequently been used, among others, by Shaler and Wulff [96], Mackenzie and Shuttleworth [70] and Scherer [92]-[93].

This model of two coalescing spheres or cylinders is commonly applied in sintering literature to describe the initial stage of sintering. In order to describe the *shape deformation* of the particles, two geometrically different models are often used, cf. Kingery and Berg [55]. Both approaches assume that the initial radii of the particles do not change during the (initial stage) sintering. These approximations are referred to as the *tangent circle models*, cf. Exner [23].

In the first model, the assumption is made that the centres of both spheres do not move during the initial stage and that the sintering occurs by material, filling in between the spheres. The neck contour is represented by a circular arc which makes tangential contact with the spheres. The consequence of this approach is that there is no conservation of volume so that the model can be applied only in the very initial stage. From this model, one automatically obtains the radius (ρ) of the circular arc of the neck region, and hence the neck curvature (κ_n) too, because $\kappa_n = -1/\rho$. For this circular arc one finds as radius,

$$\rho = \frac{r^2}{2(\ell - r)} \simeq \frac{r^2}{2\ell}, \quad (3.45)$$

since r is small.

The second model which is usually applied in the case of viscous sintering, assumes that the coalescence takes place by mutual penetration of particle pairs, i.e. the centres of the spheres are approaching. In order to preserve the volume, the superfluous material is used for filling the neck region. Again, the shape of the neck region is a circular arc which makes tangential contact with the spheres. In the case of two coalescing cylinders the conservation of volume (=surface in two dimensions) leads to the following equation

$$\frac{1}{2}\pi\ell^2 - (\ell^2 - \rho^2) \arcsin \left[\frac{\ell - s}{\ell + \rho} \right] - (r + \rho)(\ell - s) = 0,$$

where s is equal to the depth of penetration of a cylinder into the other one. Given a neck radius r , the approach of the centres of the cylinders s can be derived numerically from the equation above together with equation (3.46). The equation of volume conservation in the case of sintering spheres can be found in the review of Exner [23]. For both cases the radius of the circular arc of the neck region reads

$$\rho = \frac{r^2 - 2\ell s + s^2}{2(\ell - r)} \simeq \frac{r^2}{4\ell}. \quad (3.46)$$

Here the assumption is made that $s/\ell \simeq \rho/\ell$. In order to prescribe the time-dependence of ρ for both models as well as depth of penetration s , the equations (3.45) or (3.46) are coupled with Frenkel's relation (3.44).

Next, we will compare the approximations described above for the coalescence rate and the shape evolution with the expressions that are obtained in section 3.2. Therefore,

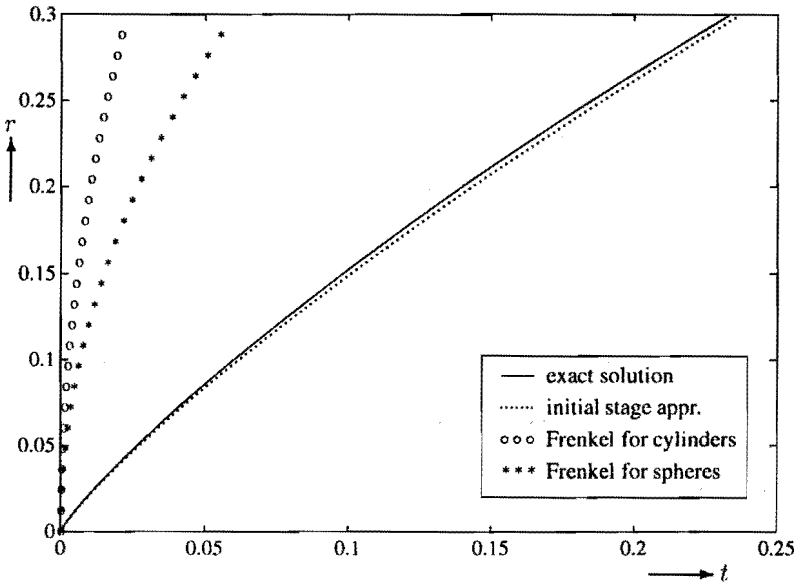


Figure 3.5 The matching of the approximate initial neck radius r for the coalescing cylinders compared with both the exact analytical solution and the (dimensionless) Frenkel equations which are often applied to approximate r in the early stage.

we consider the initial-stage approximation (3.28) and compare that expression to the dimensionless Frenkel relations, i.e. from (3.44) we find

$$t(r) = \frac{r^2}{C_F}.$$

In figure 3.5 we have plotted these relations for the two coalescing cylinders (bullets and $C_F = 4$) and two spheres (asterisks and $C_F = 3/2$) each. Moreover, both the exact solution and the initial-stage expression (3.28) for these two coalescing cylinders are printed too (solid and dotted line respectively). The figure shows that the prediction of the neck radius evolution using the Frenkel model is going much faster as compared with the growth-rate derived from both the analytical and the approximate solution for the coalescing cylinders. From this observation we expect that the Frenkel model is not correct for the three-dimensional case either, since in section 8.3 it will be shown numerically that the initial-stage coalescence rate of two spheres is of the same order as in the cylindrical case.

At the end of section 3.3 we showed that the coalescence of a cylinder on a half-space behaves in a similar way as the two cylinder case. This is an important result because this neck growth behaviour will most likely apply in the case of the coalescence of the two unequal cylinders too; since both problems considered may be regarded as limiting cases for the coalescing of unequal cylinders. Hence we propose to use the initial-stage approximation (3.28) in both the two- and the three-dimensional cases to predict the coalescence rate between two cylinders or spheres and the coalescence of them on a half-space respectively. Moreover, this behaviour can probably be applied

to treat touching boundaries which may occur during a numerical simulation; although (not modelled) other physical processes may be important too then (like van der Waals forces).

Next, we consider the tangent circle model that was developed to predict the shape deformation during the evolution. First, we consider the prediction of the neck curvature which reads, in dimensionless form (cf. equation (3.46)),

$$\kappa_n(r) = -\frac{1}{\rho} = -\frac{4}{r^2}. \quad (3.47)$$

If we compare this approximate neck curvature to the exact neck curvature (3.18), we see that the latter curvature is a factor $1/r$ larger. This is also in agreement with the experimental observations as are performed by Exner and Petzow [22]. They observed in experiments of sintering glassy spheres that in reality the neck curvature is *sharper* than the one given by the tangent-circle approximation and that this effect is dependent on the chemical environment in which the sintering is performed. This is not surprising since the tangent-circle model does not have any relation with the real governing flow field equations.

Second, we compare the relative shrinkage rate as predicted by the tangent-circle approximation with the exactly derived solution. In order to obtain the dimensionless relative shrinkage rate s as approximated by the tangent-circle model, it is assumed that $s \simeq \rho$. Hence we find from equation (3.47) that

$$s(r) \simeq \frac{r^2}{4},$$

which is equal to the approximation (3.20) that is deduced from the exact analytical shape deformation.

Another application of the expressions deduced is that they can be used to predict the surface tension γ of glass at a given temperature, since the analytical solutions are in good agreement with experimental results, cf. De With and Corbijn [113] and Korwin *et al.* [57]-[58]. Besides using the rather complicated exact analytical solutions directly, one can apply the approximations derived previously. Therefore, we have to transform these approximate solutions back to dimension-full quantities.

First, we consider the coalescence of two glass fibres with equal diameters. Substituting the definition of the characteristic time t_c (2.5) and the cylindrical radius length ℓ in the equations (3.28) and (3.29) for two equal cylinders, we obtain for the surface tension

$$\gamma \simeq \begin{cases} \frac{\pi \eta r \theta}{t} & (0 \leq r \leq 0.65\ell), \\ \frac{\ell \eta}{6t\sqrt{2}} [-12 \log \vartheta + 3\sqrt{2} \vartheta - 3\vartheta^2 + 2\sqrt{2} \vartheta^3] & (0.65\ell \leq r < \ell\sqrt{2}), \end{cases}$$

where $\theta = \log^{-1}[16\ell/r]$ and $\vartheta = (\ell\sqrt{2} - r)/\ell$. However, a practical experiment for sintering two equal coalescing cylinders (e.g. glass fibres) is not easy to set up. It is

(relatively) simpler to perform the coalescence of a glass fibre on a glassy plate. Because of this, we also give the solutions of the coalescing cylinder on a half-space in physical quantities.

Again the characteristic length ℓ is taken equal to the radius of the cylinder. From equations (3.40), (3.41) and (3.42) we derive the following relation for the surface tension as a function of the sintering time and the height of the cylinder (h), i.e.

$$\gamma \simeq \begin{cases} \frac{2\pi\eta}{t} \xi (1 - \xi + 2\xi^2) \sqrt{\ell(2\ell - h)} & (\ell < h \leq 2\ell) \\ \frac{\ell\eta}{t} \left(1.81182 + \frac{1}{\mu} - \frac{7\mu}{2} - \frac{25\mu^3}{8} \right) & (h \leq \ell) \\ \frac{2\ell^2\eta}{th} & (h \leq 0.2\ell), \end{cases}$$

where

$$\xi = 2 \log \left[\frac{64\ell}{2\ell - h} \right] \quad \text{and} \quad \mu = \frac{h}{\sqrt{4\ell^2 + 3h^2}}.$$

For the surface tension as a function of the neck radius and time we obtain from equation (3.43) in dimension-full variables

$$\gamma \simeq \frac{\pi\eta r}{t} \theta (1 - \theta + 2\theta^2) \quad (r \leq \ell).$$

Note that by applying the latter equation, we might also use the initial-stage approximation for the two equal coalescing cylinders, since the leading term of the above equation is the same.

As we mentioned in subsection 1.2.1, De With and Corbijn [113] considered the sintering of a fibre on a glassy plate. They used both the experimentally obtained height h of the cylindrical shape and Hopper's exact analytical solution to determine the surface tension γ of glass at relatively low temperatures (600° C). They mention that both the accuracy of the viscosity data and the temperature sensitivity of the viscosity are important limiting factors for obtaining an accurate surface tension value γ this way.

NUMERICAL SOLUTION OF THE STOKES PROBLEM

In this chapter we describe the numerical solution of the boundary value problem, e.g. the Stokes equations, at a fixed time. Since the velocity field of this boundary is required only, the problem is ideally suited to be solved by a Boundary Element Method (BEM). Therefore the boundary will be discretized into a sequence of elements and the velocity and surface tension are written in terms of their values at a sequence of nodal points. From the discretized form of the governing integral equation a full rank system of linear algebraic equations is obtained for the unknown velocity field.

Next, we pay special attention to the problems that can occur by the numerical approximation of the curvature, especially when at a certain point of the boundary a cusp arises. In principle, the curvature at this point can become very large in magnitude; as a consequence the approximation error may be large due to numerical cancellation.

Finally, we propose an algorithm for a fairly optimal grid (re)distribution based on equidistributing the curvature of the boundary. The aim of that algorithm is twofold. First, the number and position of the discretization points are nearly optimized, which is important in the view of minimalization of the computational costs per time step. Secondly, the algorithm treats cusp regions so that the curvature of this particular region is preserved after the redistribution to avoid (numerical) oscillations in the computed velocity field.

4.1 SOLVING A FREDHOLM INTEGRAL EQUATION OF THE SECOND KIND

We briefly consider numerical approximation methods, more in particular projection methods, to solve a Fredholm integral equation of the second kind. Consider the following equation

$$\lambda\psi - \mathcal{A}\psi = f, \tag{4.1}$$

where \mathcal{A} is an operator from a Banach space, say X , into the same Banach space. The operator \mathcal{A} is defined by

$$\mathcal{A}\psi(x) = \int_I K(x, y)\psi(y) dy \quad (x \in I),$$

where the kernel $K(x, y)$ is weakly singular and the interval of integration I is closed. Hence the operator \mathcal{A} is compact. Without loss of generality, we may assume λ to be equal to 1.

The operator \mathcal{A} will be approximated by a sequence of bounded finite rank operators (\mathcal{A}_N) . We achieve this by projecting the solution ψ onto finite dimensional subspaces. Other approximation techniques for integral equations can be found in the books of Hackbusch [34] and Kress [59], for instance. We start by providing some general properties of such projection operators like their convergence and error estimation; next, we overview two special cases of projection methods that are of interest for us, i.e. the *collocation method* in which the projection will be prominent and *Galerkin's method* where the subspaces come to the front.

Let $X_N \subset X$ be a sequence of subspaces which, from a practical point of view, are assumed to be finite dimensional. Moreover, let the finite rank operator $\mathcal{P}_N : X \rightarrow X_N$ be a projection from X onto X_N ; i.e. the following properties are satisfied,

$$\mathcal{P}_N = \mathcal{P}_N^2 \quad (4.2)$$

$$\text{Range}(\mathcal{P}_N) = X_N, \text{ i.e. } \mathcal{P}_N \psi_N = \psi_N \quad (\psi_N \in X_N). \quad (4.3)$$

Next, we define the finite rank operator $\mathcal{A}_N := \mathcal{P}_N \mathcal{A} \mathcal{P}_N$. Replacing \mathcal{A} by \mathcal{A}_N in equation (4.1) gives

$$\psi - \mathcal{A}_N \psi = f. \quad (4.4)$$

Then multiplying equation (4.4) by \mathcal{P}_N and using the properties (4.2)-(4.3) yields the following approximate equation in the finite dimensional subspace X_N

$$\psi_N - \mathcal{A}_N \psi_N = f_N, \quad (4.5)$$

where $f_N = \mathcal{P}_N f$. We will show that for \mathcal{A}_N sufficiently close to \mathcal{A} equation (4.5) is uniquely solvable; an error estimate for ψ_N is contained in the following theorem,

Theorem 4.1 *Let $\mathcal{A} : X \rightarrow X$ be a compact operator such that $(\mathcal{J} - \mathcal{A})$ is injective and let \mathcal{P}_N be a projection from X onto a finite dimensional subspace X_N . Suppose for the finite rank projection $\mathcal{A}_N = \mathcal{P}_N \mathcal{A} \mathcal{P}_N$ there is the estimate*

$$\|(\mathcal{J} - \mathcal{A})^{-1}\| \|\mathcal{A}_N - \mathcal{A}\| < \frac{1}{4}. \quad (4.6)$$

Then for all $f \in X$ the projection equation (4.5) is uniquely solvable and if ψ is the solution of equation (4.1) the following error estimation holds

$$\|\psi_N - \psi\| \leq \|(\mathcal{J} - \mathcal{A})^{-1}\| \left(M \|\mathcal{A} - \mathcal{A}_N\| \|f\| + \|(\mathcal{J} - \mathcal{P}_N) f\| \right), \quad (4.7)$$

where M is a positive constant depending on \mathcal{A} .

Proof. From the assumptions that both $(\mathcal{J} - \mathcal{A})$ is injective and the estimate (4.6), we deduce

$$\begin{aligned} (\mathcal{J} - \mathcal{A}_N)^{-1} &= [\mathcal{J} - (\mathcal{J} - \mathcal{A})^{-1}(\mathcal{A}_N - \mathcal{A})]^{-1}(\mathcal{J} - \mathcal{A})^{-1} \\ &= \left(\sum_{k=0}^{\infty} [(\mathcal{J} - \mathcal{A})^{-1}(\mathcal{A}_N - \mathcal{A})]^k \right) (\mathcal{J} - \mathcal{A})^{-1}. \end{aligned}$$

Using the relation above and estimate (4.6), it can be seen that

$$\|(\mathcal{J} - \mathcal{A}_N)^{-1}\| \leq \frac{\|(\mathcal{J} - \mathcal{A})^{-1}\|}{1 - \|(\mathcal{J} - \mathcal{A})^{-1}\| \|\mathcal{A}_N - \mathcal{A}\|} < \frac{4}{3} \|(\mathcal{J} - \mathcal{A})^{-1}\|, \quad (4.8)$$

hence $(\mathcal{J} - \mathcal{A}_N)^{-1}$ exists and is bounded. Moreover, using (4.6) and (4.8) the estimation

$$\|(\mathcal{J} - \mathcal{A}_N)^{-1}\| \|\mathcal{A} - \mathcal{A}_N\| < \frac{1}{3}, \quad (4.9)$$

holds. Then, following a similar procedure as described above, we find

$$(\mathcal{J} - \mathcal{A})^{-1} = \left(\sum_{k=0}^{\infty} [(\mathcal{J} - \mathcal{A}_N)^{-1}(\mathcal{A} - \mathcal{A}_N)]^k \right) (\mathcal{J} - \mathcal{A}_N)^{-1} := (\mathcal{J} + \mathcal{S}_N)(\mathcal{J} - \mathcal{A}_N)^{-1}, \quad (4.10)$$

and applying the estimates (4.8) and (4.9) yields

$$\|\mathcal{S}_N\| \leq \frac{\|(\mathcal{J} - \mathcal{A}_N)^{-1}\| \|\mathcal{A} - \mathcal{A}_N\|}{1 - \|(\mathcal{J} - \mathcal{A}_N)^{-1}\| \|\mathcal{A} - \mathcal{A}_N\|} < 2 \|(\mathcal{J} - \mathcal{A})^{-1}\| \|\mathcal{A} - \mathcal{A}_N\|. \quad (4.11)$$

Using successively the equations (4.1), (4.10) and (4.5), we deduce

$$\begin{aligned} \psi - \psi_N &= (\mathcal{J} - \mathcal{A})^{-1}f - \psi_N \\ &= (\mathcal{J} - \mathcal{A})^{-1}[\mathcal{P}_N f + (\mathcal{J} - \mathcal{P}_N)f] - \psi_N \\ &= (\mathcal{J} + \mathcal{S}_N)\psi_N + (\mathcal{J} - \mathcal{A})^{-1}(\mathcal{J} - \mathcal{P}_N)f - \psi_N \\ &= \mathcal{S}_N(\mathcal{J} - \mathcal{A}_N)^{-1}\mathcal{P}_N f + (\mathcal{J} - \mathcal{A})^{-1}(\mathcal{J} - \mathcal{P}_N)f. \end{aligned}$$

If we take the norm of the equation above and use the estimates (4.8) and (4.11), we arrive at the estimate (4.7) with $M = 8 \|(\mathcal{J} - \mathcal{A})^{-1}\|/3$. \square

Theorem 4.1 states that for a finite rank operator \mathcal{A}_N , sufficiently close to \mathcal{A} , the operator $(\mathcal{J} - \mathcal{A}_N)$ is invertible. The number $\frac{1}{4}$ in the estimate (4.6) is sufficient to prove this theorem. In practice however, the term $\|(\mathcal{J} - \mathcal{A})^{-1}\| \|\mathcal{A}_N - \mathcal{A}\|$ will be much smaller since \mathcal{A}_N is close to \mathcal{A} . The error estimate (4.7) denotes that the error $\|\psi_N - \psi\|$ corresponds to the error that is introduced by the projection, i.e. this error estimate is quasi-optimal. Hence the error analysis of the approximate equation (4.5) is reduced to the error estimation for $\mathcal{A} - \mathcal{P}_N \mathcal{A} \mathcal{P}_N$ and $f - \mathcal{P}_N f$.

Now, we consider the *collocation method*; this projection method is usually referred to as the BEM. In this method, we choose a set of nodal points on I , say $x^{i,N}$ ($i = 1, \dots, N$), where N is the total number of points and as Banach space X we take $C(I)$, i.e. the space

of continuous functions. Let X_N be an interpolation subspace, then the interpolation of a function $\psi \in X$ by $\psi_N \in X_N$ is accomplished by

$$\psi_N(x^{i,N}) := \psi(x^{i,N}), \quad i = 1, \dots, N. \quad (4.12)$$

This equation defines a projection \mathcal{P}_N from X onto X_N , i.e.

$$\mathcal{P}_N \psi = \psi_N = \sum_{i=1}^N \psi(x^{i,N}) \phi^{i,N},$$

where $\{\phi^{i,N}\}$ is an independent set in $C(I)$ with $\phi^{i,N}(x^{j,N}) = \delta_{ij}$. Hence the projection equation (4.5) applies which is equivalent to the system of equations

$$\psi_N(x^{i,N}) - (\mathcal{A}_N \psi_N)(x^{i,N}) = f_N(x^{i,N}), \quad i = 1, \dots, N,$$

where

$$\mathcal{A}_N \psi_N = \sum_{i,j=1}^N \psi_N(x^{i,N}) \int_I K(x^{i,N}, y) \phi^{i,N}(y) dy,$$

Substituting the definition of the projection (4.12) for f_N and $\mathcal{A}_N \psi_N$ in the above equation, we arrive at the collocation equation

$$\psi_N(x^{i,N}) - (\mathcal{A} \psi_N)(x^{i,N}) = f(x^{i,N}), \quad i = 1, \dots, N. \quad (4.13)$$

Thus the collocation method considers the integral equation at the discretization nodes only; because of this the points $x^{i,N}$ are called *collocation points*. The next step is to substitute

$$\psi_N = \sum_{i=1}^N \alpha_i \phi^{i,N}$$

into equation (4.13) which produces a square full rank system of linear algebraic equations for the unknowns α_i . Note that the interpolation space X_N depends on the choice of $\phi^{i,N}$ and is related to the collocation points. As stated by the estimate (4.7), the error of the approximate solution is related to the interpolation method. Usually, truncated piecewise Lagrangian interpolation polynomials are taken for the *basis functions* $\phi^{i,N}$. Then, according to Hackbusch [34], the discretization error will be of order h^{q+1} where q is the polynomial degree and h is the maximum distance between two successive nodes.

In the case of Galerkin's method we require a Hilbert space with an inner product $\langle \cdot, \cdot \rangle$ (cf. equation (2.28)) and a sequence of finite dimensional subspaces X_N in X with properties $X_N \subset X_{N+1}$ and the closure of $(\cup X_N)$ is X . Among the variety of linear operators \mathcal{P}_N that can be used to project X onto X_N we employ *orthogonal projections*, i.e. the projections which are *self-adjoint*. Then it can be seen that $\mathcal{P}_N \rightarrow \mathcal{J}$ in a pointwise sense (see also Weidmann [109], pp. 81-85). Using these projections to define the finite rank operator $\mathcal{A}_N = \mathcal{P}_N \mathcal{A} \mathcal{P}_N$, it can be seen that $\|\mathcal{A} - \mathcal{A}_N\| \rightarrow 0$ ($N \rightarrow \infty$) (Weidmann [109], p. 136). Hence there is always an N_0 so that for $N > N_0$ the property (4.6) in theorem 4.1 is satisfied. For the Hilbert space X we take $L_2(I)$. Now, we choose an

orthonormal basis for the subspace X_N which is denoted again by $\phi^{i,N}$. The finite rank projection \mathcal{P}_N is defined by

$$\mathcal{P}_N \psi = \sum_{i=1}^N \langle \psi, \phi^{i,N} \rangle \phi^{i,N}.$$

Using the definition above, the projection equation (4.5) is equivalent to

$$\langle \psi_N, \phi^{i,N} \rangle - \langle \mathcal{A}_N \psi_N, \phi^{i,N} \rangle = \langle f_N, \phi^{i,N} \rangle \quad i = 1, \dots, N.$$

Because of the self-adjointness of \mathcal{P}_N and relation (4.3) it follows that

$$\langle f_N, \phi^{i,N} \rangle = \langle \mathcal{P}_N f, \phi^{i,N} \rangle = \langle f, \mathcal{P}_N \phi^{i,N} \rangle = \langle f, \phi^{i,N} \rangle,$$

and similarly holds

$$\langle \mathcal{A}_N \psi_N, \phi^{i,N} \rangle = \langle \mathcal{A} \psi_N, \phi^{i,N} \rangle.$$

We thus arrive at the discrete Galerkin equation

$$\langle \psi_N, \phi^{i,N} \rangle - \langle \mathcal{A}_N \psi_N, \phi^{i,N} \rangle = \langle f_N, \phi^{i,N} \rangle \quad i = 1, \dots, N. \quad (4.14)$$

Hence this method consists of finding the function $\psi_N \in X_N$ that satisfies the equation above. The advantage of Galerkin's method is that a symmetric kernel yields a symmetric matrix. However, the above equation also shows that Galerkin's method requires an additional integration for each matrix element as compared to the collocation method. Because of this double integration, a collocation method will be faster to compute and is therefore the most recommendable for practical use. It appears however that the error analysis of Galerkin's method gives more satisfactory results as compared to the collocation method which explains their usage in many theoretical outlines. In general, error estimates for collocation methods are based on the equivalence that can be established between certain Galerkin methods, cf. Arnold and Wendland [5].

Finally we consider the case that integral equation (4.1) is defined for a boundary curve Γ . When approximating this integral operator by a projection method, the error estimate (4.7) still holds. However, an extra error source occurs when replacing the boundary curve by a polygonal approximation (which one normally has to find as an exact analytical description of this curve is not available in general).

4.2 IMPLEMENTING THE BEM FOR THE STOKES PROBLEM

The implementation of the BEM is outlined that is applied to discretize the integral formulation for the Stokes problem as is presented in the sections 2.2 and 2.3. In particular we consider the discretization of those integral equations in the case of a multiply connected domain. Note that the implementation in the case of a simply connected domain is straight forward by ignoring the sink contribution part. Books that

describe the implementation of the BEM are e.g. Becker [7], Brebbia *et al.* [8]-[9] and Jawsom and Symm [52].

Each separate curve Γ_m of the boundary of the multiply connected domain is divided into elements which are defined by a set of nodal points, that are numbered counter-clockwise. Let L_m be equal to the number of elements of this particular curve; a specific j element will be referred to with a superscript ' j ' like Γ_m^j . The exact boundary is replaced by a *polygon* which consists of the union of all those elements. The number of nodes depends on the degree of polynomial approximation used. We apply the standard Lagrangian polynomial approximations of both degree one (linear) and two (quadratic). Let N be the total number of collocation points, denoted by \mathbf{x}^i , summed over all the boundary curves of the domain. The boundary velocity and tension will be written in terms of their values at the nodal points and the polynomial approximation that is used.

The following polynomial functions $\hat{\mathbf{v}}^m$ and $\hat{\mathbf{b}}^m$ apply for such a typical element Γ_m^j ,

$$\hat{\mathbf{v}}^m = \Phi \mathbf{v}^{m,j} \quad \text{and} \quad \hat{\mathbf{b}}^m = \Phi \mathbf{b}^{m,j}, \quad (4.15)$$

where Φ is a $2 \times 2q$ matrix of the Lagrangian finite element type polynomials $\phi_i(s)$, $-1 \leq s \leq 1$, i.e.

$$\Phi(s) = \begin{bmatrix} \phi_1 & 0 & \phi_2 & 0 & \dots & \phi_q & 0 \\ 0 & \phi_1 & 0 & \phi_2 & \dots & 0 & \phi_q \end{bmatrix}.$$

The number $q-1$ is equal to the degree of the polynomial approximation. In the case that *linear* elements are applied those polynomials are equal to

$$\phi_1(s) = \frac{1}{2}(1-s) \quad \phi_2(s) = \frac{1}{2}(1+s), \quad (4.16)$$

and for the *quadratic* elements holds

$$\phi_1(s) = \frac{1}{2}s(s-1) \quad \phi_2(s) = 1-s^2 \quad \phi_3(s) = \frac{1}{2}s(s+1). \quad (4.17)$$

Moreover, the vectors $\mathbf{v}^{m,j}$ and $\mathbf{b}^{m,j}$ in equation (4.15) are of length $2q$ and consist of the velocity and tension vectors of the q successive nodes of the element Γ_m^j . Such an element curve written in parametric form, say $\mathbf{y}(s)$, can also be expressed in terms of functions of the same interpolant, i.e.

$$\mathbf{y}(s) = \phi_i(s)\mathbf{y}^i, \quad (4.18)$$

where \mathbf{y}^i denote the collocation points of the considered element.

Substituting the polynomials (4.15) into the integral equation (2.52) subjected to the discretized boundary condition, the following equation is obtained for an *arbitrary* collocation point $\mathbf{x}^p \in \Gamma_m$

$$\begin{aligned} c_{ii}^p v_i^{m,p} + \sum_{k=0}^M \sum_{j=1}^{L_k} \left(\int_{\Gamma_k^j} q_{li}(\mathbf{x}^p, \mathbf{y}) \hat{v}_i^k d\Gamma_y + n_l^{m,p} \int_{\Gamma_k^j} \bar{q}_i \hat{v}_i^k d\Gamma \right) + \varphi_i^{mr,p} \int_{\Gamma_m^j} \varphi_i^{mr} \hat{v}_i^m d\Gamma \\ = \sum_{k=0}^M \sum_{j=1}^{L_k} \left(\int_{\Gamma_k^j} u_{li}(\mathbf{x}^p, \mathbf{y}) \hat{b}_i^k d\Gamma_y + n_l^{m,p} \int_{\Gamma_k^j} \bar{u}_i \hat{b}_i^k d\Gamma \right). \end{aligned} \quad (4.19)$$

Here the index r sums over the three types of rigid-body movements φ^{mr} of the node \mathbf{x}^p and $\mathbf{n}^{m,p}$, $\mathbf{v}^{m,p}$ are the outer normal and the unknown velocity in node 'p' situated at Γ_m respectively. After substitution of the interpolant of the element boundary (4.18), the following five typical integrals are obtained that have to be computed for each element,

$$\int_{-1}^1 \phi_i q_{kl}(\mathbf{x}^p, \mathbf{y}) |J(\mathbf{y})| ds, \quad \int_{-1}^1 \phi_i u_{kl}(\mathbf{x}^p, \mathbf{y}) |J(\mathbf{y})| ds, \quad (4.20)$$

$$\int_{-1}^1 \phi_i \bar{q}_k(\mathbf{y}) |J(\mathbf{y})| ds, \quad \int_{-1}^1 \phi_i \bar{u}_k(\mathbf{y}) |J(\mathbf{y})| ds, \quad (4.21)$$

$$\int_{-1}^1 \phi_i \varphi_k^{lm}(\mathbf{y}) |J(\mathbf{y})| ds, \quad (4.22)$$

where $|J(\mathbf{y})|$ is the Jacobian, i.e.

$$|J(\mathbf{y})| = \sqrt{(\phi'_i y'_1)^2 + (\phi'_i y'_2)^2},$$

and the prime ' denotes the derivative with respect to s .

These integrals are numerically approximated by applying a Gaussian quadrature formula, cf. Stroud and Secrest [99]. Hence the integrals are approximated by a finite sum from which the terms consists of integrand evaluations at a number of integration points, multiplied by an associated weighting factor. Normally, a four-point Gauss quadrature formula is applied in the linear element solution and a six-point formula in the quadratic element case. Moreover, we observe that the integrals (4.21) and (4.22) are independent of \mathbf{x}^p , so these have to be computed only once when \mathbf{x}^p is varied over all the collocation points.

However, when \mathbf{x}^p is also a nodal point of the element under consideration, the integrands of (4.20) will have a *singularity* in the integration domain so that some extra effort is needed in order to approximate these integrals correctly. In the case of the linear element implementation, the integrals (4.20) can be calculated analytically. Therefore, we consider the parametric representation of the element (4.18) with the Lagrangian polynomials (4.16), i.e. i is a summation over 1-2, and substitute $\mathbf{x}^p = \mathbf{y}^j$ ($j = 1, 2$). Then, it can easily be seen that

$$\int_{-1}^1 \phi_i q_{kl}(\mathbf{y}^j, \mathbf{y}) |J(\mathbf{y})| ds = 0, \quad (4.23)$$

and

$$\int_{-1}^1 \phi_i u_{kl}(\mathbf{y}^j, \mathbf{y}) |J(\mathbf{y})| ds = \frac{1}{8\pi\sqrt{A}} \left[(\delta_{k1}\delta_{l2} + \delta_{k2}\delta_{l1}) a_k a_l + \delta_{kl} a_k^2 - \frac{1}{2} \delta_{kl} A (\log A - 1 - 2(\delta_{i1}\delta_{j1} + \delta_{i2}\delta_{j2})) \right], \quad (4.24)$$

where $a_k = y_k^2 - y_k^1$ and $A = a_1^2 + a_2^2$. In the case of the quadratic element implementation, the integrals (4.20) can be rewritten, after some analytical manipulation, in a non-singular integral and a part that contains a logarithmic singularity, cf. Van de Vorst *et al.* [103]. Thereafter, the non-singular integral can be approximated by applying a normal Gaussian quadrature formula and the singular integrals will be calculated using a Logarithmic Gaussian quadrature formula.

Equation (4.19) written in matrix-vector notation reads

$$\left(\mathbf{H}^p + \mathbf{n}^{m,p} \mathbf{h}^T \right) \mathbf{v} + \boldsymbol{\varphi}^{mk,p} (\mathbf{a}^{mk})^T \mathbf{v}^m = \left(\mathbf{G}^p + \mathbf{n}^{m,p} \mathbf{g}^T \right) \mathbf{b}. \quad (4.25)$$

Here \mathbf{v} and \mathbf{b} are vectors of length $2N$ that represents the velocity and tension of all successive nodal boundary points, e.g. for example

$$\mathbf{v} = \left(v_1^1, v_2^1, v_1^2, v_2^2, \dots, v_1^N, v_2^N \right)^T.$$

The vectors \mathbf{h} and \mathbf{g} are derived from the sink part, i.e. vectors of length $2N$ and the coefficients are of integral type (4.21), \mathbf{a}^{mk} is gained from the rigid-body movement deflation part and consists of the integrals of type (4.22) along the boundary Γ_m and \mathbf{v}^m is the vector of successive nodal velocities of the latter boundary curve. The $2 \times 2N$ matrices \mathbf{H}^p , \mathbf{G}^p are obtained from the point force contribution part in (4.19), thus the matrix coefficients are of integral type (4.20). Moreover, the coefficients c_{ii}^p are incorporated in the matrix \mathbf{H}^p .

The latter coefficients are equal to $\frac{1}{2} \delta_{ii}$ for nodes in which the boundary curve does not have a discontinuity what is the case when constant elements are applied. In general for higher order elements, the boundary curve will be discontinuous at the nodal points that connect two successive elements, e.g. corner nodes of an element. In that case, the coefficients c_{ii}^p can be obtained analytically, cf. Hartmann [36]. However, it is common to avoid the computation of those coefficients by considering rigid-body motions, i.e. the above BEM matrices have to apply to any physical problem for which the solution does not depend on the geometry. Since a rigid-body motion does not result in any tension onto the shape, the coefficients H_{ij}^p ($i=1,2$ and $j = 2p - 1, 2p$) can be obtained at the following way

$$H_{i2p-1}^p = - \sum_{\substack{j=1 \\ j \neq p}}^N H_{i2j-1}^p \quad \text{and} \quad H_{i2p}^p = - \sum_{\substack{j=1 \\ j \neq p}}^N H_{i2j}^p \quad (i = 1, 2).$$

Varying the point \mathbf{x}^p in the discretized equation (4.25) over all the collocation points, the following square full rank system of $2N$ linear algebraic equations with $2N$ unknowns is derived,

$$\mathcal{H}(\mathbf{x}) \mathbf{v} = \mathcal{G}(\mathbf{x}) \mathbf{b}(\mathbf{x}), \quad (4.26)$$

where \mathbf{x} is the vector of length $2N$ that consists of all successive collocation points.

The unknowns \mathbf{v} are obtained after solving the above square full rank system by Gaussian elimination and partial pivoting (LU-decomposition). A direct solver is used since the matrix \mathcal{H} is not symmetric and does not have a sparse structure. Each nodal

point is in the BEM formulation connected to all the other nodes as can be observed from the above outline of the system derivation.

After solving the system (4.26) we have to perform a time step. In section 2.1, equation (2.14), this boundary movement is modelled by considering the boundary curve as material points. Then the trajectories of those points can be followed by using the Lagrangian representation of the velocity. In particular for each collocation point holds

$$\frac{d\mathbf{x}^i}{dt} = \mathbf{v}^i.$$

Using these latter relation together with equation (4.26) yields the following $2N$ non-linear system of Ordinary Differential Equations (ODEs),

$$\frac{d\mathbf{x}}{dt} = \mathcal{H}^{-1}(\mathbf{x}) \mathcal{G}(\mathbf{x}) \mathbf{b}(\mathbf{x}). \quad (4.27)$$

In chapter 5 we will consider the numerical integration of the above system.

4.3 PROBLEMS WITH THE APPROXIMATION OF THE CURVATURE

Here we will discuss the numerical approximation of the body force $\mathbf{b} = -\kappa \mathbf{n}$. We analyze the numerical problems when collocation points are getting close to each other during the boundary movement. In particular we consider cusp regions since here the curvature becomes very large in magnitude. Moreover, in such a region the nodes have to lie close to each other because we expect large variations of the boundary velocity field there.

A local method is used to approximate the surface tension vector \mathbf{b}^i at the boundary nodes. The accuracy of these approximations has to be of at least the same order as the BEM that is applied. In the case of linear elements, it is sufficient to use a second order accurate approximate curvature, i.e. similar to the computed velocity field. Therefore, both the curvature and outer normal are found by fitting a quadratic polynomial at the nodal point, say \mathbf{x}^2 , its neighbours \mathbf{x}^1 and \mathbf{x}^3 ; e.g. using the polynomials (4.17) together with equation (4.18) we obtain

$$\mathbf{x}(s) = \phi_i(s) \mathbf{x}^i. \quad (4.28)$$

For the approximate outer normal at the nodal point $\mathbf{x}^2 = \mathbf{x}(0)$ yields

$$\begin{aligned} \mathbf{n}^2 = \mathbf{n}(0) &= \frac{1}{\sqrt{(x_1')^2 + (x_2')^2}} \begin{pmatrix} x_2' \\ -x_1' \end{pmatrix} \\ &\doteq \frac{1}{\sqrt{(x_1^3 - x_1^1)^2 + (x_2^3 - x_2^1)^2}} \begin{pmatrix} x_2^3 - x_2^1 \\ x_1^1 - x_1^3 \end{pmatrix}, \end{aligned} \quad (4.29)$$

and for the curvature we obtain

$$\begin{aligned}\kappa(0) &= \frac{x'_1 x''_2 - x'_2 x''_1}{((x'_1)^2 + (x'_2)^2)^{\frac{3}{2}}}\Big|_{s=0} \\ &\doteq \frac{4((x_1^3 - x_1)(x_2 - 2x_2^2 + x_2^3) - (x_2^3 - x_2)(x_1 - 2x_1^2 + x_1^3))}{((x_1^3 - x_1)^2 + (x_2^3 - x_2)^2)^{\frac{3}{2}}}.\end{aligned}\quad (4.30)$$

Combing equations (4.29) and (4.30) gives the numerical approximation of \mathbf{b}^2 .

The quadratic element solution is third order accurate so that a higher order approximation of curvature and outer normal are required. We apply in this case a fourth order Lagrangian polynomial in order to avoid numerical oscillations as much as possible. Hence the surface tension in, say \mathbf{x}^3 , is found by a fit through that point and its neighbours \mathbf{x}^1 , \mathbf{x}^2 , \mathbf{x}^4 and \mathbf{x}^5 . From the first expressions on the right of (4.29) and (4.30), those approximations at the node \mathbf{x}^3 ($s = 0$) are obtained by the noting that

$$\begin{aligned}x'_i(0) &= \frac{1}{6}(x_i^1 - 8x_i^2 + 8x_i^4 - x_i^5) \\ x''_i(0) &= \frac{1}{3}(-x_i^1 + 16x_i^2 - 30x_i^3 + 16x_i^4 - x_i^5).\end{aligned}\quad (4.31)$$

This way we find the surface tension \mathbf{b}^i at all nodes; this expression will be used henceforth. The stress at any point of an arbitrary element is obtained from the polynomial fit (4.17) in combination with the BEM applied.

As already mentioned, problems are arising when approximating the surface tension of a cusp region during the shape evolution. In the neighbourhood of such a point the nodes must lie close to each other since both the curvature and the unknown velocity have large variations in magnitude in relation to the relatively small curve length of that particular boundary part. During the deformation of such a cusp region those nodal points are even coming closer together, which causes errors in the numerical approximation of the tension vector, especially the curvature. Hence the computed surface tension can deviate considerably from the exact tension and soon oscillations will develop. These oscillations result from the following feedback cycle: small errors in the approximate collocation points produce local variations in the computed velocities of the nodes, causing uneven advancement of these points which yields larger errors in the approximation. This process can lead to instabilities and wrong curves and even a complete breakdown of the numerical simulation.

To be more specific, we consider the coalescence of two equal cylinders where the collocation points are *fixed* during the evolution. The numerical time integration is performed by applying the BDF-method as is outlined in chapter 5. In figure 4.1 the development of the curvature of the neck point as time proceeds is shown. Here we have used linear elements. As can be observed from that plot, large oscillations develop after a small period of time which eventually become smaller. This is in contradiction to the analytical relation that we derived for this neck curvature, cf. equation (3.18): the curvature has to behave as a smooth decreasing function of the contact radius between both cylinders. In the figure is also plotted the shape evolution of those coalescing

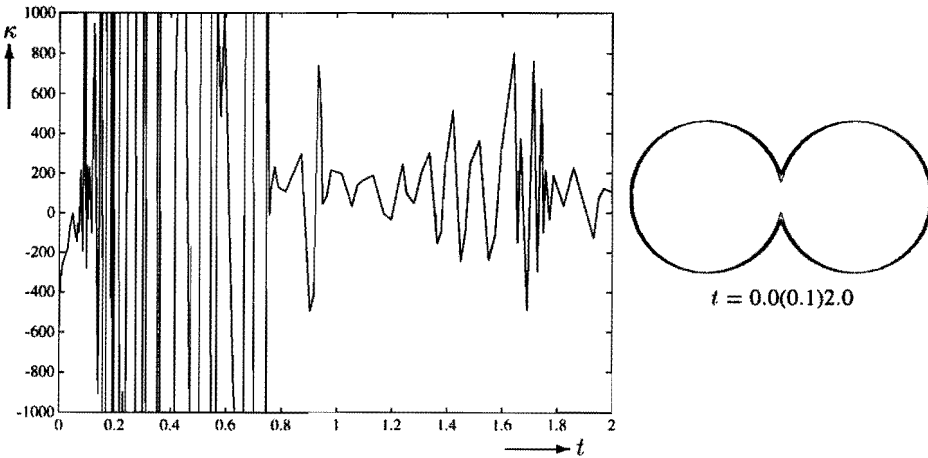


Figure 4.1 The curvature of the cusp point of two equal coalescing cylinders when the same mesh is used throughout a (linear element) simulation. Large oscillations develop when the trajectories of the nodal points in the cusp region come close to each other and even the coalescence stops as is shown by the shape evolution plot of those cylinders on the right.

cylinders as is obtained from the simulation at a subsequent number of times. It is dramatically to see that the coalescence stops after a initial time period which is also contrary to the exact analytical solution. A similar behaviour was observed for the quadratic element case, where the integration even stops after a small period of time.

The occurring of oscillations in the approximate neck curvature is due to numerical cancellation. This can be seen as follows: each collocation point in both the coordinate directions has a discretization error. For the origin of this error we can distinguish between the following three types of error sources. A *spatial* error, i.e. the error that is made by the approximation of the boundary by a polygon, secondly the error due to the usage of a Gaussian quadrature formulae in order to approximate the element integrals and finally the *time* discretization error that arises from the time integration method. Hence we can say that the computed boundary deviates order the discretization error from the exact curve. When approximating the surface tension at the nodal points where the mesh is fine, we loose some accuracy by the computation of both the curvature and outer normal because the points are necessarily very close to each other. Then both the numerator and denominator of the quotient of the approximate curvature will be of order the discretization error in magnitude. Hence the computed curvature can deviate considerably from the exact curvature.

This can be illustrated by considering the above coalescing cylinders example. This particular simulation is performed by applying an absolute error tolerance equal to 10^{-4} and a relative tolerance equal to 10^{-3} for smooth parts and 10^{-5} for cusp regions. Therefore in this case we can assume that the time discretization error is the *dominant* error. The collocation points of the upper cusp region at $t = 0.1$ are printed in table 4.1. As can be observed from this table, the nodes are very close to each other in the neighbourhood of the cusp point \mathbf{x}^2 . Furthermore, we have printed the approximated

i	x_1^i	x_2^i	$x_1^{i-1} - x_1^{i+1}$	$x_2^{i-1} - x_2^{i+1}$	$x_2^{i-1} - x_2^i$	$x_2^i - x_2^{i+1}$	κ^i
⋮	⋮	⋮	⋮	⋮	⋮	⋮	⋮
14	0.13443249	0.43765475					
15	0.07173674	0.34557171	0.957356E-01	0.156354E-00	0.920830E-01	0.642706E-01	1.281
16	0.03869690	0.28130115	0.511973E-01	0.105965E-00	0.642706E-01	0.416946E-01	1.034
17	0.02053946	0.23960658	0.292571E-01	0.660955E-01	0.416946E-01	0.244009E-01	-0.418
18	0.00943983	0.21520568	0.177798E-01	0.360541E-01	0.244009E-01	0.116532E-01	-4.145
19	0.00275969	0.20355250	0.924773E-02	0.152090E-01	0.116532E-01	0.355579E-02	-8.749
20	0.00019209	0.19999671	0.275969E-02	0.357697E-02	0.355579E-02	0.211846E-04	-54.540
21	0.00000000	0.19997553	0.384188E-03	0.000000E-00	0.211846E-04	-0.211846E-04	-1148.215
22	-0.00019209	0.19999671	0.275969E-02	-0.357697E-02	-0.211846E-04	-0.355579E-02	-54.540
23	-0.00275969	0.20355250	0.924773E-02	-0.152090E-01	-0.355579E-02	-0.116532E-01	-8.749
24	-0.00943983	0.21520568	0.177798E-01	-0.360541E-01	-0.116532E-01	-0.244009E-01	-4.145
25	-0.02053946	0.23960658	0.292571E-01	-0.660955E-01	-0.244009E-01	-0.416946E-01	-0.418
26	-0.03869690	0.28130115	0.511973E-01	-0.105965E-00	-0.416946E-01	-0.642706E-01	1.034
27	-0.07173674	0.34557171	0.957356E-01	-0.156354E-00	-0.642706E-01	-0.920830E-01	1.281
28	-0.13443249	0.43765475					
⋮	⋮	⋮	⋮	⋮	⋮	⋮	⋮

Table 4.1 The collocation points of the upper cusp region for the two equal coalescing cylinders using a fixed mesh at time $t = 0.1$. Cancellation in the computation of the cusp ($i = 21$) curvature occurs when two successive point coordinates in the 2-direction are subtracted (by the computation of the numerator of equation (4.30)) and by the computation of $x_1^{i-1} - x_1^{i+1}$.

curvature κ^i by applying equation (4.30). In order to obtain this approximation, we have to compute the following terms (that are also printed),

$$x_j^{i-1} - 2x_j^i + x_j^{i+1} = (x_j^{i-1} - x_j^i) - (x_j^i - x_j^{i+1}),$$

occurring in the numerator and

$$x_j^{i-1} - x_j^{i+1},$$

being part of the denominator. From this table we observe that due to numerical cancellation, the approximated cusp curvature is useless as

$$\kappa^{21} = \frac{-4(x_2^{20} - 2x_2^{21} + x_2^{22})}{(x_1^{20} - x_1^{22})^2} = \frac{-4 \cdot 4.23692 \cdot 10^{-5}}{(3.84188 \cdot 10^{-4})^2} = -1148.2,$$

i.e. both the numerator and the denominator are smaller than the discretization error. By lowering the time integration tolerance, the problem of a worse approximated cusp curvature still remains because then one of the other error sources will become dominant. Note that it generally does not make any sense to minimize all the error sources since then the total computing time may become prohibitively large.

The example above shows that the mesh has to be checked each time step in such a way that the collocation points do not get too close to each other in a cusp region. On the other hand, it seems satisfactory that those points lie close to each other because of the to be expected large variations of the velocity and surface tension in such a region. These two conflicting aspects have to be wrought together in an algorithm that takes care of the mesh verification and redistribution as will be the subject of the remaining part of this chapter.

4.4 MESH REDISTRIBUTION AND VERIFICATION

We present an algorithm for a fairly optimal mesh generation based on equidistributing the curvature of the boundary. The aim of this algorithm is twofold. Firstly the number and place of the discretization points is optimized, which is important because the computational costs per time step are proportional to $(2N)^3$. Secondly this algorithm treats regions with sharp corners (cusps) in a special way in order to avoid cancellation in the computation of the curvature of a cusp region as much as possible.

In the case of a multiply connected domain the algorithm presented treats the outer and all inner boundary curves separately, keeping most of the redistribution parameters that follow below constant for those curves. Therefore, it suffices to consider the redistribution algorithm for a simply connected domain only, as will be done in the remainder. The parameters that are curve dependent in the case of a multiply connected domain will be indicated explicitly. Moreover, we assume that the exact boundary, say Γ , of the fluid region can be described by a parametric equation with respect to the arc length s , i.e.

$$\mathbf{x}(s) \in \Gamma, \quad 0 \leq s \leq s_e \quad \text{and} \quad \mathbf{x}(0) = \mathbf{x}(s_e). \quad (4.32)$$

Only an equidistribution of the curvature is performed; an equidistribution of the boundary velocity field, as was outlined for example by Dritschel [20] to perform vorticity computations, will not be necessary here. In general, when the velocity and the curvature of the boundary are considered as a functions of the arc length, one observes that the velocity as function of the arc length is a much "smoother" function than the curvature. Furthermore it was seen that at places where the size of the velocity field is changing rapidly over a small part of the boundary, the curvature is also rapidly changing in size, i.e. the mesh is already finer there. When the velocity is large on a considerable part of the boundary, and the curvature is of moderate size everywhere, that part is moving as a whole but the shape as such is not deforming much, i.e. a finer mesh is not necessary. An example of such a quickly moving geometry is the n-shaped region as is demonstrated in section 5.1, figure 5.3.

Firstly, we will derive properties for the step-length between two successive nodes, which have to be fulfilled for all mesh points that are generated. Let $\mathbf{x}^{i-1} = \mathbf{x}(s_{i-1})$ and $\mathbf{x}^i = \mathbf{x}(s_i)$ be two given successive nodal points and denote the distance between those points by $h_i := s_i - s_{i-1}$; *the step-length*. The next node \mathbf{x}^{i+1} has to lie at a distance h_{i+1} from \mathbf{x}_i , such that the following conditions (4.33), (4.34) and (4.36) are satisfied. Let h_{\min} and h_{\max} be two positive constants given bounds for the step-length

$$h_{\min} \leq h_{i+1} \leq h_{\max}. \quad (4.33)$$

Furthermore let the collocation points be quasi-uniformly distributed, i.e.

$$\frac{h_i}{\alpha} \leq h_{i+1} \leq \alpha h_i, \quad (4.34)$$

where α is a given parameter, larger than 1. Next, define the *curvature density*, say ε_κ , of the boundary as

$$\int_\Gamma |\kappa(s)| ds = P \varepsilon_\kappa, \quad (4.35)$$

where P is a prescribed number, given by the user, and which is approximately equal to the total number of nodes that the algorithm will find eventually. In the case of a multiply connected domain, the number P will be approximately equal to the total number of collocation points of all the separate curves together. The number of points that will be invested in every individual curve is equal to a percentage of P obtained from the division of the total length of all boundary curves together by the length of the curve considered. That number is used to compute the curvature density of that particular curve.

The curvature of the boundary between two successive nodes integrated over the arc has to be smaller than the curvature density, i.e. the following *equidistribution condition* has to hold (approximately),

$$\int_{s_i}^{s_{i+1}} |\kappa(s)| ds = \varepsilon_{\kappa}. \quad (4.36)$$

With $h_{\varepsilon_{\kappa}}$ we denote the step-length such that the equality from (4.36) holds, i.e. $s_{i+1} = s_i + h_{\varepsilon_{\kappa}}$.

When the curvature is very large on a certain part of the boundary, i.e. in a cusp region, it may happen that the proposed $h_{\varepsilon_{\kappa}}$ is smaller than the lower bound h_{\min} . However, we take as next step h_{\min} , although condition (4.36) is not satisfied then. A justification for this will be given in chapter 6. There we show that it is not possible to approximate the correct cusp curvature and that we have to proceed judiciously in choosing the ‘‘cusp discretization’’: the cusp point and its neighbouring points have to be chosen such that the cusp curvature does not change dramatically.

From equations (4.33), (4.34) and (4.36), we see that the distance between \mathbf{x}^i and the proposed next nodal point \mathbf{x}^{i+1} is equal to

$$h_{i+1} = \max \left(h_{\min}, \frac{h_i}{\alpha}, \min(h_{\max}, \alpha h_i, h_{\varepsilon_{\kappa}}) \right). \quad (4.37)$$

However, this proposed h_{i+1} may be too large when it turns out that an appropriate step-length further on is not possible due to an increasing magnitude of the curvature; namely if at the next node, a step-length h_{i+2} is proposed that is larger than what is reasonably according to previous selected step-lengths, i.e.

$$h_{i+2} > \max \left(h_{\min}, \frac{h_{i+1}}{\alpha} \right).$$

Thus, we have to build in a mechanism that investigates whether the choice of node \mathbf{x}^{i+1} , i.e. step-length h_{i+1} , will not require the step-length for succeeding nodes to become larger than permitted! This means that we have to scan the curvature behaviour for increasing arc length s .

At first sight, it seems obvious to choose a control mechanism that uses the derivative of the curvature with respect to the arc length; however for a boundary with a rapidly changing though moderately valued curvature, the information of the derivative, derived numerically, is useless. See for example figure 4.2, taken from Hopper [42], in which the curvature with respect to the arc length of that particular shape is plotted. Hence, we

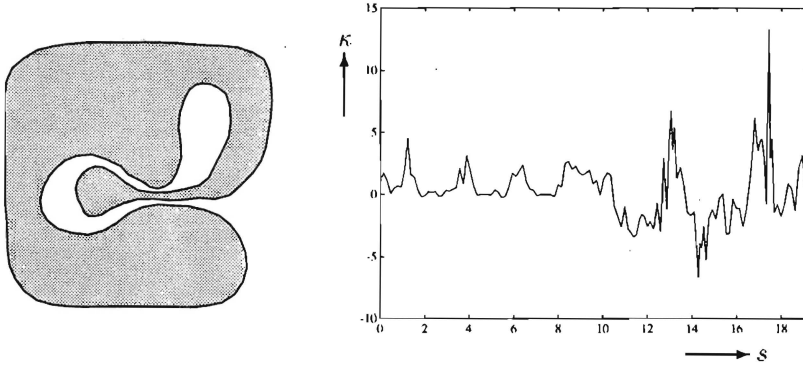


Figure 4.2 The curvature as function of the arc length s of the left figure. The derivative of this curvature with respect to the arc length is becoming large at some parts of the boundary, while the curvature is only moderately varying.

have developed the following simple algorithm for testing and correcting the step-length h_{i+1} .

We say that the step-length h_{i+1} is a *correct one*, when for all subsequent smallest new step-lengths $\hat{s}_j, j = 0, \dots, m$, where

$$\hat{s}_j := s_i + \sum_{p=0}^j \frac{h_{i+1}}{\alpha^p}, \tag{4.38}$$

and m is an integer such that

$$\frac{h_{i+1}}{\alpha^m} \geq h_{\min} \quad \text{and} \quad \frac{h_{i+1}}{\alpha^{m+1}} < h_{\min},$$

the curvature equidistribution holds,

$$\int_{\hat{s}_j}^{\hat{s}_{j+1}} |\kappa(s)| ds \leq \varepsilon_\kappa, \quad j = 0, \dots, m - 1. \tag{4.39}$$

When this h_{i+1} turns out not to satisfy the requirement (4.39), this step-length is made somewhat smaller, more precisely

$$h_{i+1} = \max \left(h_{\min}, \frac{h_i}{\alpha}, \beta h_{i+1} \right),$$

where β is a given number, smaller than 1. Next this new h_{i+1} is tested at the above described way again. This procedure can be continued until the step-length is equal to $\max(h_{\min}, h_i/\alpha)$. Note that both h_{\min} and h_i/α are acceptable values since these are generated at the previous step of the algorithm. The algorithm described above can be written in the following pseudo code

```

correct=false
while (( $h_{i+1} \leq \text{Min}(\alpha h_{\min}, \text{Max}(h_{\min}, h_i/\alpha))$ )  $\vee$  (correct)) do
  fail=false
   $\hat{s} = s_i + h_{i+1}$ 
   $\hat{h} = h_{i+1}/\alpha$ 
  while (( $\hat{h} \leq h_{\min}$ )  $\vee$  (fail)  $\vee$  ( $\hat{s} \geq s_\epsilon$ )) do
    fail=Integral( $\kappa, \hat{s}, \hat{s} + \hat{h}$ ) >  $\epsilon_\kappa$ 
     $\hat{s} = \hat{s} + \hat{h}$ 
     $\hat{h} = \hat{h}/\alpha$ 
  od
  if (fail) then  $h_{i+1} = \text{Max}(h_{\min}, h_i/\alpha, \beta h_{i+1})$ 
    else correct=true
  fi
od

```

This algorithm may look very time consuming; however, by choosing the bounds $h_{\max}/h_{\min} \approx 100$, say and the factor α is not too close to 1 this is not so dramatic. In our examples the CPU time for generating a complete mesh was a small percentage of the costs per time step only.

Next, we discuss how a cusp region is discretized. To do this, we derive properties that have to be satisfied for the newly discretized boundary part. We denote $\mathbf{x}^c := \mathbf{x}(s_c)$ the cusp point and by \mathbf{x}^{c-1} and \mathbf{x}^{c+1} the neighbouring nodes of the cusp point, where $s_{c-1} < s_c < s_{c+1}$.

The first criterion that has to be satisfied is that the distance between the neighbouring nodes and the cusp point is the *same*, and that the step-length is bounded as in (4.33), i.e.

$$h_{\min} \leq |s_c - s_{c-1}| = |s_{c+1} - s_c| \leq h_{\max}. \quad (4.40)$$

Furthermore, we have to avoid cancellation in the computation of the approximate cusp curvature. This means that the distance between the cusp point neighbours has to be larger than a certain lower bound d_{\min} , i.e.

$$\|\mathbf{x}^{c+1} - \mathbf{x}^{c-1}\| \geq d_{\min}, \quad (4.41)$$

where d_{\min} is taken of the order h_{\min} (we used $d_{\min} = 2h_{\min}$).

Another property is the equidistribution of the curvature, i.e. equation (4.36). In general, this condition is not fulfilled when the cusp curvature is large; however during the deformation of this particular region, the cusp curvature is getting smaller and it may be possible that this condition can be satisfied.

From the above properties, we obtain a step-length, which is denoted by h_c , between the cusp and the proposed new neighbouring cusp points. The new approximate cusp curvature, which in the case of linear elements is computed by fitting a quadratic interpolation polynomial through the cusp node and its neighbours, is not the same as

the old cusp curvature. The size of this new cusp curvature is unpredictable. However, we want to avoid the influence of this new cusp curvature in the computation further on. This is performed by *shifting* the cusp point a bit such that the cusp curvature is equal to the old curvature; more details can be found in the next section. In the quadratic element case, we will also use this algorithm since it is sufficient that the cusp curvature is nearly the same as the old curvature.

Using the ideas above, the collocation points are redistributed. If the boundary has cusp regions, the node redistribution takes place starting from the discretized cusp (where h_c is already known), to the *middle* of the boundary part between those cusps. After this, the nodes are somewhat shifted in the middle such that the mesh conditions (4.37) are satisfied. If the boundary does not have cusps, one node of the old mesh is kept fixed and the other nodes are generated relatively to this fixed node. When the boundary is symmetric, a mesh generation is performed on to the symmetric part only, i.e. the nodes of the complete boundary are also chosen symmetrically.

So far, we did not mention anything about the mesh verification, i.e. when the decision is made to perform a node redistribution. In view of efficiency of the time integration method, as discussed in chapter 5, it is not wise to redistribute the nodes at each successful integration step since restarting the time integration can be very costly. Therefore, we have developed an algorithm that decides when a redistribution has to be performed. A redistribution is subjected to the following rules: firstly, the same mesh may not be used more or less integration steps than given by a certain upper bound (user supplied) and a lower bound. Secondly, the distance of each two successive collocation points has to lie between the bounds h_{\min} and h_{\max} . Finally, in order to avoid cancellation by the computation of a cusp curvature, the distance between the two cusp neighbour points is required to be larger than the lower bound h_{\min} .

Another point of concern that occurs in the case of the simulation of a multiply connected domain is the possibility of vanishing holes. The inner hole area may not become too small in order to avoid errors in the generation of this hole curve. Therefore, we checked the inside hole area at each successful integration step. If we detect that such an area is smaller than a prescribed value (that is approximately equal to the discretization error expected) this curve will totally be removed, i.e. we let the hole vanish completely.

4.5 ALGORITHMIC CONSIDERATIONS OF THE MESH REDISTRIBUTION

In this section we comment on the numerical implementation of the algorithm that is described in the previous section. Firstly, we introduce a discretized version of the arc length and show how a point $\mathbf{x}(s)$ is found. Secondly, we give the curvature equidistribution condition which is used in the numerical scheme. Finally, we discuss some properties of the cusp detection and discretization algorithm.

In the numerical algorithm we are starting with an already discretized boundary, which will be referred to as the *old* nodes $\tilde{\mathbf{x}}^i$ ($1 \leq i \leq N$). For practical application of the

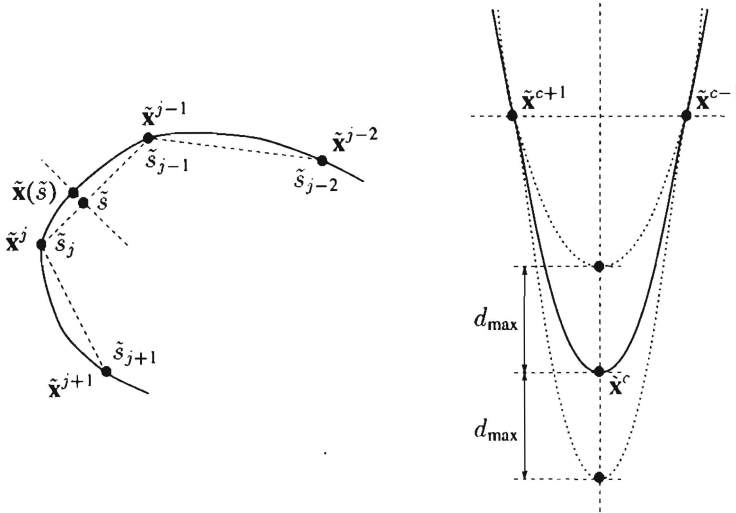


Figure 4.3 The first figure shows how the point $\tilde{\mathbf{x}}(\tilde{s})$ is found. The second figure is showing the direction in which the cusp point is shifted, such that the cusp curvature has a prescribed value.

ideas of the previous section, we have to define a discretized version of the arc length, say \tilde{s} , i.e. how a point $\tilde{\mathbf{x}}(\tilde{s})$ has to be found, and what is meant by the curvature $\tilde{\kappa}(\tilde{s})$.

In the numerical algorithm we use as a discretization of the arc length the straight-line distance between two successive old nodes, i.e.

$$\tilde{s}_i = \tilde{s}_{i-1} + \|\tilde{\mathbf{x}}^i - \tilde{\mathbf{x}}^{i-1}\| \quad (2 \leq i \leq N + 1), \tag{4.42}$$

where $\tilde{s}_1 = 0$ and $\tilde{\mathbf{x}}^{N+1} = \tilde{\mathbf{x}}^1$. A nodal point at a certain arc length, say \tilde{s} , is found by fitting a quadratic polynomial through three successive old nodes, say $\tilde{\mathbf{x}}^{j-1}$, $\tilde{\mathbf{x}}^j$ and $\tilde{\mathbf{x}}^{j+1}$, where j is taken such that

$$|\tilde{s}_j - \tilde{s}| \leq \min(|\tilde{s}_{j-1} - \tilde{s}|, |\tilde{s}_{j+1} - \tilde{s}|). \tag{4.43}$$

Assuming that $\tilde{s} < \tilde{s}_j$, the node $\tilde{\mathbf{x}}(\tilde{s})$ is at the intersection of this quadratic polynomial with the straight line in the direction normal to the straight line through the old points 'j - 1' and 'j', and through the point on this straight line that has a distance $\tilde{s}_j - \tilde{s}$ with the node $\tilde{\mathbf{x}}^j$ (see figure 4.3).

The approximate curvature $\tilde{\kappa}_i$ of the old nodes is found as described in section 4.3. The curvature at a certain value of the arc length, i.e. $\tilde{\kappa}(\tilde{s})$, is derived in the same way as a boundary point was found; however, now through linear interpolation. In our algorithm we derive an approximation of h_{ε_κ} using the linear discrete form of (4.36), which is given by

$$h_{\varepsilon_\kappa} (|\tilde{\kappa}(\tilde{s}_i + h_{\varepsilon_\kappa})| + |\tilde{\kappa}(\tilde{s}_i)|) = 2\varepsilon_\kappa. \tag{4.44}$$

This equation is solved using a bisection method.

In principle we have a set of nodal points that discretize a particular boundary curve and no information about whether that boundary has cusp regions. If the latter is true,

we have to know the exact place of all the cusp points in order to derive a correct node redistribution. Therefore, the following algorithm is developed.

First, we select a subset of nodes $\tilde{\mathbf{x}}^c$ for which the angle of the straight lines through $\tilde{\mathbf{x}}^c$ and both neighbour points is smaller than a prescribed value (θ_{\max}) together with the exceeding of a given curvature under bound (κ_{\min}) for that particular node. These requirements can be expressed by the following equations

$$\arccos \left(\frac{\|\tilde{\mathbf{x}}^c - \tilde{\mathbf{x}}^{c-1}\|^2 + \|\tilde{\mathbf{x}}^{c+1} - \tilde{\mathbf{x}}^c\|^2 - \|\tilde{\mathbf{x}}^{c+1} - \tilde{\mathbf{x}}^{c-1}\|^2}{2\|\tilde{\mathbf{x}}^c - \tilde{\mathbf{x}}^{c-1}\|\|\tilde{\mathbf{x}}^{c+1} - \tilde{\mathbf{x}}^c\|} \right) \leq \theta_{\max} \quad (4.45)$$

$$\kappa^c \geq \kappa_{\min}.$$

In our code we normally use $\theta_{\max} = 0.9\pi$ and $\kappa_{\min} = 10$. Furthermore, we also select nodes for which both the *neighbouring points* satisfy relation (4.45). Thus we are searching for the two typical shapes as are shown in figure 4.4. If this redistribution is

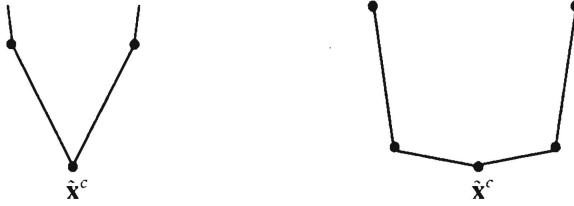


Figure 4.4 Configurations of nodes that possibly can represent a cusp region.

not the generation of the starting geometry, the old cusp points that exceed the curvature lower bound and which stayed unnoticed by the algorithm above are also added to the subset of “cusp points”. Redundancy is avoided by the additional requirement that cusp points may not lie too close to each other, i.e. both the difference between the two point label numbers and the actual distance between those points has to be larger than a prescribed value. If this occurs and one of the points is by an earlier redistribution identified as a cusp, then that particular point will be kept in the subset. Otherwise, both points are replaced by the point with label number equal to the average of those removed points.

The above outlined detection algorithm will generate a large subset in the case of an almost vanished hole curve. Because of this it is assumed that this curve does not have any cusps at all. In general, such a hole is a circular form and does not have any sharp corners. The detection of such a kind of shape is performed by computing the area that is enclosed by the curve; when this area is smaller in magnitude than a prescribed value all the cusp points are removed.

From the requirements (4.40) and (4.41) we obtain new neighbouring points for every cusp point of the above defined subset. These points are computed using a straight line representation through the two successive old nodes which are lying between the proposed arc length ($\hat{s} = \hat{s}_c \pm h_c$). A linear interpolation is carried out instead of a quadratic interpolation; this is to avoid interpolation errors which occur when the cusp curvature is large and the old nodes are not distributed nicely in the cusp region.

We require also that the new approximate cusp curvature is equal to the old cusp curvature. To perform this, the cusp point is shifted a bit over the straight line through the old cusp point, in the direction normal to the straight line through the new neighbouring nodes; or, when the new nodes are lying further apart than the old neighbours, through these old nodes (see also figure 4.3). The cusp node may be shifted over a maximum a distance d_{\max} , i.e.

$$\|\hat{\mathbf{x}}^c - \mathbf{x}^c\| \leq d_{\max}, \quad (4.46)$$

where d_{\max} is also of the order h_{\min} (we used $d_{\max} = 0.25h_{\min}$). If it is not possible to find a new cusp point on this line, the cusp point is shifted over a distance d_{\max} on this line, such that the new cusp curvature is as close as possible to the old curvature. Note that when starting a computation, the curvature of the cusp points of the initial boundary are unknown. These initial cusp curvatures may be user specified, or they are computed from the initial nodes.

4.6 DISCUSSION OF MESH REDISTRIBUTION RESULTS

We will demonstrate the usefulness of the node redistribution algorithm as is outlined above. This is performed by showing the simulation of some typical cusp regions. In particular, the solutions found for the coalescence of two cylinders both with equal and different radii are compared with the exact analytical solutions. The latter example will show the correctness of the assumption that the cusp point, i.e. the point where initially the largest curvature exists, can be taken the *same* mass-point during the simulation. Besides *concave* cusp regions, we show that *convex* regions with a sharp corner can be handled by the code too.

The first example is the coalescence of two equal cylinders. We will compare the derived numerical results to the analytical solution of section 3.1 (cf. equations (3.5) and (3.8)). The initial radius is taken $\frac{1}{2}\sqrt{2}$; then the final shape of the coalescence is a cylinder with radius 1. The initial contact radius r is set equal to 0.14. Substituting this in equation (3.18) describing the exact neck curvature yields a value of approximately -707. The starting collocation points of the shape are derived from the exact solution. Only nodes from the first quadrant are needed because of the double symmetry of the body. This symmetry is preserved during the calculation. For the node distribution algorithm we used as bounds for the step length, $h_{\min} = 0.005$ and $h_{\max} = 0.15$; the uniformly distribution factor α is taken equal to 1.5 and the number P equal to 25 for the first quadrant shape part. Furthermore, this simulation is performed by applying linear elements and the time integration tolerance parameters are taken similar to the ones used in section 4.3. The maximum number of integration steps that may employ the same mesh is taken equal to 10.

In figure 4.5 we compare the upper cusp point curvature (also called neck curvature) obtained by the numerical simulation (solid line) to the analytical curvature of the neck (dashed line). Here, we have also plotted the transformation of the fluid region in time

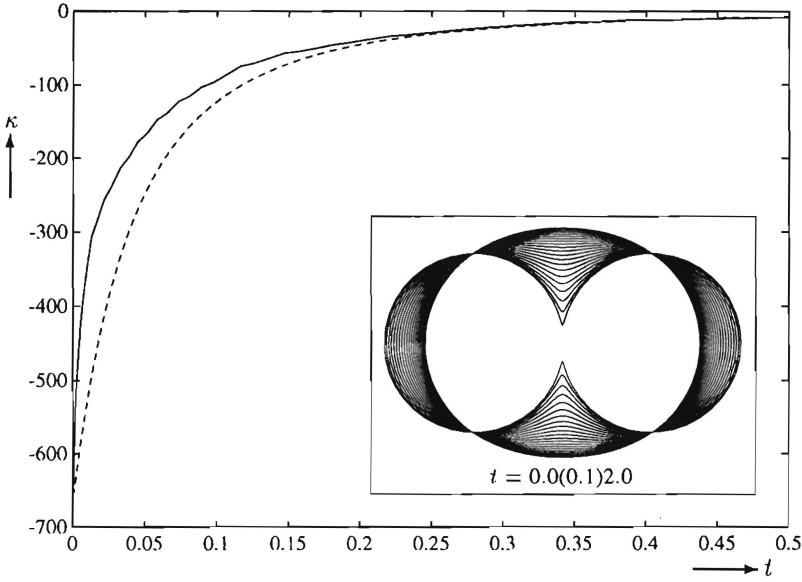


Figure 4.5 The neck curvature obtained by numerical simulation (solid line), is compared with the exact analytical curvature of the neck (dashed line) for the coalescence of two equal cylinders.

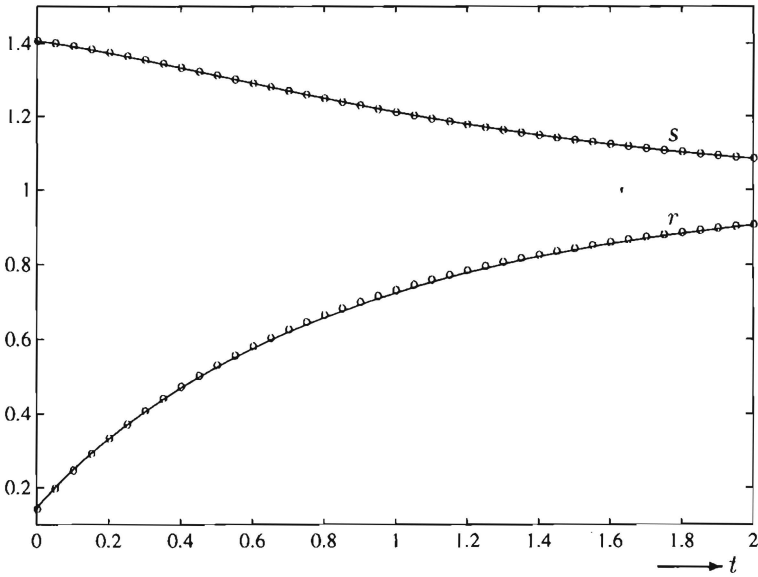


Figure 4.6 The contact radius r and the shrinkage s , both obtained by numerical simulations (solid lines), are compared with the analytical solutions (bullets) for the coalescence of two equal cylinders.

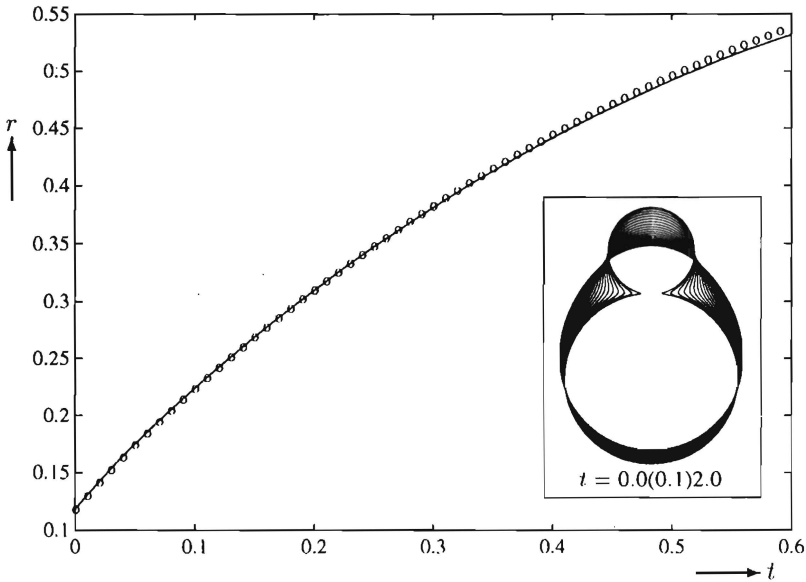


Figure 4.7 The well-matching of the contact radius r obtained numerically (solid line) compared with the exact neck radius (bullets) for the coalescence of a cylinder with initial radius 0.5 onto a cylinder with initial radius 1.

at $t = 0.0(0.1)2.0$. When we compare this figure with figure 4.1 of section 4.3 where the mesh was taken fixed, we see that the numerical neck curvature does not show any oscillatory behaviour now. However, the numerical neck curvature differs quite a bit from the exact curvature in the early stage of the coalescence; but when time is increasing, both curvatures are getting very close to each other. This difference does not have any effect on the coalescing rate of the cylinders as is shown in figure 4.6. In that figure we have plotted the contact radius r and the shrinkage s obtained both by the numerical and analytical solution. When we compare the numerical contact radius (solid line) to the analytical contact radius (bullets), we see an almost matching of both solutions, even in the initial stage when the numerical neck curvature differs. An explanation for this observation will be given in chapter 6. In section 5.4 is discussed more about the behaviour of the numerical solution for a similar coalescence (in particular in relation with the time integration method).

Secondly, we consider the coalescence of two cylinders with unequal initial radii. As already mentioned, this simulation is performed in order to justify the assumption that during a cusp simulation the cusp point, i.e. the point with the largest curvature, will be the same material point during the evolution. Note that this cannot be verified analytically since that solution is based on an intermediate between the Eulerian and Lagrangian description (cf. appendix A). By using the previous example, this can also not be justified, because from symmetry considerations the cusp point has to lie on the symmetry axis during the evolution.

We have taken the radius of the largest cylinder equal to 1 and the other is set equal

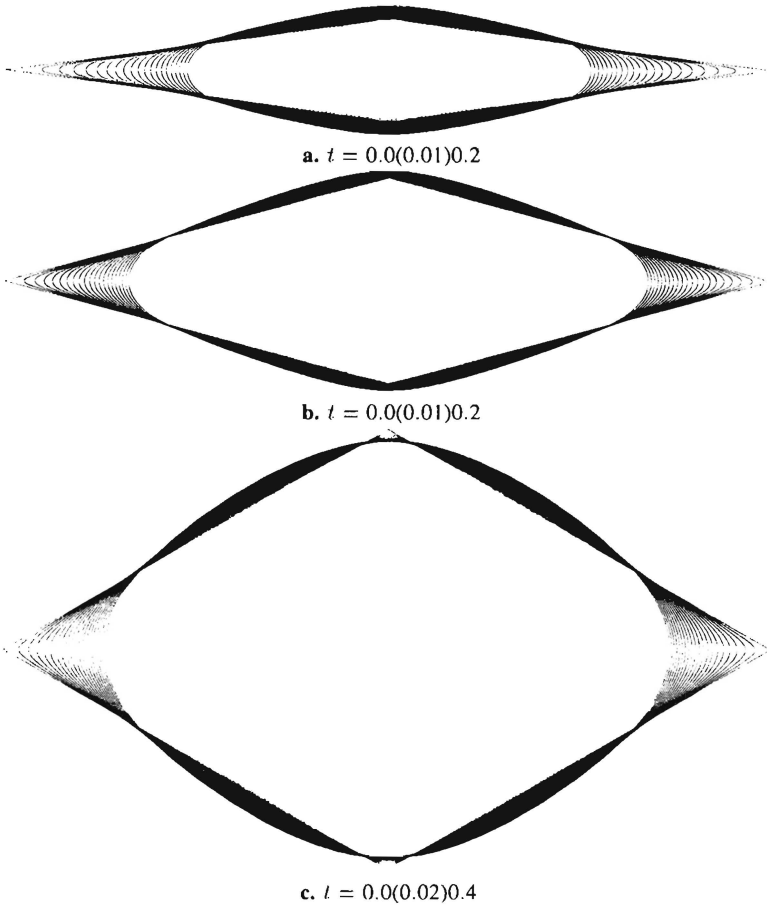


Figure 4.8 Three sintering rhomboidal shapes illustrate the usefulness of the redistribution algorithm for convex domains. The sharpest angle of the initial geometries is taken equal to 15,30 and 60 degrees respectively.

to 0.5; the initial contact radius between both cylinders was equal to 0.12. The initial mesh is obtained by applying the analytical solution as is found by Richardson [89] (cf. section 3.1 equations (3.9) and (3.10)), where the parameters of this solution are set equal to $\alpha = 0.888$ and $\beta = 0.942$ in order to obtain the initial geometry. In this case we apply quadratic elements and the node redistribution parameters are chosen similar as in the previous example, except for the lower bound h_{\min} which is equal to 0.001 and the equidistribution number which is doubled. Moreover, the time integration tolerances are all lowered by a factor of 10.

Figure 4.7 is showing the well-matching of the numerically obtained contact radius development (solid line) compared to the exact analytical solution. In the numerical case, it appears that the cusp point is also the neck point of these two coalescing cylinders (from which the contact radius is computed). The matching of both solutions is giving a

justification to keep the point with initially largest curvature as the representation of the cusp point during the evolution as is performed by the node redistribution algorithm.

Till now, we demonstrated the redistribution algorithm to simulate concave cusp regions, i.e. when viewed from inside the fluid. The algorithm is well-suited to be applied for convex cusp regions too. In order to illustrate this we consider some rhombic fluid domains. In figure 4.8 the simulation results for three rhombic geometries is shown. The largest diagonal line inside those shapes is taken equal to 2 and the angle of the lines that define the sharpest corners is initially set equal to 15, 30 and 60 degrees respectively. The same program parameters are used as in the case of the two unequal coalescing cylinders example. During the initial stage, the plots show that the shapes deform inside the prescribed initial geometry of the sharpest corner parts.

TIME INTEGRATION

The movement of the boundary is modelled by considering the boundary curve as material points. The trajectories of those points can be followed by applying the Lagrangian representation for the velocity. In particular, when we consider the nodal points of the discretized version of the integral formulation, we obtain $2N$ non-linear ODEs. Here, we will formally denote these ODEs by

$$\frac{d\mathbf{x}}{dt} = \mathcal{H}^{-1}(\mathbf{x}) \mathcal{G}(\mathbf{x}) \mathbf{b}(\mathbf{x}). \quad (5.1)$$

In this chapter we consider the numerical integration of this system of ODEs. First, we will show that depending on the geometrical shape, the system can be *stiff*. Hence, we propose to use a BDF-scheme for solving those equations, for which the numerical implementation will be outlined. In particular we will high-light some important features like the approximation of the Jacobian matrix and the continuation of integration after a mesh redistribution.

5.1 STIFFNESS

There are various definitions of “stiffness” in the literature. Before defining the concept of stiffness that is used in this thesis, we first introduce some notation. Let $\lambda_i = \lambda_i(\mathbf{x})$ be the eigenvalues of the Jacobian matrix $\mathcal{J}(\mathbf{x})$ of the system (5.1), where

$$\mathcal{J}(\mathbf{x}) = \frac{\partial}{\partial \mathbf{x}} \left(\mathcal{H}^{-1}(\mathbf{x}) \mathcal{G}(\mathbf{x}) \mathbf{b}(\mathbf{x}) \right), \quad (5.2)$$

which is taken at relevant nodal points \mathbf{x} . Furthermore, let ρ denote the spectral radius of \mathcal{J} , i.e.

$$\rho = \max_{i=1}^{2N} |\lambda_i|.$$

Then, we will call the system of ODEs (5.1) *stiff* on an interval $[a, a+T]$ if

$$\max_{t \in [a, a+T]} \rho(\mathcal{J}(\mathbf{x}(t))) T \gg 1. \quad (5.3)$$

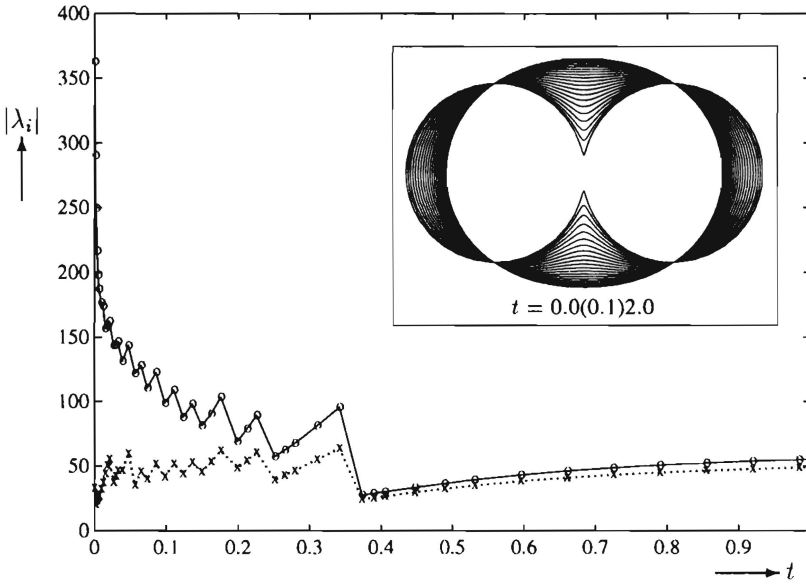


Figure 5.1 The spectral radius ρ development (solid line) compared to the absolute eigenvalue second in magnitude (dotted line) of the numerically obtained (exact) Jacobian of two equal coalescing cylinders is showing stiffness in the initial stage of the coalescence. The jumps in the spectral radius are caused by node redistributions.

An arbitrarily sintering geometry is deforming to a steady state as time increases. In particular for the two-dimensional case, the domain transforms itself into a circular disk with an area that remains constant during the deformation. In section 2.1 is shown that the rate of work done by the surface tension on the boundary is equal to the rate of dissipation of mechanical energy *within* the geometry, i.e.

$$\int_{\Gamma} v_i b_i d\Gamma = - \int_{\Gamma} \kappa v_i n_i d\Gamma = 2 \int_{\Omega} \varepsilon_{ij} \varepsilon_{ij} d\Omega \geq 0.$$

A circular curve minimizes this deformation energy (i.e. the curvature is constant) and using the continuity equation it follows that the left hand-side of the above equation is equal to zero. Consequently, \mathbf{v} can represent rigid-body motions only. However, degrees of freedom are removed from the ODE (5.1) so that this velocity field has to be equal to zero. Note that for a circular boundary, the right hand-side of the integral equation, i.e. $\mathcal{G}\mathbf{b}$, is also equal to zero, so that \mathcal{J} and thus all λ_i are equal to zero.

According to definition (5.3), the system of ODEs (5.1) will be stiff on an interval if the spectral radius ρ is large and the interval length is substantially larger than $1/\rho$. It is impossible to derive an analytical expression for the Jacobian (5.2) or the spectral radius in this particular case. Because of this fact, the appearance of stiffness is demonstrated by a couple of simple but typical examples that represent the basic evolution problems in sintering.

Firstly, we consider the evolution of the coalescence of two equal cylinders. These coalescing cylinders demonstrate the boundary deformation of the sintering phenomenon

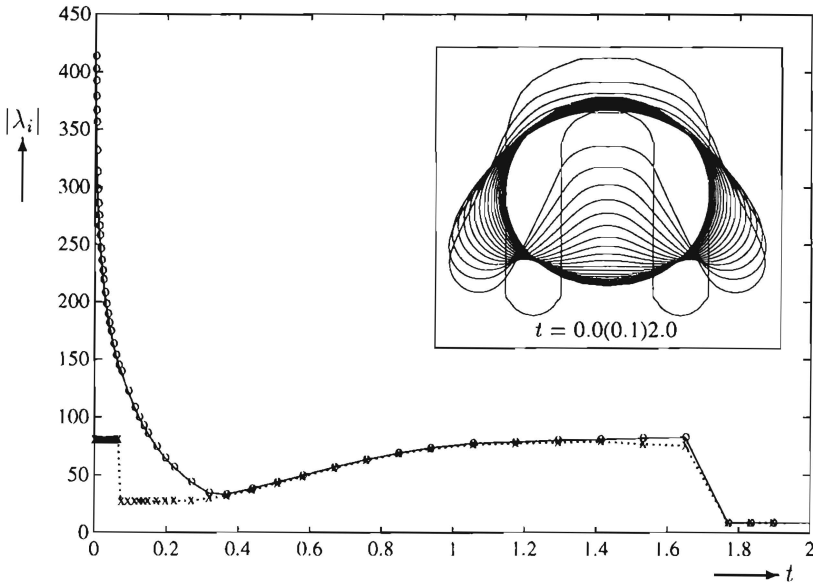


Figure 5.2 The spectral radius ρ development (solid line) compared to the second largest absolute eigenvalue (dotted line) of the Jacobian of a n -shaped region is showing that the ODEs are stiff when larger parts of the shape are moving fast (during the initial stage).

very well. In the early stage of the coalescence, the boundary curvature is very large in the region where both cylinders are touching (almost a *cusp*); in later stages the shape is becoming “smoother”, i.e. the curvature is only moderately varying everywhere. Thus during this evolution, the shape is undergoing a deformation that can occur and is relevant to all other cases of viscous sintering simulations.

The initial radius of both cylinders is taken $\frac{1}{2}\sqrt{2}$ and the contact line between those cylinders is set equal to 0.14. In figure 5.1 we have plotted the spectral radius (solid line) of the numerically obtained (exact) Jacobian computed after every successful integration time step, when the fluid is transforming itself into a circle as time evolves. The spectral radius is compared to the eigenvalue second in magnitude (dotted line). From the difference in size at the initial stage of the coalescence, we conclude that there are smoother modes (of the linearized problem) that ask for larger steps on an interval that is substantially larger than $\mathcal{O}(\rho^{-1})$; hence the ODEs are *stiff* in that region. Here, the problem was solved using *linear* boundary elements (the jumps in the spectral radius are caused by the node redistribution algorithm). After performing such a redistribution, the trajectories of a different set of particles may be being followed. As can be seen from the figure, the stiffness of the ODEs can change drastically. From this figure, we also observe that as time increases the stiffness is disappearing; because the boundary is almost becoming a circle. This can be concluded from the time step that is used during later stages; apparently both eigenvalues are not relevant for the evolution anymore.

However, the ODEs for a smooth curved geometry can be stiff too. This occurs when larger parts of the shape are moving fast. To illustrate this behaviour we show a

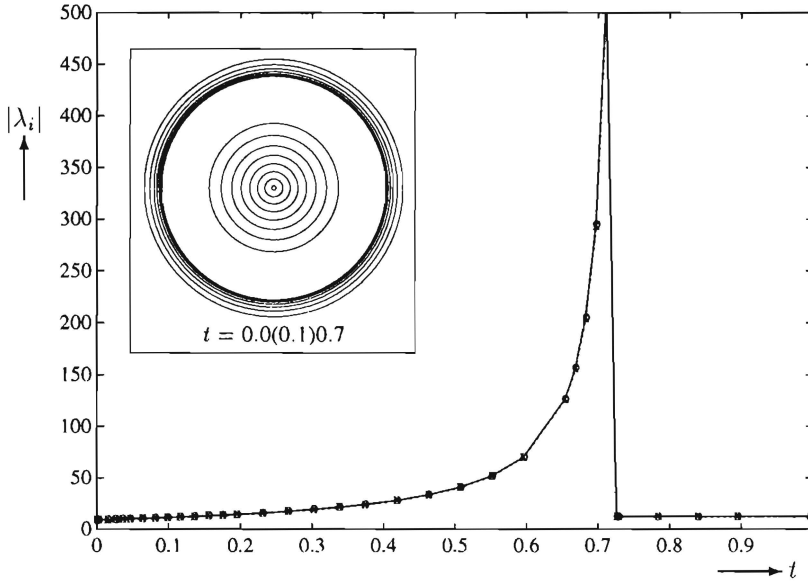


Figure 5.3 The two largest eigenvalues of the Jacobian during the shrinkage of a circular annulus are almost identical as time evolves. The increase of both values as the inside hole is nearly vanished is due to the curvature increase of the hole. The vanishing of the hole can still be called *stiff* since both the boundaries evolve at different time scales.

n-shaped region in figure 5.2. The development of the two largest (absolute) eigenvalues of the Jacobian are also plotted. Again, we observe a large difference between these two values during the initial time stage when the shape is stretching itself. Later, the magnitude of these eigenvalues become very close (and to the rest as well).

Another typical sintering phenomenon is the shrinkage and vanishing of holes inside the fluid region. In order to investigate whether stiffness is present in such a type of problem we consider the most simple example that covers all effects: the shrinkage of a circular annulus. For this example we have taken the initial outer radius equal to 1 and the inner radius equal to 0.5. In figure 5.3 is shown the spectral radius development (solid line) compared to the second largest eigenvalue (dotted line) of the Jacobian computed after every time step for this particular simulation: both values remain almost identical as time evolves. The large increase of the values as the inside hole has nearly vanished is due to the curvature of the hole boundary since this is asymptotically tending to infinity. We observed that there were more such larger eigenvalues (depending on the number of nodes that discretized the hole). As can be obtained from the exact analytical solution of this problem, cf. Van de Vorst [107], the hole is completely vanished at a finite time, viz. $t = \sqrt{3} - 1$; there is not any activity of the fluid afterwards (see figure). Near to the vanishing of such a hole again *stiffness* occurs as there are two time scales: the evolution of the inside hole curve and the outer boundary curve.

As the examples above illustrate, the ODEs (5.1) that have to be integrated can have widely differing time constants. Therefore, we have used the variable step, variable order BDF-method, as is implemented in the solver LSODE, cf. Hindmarsh [38] - [39], for

obtaining the solution of the examples above. We also observed from those simulations, that nearly all the eigenvalues are real and negative; only a few eigenvalues have a small imaginary part (order 10^{-3}). Because of this, we do not expect to have any efficiency problems for the higher order BDF-methods, since those methods tend to take very small steps in order to provide stability when the Jacobian has eigenvalues with large imaginary parts but small negative real parts, cf. Brenan *et al.* [10] or Hindmarsh [40].

5.2 APPROXIMATION OF THE JACOBIAN

Since the BDF-method is an implicit linear multistep method, the corrector equation has to be solved by some iteration method. In LSODE this is performed by applying a modified Newton iteration, cf. Hindmarsh [39]. This implies that the code requires the Jacobian (5.2) of the system of ODEs.

As we remarked in the previous section, it is practically impossible to derive an analytical expression for the Jacobian. A numerical approximation of the exact Jacobian (5.2) would be extremely time consuming: one Jacobian evaluation requires the assembling and solution of the system of equations $2N$ times. However, it is not necessary to have exact Jacobians anyway, since the BDF-solver is using a modified Newton method, i.e. the same Jacobian is used in subsequent (Newton) iterations and for several time integration steps. Therefore, we will use an approximate Jacobian. The derivation of this approximation is outlined for a simply connected domain in the remaining part of this section.

Denote by $\hat{\mathbf{x}}_{j,k}$ the vector of all boundary nodes whereby of the nodal point 'j' is perturbed with a small value, say ε ($\varepsilon \ll 1$) in the k^{th} -direction ($k = 1, 2$), i.e.

$$\hat{\mathbf{x}}_{j,k} = \mathbf{x} + \varepsilon \mathbf{e}_{2j-k} = \left(x_1^1, x_2^1, \dots, x_1^j + \varepsilon, x_2^j, \dots, x_1^N, x_2^N \right)^T.$$

Furthermore, we assume that $\hat{\mathbf{v}}_{j,k}$ is the solution of the system (5.1) for this perturbed boundary, thus

$$\mathcal{H}(\hat{\mathbf{x}}_{j,k}) \hat{\mathbf{v}}_{j,k} = \mathcal{G}(\hat{\mathbf{x}}_{j,k}) \mathbf{b}(\hat{\mathbf{x}}_{j,k}).$$

By Taylor expansion in ε of these quantities up to first order we find

$$\left(\mathcal{H} + \varepsilon \delta \mathcal{H}_{j,k} \right) (\mathbf{v} + \varepsilon \delta \mathbf{v}_{j,k}) \doteq \left(\mathcal{G} + \varepsilon \delta \mathcal{G}_{j,k} \right) (\mathbf{b} + \varepsilon \delta \mathbf{b}_{j,k}). \quad (5.4)$$

Here, both $\delta \mathcal{H}_{j,k}$ and $\delta \mathcal{G}_{j,k}$ are sparse matrices which are containing the derivatives of the integrals (4.20) with respect to x_k^j . The non-zero elements of these matrices have row indices '2j-1' and '2j' and column indices from '2j-1-p' to '2j+p', where p is equal to 2 in the case of linear elements or when node 'j' is the mid-point of a quadratic element; p is equal to 4 when quadratic elements are applied and node 'j' is one of the corners of the element. The vector $\delta \mathbf{b}_{j,k}$ has non-zero elements for the same indices as the columns of the above matrices in the case of a mid-point when quadratic elements are used. Moreover, we remark that the vector $\delta \mathbf{v}_{j,k}$ approximates the $(2j-k)^{\text{th}}$ column of the Jacobian \mathcal{J} . Thus, using the exact solution (5.1), and omitting the higher order terms

in (5.4), we obtain the following first order approximation for the $(2j - k)^{th}$ column of \mathcal{J} ,

$$\delta \mathbf{v}_{j,k} \doteq \mathcal{H}^{-1} \left(\mathcal{G} \delta \mathbf{b}_{j,k} + \delta \mathcal{G}_{j,k} \mathbf{b} - \delta \mathcal{H}_{j,k} \mathbf{v} \right). \quad (5.5)$$

The above approximation is not expensive to compute compared to the numerical exact Jacobian: when a new Jacobian evaluation is required, LSODE is asking for this Jacobian *after* a call which solves the system of equations (5.1) for this boundary. Thus the matrix \mathcal{G} , the LU-decomposition of the matrix \mathcal{H} , and the vectors \mathbf{b} and \mathbf{v} are already available. And because of the sparsity of the derivative matrices $\delta \mathcal{H}_{j,k}$ and $\delta \mathcal{G}_{j,k}$, and the vector $\delta \mathbf{b}_{j,k}$, the computational costs to approximate the total Jacobian \mathcal{J} will be of the order of four times the costs of assembling the system of equations whereby we note that the system assembling is the most expensive part of the solution process. Furthermore, we have to perform a forward and backward substitution of $2N$ right-hand sides with respect to \mathcal{H} ($\sim 8N^3$). Therefore, we still are not satisfied with the required computational effort to obtain this approximate Jacobian.

We note that the computing costs of that Jacobian will be reduced considerably when the terms $\delta \mathcal{G}_{j,k} \mathbf{b} - \delta \mathcal{H}_{j,k} \mathbf{v}$ may be omitted: besides $2N$ forward and backward substitutions of $\mathcal{G} \delta \mathbf{b}_{j,k}$, that right-hand side will require six matrix-vector operations only ($\sim 16N^2$). Furthermore, the computation will become very simple too. Therefore, we will analyze and quantify the contributions of the different terms in the vector

$$\mathcal{G} \delta \mathbf{b}_{j,k} + \delta \mathcal{G}_{j,k} \mathbf{b} - \delta \mathcal{H}_{j,k} \mathbf{v} \quad (5.6)$$

in order to reduce the computational effort.

We recall that the element matrix coefficients of the matrices \mathcal{G} and \mathcal{H} , say G^{mn} and H^{mn} respectively, typically consist of the following integrals, cf. (4.20),

$$\begin{aligned} G^{mn} &= \int_{-1}^1 \phi_p(s) u_{mn}(\mathbf{x}, \mathbf{y}(s)) |\mathbf{J}(\mathbf{y}(s))| ds; \\ H^{mn} &= \int_{-1}^1 \phi_p(s) q_{mn}(\mathbf{x}, \mathbf{y}(s)) |\mathbf{J}(\mathbf{y}(s))| ds, \end{aligned} \quad (5.7)$$

where \mathbf{y} is the interpolant of the element boundary, i.e. $\mathbf{y}(s) = \phi_i \mathbf{y}^i$ and \mathbf{y}^i are the element nodes. The derivative of those integrals with respect to x_k^j can be distinguished as one of three different types. If row derivatives are considered then x_k^j is equal to a component of \mathbf{x} ; in the case of a column derivative, x_k^j is equal to a coordinate of a nodal point from the boundary interpolant \mathbf{y} ; or at the intersection of a row and column, x_k^j is equal to

both. The derivatives of the integrals (5.7) can be expressed in the following way,

$$\begin{aligned}\partial(G^{mn}) &= \int_{-1}^1 \phi_p \left[u_{mn} \partial(|J|) + \right. \\ &\quad \left. \frac{|J|}{4\pi R^2} \left[r_m \partial(r_n) + r_n \partial(r_m) - \left(\frac{r_m r_n}{R^2} + \frac{\delta_{nm}}{2} \right) \partial(R^2) \right] \right] ds, \\ \partial(H^{mn}) &= \int_{-1}^1 \frac{\phi_p}{\pi R^4} \left[r_m r_n \partial(r_1 y'_2 - r_2 y'_1) + \right. \\ &\quad \left. (r_1 y'_2 - r_2 y'_1) \left(r_m \partial(r_n) + r_n \partial(r_m) - \frac{2r_m r_n \partial(R^2)}{R^2} \right) \right] ds.\end{aligned}\tag{5.8}$$

Here the operator $\partial(\cdot)$ represents the derivative with respect to x_k^j , i.e.

$$\begin{aligned}\partial(r_m) &= \begin{cases} \delta_{mk} & x_k^j = x_k \\ -\delta_{mk} \phi_i & x_k^j = y_k^i, \end{cases} & \partial(R^2) &= \begin{cases} 2r_k & x_k^j = x_k \\ -2\phi_i r_k & x_k^j = y_k^i, \end{cases} \\ \partial(|J|) &= \begin{cases} \phi'_i y'_k |J|^{-1} & x_k^j = y_k^i \\ 0 & \text{else,} \end{cases} \\ \partial(r_1 y'_2 - r_2 y'_1) &= \begin{cases} \delta_{1k} y'_2 - \delta_{2k} y'_1 & x_k^j = x_k \\ (\delta_{2k} - \delta_{1k})(\phi'_i r_{3-k} + \phi_i y'_{3-k}) & x_k^j = y_k^i. \end{cases}\end{aligned}$$

Note that in the case of $x_k^j = x_k = y_k^i$, i.e. the intersection of a row and column, both derivatives have to be added. Therefore, we may consider both the column and the row derivatives separately in order to quantify the contribution of those integrals. The non-zero terms of the vector $\delta \mathbf{b}_{j,k}$ have indices from '2j - 5' to '2j + 2', i.e.

$$\partial(\mathbf{b}^p) = -\partial(\kappa^p \mathbf{n}^p) = -\partial(\kappa^p) \mathbf{n}^p - \kappa^p \partial(\mathbf{n}^p) \quad \text{for} \quad (p = j - 1, j, j + 1), \tag{5.9}$$

where

$$\begin{aligned}\partial(n_m^p) &= \frac{(\delta_{pj-1} - \delta_{pj+1})}{e_{13}^p} \left[(\delta_{k1} \delta_{m1} - \delta_{k2} \delta_{m2}) n_1^p n_2^p + (\delta_{k2} \delta_{m1} - \delta_{k1} \delta_{m2}) (n_k^p)^2 \right], \\ \partial(\kappa^p) &= \frac{3(\delta_{pj+1} - \delta_{pj-1})}{(e_{13}^p)^2} (x_k^{p+1} - x_k^{p-1}) \kappa^p + \\ &\quad \frac{8(\delta_{2k} - \delta_{1k})}{(e_{13}^p)^3} \left[(\delta_{pj+1} - \delta_{pj}) x_{3-k}^{p+1} + (\delta_{pj-1} - \delta_{pj+1}) x_{3-k}^p + (\delta_{pj} - \delta_{pj-1}) x_{3-k}^{p-1} \right],\end{aligned}$$

and $e_{13}^p = |\mathbf{x}^{p+1} - \mathbf{x}^{p-1}|$.

Firstly, we estimate the size of the column integrals of the matrices involved in the vector (5.6), i.e. $x_k^j = y_k^i$. This is done by applying linear elements; those integrals are simpler to analyze, as compared to the case of quadratic elements. It is believed that the following estimates do roughly hold for these latter elements too, since those

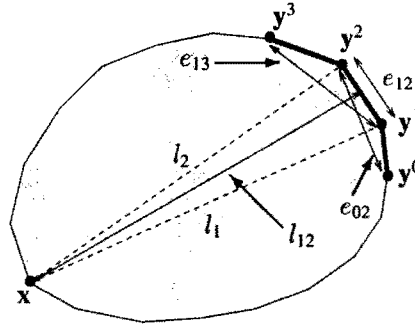


Figure 5.4 Notation of defined lengths when the distance between point x and the considered linear element is large.

interpolation functions will cause in the integrals minor changes only. From equation (5.8) we deduce the following estimates,

$$\begin{aligned} G^{mn} &\sim \frac{|J|}{4\pi} \int_{-1}^1 (1 - \log R) ds, \\ \partial(H^{mn}) &\sim \frac{1}{2\pi} \int_{-1}^1 \frac{ds}{R} + \frac{9|J|}{\pi} \int_{-1}^1 \frac{ds}{R^2}, \\ \partial(G^{mn}) &\sim \frac{1}{2} \int_{-1}^1 \phi_p u_{mn} ds + \frac{5|J|}{4\pi} \int_{-1}^1 \frac{ds}{R}. \end{aligned} \quad (5.10)$$

Using the relations (3.3.16), (3.3.19) and (3.3.33) of Abramowitz and Stegun [1], we obtain as analytical solution for the integrals above

$$\begin{aligned} \int_{-1}^1 \frac{ds}{R} &= \frac{2}{e_{12}} \log \left| \frac{l_1 + l_2 + e_{12}}{l_1 + l_2 - e_{12}} \right|, & \int_{-1}^1 \frac{ds}{R^2} &= \frac{4}{\sqrt{c}} \arctan \left(\frac{\sqrt{c}}{l_1^2 + l_2^2 - e_{12}^2} \right), \\ \int_{-1}^1 (1 - \log R) ds &= 4 - \log(l_1 l_2) + \frac{l_2^2 - l_1^2}{e_{12}^2} \log \left(\frac{l_1}{l_2} \right) - \frac{c}{4e_{12}^2} \int_{-1}^1 \frac{ds}{R^2}, \end{aligned} \quad (5.11)$$

where $l_i = |\mathbf{x} - \mathbf{y}^i|$, $e_{12} = |\mathbf{y}^2 - \mathbf{y}^1| = 2|J|$ and $c = ((l_1 + l_2)^2 - e_{12}^2)(e_{12}^2 - (l_1 - l_2)^2)$ respectively. If the distance between the point x and the element (l_i) is large compared to the element size (e_{12}), then we can say that $l_1 \approx l_2 \approx l_{12}$, where by l_{12} we have denoted the distance between x and the mid-point of the element, cf. figure 5.4. The integrals (5.11) can then be approximated as follows,

$$\begin{aligned} \int_{-1}^1 \frac{ds}{R} &= \frac{2}{l_{12}} + \mathcal{O}\left(\frac{e_{12}}{l_{12}^2}\right), & \int_{-1}^1 \frac{ds}{R^2} &= \frac{2}{l_{12}^2} + \mathcal{O}\left(\frac{e_{12}^2}{l_{12}^4}\right), \\ \int_{-1}^1 (1 - \log R) ds &= 2(1 - \log l_{12}) + \mathcal{O}\left(\frac{e_{12}^2}{l_{12}^2}\right). \end{aligned}$$

Combining these approximations with the integrals of equation (5.10) we obtain the following estimates for the latter integrals,

$$\begin{aligned}
 G^{mn} &= \frac{(1 - \log l_{12})e_{12}}{4\pi} + \mathcal{O}\left(\frac{e_{12}^3}{l_{12}^2}\right), \\
 \partial(H^{mn}) &= \frac{1}{\pi l_{12}} + \mathcal{O}\left(\frac{e_{12}}{l_{12}^2}\right), \\
 \partial(G^{mn}) &= \frac{1}{e_{12}} \int_{-1}^1 \phi_p u_{mn} |J| ds + \frac{5e_{12}}{4\pi l_{12}} + \mathcal{O}\left(\frac{e_{12}^2}{l_{12}^2}\right) \\
 &= \frac{(1 - \log l_{12})l_{12} + 5e_{12}}{4\pi l_{12}} + \mathcal{O}\left(\frac{e_{12}^2}{l_{12}^2}\right).
 \end{aligned} \tag{5.12}$$

The above approximations are not valid when \mathbf{x} is close to this particular element. This occurs when \mathbf{x} is a neighbouring node of the same boundary curve, or if two boundaries are almost touching. When \mathbf{x} is a point of the (linear) element, the integrals H^{mn} and G^{mn} can be solved analytically, i.e. recalling equations (4.23) and (4.24)

$$H^{mn} = 0$$

$$\begin{aligned}
 G^{mn} &= \frac{1}{8\pi e_{12}} \left[(\delta_{m1}\delta_{n2} + \delta_{m2}\delta_{n1}) a_m a_n + \right. \\
 &\quad \left. \delta_{mn} \left(a_n^2 - e_{12}^2 (\log e_{12} - \frac{1}{2} - \delta_{p1}\delta_{i1} - \delta_{p2}\delta_{i2}) \right) \right]
 \end{aligned}$$

where $a_m = (y_m^2 - y_m^1)$ and $\mathbf{x} = \mathbf{y}^i$. Again we can take the derivative of the latter equation with respect to y_k^i and approximate the size of these derivatives, we find

$$\partial(G^{mn}) = \mathcal{O}(1).$$

Moreover, it can be seen that in this case

$$G^{mn} \approx \frac{e_{12}}{8\pi} \left(1 + \delta_{mn} \left(\frac{3}{2} - \log e_{12} \right) \right) = \mathcal{O}(e_{12}).$$

From both the above approximations, we see that the integrals behave in a similar way as the integrals of equation (5.12). Because of this, it is assumed that the column integrals that are not covered by one of the above two cases, behave in a similar way too.

The column contribution of the various terms of the right hand-side vector (5.6) can now be estimated separately after quantifying the vectors \mathbf{v} , \mathbf{b} and $\delta\mathbf{b}$ for this particular element. From the assumption that the boundary nodes are uniformly distributed, we obtain using the discretized expression for the nodal curvature κ , cf. equation (4.30), that the vector \mathbf{b} for this element can be estimated through

$$b_i = -\kappa n_i = \mathcal{O}\left(\frac{e_{12}}{e_{02}^2} + \frac{e_{12}}{e_{13}^2}\right), \tag{5.13}$$

where e_{02} is the distance between the second element node and the other nodal neighbour point of the starting point of this element, analogically the distance e_{13} is defined (see also figure 5.4). From equation (5.9) and the above approximation, we find that

$$\delta b_i = \mathcal{O}\left(\frac{e_{12}}{e_{02}^3} + \frac{e_{12}}{e_{13}^3}\right). \quad (5.14)$$

Furthermore, we observed for a large number of simulations that the maximum values of the boundary velocity \mathbf{v} is nearly almost of order 1 or smaller. Using the latter observation and the approximations (5.12)-(5.14), the column contribution of the various terms of the vector $\mathcal{G}\delta\mathbf{b}_{j,k} + \delta\mathcal{G}_{j,k}\mathbf{b} - \delta\mathcal{H}_{j,k}\mathbf{v}$ can be estimated as follows

$$\begin{aligned} \delta\mathcal{H}_{j,k}\mathbf{v} &= \mathcal{O}\left(\frac{1}{l_{12}}\right) \\ \delta\mathcal{G}_{j,k}\mathbf{b} &= \mathcal{G}\mathcal{O}\left(\frac{1}{e_{02}^2} + \frac{1}{e_{13}^2}\right) \\ \mathcal{G}\delta\mathbf{b}_{j,k} &= \mathcal{G}\mathcal{O}\left(\frac{e_{12}}{e_{02}^3} + \frac{e_{12}}{e_{13}^3}\right) \end{aligned} \quad (5.15)$$

Note that the term $\delta\mathcal{H}_{j,k}\mathbf{v}$ is small compared to both other terms indeed. When the element is a piece of a “smooth” part of the boundary, both e_{02} and e_{13} are $\mathcal{O}(e_{12})$ so that $\delta\mathcal{G}_{j,k}\mathbf{b}$ and $\mathcal{G}\delta\mathbf{b}_{j,k}$ are of the same order. However, when that piece of boundary is curved or situated in the neighbourhood of a cusp then $e_{02} \ll e_{12}$ and/or $e_{13} \ll e_{12}$ so that the term $\mathcal{G}\delta\mathbf{b}_{j,k}$ will be the leading term of this vector.

In the case of a row derivative, i.e. $x_k^j = x_k$, than the term $\delta\mathcal{G}_{j,k}\mathbf{b} - \delta\mathcal{H}_{j,k}\mathbf{v}$ is equal to the discretized version of the derivative of the original integral formulation with respect to x_k . Consequently, $\delta\mathcal{G}_{j,k}\mathbf{b} - \delta\mathcal{H}_{j,k}\mathbf{v}$ is equal to a linear combination of $\partial v_i / \partial x_k$. Since the latter derivatives are occurring in the stress tensor too, we assume that these derivatives at the boundary can be quantified to be of the order of the local boundary curvature. Hereby, we used that the stress in the normal direction at the boundary is proportional to that curvature. From this assumption and equation (5.13), it follows that in the case of a row derivative

$$\delta\mathcal{G}_{j,k}\mathbf{b} - \delta\mathcal{H}_{j,k}\mathbf{v} = \mathcal{O}\left(\frac{e_{12}}{e_{02}^2} + \frac{e_{12}}{e_{13}^2}\right), \quad (5.16)$$

which is in size similar as we obtained for the case of a column derivative.

From the analysis above and equation (5.5), it follows that we can approximate the $(2j - k)^{\text{th}}$ column $\delta\mathbf{v}_{j,k}$ of the Jacobian \mathcal{J} by,

$$\delta\mathbf{v}_{j,k} \doteq \mathcal{H}^{-1} \mathcal{G} \delta\mathbf{b}_{j,k}. \quad (5.17)$$

This approximation is valid even when the ODEs are not stiff since then a rough approximation of the Jacobian will be sufficient. In section 5.4 we will show that accurate results are obtained for two model examples of the previous section using this approximate Jacobian for both the linear and quadratic element solution.

5.3 RESTART OF INTEGRATION AFTER A NODE REDISTRIBUTION

In section 4.4 we presented an algorithm for an optimal node redistribution based on equidistributing the curvature of the boundary. After a node redistribution, the (material) points of which the trajectories were being followed also change, i.e. the set of ODEs can completely change its character. This is also illustrated by figure 5.1, where the “jumps” in the spectral radius are due to this node redistribution. After such a redistribution the time integration is started without any information of the previous time step. The spectral radius development of both other examples does not show such a jumping behaviour after a node redistribution. This can be explained from the similarity of the particle trajectories in the neighbourhood of a particular node for such smooth shapes. Therefore in this case, it is not necessary to redistribute the nodal points frequently, thus a restart of the time integration with these new mesh will not yield much; however, the latter does make sense for shapes with an evolving cusp, since the position of nodes near the cusp region have to be controlled well in order to obtain a realistic value for the cusp curvature.

When we like to restart the time integration, LSODE has to be started without further information, i.e. the order of the method is equal to 1 and the initial step size is set by the program. However, we want the BDF-solver to continue with the order and step-size equal to the latest value before the node redistribution was carried out. We will show below that under certain conditions it is possible to perform such a restart. Before doing this, we first have to dwell on some aspects of the implementation of the BDF-method in LSODE which is also discussed in Gear [27] and Hindmarsh [38]-[39].

The code LSODE is based on the *Nordsieck representation* of the fixed step size BDF-methods. For the solution of the ODEs at time $t = t_{i+1}$ the original p^{th} order BDF-method needs the actual values of the boundary nodes at previous times t_i, \dots, t_{i-p+1} and the velocity of the boundary at t_i as well. When this p^{th} order BDF-method is expressed in the so-called Nordsieck representation, the boundary at $t = t_i$ and the first till the p^{th} derivative (with respect to t) of this boundary are required. Thus, the Nordsieck vector, say \mathbf{z}^i , can be expressed as

$$\mathbf{z}^i = \left(\mathbf{x}(t_i), h \frac{d\mathbf{x}}{dt}(t_i), \dots, \frac{h^p}{p!} \frac{d^p \mathbf{x}}{dt^p}(t_i) \right)^T,$$

where h is the step size that will be applied. The advantage of this representation is that when the step size h is changed, the Nordsieck vector for this new step size is easy to find. The Nordsieck vector is also used to predict the solution at the next time level $t_{i+1} = t_i + h$, i.e.

$$\mathbf{x}(t_{i+1}) = \mathbf{x}(t_i) + h \frac{d\mathbf{x}}{dt}(t_i) + \dots + \frac{h^p}{p!} \frac{d^p \mathbf{x}}{dt^p}(t_i). \quad (5.18)$$

This is then the starting vector for the Newton iteration for solving the corrector BDF. LSODE is using this particular initial guess of the next time level geometry to determine the velocity field at that level and to update the Jacobian eventually.

Furthermore, this predictor is used for estimating the local integration error; indeed LSODE applies the following automatic step size and order selection strategy (see also Hindmarsh [39]). At each step, an estimate of the local error for the present method of order p is obtained from the difference between the predictor (5.18) and the final corrected values of $\mathbf{x}(t_{i+1})$. From this local error vector a step size h is deduced that satisfies the required tolerance. When this tolerance is not reached, the computed step size will be used to redo this particular step. After $p + 1$ steps with the same value for h , the order and/or step size will be updated: besides for the method of order p , error estimates are formed for methods of order $p - 1$ and $p + 1$ too. From these three error estimates new step sizes h are computed. Based solely on efficiency considerations, the new order method is chosen so that the new step size will be maximal in magnitude. For the simulation of sintering problems, we observed that with very small tolerances, LSODE will try to solve the ODEs with the largest possible order method; by lowering the tolerance to more practical applied values, it has the tendency to use a method of order two or three.

In order to continue with LSODE after a node redistribution, with the same order and step size as before the redistribution, the Nordsieck vector for those new nodes is required, i.e. the first till the p^{th} derivative (with respect to t) of these nodal points. We now outline the procedure for finding the higher order derivatives.

In principle, we have the Nordsieck vector, e.g. the derivatives, for the old nodal points. The boundary is found by a Lagrangian polynomial interpolation through these points, i.e. in the notation of section 4.2,

$$\mathbf{y}(s) = \phi_j(s)\mathbf{y}^j,$$

where $-1 \leq s \leq 1$ and $j=1,\dots,q$. The number $q-1$ is equal to the degree of the polynomial approximation. Since the interpolation polynomials ϕ_j are independent of time, the k^{th} derivative with respect to t of the above equation is equal to

$$\frac{d^k \mathbf{y}}{dt^k}(s) = \phi_j(s) \frac{d^k \mathbf{y}^j}{dt^k}.$$

In this way, we see that the problem of finding the new Nordsieck vector can be reduced to an interpolation problem using the old Nordsieck vector.

We do not want the interpolation error which is introduced by this interpolation, to influence the new Nordsieck vector. By taking into consideration the multiple usage of the predictor (5.18) for the next level geometry as is mentioned before, we have to avoid that the accuracy of this initial guess is affected by the interpolation. So the degree of the Lagrangian polynomials has to be large enough to ensure that the resulting error be smaller than the smallest component of the Nordsieck vector. Because of this we applied a polynomial interpolation of degree five.

Note that also the *spatial* discretization error induced by the BEM will affect the actually found velocity \mathbf{v} at the new nodal points. In particular during the initial stage of a cusp evolution, one can observe that the velocity field as is obtained from interpolating the old Nordsieck vector can differ in all digits and for all points from the actual

velocity field of the new discretized boundary. This large difference is caused by the ill-conditioning of the boundary value problem for such kind of shapes, see also chapter 6. Consequently, the initial guess that is obtained from the interpolated Nordsieck vector will have a large error too, irrespective of the quality of that interpolation. Note, that also interpolation problems might occur in the neighbourhood of such a cusp point since the redistribution algorithm is effectively smoothing this part of the boundary somewhat. Through this larger error in the predictor, the step size and order selection strategy of LSODE can easily be disturbed besides possible problems of the convergence of the Newton iteration. From this point of view, it does not seem quite meaningful to restart with the same order and step size. However, by improving the initial guess, it may be possible to continue the integration with a second order method. Since we observed that LSODE does have serious difficulties by restarting the integration when no further information is given (see also section 5.4), this can sometimes mean a considerable saving in computer time.

As a satisfactory choice for the predictor we found by solving the problem for this new grid first and then replacing the first derivative in the new Nordsieck vector by the thus obtained exact $h v$. In this way we obtain a predictor that is much closer to the corrected value after the Newton iteration. This requires an extra assembling and solution of the system of equations; however, we also observed that this investment was decreasing the *total* computing time considerably (see section 5.4), since there was less overhead in restarting and the error control was not affected either.

For a smooth geometry, the difference between the velocity field as obtained from the interpolated old Nordsieck vector and the exact velocity of the new boundary is not so dramatically large: this error is of the same order as the anticipated discretization error. In order to build in an extra safe guard, we replace the first derivative in the Nordsieck vector by the exact computed $h v$ for the new boundary too.

The algorithm used for determining the Nordsieck vector for the new nodes is the following. First, for every new nodal point obtained by the node redistribution algorithm, we seek two successive points from the old grid which are the neighbouring points of this new node, i.e. the new node is lying between those two old points. Then we obtain an approximation of the boundary in this particular region by interpolation at three old points at both sides of this new node. Next, we *replace* the new node, by a point that is lying on the approximated boundary region and that is closest to this node. This point is chosen as the new grid point and is incorporated in the Nordsieck vector. After this procedure is carried out for the complete grid, we solve the system of equations for this new mesh and we replace the first derivative in the Nordsieck vector by the (exact) calculated $h v$ for the reason mentioned above. In the next section we will demonstrate the usefulness of this method.

5.4 NUMERICAL EXPERIMENTS AND DISCUSSION

Here, we will first demonstrate that the approximated Jacobian of section 5.2 is performing well when used by the time integrator. Afterwards, we show the advantages of the algorithm to restart LSODE after a node redistribution, as described in the previous section. In the following simulations, all the program parameters that occur in the redistribution algorithm and the time integrator will be the same for each test problem.

To illustrate that the approximation derived for \mathcal{J} is sufficient, we compare the numerical solutions of the example problems of section 5.1 when both the numerical exact Jacobian and the approximation (5.17) are used by LSODE. These solutions are compared to the exact analytical solution at some characteristic boundary points and at a fixed number of times, which will not necessarily be the time levels of the integrator. The solution at such an intermediate point in time is found by applying the interpolation facility of LSODE. Since we compare the numerical solutions to the exact analytical solution in relation to the Jacobian that is used, both the actual error size and source (spatial and/or time) are not important for the moment. Here, the only interest is the question whether this error is *behaving in a similar way* for both Jacobians: if so we can conclude that the approximated Jacobian is sufficient. Furthermore, we will compare other important properties as: the size and total number of time steps, the number of Jacobian evaluations and the order of the BDF-method respectively. We also show that this approximate Jacobian can be used successfully in the case of the quadratic element solution.

We consider the two equal coalescing cylinders first. For the error control in the time integrator LSODE we used a global absolute error tolerance parameter equal to 10^{-4} ; the relative error parameter was taken component wise. This relative error was set equal to 10^{-3} for the “smooth” parts of the boundary and equal to 10^{-5} for the nodes in the touching region of both cylinders. A node redistribution was carried out when the nodal points were coming too close to each other (10^{-3}) and in general after each fifteen consecutive steps. The minimum and maximum distance between two successive nodes (used in the redistribution algorithm) was set equal to $5 \cdot 10^{-3}$ and 0.15 respectively.

We have compared the difference in both the coalescence rates (e_r) and the shrinkage (e_s) between the analytical and numerical solutions. These particular two boundary points are chosen since the coalescing rate represents the point where the boundary is undergoing the largest deformation and on the other hand, the point that denotes the shrinkage rate represents a part of the boundary which is hardly deforming. In figure 5.5 is plotted those mentioned absolute differences at a sequence of times $t = 0.0(0.05)2.0$. The solid lines in the plots indicate that the exact Jacobian is used by the simulation; otherwise (dotted lines) the approximation (5.17) is used. The difference in the coalescence rate is marked by circles and the shrinking error is denoted by “x”-marks.

As can be observed from this figure, the error behaviour of the numerical solution that is obtained by employing the approximated Jacobian is matching quite well with the error behaviour in the case of exact Jacobians. We see that this is valid when the

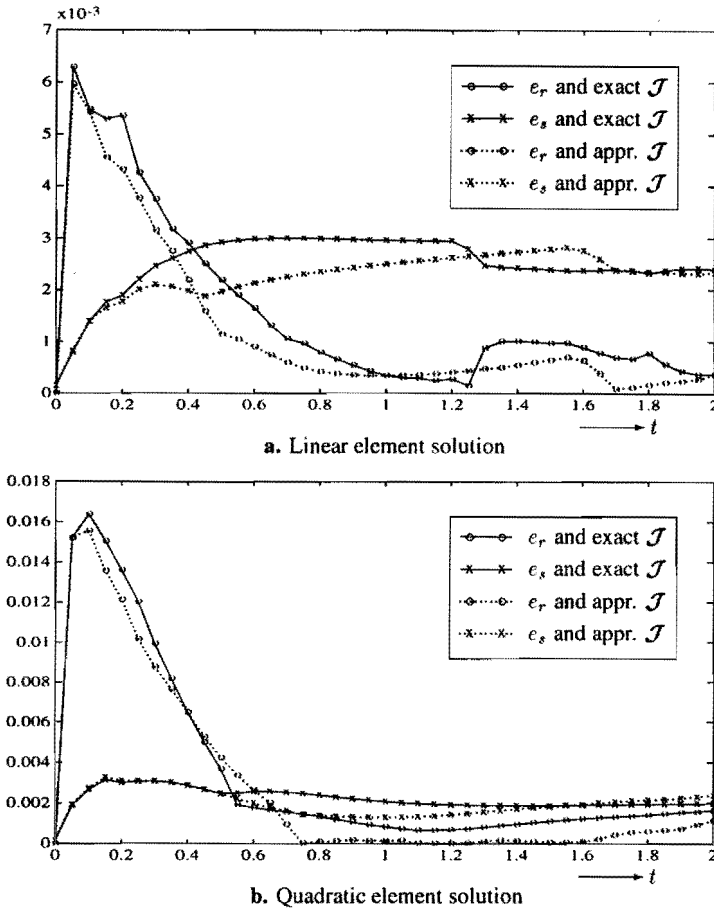
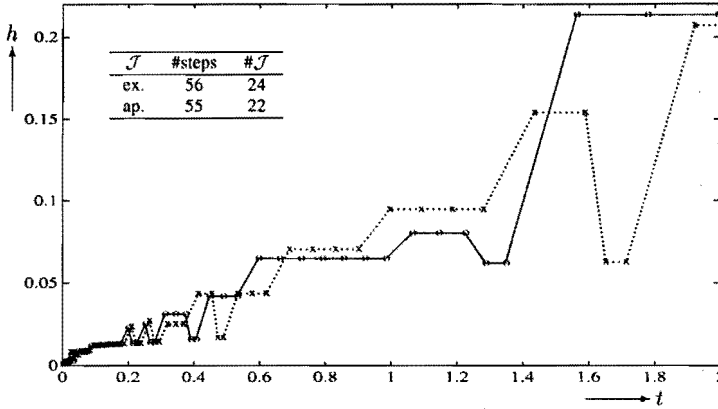
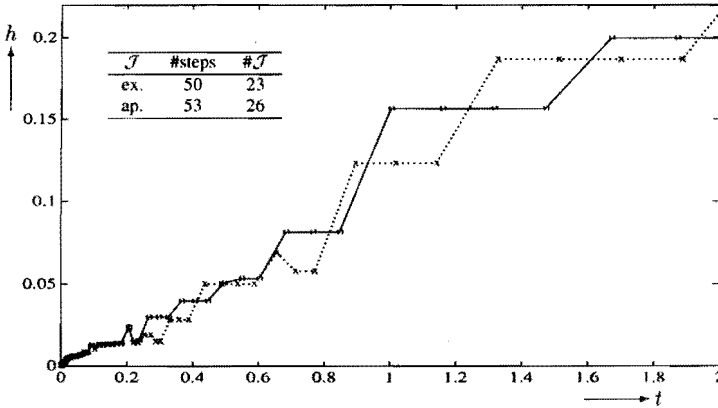


Figure 5.5 For the case of the coalescing cylinders is shown the similar error behaviour between the exact analytical solution and the numerical solutions obtained by using the exact and the approximated Jacobian for both the linear element (a) implementation as well as when quadratic elements (b) are applied. The solid lines represent the error in the case that the exact Jacobian is used and the dotted lines are derived for the approximation. Furthermore, e_r is the absolute error in the coalescing rates (circle-marks) and e_s is the difference in particle shrinkage (x-marks).

shape has parts with large varying curvature as well as when the boundary is smoother. In section 5.2 we found that for the latter case the approximate Jacobian may have a large error. However, we observe that this error does not influence the numerical solution. Furthermore, this similar error behaviour is valid for both the linear and quadratic element implementations. The reason that for the initial stage the error in the coalescence rate is much larger than during the rest of the simulation, is due to the difficulty of quadratic elements to follow sharp cusps; it has the tendency to smooth the cusp region much faster so that the coalescence is proceeding quicker too. However, this is not influencing the error at later time stages through the conditioning of the problem



a. Linear element solution



b. Quadratic element solution

Figure 5.6 The step size (h) development of the time integrator using the approximate Jacobian (x-marks and dotted line) is showing in the case of the coalescing cylinders a similar behaviour as when the exact Jacobian is applied (circles and solid line). This behaviour is obtained for both the linear (a) and the quadratic element implementation (b). The tables are showing the roughly similar behaviour in the total number of time steps ($\#steps$) and Jacobian updates ($\#\mathcal{J}$). After a node redistribution, the time integration was started without further information.

as can be seen from the figure.

In figure 5.6 the step size development of LSODE is plotted for both Jacobians, showing a similar behaviour also. The order development of the BDF-method (not shown) was also behaving similarly. Here, LSODE is started after a redistribution without any further information from the previous time level. The decrease in step size for the linear element solution with the approximate Jacobian at the later stage is due to a restart after a node redistribution (see also table 5.1 in further, where all characteristics of this particular evolution is printed). The tables that are printed in this figure are showing a similar behaviour between the total number integration steps ($\#steps$) as well

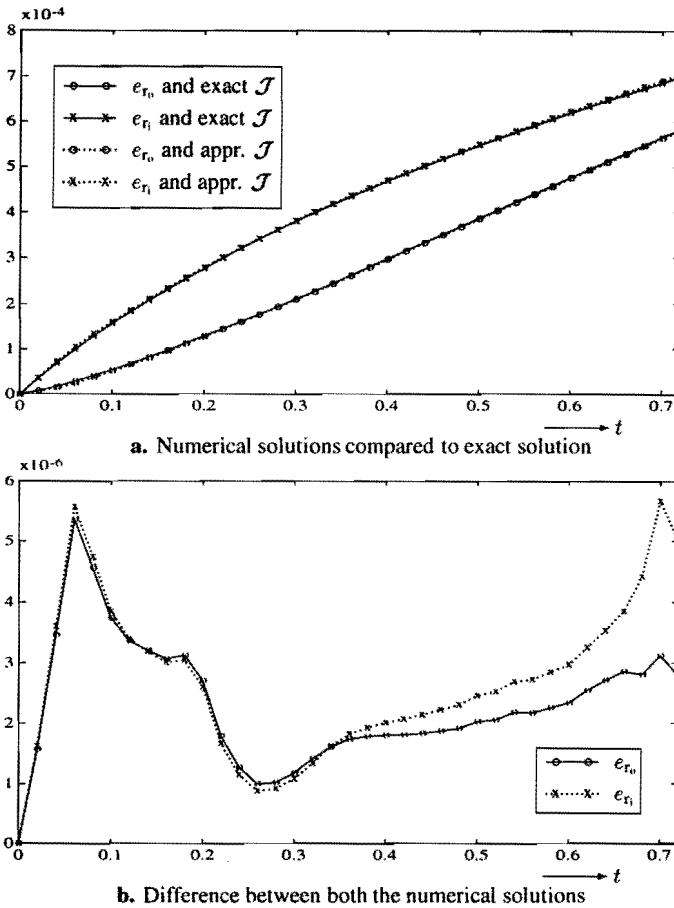


Figure 5.7 For the case of the circular annulus shrinkage is shown in **a** the identical error behaviour of the exact analytical solutions of both the inner (e_{r_i}) and outer (e_{r_o}) radius compared to the numerical solutions obtained by using both Jacobians and linear elements. Figure **b** shows that the difference between both the numerical solutions is of the order of the time integration tolerance (10^{-6}). In the latter plot, the solid line represents the error in the outer radius and the dotted line is the difference between the inner radius solutions.

as the total Jacobian updates ($\#\mathcal{J}$). All the similarities mentioned above seem to indicate that the Jacobian approximation (5.17) is sufficient for all kinds of simply connected domains.

Next, we show that this approximation is also valid in the case of multiply connected domains, by considering the shrinking circular annulus example. For the error control in LSODE we used a global absolute and relative tolerance equal to 10^{-6} . The node redistribution was carried out when nodes were coming too close to each other (10^{-3}) and in general after each 25 consecutive steps. The minimum and maximum distance between two successive nodes was taken the same as in the previous example. In figure

5.7 we plotted the absolute error development between the exact analytical solutions, found by applying both Jacobians when linear elements are applied at a sequence of time points $t = 0.0(0.02)0.72$. The reason that the error in both numerical solutions are identical is caused by the fact that we have taken the time tolerance much smaller than the spatial error tolerance: thus the actual error that this plot shows is due to the spatial discretization. In order to show that the approximated Jacobian is performing well too for this particular case, we have plotted the absolute difference between these numerical solutions. As can be seen this difference is of the order of the tolerance of the time integrator. Again, we observed that the step size and order development of LSODE using both Jacobians shows a similar behaviour too. However, the exact Jacobian solution needed a lower number of time steps (33) and Jacobian updates (11) than the other solution method (40 time steps and 15 Jacobian updates). These values do still not justify the use of the better and much expensiver approximation (5.5). We obtained similar results for the quadratic element implementation. From this, we can conclude that the approximate Jacobian is sufficient for multiply connected domains too.

We consider the above two example problems to be illustrative for all kind of other sintering problems, cf. 5.1. Note that all the simulation examples which are carried out in this thesis are computed using the approximated Jacobian. From now on, when we refer to the Jacobian \mathcal{J} , we actually mean the approximation (5.17).

The savings in computational costs that can be achieved by applying the restarting algorithm of section 5.3 after a node redistribution in the case that a cusp is involved during the evolution will be shown by an example of two equal coalescing cylinders. In table 5.1 the subsequent time steps (t_i) are printed for the case that after a node redistribution (*rd*) the restart of the time integration has been carried out without further information, i.e. the starting order of the method is equal to 1 and the initial step size will be set by LSODE. Here, we used the linear element implementation. N is the total number of points and $\#\mathcal{H}^{-1}\mathcal{G}$ is the *total* number of times that the assembling and solving of the system of equations is carried out up to and including the time t_i . By *area* is denoted the total area of the fluid region (which has to be preserved during the evolution). The (relative) change of this total area, compared to the area of the original shape, is also printed. These numbers in the table show that the relative error in the area is caused by the node redistribution algorithm only.

From table 5.1 we also observe that the order of the BDF-method is nearly equal to one during the cusp evolution, i.e. a backward Euler method is used. Furthermore, this table shows the computational costs of a *restart* caused by a node redistribution: 2-7 times the assembling and solution of the system of equations and 1-2 Jacobian updates. These large numbers are caused by wrong choices of the initialization when using LSODE as a "black box". Thus, LSODE has serious difficulties to restart the integration during this evolution period. Note that this table also shows the behaviour of the order and step size selection strategy of LSODE as we described in section 5.3.

In table 5.2 is printed the integration steps for the same problem when the order and step size are set the same as before the node redistribution. Here the Nordsieck vector for the new nodes was found by interpolating the old Nordsieck vector using Lagrangian polynomials with degree five, as was outlined in section 5.3. Furthermore, the first

SENSITIVITY ANALYSIS

We consider more in detail the question of the conditioning of the sintering problem with respect to the evolution of sharply curved domains based on a simple but typical example, viz. the evolution of the coalescence of two equal cylinders. This example demonstrates the main features of the cusp evolution of the sintering phenomenon very well. Moreover, the exact analytical solution is available. By using this analytical solution we are able to give a fairly quantitative sensitivity analysis; i.e. we can investigate the influence of a perturbation of the initial radius R , the contact radius r and the neck curvature on the shape and curvature of the region where those cylinders are touching. From this analysis we will draw conclusions about the conditioning of the coalescence as an evolutionary problem and as boundary value problem at each time step as well. As a result, we can explain the observation in section 4.6 that both the exact and numerical neck curvature differ quite a bit in the early stage of the coalescence while this difference does not show any noticeable effect on the neck radius development.

6.1 PERTURBATION ANALYSIS OF TWO COALESCING CYLINDERS

In this section we will investigate the effect of a perturbation of the initial radius R , the contact radius r and the neck curvature on the shape and neck curvature evolution of two equally sized coalescing cylinders. As we already mentioned in section 5.1, this coalescence problem demonstrates the boundary deformation of a cusp-like region very well.

In chapter 3 we presented the analytical solution for the coalescence of two equal cylinders with initial radius $R = 1$. From the parametric equations (3.14) we obtain for the coalescing equal cylinders with arbitrarily radius R and centres $(R, 0)$ and $(-R, 0)$

each

$$\begin{aligned} x(\theta, \nu) &= \frac{(1 - \nu^2)(1 - \nu)R\sqrt{2} \cos \theta}{(1 - 2\nu \cos 2\theta + \nu^2)\sqrt{1 + \nu^2}} \\ y(\theta, \nu) &= \frac{(1 - \nu^2)(1 + \nu)R\sqrt{2} \sin \theta}{(1 - 2\nu \cos 2\theta + \nu^2)\sqrt{1 + \nu^2}} \end{aligned} \quad (6.1)$$

and for the time t (as function of ν)

$$t(\nu) = \frac{\pi R}{\sqrt{2}} \int_{\nu}^1 \frac{dk}{k\sqrt{1 + k^2}K(k)}. \quad (6.2)$$

Moreover, from (3.15) and (3.16) we obtain for the contact radius r as function of ν

$$r(\nu) = \frac{(1 - \nu)R\sqrt{2}}{\sqrt{1 + \nu^2}}, \quad (6.3)$$

and vice versa

$$\nu(r) = \frac{2R^2 - r\sqrt{4R^2 - r^2}}{2R^2 - r^2}. \quad (6.4)$$

The neck curvature is equal to

$$\kappa_n(r) = -\frac{4R^2}{r^3} + \frac{3}{r}. \quad (6.5)$$

In the following subsections we will perform a perturbation analysis by applying this general solution.

6.1.1 Perturbation of the initial radius

Here we show that a small perturbation of the initial radius R of both cylinders, will not influence the evolution of the shape of the neck region significantly, while the neck curvature is changing dramatically. Therefore, we are interested in the change of the shape of two coalescing equal cylinders both with initial radius R each and with $\tilde{R} = R + \varepsilon$ ($\varepsilon \ll 1$) each, considered for the *same* contact radius r . The differences of both shapes is illustrated schematically in figure 6.1. Note that both the shapes are taken at a *different* time t and \tilde{t} , say, respectively. Hence we have to consider the parametric equations (6.1) as function of R and t (i.e. ν). A measure for the difference between both shapes is given by the derivative of x, y with respect to R .

Substituting equation (6.3) into the parametric relations (6.1) yields

$$\begin{aligned} x(\theta, \nu) &= \frac{r(1 - \nu^2) \cos \theta}{1 + \nu^2 - 2\nu \cos 2\theta} \\ y(\theta, \nu) &= \frac{r(1 + \nu)^2 \sin \theta}{1 + \nu^2 - 2\nu \cos 2\theta}. \end{aligned} \quad (6.6)$$

For the derivative of ν with respect to R , we obtain after squaring, taking the derivative

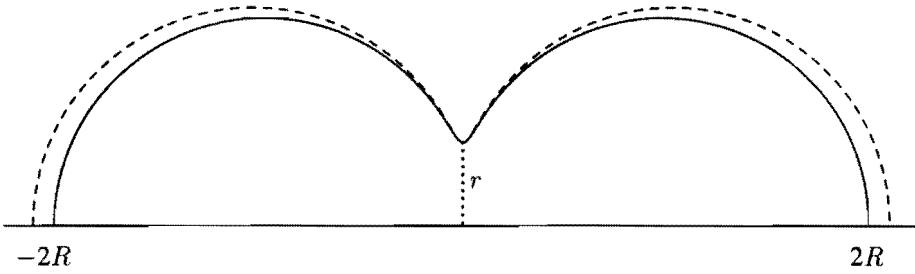


Figure 6.1 The upper cross-section of the coalescing equal cylinders with both initial radii R (solid line) and $R + \epsilon$ (dashed line) respectively, considered for the same neck radius r .

from equation (6.3) and using the inverse relation (6.4)

$$\frac{\partial \nu}{\partial R} = \frac{2R(1 - \nu)^2}{r\sqrt{4R^2 - r^2}}. \quad (6.7)$$

By taking the derivative of the parametric equations (6.6) with respect to R and substituting equation (6.7) yields

$$\begin{aligned} \frac{\partial x}{\partial R} &= \frac{4R(1 - \nu)^2[(1 + \nu^2)\cos 2\theta - 2\nu]\cos \theta}{\sqrt{4R^2 - r^2}(1 + \nu^2 - 2\nu\cos 2\theta)^2} \\ \frac{\partial y}{\partial R} &= \frac{8R(1 + \nu)(1 - \nu)^3\sin \theta\cos^2 \theta}{\sqrt{4R^2 - r^2}(1 + \nu^2 - 2\nu\cos 2\theta)^2}. \end{aligned} \quad (6.8)$$

We can find upper bounds for those derivatives as follows.

Because of symmetry, we look at the first quadrant of the shape only, i.e. $\theta \in [0, \pi/2]$ and $x, y \geq 0$. After substituting $\xi = \cos \theta$ and $\bar{r} = r/(\sqrt{2}R)$ in (6.8) we derive

$$\begin{aligned} \frac{\partial x}{\partial R} &= \frac{2\sqrt{2}(1 - \nu)^2[2(1 + \nu^2)\xi^2 - (1 + \nu)^2]\xi}{\sqrt{2 - \bar{r}^2}((1 + \nu)^2 - 4\nu\xi^2)^2} \\ \frac{\partial y}{\partial R} &= \frac{4\sqrt{2}(1 + \nu)(1 - \nu)^3\xi^2\sqrt{1 - \xi^2}}{\sqrt{2 - \bar{r}^2}((1 + \nu)^2 - 4\nu\xi^2)^2}. \end{aligned} \quad (6.9)$$

Note that the parameters ξ , ν and \bar{r} are varying between 0 and 1. Moreover, we are mainly interested in the change of the shape of the neck region, i.e. ξ is small. Substituting equation (6.6) and the relation

$$\frac{1 - \nu}{1 + \nu} = \frac{\bar{r}}{\sqrt{2 - \bar{r}^2}}, \quad (6.10)$$

into equation (6.9), we obtain

$$\begin{aligned}\frac{\partial x}{\partial R} &= \frac{2xy[2(1+\nu^2)\xi^2 - (1+\nu)^2]}{Rr(2-\bar{r}^2)(1+\nu)^2\sqrt{1-\xi^2}} \\ \frac{\partial y}{\partial R} &= \frac{2\sqrt{2}xy\xi}{R^2(2-\bar{r}^2)^{\frac{3}{2}}}.\end{aligned}$$

When $\xi = 0$, the expression $|2(1+\nu^2)\xi^2 - (1+\nu)^2|$ is maximal ($= (1+\nu)^2$) as considered to be a function of ξ . From this and $0 \leq \bar{r} < 1$, we deduce the following upper bounds

$$\left| \frac{\partial x}{\partial R} \right| \leq \frac{2xy}{Rr\sqrt{1-\xi^2}} \quad \text{and} \quad \left| \frac{\partial y}{\partial R} \right| \leq \frac{2\sqrt{2}xy}{R^2}. \quad (6.11)$$

Remark that in the neck region the number y/r is bounded and both x and ξ are small. From this observation and the estimates (6.11) we draw the conclusion that a perturbation of the initial radius R of the coalescing cylinders will not change much the *neck region shape* measured at a point where the contact radius r is the same for both, even when r is small. This behaviour is also demonstrated in figure 6.1.

However, the *neck curvature* does change dramatically when the contact radius is small. This can be illustrated by computing the derivative of the curvature with respect to R in the neck. From the relation for the exact neck curvature (6.5), the derivative by constant radius r is given by

$$\frac{\partial \kappa_n}{\partial R} = -\frac{8R}{r^3}.$$

This derivative becomes very large in magnitude when the contact radius r is small, hence the curvature may change a lot from a very small perturbation of the initial radius R of these two coalescing cylinders!

A measure for the difference between t and \hat{t} is given by the derivative of t with respect to R . Taking the derivative of equation (6.2) and substituting (6.3) and (6.7), we find

$$\frac{\partial t}{\partial R} = \frac{t}{R} - \frac{\pi\bar{r}\sqrt{1+\nu^2}}{\nu K(\nu)\sqrt{2(2-\bar{r}^2)}}. \quad (6.12)$$

Recalling the asymptotic expansions for the complete elliptic integral $K(\nu)$, i.e. equations (3.23) and (3.24),

$$\begin{aligned}K(\nu) &= \frac{1}{2} \log \frac{16}{1-\nu^2} + \mathcal{O}\left((1-\nu^2)\log(1-\nu^2)\right) \quad (\nu \rightarrow 1) \\ K(\nu) &= \frac{\pi}{2} \left[1 + \frac{1}{4}\nu^2 + \mathcal{O}(\nu^4)\right] \quad (\nu < 1),\end{aligned} \quad (6.13)$$

we obtain that when the time t is not too large, say for values of $\nu > 0.1$ (e.g. $r \leq 0.9R\sqrt{2}$), the derivative (6.12) is small. Hence we conclude that when the initial radius R is perturbed, the time-scale of the neck evolution will not change much.

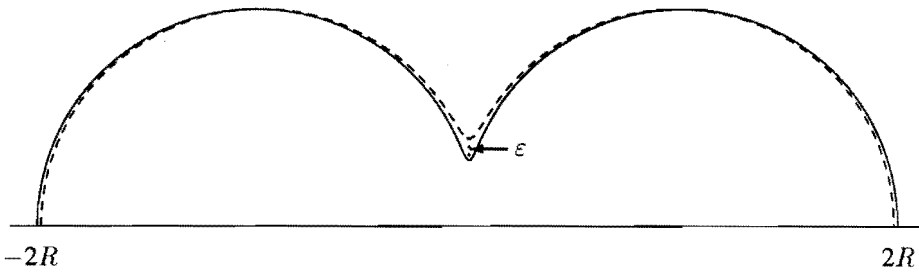


Figure 6.2 The upper cross-section of the coalescing equal cylinders with neck radius r (solid line) and $r + \epsilon$ (dashed line), at a later time.

From the observations above, we draw the conclusion that the *global* shape of the neck region, by a given contact radius, is effectively independent of the initial radius R of both coalescing cylinders; although the curvature of the neck (*local* effect) can be rather different at an early stage of the coalescence.

6.1.2 The Evolution of the Neck Region

In the following analysis, we show that when the contact radius r is getting somewhat larger, the shape of the neck region is not perturbed significantly. However again, a small perturbation of the contact radius is changing the neck curvature dramatically! Moreover, we show that the neck evolution is a “smooth” function of time.

For this we consider the shape of two coalescing equal cylinders both with initial radius R at time t when the contact radius is r and at time \hat{t} with contact radius is $r + \epsilon$ ($\epsilon \ll 1$), which is also illustrated schematically in figure 6.2. Hence we have to consider the parametric equations (6.1) as function of r and t . The measure for the difference between both shapes is given by the derivative of x, y with respect to r .

For the derivative of ν with respect to r , we obtain after squaring, taking the derivative from equation (6.3) and using the relation (6.4)

$$\frac{\partial \nu}{\partial r} = -\frac{2R^2(1 - \nu)^2}{r^2\sqrt{4R^2 - r^2}}. \tag{6.14}$$

By taking the derivative of the parametric equations (6.6) with respect to r and considering only the first quadrant, we obtain after substitution of ξ, \bar{r} and equation (6.14)

$$\begin{aligned} \frac{\partial x}{\partial r} &= \frac{(1 - \nu^2)\xi}{(1 + \nu)^2 - 4\nu\xi^2} + \frac{2(1 - \nu)^2[(1 + \nu)^2 - 2(1 + \nu^2)\xi^2]\xi}{\bar{r}\sqrt{2 - \bar{r}^2}((1 + \nu)^2 - 4\nu\xi^2)^2} \\ \frac{\partial y}{\partial r} &= \frac{(1 + \nu)^2\sqrt{1 - \xi^2}}{(1 + \nu)^2 - 4\nu\xi^2} - \frac{4(1 + \nu)(1 - \nu)^3\xi^2\sqrt{1 - \xi^2}}{\bar{r}\sqrt{2 - \bar{r}^2}((1 + \nu)^2 - 4\nu\xi^2)^2}. \end{aligned} \tag{6.15}$$

Again our interest is mainly the neck region, i.e. ξ is small. Substituting equations (6.6)

and (6.10) into equation (6.15) yields

$$\begin{aligned}\frac{\partial x}{\partial r} &= \frac{y\xi}{R\sqrt{2(1-\xi^2)(2-\bar{r}^2)}} + \frac{y^2\xi\sqrt{2}[(1+\nu)^2 - 2(1+\nu^2)\xi^2]}{R(1-\xi^2)(1+\nu)^2(2-\bar{r}^2)^{\frac{3}{2}}} \\ \frac{\partial y}{\partial r} &= \frac{y}{r} - \frac{2\sqrt{2}xy\xi}{rR(2-\bar{r}^2)^{\frac{3}{2}}}.\end{aligned}$$

Applying similar arguments as is done in subsection 6.1.1, we obtain the following upper bounds

$$\begin{aligned}\left|\frac{\partial x}{\partial r}\right| &\leq \frac{y\xi}{R\sqrt{2(1-\xi^2)}} \left(1 + \frac{2y}{\sqrt{1-\xi^2}}\right) \\ \left|\frac{\partial y}{\partial r}\right| &\leq \frac{y}{r} \left(1 + \frac{2\sqrt{2}x\xi}{R}\right).\end{aligned}\tag{6.16}$$

In the neck region y is $\mathcal{O}(r)$ and both x and ξ are small, i.e. from equation (6.16) we conclude again that a small change of the contact radius r of the coalescing cylinders will not perturb the shape of the neck region, even when r is small.

The relation (6.5) for the (exact) neck curvature also gives information about the effect of a change of the contact radius r on this curvature. From equation (6.5) it follows that the derivative of the neck curvature, with respect to r , is given by

$$\frac{\partial \kappa_n}{\partial r} = \frac{12R^2}{r^4} - \frac{3}{r^2}.$$

Hence a small change of the contact radius r has an $\mathcal{O}(r^{-4})$ effect on the neck curvature, i.e. when the contact radius is small the curvature is changed dramatically.

Conversely, we also have,

$$\frac{\partial r}{\partial \kappa_n} = \frac{r^4}{12R^2 - 3r^2},$$

i.e. a change of the neck curvature gives only an $\mathcal{O}(r^4)$ effect on the contact radius r .

A measure for the time difference between the shapes at time t and \hat{t} is given by the derivative of t with respect to r , i.e. taking the derivative of the integral relation (6.2) and using equations (6.3) and (6.14) yields

$$\frac{\partial t}{\partial r} = \frac{\pi\sqrt{1+\nu^2}}{2\nu\mathbf{K}(\nu)\sqrt{2-\bar{r}^2}}.\tag{6.17}$$

From the asymptotic expansions (6.13) it follows that the derivative (6.17) is small, when the time t is not too large. We conclude that the neck evolution is a smooth function of time.

The above analysis shows that a small change of the contact radius is hardly perturbing the global shape of the neck region. Only the curvature of the neck (a local effect) is changed dramatically when r is small.

6.2 IMPLICATIONS FOR THE NUMERICAL SOLUTION

In the two previous subsections, we have shown that a perturbation of the initial radius R or the contact radius r is hardly changing the *global* shape of the neck region, even in the early stage of the coalescence, i.e. when the contact radius is small. However, the neck curvature is changed dramatically in both cases when r is small. This has an effect on the shape of the neck region that is noticeable only *locally*, i.e. in the neighbourhood of the neck point.

From this, we conclude that the problem of two coalescing cylinders is well-conditioned from an evolutionary point of view. However, if we consider the problem that has to be solved for a fixed boundary at each time step, i.e. the boundary value problem, especially in the early stage of the coalescence; it is ill-conditioned because of the dramatically changing neck curvature.

In practice, this implies that we have to start with a shape that has a contact radius such that the neck curvature is not too large (we used approximately 10^3). Furthermore, we have shown that a change of the neck curvature does not result in a noticeable change of shape of the neck region. Therefore it is sufficient that the approximate neck curvature be of the *order* of the exact curvature, and that during the computation this approximate neck curvature is not changing significantly due to node redistribution.

This analysis explains the effect that we observed by considering the numerical neck curvature development of two equal coalescing cylinders in section 4.6. There we saw that this curvature development differs considerably with the exact solution during the early stage without a noticeable effect on the contact radius development.

THE SINTERING OF TWO-DIMENSIONAL SHAPES

Results of numerical simulation for a number of two-dimensional sintering geometries are presented to demonstrate both some typical evolution properties and the usefulness of the numerical code developed. In particular a few analytical densification models are compared with the results obtained by the simulation of two-dimensional shapes, which give some quantitative insights in the applicability of those models. Also the sintering of cylindrical packings is considered. It is shown that the unit problem of two equal coalescing cylinders can be used to describe the sintering behaviour of a regular and equally sized particle packing. In the case of an irregular packing, effects are shown that occur due to these irregularities.

7.1 SHRINKAGE MODELS COMPARED TO NUMERICAL SIMULATIONS

One important issue in sintering research is the quantification of the rest-porosity of the gel after sintering. The scientific interest for this densification process is to understand the magnitude of the driving force for this process and to deduce how the driving force and thus the densification rate are affected by the gel microstructure. As we mentioned in section 1.1, the gel microstructure is depending on the gelation process and preparation conditions. In this section we briefly overview three analytical shrinkage relationships which have been applied in literature to predict the densification rate of a shrinking gel. We then compare these models to the numerical simulation results of two-dimensional shapes with holes inside. Although a number of these models are developed for a really three-dimensional sintering compact, the comparison with the numerical results give some quantitative insight in the reliability and limitations of those approximations.

The first approach we discuss is the model of Mackenzie and Shuttleworth [70] for the late-stage viscous sintering of a compact (MS-model). As mentioned in the introduction, this formulation is also referred to as the *closed pores model*. The densification results

from the shrinkage of spherical pores distributed throughout the compact. Moreover, it is assumed that all the pores have an identical radius. The velocity field of such a pore can easily be obtained and after applying Frenkel's energy balance one derives an analytical relationship between the relative density of the compact and the reduced time. The MS-model in full dimensional variables gives the following densification rate

$$K_3(t - t_0) = \frac{2}{3} \left(\frac{3}{4\pi} \right)^{\frac{1}{3}} \int_{\hat{\rho}_0}^{\hat{\rho}} \frac{ds}{(1-s)^{\frac{2}{3}} s^{\frac{1}{3}}},$$

where

$$K_3 = \frac{\gamma n^{\frac{1}{3}}}{\eta}; \quad \hat{\rho}_0 = \frac{\rho_0}{\rho_s}; \quad \hat{\rho} = \frac{\rho}{\rho_s} \quad \text{with} \quad 0 < \hat{\rho}_0 \leq \hat{\rho} < 1.$$

Here ρ is the bulk density of the gel, ρ_0 is the initial bulk density (at $t = t_0$), ρ_s is the density of the solid phase (skeletal density) and n is the number of closed pores per unit of volume of solid phase. After integration of the right-hand side of the equation above, we obtain

$$K_3(t - t_0) = \frac{2}{3} \left(\frac{3}{4\pi} \right)^{\frac{1}{3}} \left(\frac{1}{2} \log \left[\frac{(1+a_0)^3(1+a^3)}{(1+a)^3(1+a_0^3)} \right] + \sqrt{3} \arctan \left[\frac{2\sqrt{3}(a_0 - a)}{3 + (2a_0 - 1)(2a - 1)} \right] \right), \quad (7.1)$$

where

$$a_0 = \left(\frac{1 - \hat{\rho}_0}{\hat{\rho}_0} \right)^{\frac{1}{3}} \quad \text{and} \quad a = \left(\frac{1 - \hat{\rho}}{\hat{\rho}} \right)^{\frac{1}{3}}.$$

In the two-dimensional plane, we can deduce an analogous MS-model by assuming that the densification results from the shrinkage of uniform cylindrical pores distributed throughout the fluid. The derivation of this shrinkage equation is similar to the outline of Mackenzie and Shuttleworth [70] where the pores are modelled by spheres. The following densification rate is then obtained

$$\begin{aligned} K_2(t - t_0) &= \frac{1}{\sqrt{\pi}} \int_{\hat{\rho}_0}^{\hat{\rho}} \frac{ds}{\sqrt{s(1-s)}} \\ &= \frac{1}{\sqrt{\pi}} \left[\arcsin(1 - \hat{\rho}_0) - \arcsin(1 - \hat{\rho}) \right], \end{aligned} \quad (7.2)$$

where $K_2 = \gamma\sqrt{n}/\eta$. Further on, we refer to equation (7.1) as the 3D MS-model and by 2D MS-model is meant equation (7.2).

The second approach we describe is the so-called *open-pores model* of Scherer [92] which is used to analyze the early and intermediate stage of the sintering process. As was stated in the introduction (cf. 1.2.1), in this description it is assumed that the gel can be modelled as a regular three-dimensional array of interconnected liquid cylinders, see also figure 1.4. For the unit cell that represents this structure, a cubic is taken which is characterized by the edge length and the cylinder radius (figure 1.4a). After

approximating the flow field of this unit cell and using Frenkel's energy balance the following equation can be deduced

$$K_3(t - t_0) = \frac{1}{2^{\frac{1}{6}}} \left(\frac{1}{2} \log \left[\frac{(1 - b_0 + b_0^2)(1 + b)^2}{(1 - b + b^2)(1 + b_0)^2} \right] + \sqrt{3} \arctan \left[\frac{2\sqrt{3}(b_0 - b)}{3 + (2b_0 - 1)(2b - 1)} \right] \right), \quad (7.3)$$

where

$$b = \left(\frac{2(1 + \cos \frac{1}{3}\varphi)}{1 - 2\cos \frac{1}{3}\varphi} \right)^{\frac{1}{3}}; \quad \varphi = \arctan \left[\frac{8\sqrt{2\hat{\rho}(\pi^3 - 32\hat{\rho})}}{\pi^3 - 64\hat{\rho}} \right] + 2\pi,$$

and b_0 is found by substituting φ_0 in the relation for b . The variable φ_0 is similarly defined by using $\hat{\rho}_0$ instead of $\hat{\rho}$ in the equation above. Equation (7.3) applies for $0 \leq \hat{\rho} \leq 0.942$ only, since it can be shown that at the density $\hat{\rho} = 0.942$ the parallel cylinders of the unit cell touch. Next, each cell contains an isolated pore so that the MS-model applies. Note that the equation presented above is not equal to the analytical form as was deduced in Scherer [92]. After some analytical manipulation, his rather complicated equation(s) can be rewritten as (7.3). The equation in its present form shows much similarity with the relation obtained with the MS-model.

The third approach we mention is an extension of Scherer's open-pores model to describe the densification rate of a gel on a rigid substrate. This model is developed in Scherer and Garino [94] and represents the gel by cylindrical tubes whose axes are normal to the substrate. Hence this model may probably more apply to two-dimensional sintering problems like the ones we consider here. In [94] the following analytical relationship between the density and the reduced time is given,

$$K_3(t - t_0) = \frac{2}{\hat{\rho}_0^{\frac{1}{3}} \sqrt{\pi}} \left(3(\sqrt{1 - \hat{\rho}_0} - \sqrt{1 - \hat{\rho}}) + 2 \arctan \left[\frac{\sqrt{1 - \hat{\rho}_0} - \sqrt{1 - \hat{\rho}}}{1 + \sqrt{(1 - \hat{\rho}_0)(1 - \hat{\rho})}} \right] \right), \quad (7.4)$$

where $\hat{\rho}$ may vary between 0 and 1.

The dimensionless form of all analytical densification equations presented above can easily be found by skipping the factor γ/η and taking $\rho_s = 1$, hence $\hat{\rho} = \rho$. In order to show the applicability of these actually three-dimensional models to two-dimensional problems, we consider the shape of figure figure 7.1. The starting fluid geometry represents a viscous cylinder with 9 uniformly sized cylindrical pores inside. The initial radius of the circular disk is equal to 1.3 and the pores have radius 0.2 each. The centres of the pores closest to the outer boundary are equally distributed on the circle with radius 0.8. The deformation of this geometry at subsequent periods of time is plotted in this figure too.

The density ρ of the shape at a particular time is found by division of the surface occupied by fluid through the total area that the outer boundary surrounds. In figure 7.2 the numerically obtained density change is shown by a solid line as time evolves. Furthermore, we have plotted the density increase as predicted by the analytical relations mentioned above, i.e. the equations (7.1)-(7.4). In order to apply these equations, we

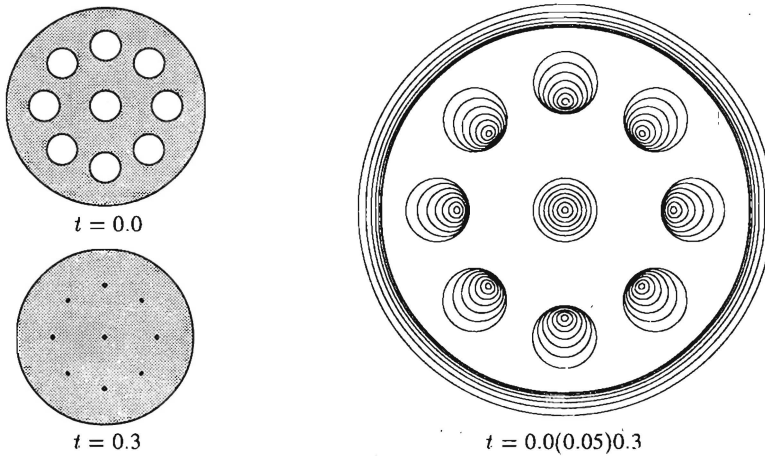


Figure 7.1 The shrinkage of a circular disk with 9 uniformly sized cylindrical pores.

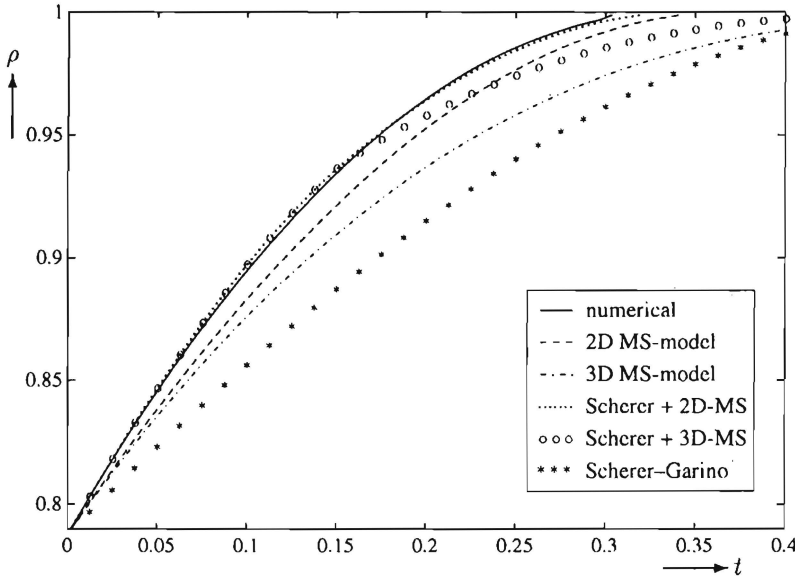


Figure 7.2 The numerical obtained density change of the geometry above compared with analytic densification rates from several models.

have set ρ_0 equal to the starting density at $t_0 = 0$. The number n is equal to the total number of pores (9) divided by the surface occupied by fluid. Moreover, Scherer's equation (7.3) has to be coupled with the MS-model to make this relation applicable for all densities. Therefore, we have used both the 2D and 3D MS-models, i.e. equations (7.2) and (7.1) respectively.

In figure 7.2 it is surprising to see the matching of Scherer's equation (7.3) in combination with the 2D MS-model, i.e. the dotted line. Since both models (7.2) and (7.4) are based on cylindrical pores geometries and the starting geometry is likewise, we

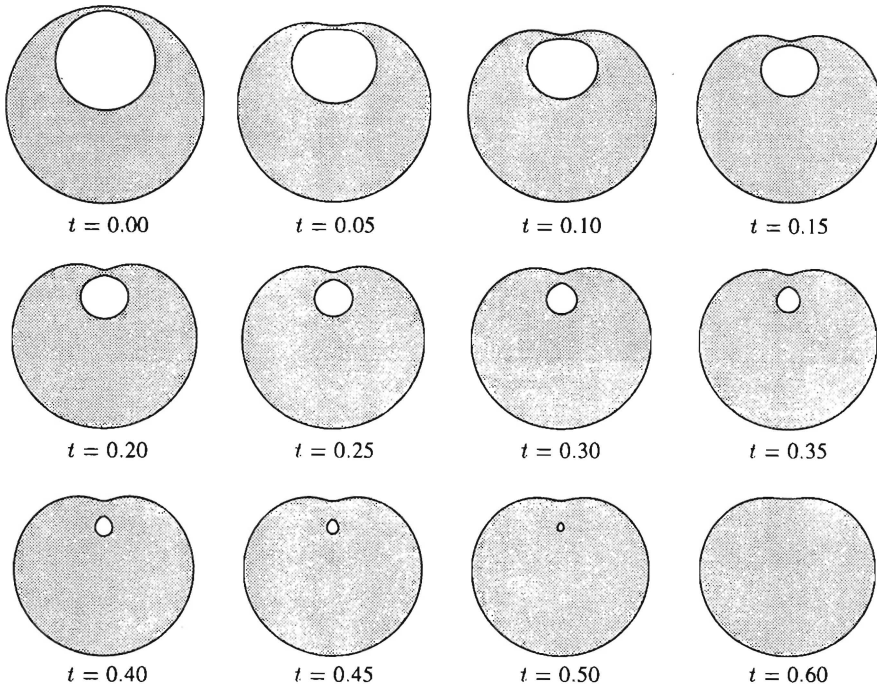


Figure 7.3 The shrinkage of a circular hole which is located close to the outer boundary of a circular fluid disk. The hole remains in the fluid and vanishes after a period of time.

should have expected better likeness between the results of the equation derived from the 2D MS-model and the Scherer–Garino equation. Comparing the densification rate obtained by the latter two equations, we see that the 2D MS-model predicts the shrinkage better for this particular example. The 3D MS-model does not give a satisfactory result at all for this two-dimensional shape. Because of this, the equation (7.1) will not be considered further. The Scherer–Garino equation does not give a satisfactory approximation either. However it will not be skipped since in the next section it is shown that this equation is applicable to predict the shrinkage of cylindrical packings. Moreover, the figure also shows a nearly *linear* shrinkage rate during a large period of time.

An effect that has to be taken into account is the influence of the pore on the outer boundary. To show this, we consider the evolution of a circular hole, situated close to the outer boundary of a fluid disk as is plotted in figure 7.3 at $t = 0$. The starting circular fluid disk has radius 1 and is centred at the origin. For the circular hole we have taken an initial radius of 0.5 and situated the midpoint of the hole at $x_2 = 0.45$ on the vertical axis. Hence, the smallest distance between a point on the hole curve and the outer boundary is 0.05.

In figure 7.3 is shown the deformation of the fluid domain at subsequent times $t = 0.0(0.05)0.50$. It is an interesting question by itself whether the hole is going outside the interior of the fluid, i.e. whether the domain will become simply connected.

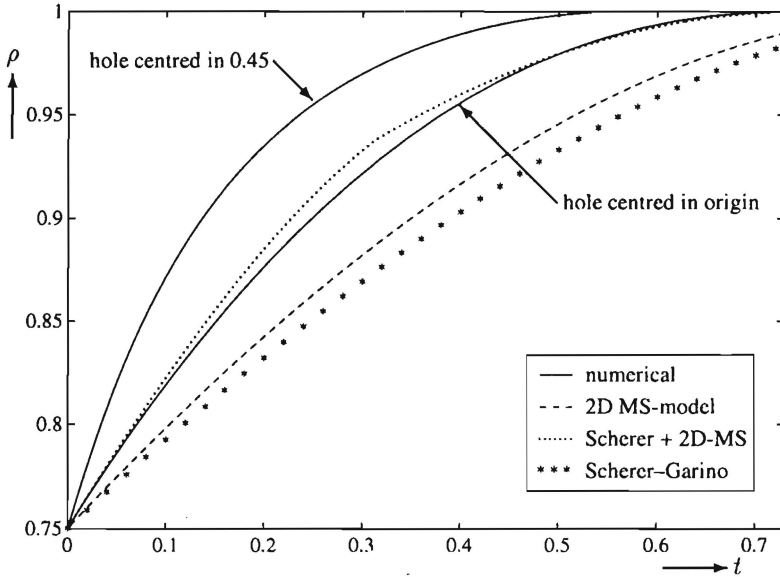


Figure 7.4 The shrinking of the hole from a circular disk that is centred at the origin compared to both the densification rate of figure 7.3 and the analytical relationships.

As can be observed, the hole *remains* in the fluid domain and is completely filled up by fluid at time $t = 0.6$. A small disturbance in the neighbourhood of the part nearest the hole is the only effect on the outer boundary.

The interesting phenomenon demonstrated by this fluid deformation is that the shrinkage rate of the hole is going faster as compared to a similarly sized hole centred at the origin. The latter problem can be solved analytically, cf. Van de Vorst [107]. Note that these geometries contain both the same amount of fluid and an equally sized interior hole. Only the position of the centre of these holes differs. In figure 7.4 the densification rate of these two problems is compared. Moreover, the shrinkage rate as predicted by the analytical models are also plotted. Here we have used similar marks for all these lines as in figure 7.2. Again we observe that Scherer's relation in combination with the 2D MS-model gives the best approximation when the hole is centred in the origin. However, when the hole is situated close to the boundary, the shrinking proceeds much faster and all analytical models fail considerably. An explanation for this difference is that for a centred hole the *total* fluid has to move in the direction of the origin. In the other case, there is not much flow occurring in the bottom part of the shape; the hole is mainly filled up by fluid flowing from upper part of the domain.

Another effect we have to investigate is the dependence of the densification rate on non-uniformly sized pores. Therefore, we consider the shrinkage of a fluid disk with initially 13 cylindrical pores as plotted in figure 7.5. The radius of the fluid disk is taken equal to 1 and the radii of the holes is varying between 0.08 and 0.23. Thus the largest hole is nearly 9 times the size of the smallest one. The figure shows that the initial larger sized holes are shrinking *significantly* faster as compared to the smaller ones as time

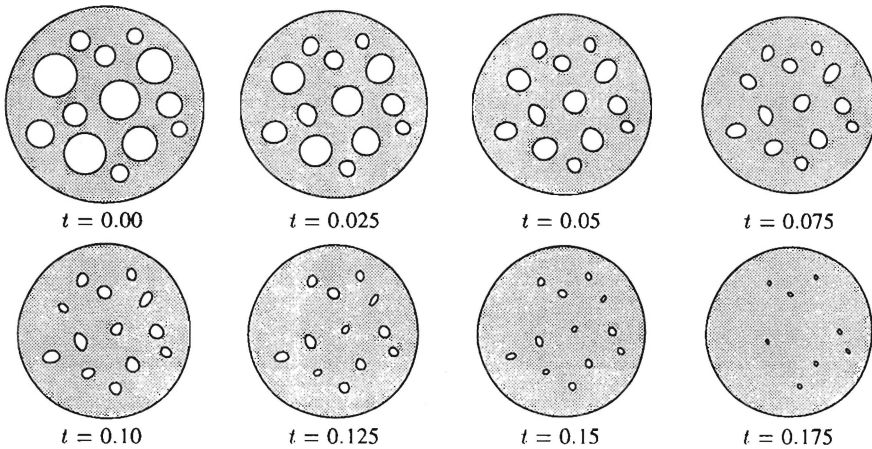


Figure 7.5 The deformation of a fluid region with nonuniform sized pores shows that the larger pores are shrinking significantly faster compared to the smaller ones.

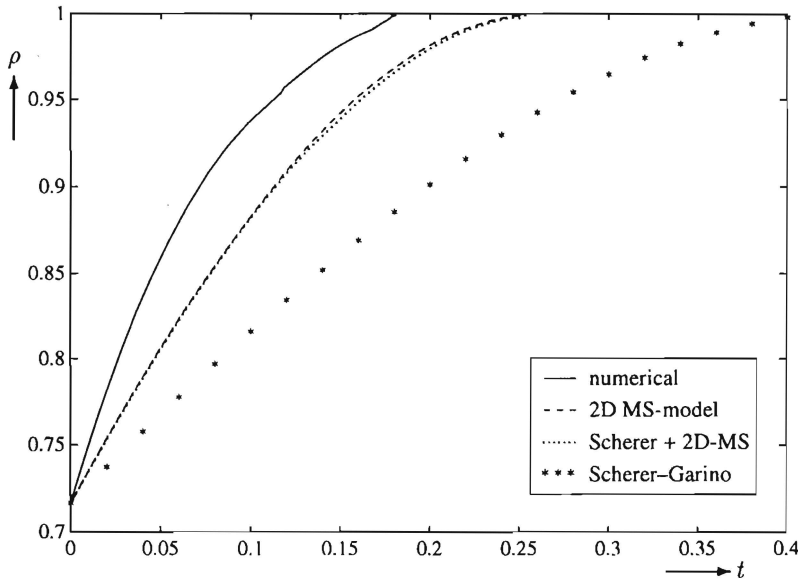


Figure 7.6 The densification rate of the above figure compared to the shrinkage as predicted by the analytical relationships.

evolves. This faster shrinking behaviour even continues when the size of these holes is becoming of the same order as the smaller holes. Hence, the larger holes are vanishing faster compared to the smaller ones, which is a remarkable phenomenon. Note that for this example we may presume that the outer boundary does not influence the shrinkage rate as in the previous example, since this curve is remaining nearly circular during the densification.

In figure 7.6 we have plotted the densification rate of this geometry obtained from the numerical simulation, by a solid line and have compared it to predictions by the

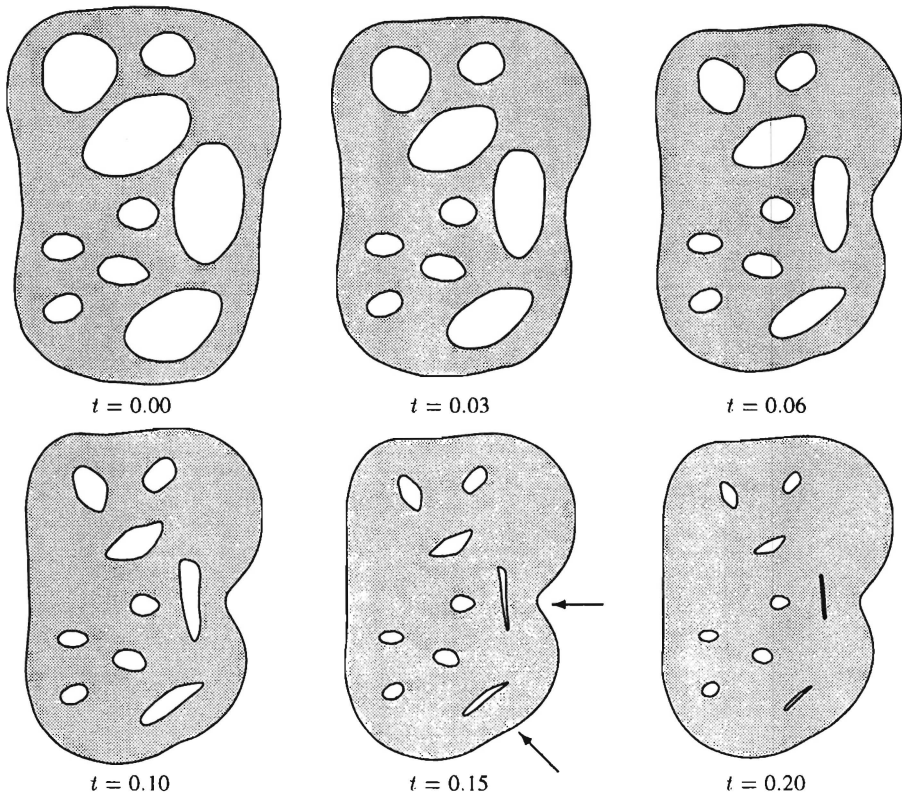


Figure 7.7 The deformation of an arbitrary fluid region with nonuniform sized pores shows both the faster shrinking of the larger pores and the touching of boundaries inside the holes. The arrows show the influence of the pores onto the outer boundary.

various analytical models. The analytical solutions are obtained by taking the number of pores equal to the initial number of holes (13). This number is kept fixed as time evolves, although it is changing during the shrinkage since not all holes vanish at the same time. This approach may be justified by the argument that one does not know when pores are vanishing during sintering in reality. The only thing that one probably knows is the pore distribution of the starting gel. The figure shows that the models do not give a satisfactory result at all. Both the Scherer's and the 2D MS-model prediction of the total densification is almost 1.5 times larger than what the numerical simulation predicts. The other two models give in this case an even worse approximation.

The failure of the analytical densification models for this particular example can be contributed to the phenomenon that larger pores are shrinking faster compared to smaller pores, since this effect is not incorporated in these models. Those models are solely based on uniformly sized and equally distributed pores. The extension of these relations to both non-uniform pore sizes and distributions is made by the assumption that the densification kinetics of such a compact is related to the *average* pore size distribution. The numerical simulation shows that this assumption does not seem to hold. Note that

ignoring the smaller pores, i.e. decreasing the number n in the analytic approximations, makes those solutions even worse since we have to divide through n in these equations. Hence the difference between the predicted densification rate and the numerical results will become larger.

Another effect to be taken care of is the touching of the boundary inside a hole. The presented numerical code cannot yet deal with situations where boundaries touch during a simulation. However, we demonstrate this phenomenon by the fluid domain as is shown in figure 7.7. In this arbitrarily shaped region we put four larger holes and five smaller ones. Again the phenomenon occurs that the larger holes are shrinking faster compared to the smaller ones. Moreover, the large holes situated at the right and bellow do influence the outer boundary during their shrinkage which results in a groove at the right and a oblique angle of the outer boundary below, i.e. the arrow marks in the figure at $t = 0.15$. The final shape shows the touching of an inner hole boundary which results in a stop of the simulation.

7.2 THE SINTERING OF CYLINDRICAL PACKINGS

In the previous chapters we discussed the coalescence of two (un)equal cylinders (cf. section 4.6). Here, we start by showing that the equal cylindrical unit problem can be applied to describe the sintering behaviour of regular and equally sized particle packings. In particular the coalescence rate can be used to obtain a better phenomenological insight into the shrinkage of the macroscopic system. Finally, we demonstrate phenomena that occur due to irregularities in the particle packings.

In the following example geometries we have set the initial radii of all cylinders equal to 0.5. The contact radius between two touching cylinders is initially taken equal to 0.095 for all neck regions. Furthermore, we use Hopper's analytical solution for the coalescence of two equal cylinders to approximate the neck regions of the initial shape (cf. section 6.1).

Figure 7.8 shows the deformation of three to six symmetrically placed equally sized cylinders with a hole in the interior of the domain. All initial shapes are constructed so that the mid-points of the cylinders are equally distributed on a circle centred at the origin. The radius of this particular circle is taken such that the distance between two successive cylindrical centres is equal to the shrinkage of two coalescing cylinders.

An interesting question is the behaviour of the neck growth between two touching cylinders of these packings compared with the exact contact radius development of two coalescing cylinders. In figure 7.9 we show the development in time of the contact radius for all the four packings. In this figure, the contact radius is plotted from the neck regions that are situated along the positive vertical symmetry axis. The exact neck radius for the coalescence of two cylinders with initial radii equal to 0.5 is also plotted.

From this picture we see that the neck growth for all four cases is of the same rate and almost equal to the contact radius development of two coalescing cylinders. From this observation we conclude that the sintering of the packings above, can in fact be described reasonably by considering the model of the coalescence of two equal cylinders.

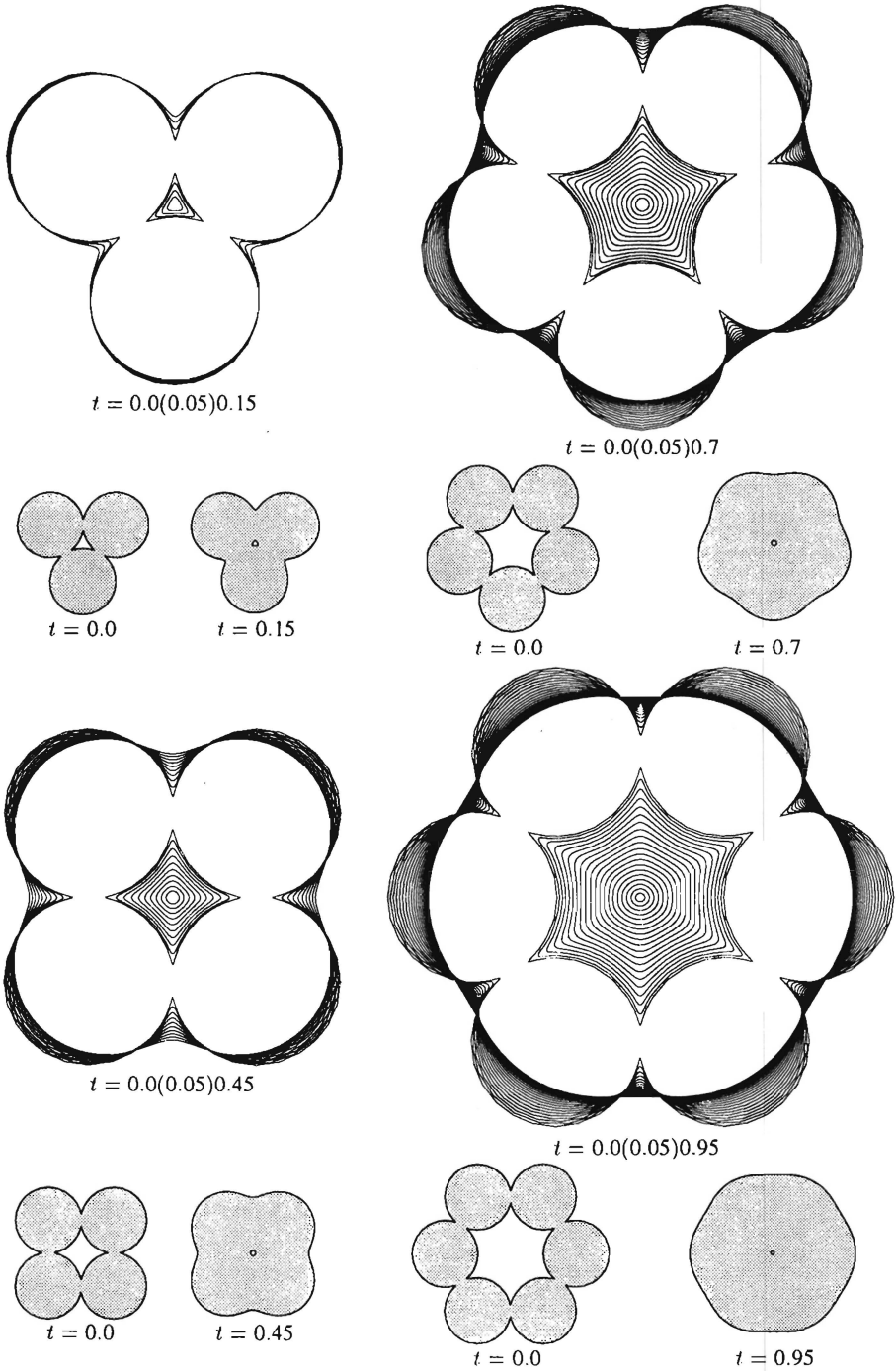


Figure 7.8 The deformation of three to six symmetrically placed equal sized cylinders.

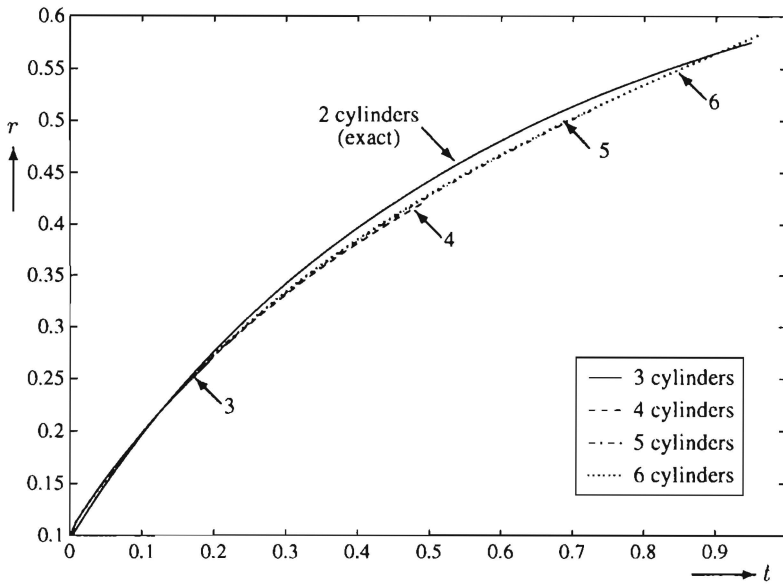


Figure 7.9 The development of the contact radius r between two cylinders of the packings of figure 7.8 compared with the exact neck growth of two coalescing cylinders.

This illustrates the importance of the exact analytical solution obtained by Hopper for this particular coalescence. Furthermore, we observe that there is even no change in the coalescence rate at times when the internal holes have almost vanished.

The importance of the numerical experiments above is that they give some justification of the modelling of the densification of equally sized particle packings based on such unit problems. An example of such a model based on unit problems that describes the deformation of a sintering compact was presented by Jagota and Dawson [49]. As mentioned in the introduction, they modelled the particle packing as a framework of links between any pair of touching spheres, and the growth of those links is described by using the behaviour of the unit problem of two coalescing spheres separately.

The shrinking of the interior holes from the packings of figure 7.8 are shown in figure 7.10. From this figure we observe that the density of the packings is increasing at a nearly *linear* rate for a large period of time. This observation can be clarified by noting that during this period, there is only a large flow activity in the neighbourhood of the touching area between two successive cylinders.

In the previous section, it was shown that the analytical densification models apply fairly well for uniform sized and equally distributed pores. Now, we compare these models to the shrinkage rate of a regular packing of equally sized cylinders. Therefore, we consider the packing of a 4×4 array of cylinders as plotted in figure 7.11. Again all the contact radii are set equal to 0.095 and the neck regions are obtained from Hopper's analytical solution. In figure 7.11 we show the densification of this particular compact. The picture on the right shows the deformation at equal periods of 0.05. It can be seen that the holes are moving further into the interior of the fluid. Moreover, all holes seem

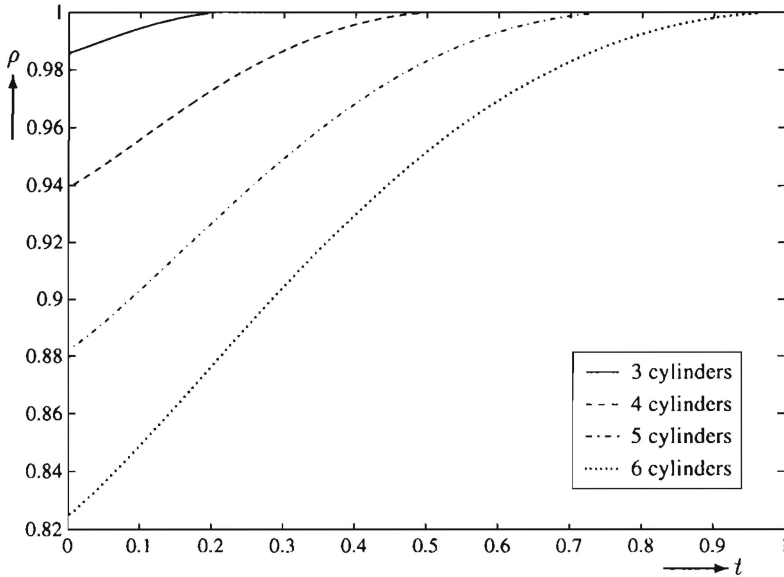


Figure 7.10 The shrinkage of the packings plotted in figure 7.8 is showing a linear behaviour for a large period of time.

to be shrinking at the same rate. Bearing in mind the uniform growth of the contact surface between all cylinders, this is something that we should have expected.

When we set the initial neck radii of the touching cylinders in the vertical direction equal to 0.3, the geometry of figure 7.12 is obtained. Because of this larger contact, the shrinkage is proceeding faster. As can be observed in the right plot of this figure, the holes deform into an ellipse-like curve. When we compare the movement of these holes with the movement in figure 7.11, it can be seen that they are situated almost at the same place in the end. This implies that the movement is going faster.

In figure 7.13 we have compared the densification rate of the packings 7.11 and 7.12 with some analytical shrinkage relations as presented in the previous section. We observe that the Scherer–Garino equation (7.4) gives the best prediction of the time when the densification is completed. The 2D MS-model does also show a good agreement with this point in time. However, when looking to the predicted densification at an intermediate time level, we see in the case that the initial neck radius between the cylinders in both directions is small (the packing 7.11), the models predict a density that is considerably larger than found by the numerical simulation. In particular Scherer’s equation (7.3) shows a large deviation. When the touching in one direction is large as compared to the other direction (the packing 7.12), a better agreement between the numerical solution and the analytical relations is obtained for the intermediate time period. We see moreover that in this case the three considered relations predict a nearly similar densification rate. Note that in the previous section, we have seen that in the case of an uniformly and equally sized cylindrical pore distribution, the model of Scherer gives the most accurate approximation of the densification rate and the Scherer–Garino

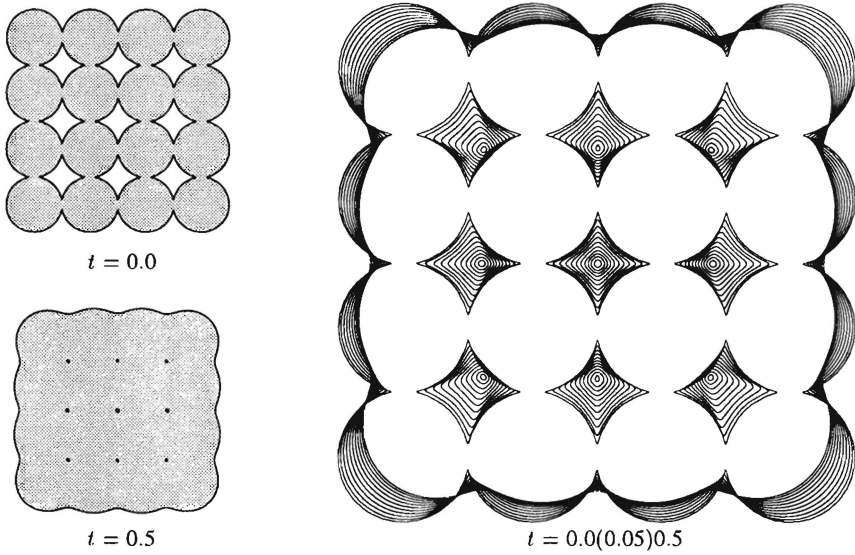


Figure 7.11 The sintering of a regular 4×4 array of cylinders with initially equal contact radii between all cylinders

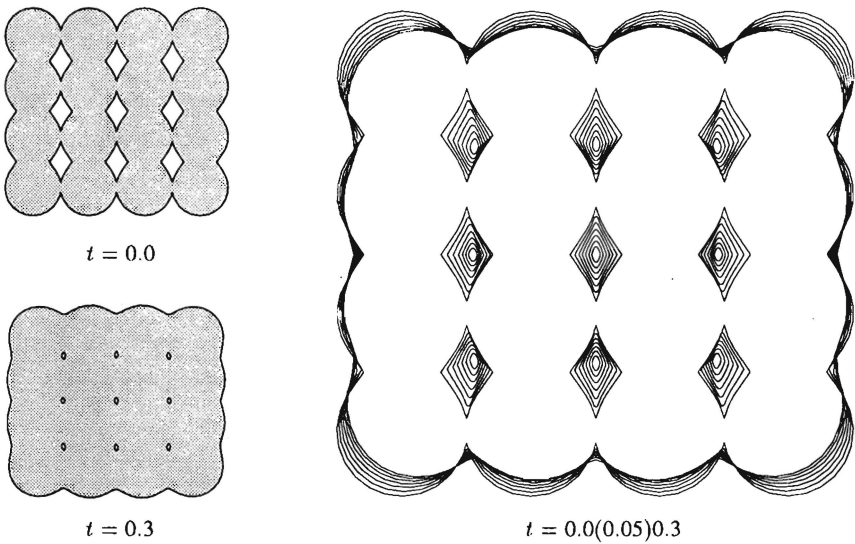


Figure 7.12 The sintering of a 4×4 array of cylinders. The initial contact radius between the cylinders in the vertical direction is set more than three times larger than in the horizontal direction

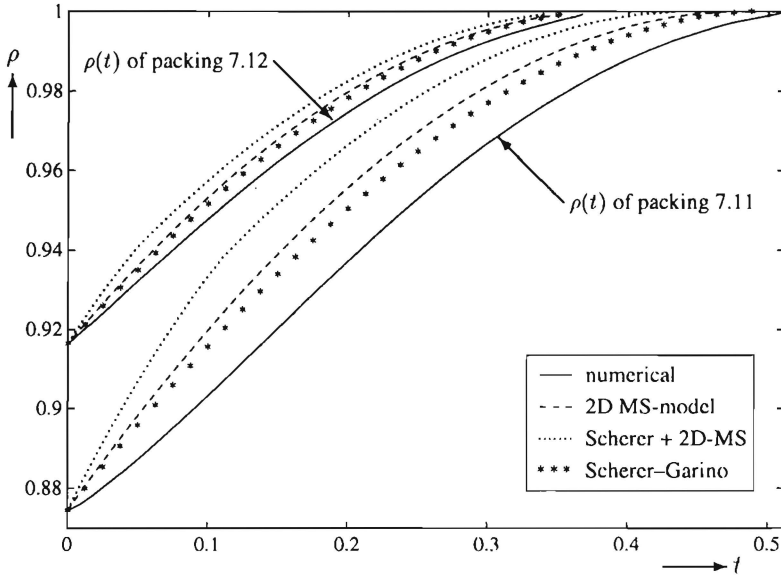


Figure 7.13 The shrinkage of both the packings on the previous page is compared to some of the analytical relationships. The Scherer–Garino equation gives the best prediction of the time when the densification is completed.

equation the worst. Here, we observe that the opposite holds. Apparently both the equations can be used to predict an upper- and lower bound for the densification kinetics of a uniform and equally sized pore distribution.

In practice, however, one does not deal with such a uniform sized pore distribution or a regular packed array of cylinders. Usually, the sintering compact is an irregular particle packing that consists of a variety of particle sizes with (often) a non-spherical (-cylindrical) form. Moreover another effect due to these irregularities has to be taken into account: the rearrangement of particles and the opening and closure of pores induced by this rearranging of particles.

The topic of the opening and closure of pores can be traced back to the asymmetry of such an irregular particle packing. In order to investigate asymmetric coalescence, Exner [22],[23] considered the behaviour of an array of three equally sized glass spheres by varying both the value of the angle between the centres of the spheres and the environment in which the sintering experiments took place. The experimental observations of these unit problems show that a small angle between the spherical centres leads to a large change of this angle during sintering; however, when the initial angle is large, it will not alter much during the coalescence anymore. Moreover, the angle development appears to be dependent on the atmosphere in which the sintering took place.

Here we consider the simulation of an array of three equally sized cylinders which are making an angle with each other; denote by α the angle between the straight lines through both the centre of the cylinder in the middle and the centres of the outer cylinders each. Hence α has a lower bound of 60° and an upper bound of 180° . The origin of such

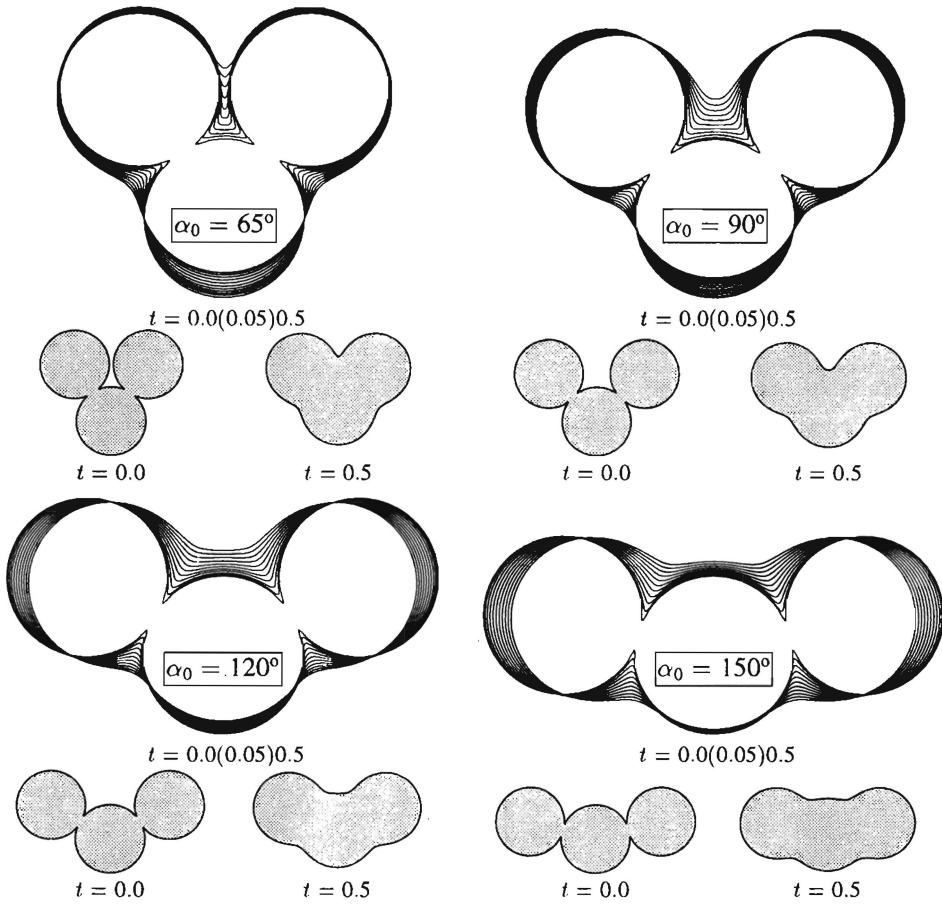


Figure 7.14 The deformation of three equal cylinders by varying the starting angle α_0 that these cylinders are making with each other.

a initial geometry is set in the centre of the mid-cylinder so that the y -axis symmetry can be employed. Both the cylindrical and the contact radii of those cylinders are chosen similar to the previously considered packings. Moreover, the initial neck regions are approximated using Hopper’s analytical solution for two equal cylinders.

In figure 7.14 we show the evolution of this three-cylinder problem at subsequent times $t = 0.0(0.05)0.5$ whereby we have taken as initial values for α , $\alpha_0 := 65^\circ, 90^\circ, 120^\circ$ and 150° respectively. Considering the shapes at time $t = 0.5$, it can be observed that when α is taken relatively small, the growth of the touching region is proceeding faster compared to the cases when α_0 is larger. This behaviour is responsible for the angle change between the three cylinders during the deformation. This change of angle between the three cylinders, say $\Delta\alpha = \alpha - \alpha_0$, is plotted in figure 7.15 for these four shape evolutions each. The figure shows that the angle α is increasing in all the four cases as time increases. Moreover, this angle is changing much when α_0 is taken small;

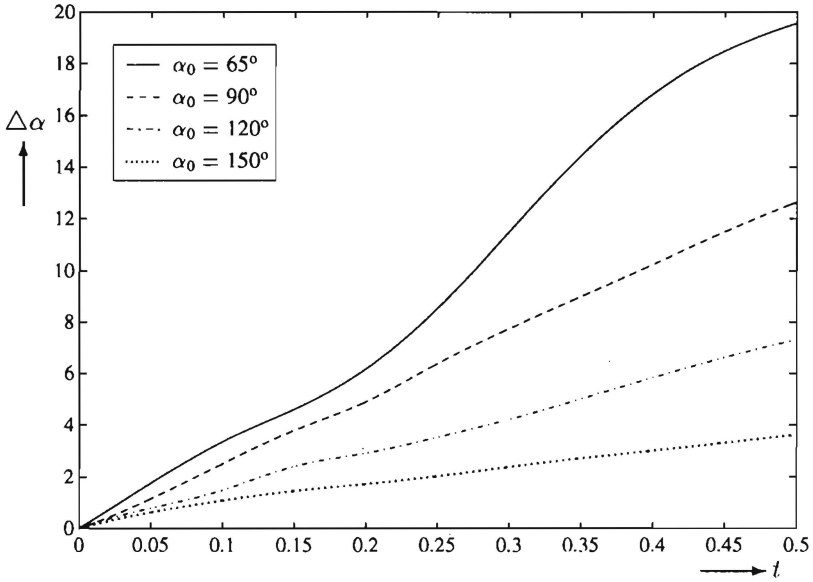


Figure 7.15 The dependence of the initial angle α_0 of the three-cylinder problem onto the change of angle $\Delta\alpha$ during the evolution.

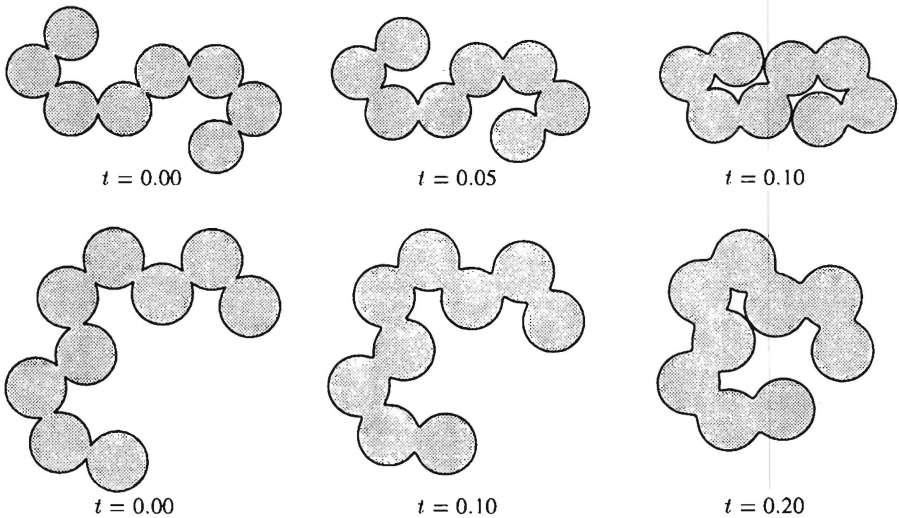


Figure 7.16 The deformation of two arbitrary chains of equal cylinders shows the non-consistency with the three-cylindrical simulations. These latter simulations predict a increase of the angle between three subsequent cylinders as can be observed from the figure above. Here, we show that this angle change is depending on the packing geometry.

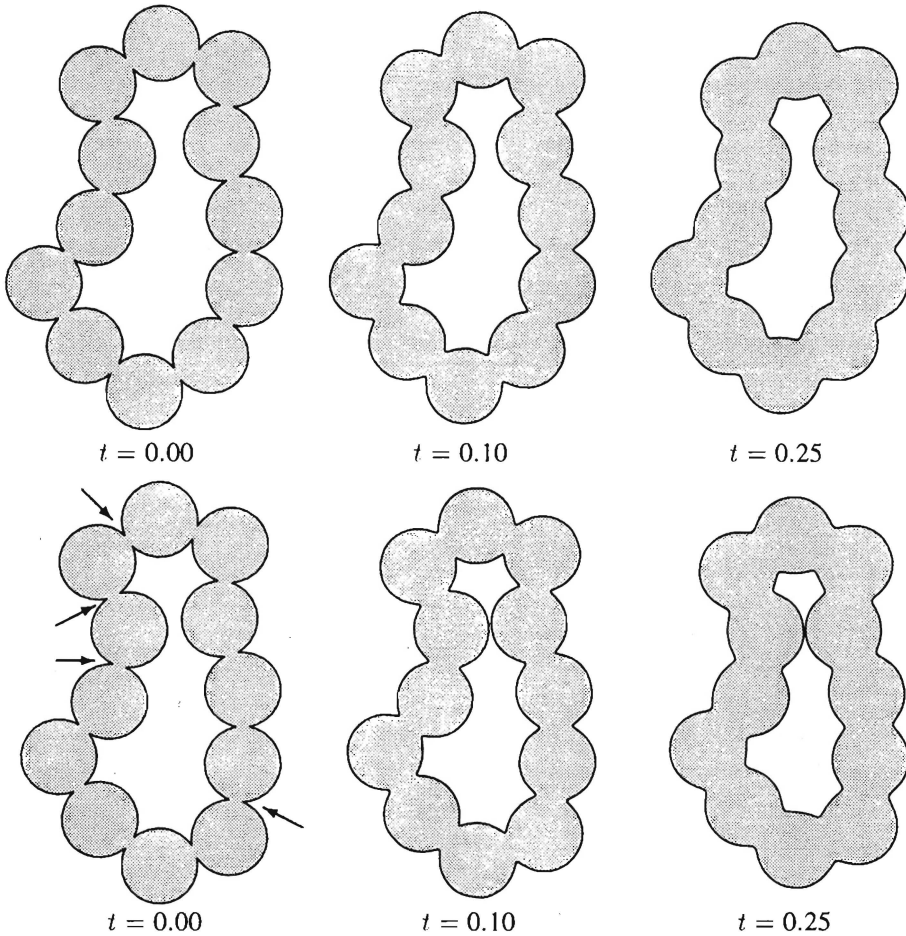


Figure 7.17 The coalescence of an arbitrary closed chain of equal cylinders demonstrates the sensitivity of such a particle chain for angle changes between three subsequent cylinders. The lower shape differs from the upper shape at four places marked by arrows.

there is not much difference for larger α_0 . Hence, the simulations provide a similar behaviour as Exner [23] observed experimentally in the case of the sintering of three glassy spheres. Note that these numerical experiments of the coalescence of three equal cylinders can be extended further by taking α_0 constant and either varying the initial contact radius or by using different initial neck regions at both sides of the coalescing cylinders. Moreover, the latter shapes may be constructed by either applying different neck curvatures on both sides of the contact line between two touching cylinders or by differing the touching rates for each cylinder which implies the lost of symmetry.

In Exner's monograph [23], a full chapter (5) is devoted to the study of such three particle models. Exner finishes that chapter by the suggestion to study the sintering of simple packings that contain more than three particles. Here we have numerically simulated the deformation of two arbitrary chains of equal coalescing cylinders to demonstrate

the difference of evolution when compared to the three cylindrical geometries above. All cylinders have a radius of 0.5 and the neck radii are taken equal to 0.095, thus similar as the considered three cylindrical geometries above. In figure 7.16 we have plotted the deformation of two chains of cylinders till the touching of two, not initially coalescing, cylinders occurs. From this figure we observe a non-consistency with the three cylindrical simulations, since the latter simulations predict an increment of the angle between three subsequent cylinders (figure 7.15). The shape evolutions of figure 7.16 demonstrate that this angle may decrease also: the angle change is depending on the packing geometry.

A geometry that Exner considers is the rounding of a closed chain of copper spheres during sintering. We have numerically simulated the deformation of such a closed chain, where the copper spheres are glassy cylinders actually. Again, all cylinder radii and coalescence rates are initially taken similar as in the examples above. In figure 7.17 we have plotted the deformation of two initially different chains of equal cylinders at three subsequent times. The initial chain of the upper sequence is approximately equal to Exner's closed chain of copper spheres; the initial chain of the lower sequence is obtained by changing the angle between three subsequent cylinders at four places. These particular places are marked by arrows.

The upper sequence shows that the inner boundary is closing up somewhat faster. The shortest distance between two opposite cylinders will not become prohibitively small, i.e. parts of the hole boundary do not touch one another somewhere. In contrast to the lower sequence, we observe the touching between two opposite cylinders at $t = 0.25$. Both simulations of figure 7.17 illustrate the sensitivity of such a particle packing in relation to the orientation of the initial geometry, i.e. the influence of a change of angle between the coalescing cylinders.

7.3 A FEW MESOCELL DENSIFICATION SIMULATIONS

In this section we apply the numerical code to simulate the densification of two more realistic geometries from a physical point of view. First, we consider the shrinkage of an aerogel which is produced in a base-catalysed way. Secondly, we simulate the coalescence of a bundle of glass fibres with various diameters till boundaries are touching.

Craievich *et al.* [19] studied the structure of aerogels which are produced by hypercritical drying of a sol-gel for various pH conditions. They use X-rays small-angle scattering to investigate the structure of the aerogels formed this way. From the scattering data, a model of the texture of these aerogels is obtained. It appears that these type of aerogels can be modelled as a sponge. A characteristic of the matrix material, i.e. the skeletal material, is that it contains closed micropores; the material itself contains meso- and macro-pores. In figure 7.18a the visualization of such a sponge is shown; in this particular case it models the texture of a base-catalysed aerogel (cf. Craievich *et al.* [19]). In this particular case the skeletal density is almost equal to the density

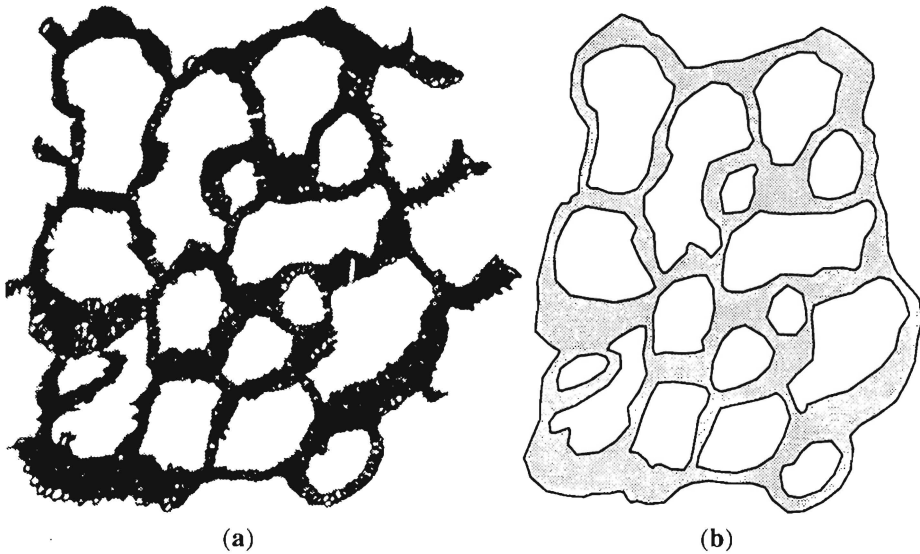


Figure 7.18 In (a) is plotted a model of an aerogel which is formed in a base-catalysed way (after Craievich *et al.* [19]). The approximation of this model that is used to simulated the densification of the aerogel is shown in (b).

of the solid phase (silica). This is in contrast to an aerogel that is formed in neutral or acid conditions: then the skeletal material contains many micropores so that the skeletal density is much lower as compared to both solid silica and a base-catalysed aerogel.

In figure 7.18b we have plotted the approximation of the texture of this particular aerogel. This geometry is used to simulate the densification of this gel. As can be seen, we have skipped all micropores. This approach is justified since during the first stage of the sintering process, the micropores are eliminated by polycondensation reactions (cf. Craievich *et al.* [19]). Because of these reactions, this stage is dominated by diffusion which results in an increase of the skeletal density. Thereafter, the meso- and macropores are eliminated by coalescence and densification through a viscous flow. From our initial geometry we have also removed all protrusions, as can be observed in the texture model. This is only done to avoid the occurrence of an early touching between two boundaries, since we cannot handle this problem yet.

The initial geometry is obtained by using a graphics tablet (Tektronix 4957) from which the input coordinates are manual digitized. These (dimensionless) coordinates are approximately ranging between (0.60,0.12) and (3.05,3.19). Furthermore, during the numerical simulation the number of collocation points is taken approximately 650. We assume that the influence of the outer boundary on the densification process, as we discussed in section 7.1, is small. This is justified since the skeletal structure along the outer boundary is the same nearly everywhere. The calculations are performed on a SiliconGraphics Power Challenge.

In figure 7.19 we show the deformation of this aerogel for increasing time. If we

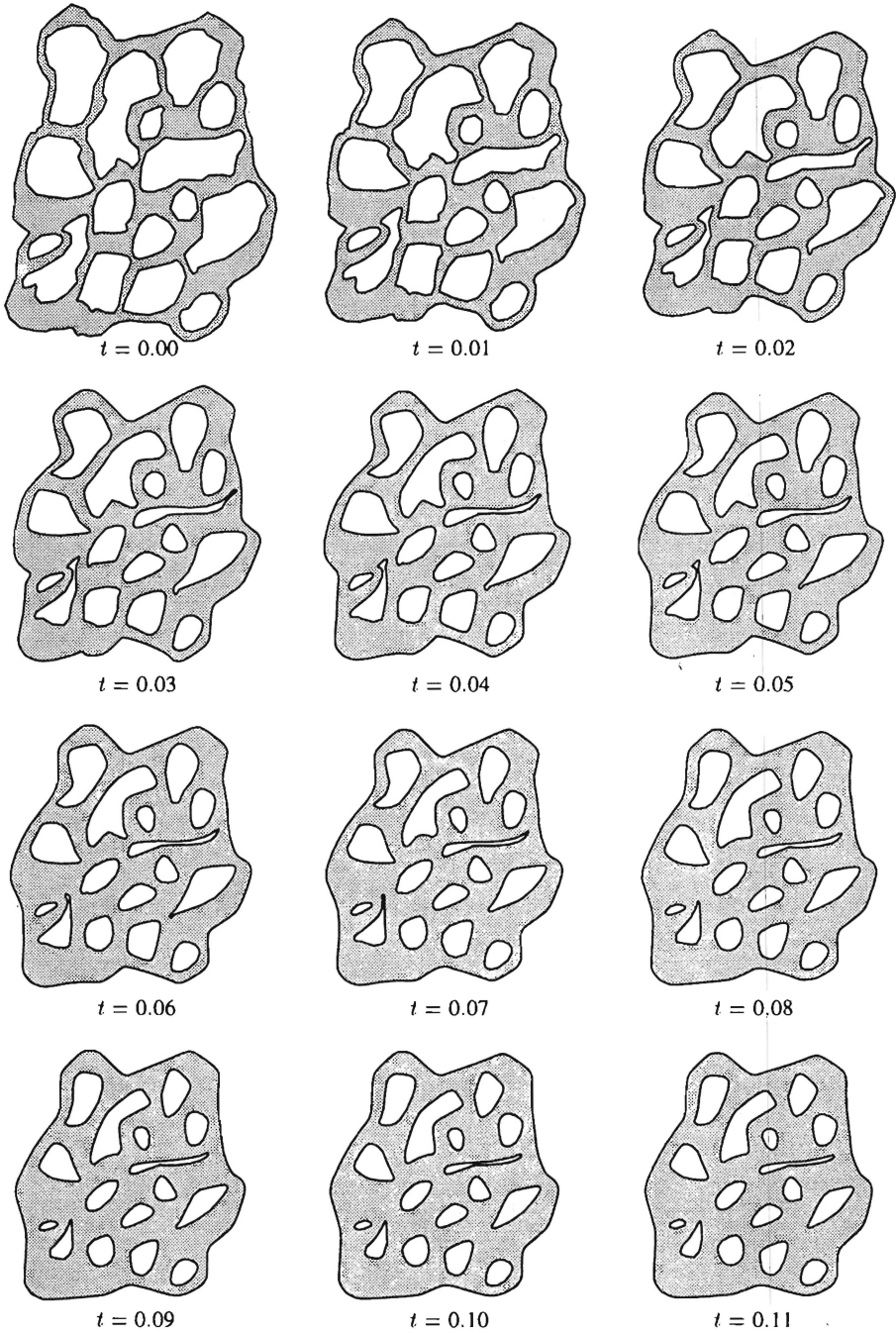


Figure 7.19 The densification of the aerogel at subsequent times. It can be seen that the macro-pores are shrinking faster compared to the meso-pores.

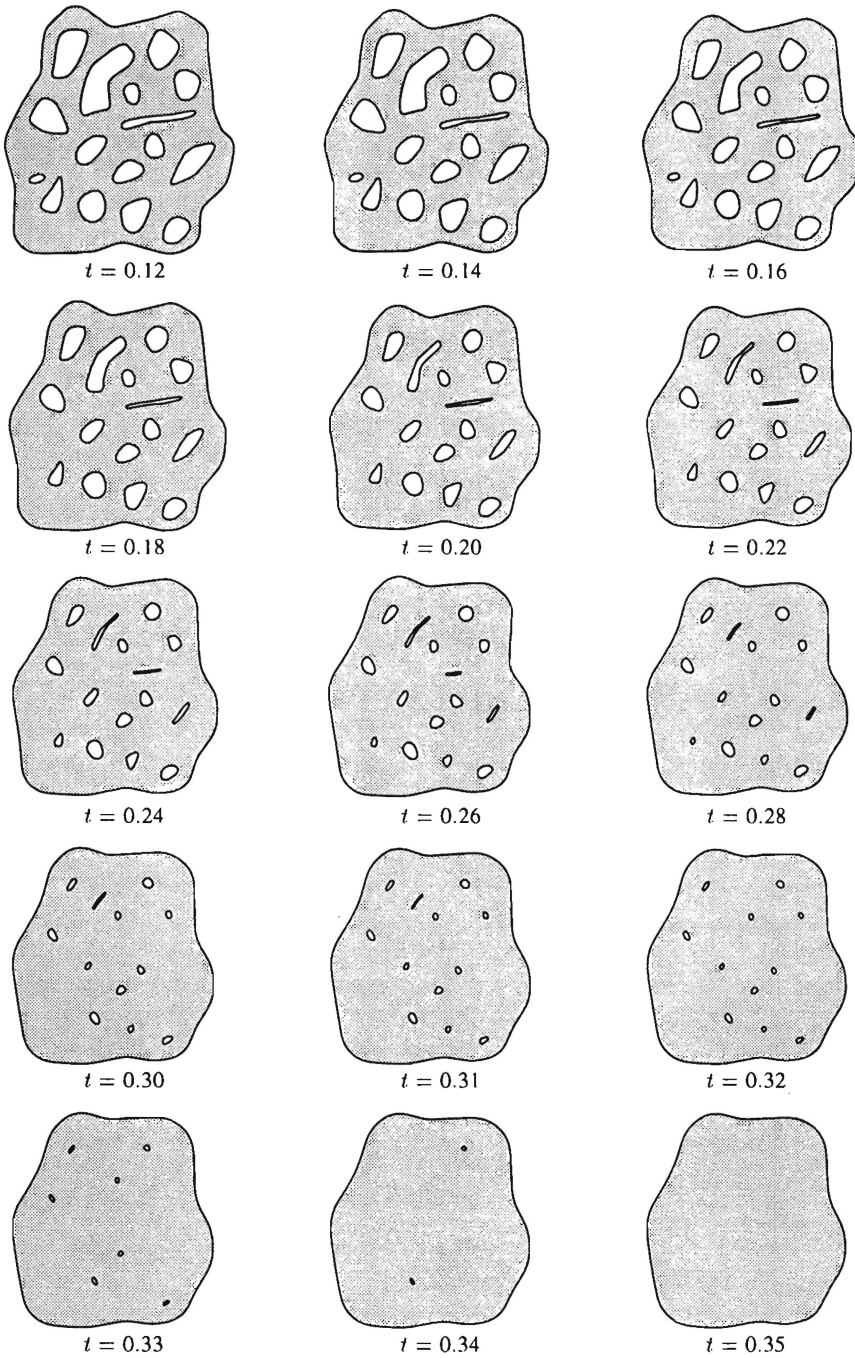


Figure 7.19 (continued) The thin elongated pores that are formed during the coalescence appear to vanish very slowly.

compare the initial geometry to the shapes obtained at later time stages, we observe that the influence of the outer boundary on the coalescence is limited to the upper left corner of the gel geometry. Furthermore, we see that the skeletal material matrix is becoming stronger as time proceeds: the amount of fluid around each pore is increasing. This means that even initially very narrow fluid channels between two neighbouring pores will become wider so that the distance between these pores is increasing. This observation implies that two pores would not coalesce to one bigger pore, i.e. such a fluid channel does not become narrower and vanishes finally.

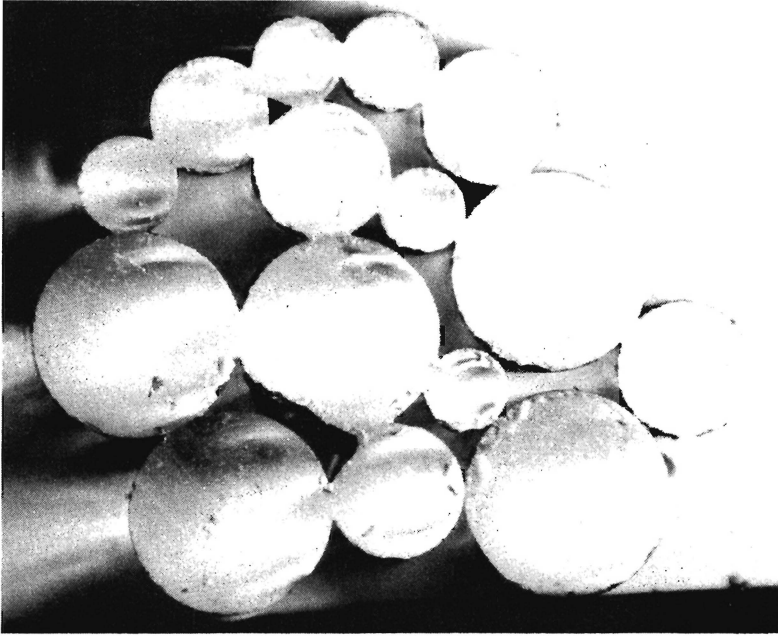
Again, it can be seen from the figure that the macro-pores are shrinking faster as compared to the meso-pores. Moreover, some of these macro-pores, especially pores with an approximately rectangular form, are deforming to thin elongated pores which do not vanish easily. This phenomenon was also observed in the simulations plotted in figure 7.7. An explanation for this effect is the following. Along the elongated sides of such a pore, the boundary is nearly a straight line, so that the curvature along these sides is approximately equal to zero. Hence the shrinkage of such a pore is driven by the small curved regions on both ends of the pore solely. This observation suggests to avoid the forming of rectangular shaped pores in the production of the aerogel as much as possible.

The second geometry we consider is the coalescence of an arbitrary bundle glass fibres with diameters ranging between 45 and 100 μm . The purpose of this particular investigation will be the comparison between both the experimentally and the numerically obtained densified shapes at various time stages. Moreover, such experiments should give some clues how to deal with touching of boundaries during the simulation of the coalescence process. More precise details will be reported in the near future.

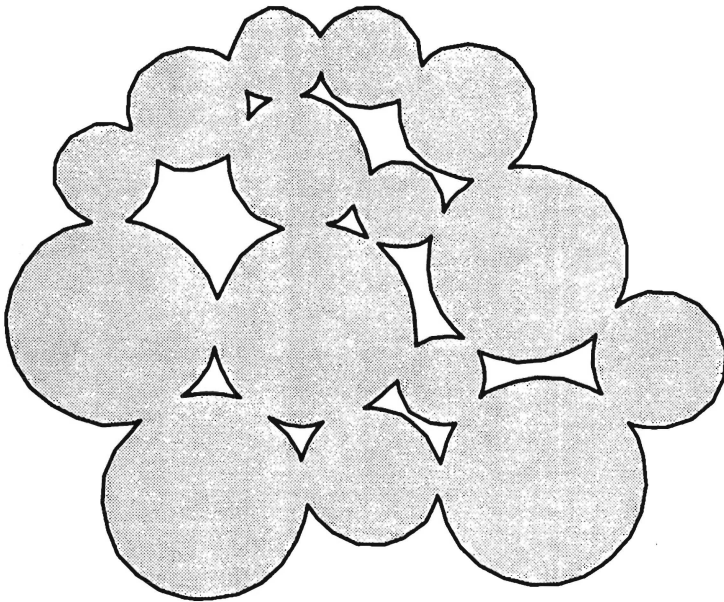
Here we start with a brief description of the way such a fibre bundle is obtained. All the fibres were drawn from a portion cut from the same batch of modified Na-K-Ba-Sr-silica glass (cf. De With and Corbijn [113]). A bundle of fibres is obtained by pre-baking. Fibres of various diameters are used since with such a set of fibres it is easier to form an irregular fibre bundle (compared to a bundle obtained from fibres with equal diameters). The pre-baking is carried out by heating up to 650° C, holding for several minutes, then cooling down to 515° C, followed by an annealing procedure to remove the residual thermal stresses (cf. De With and Corbijn [113]). The obtained pre-baked bundle is swan in a number of equally sized parts. In figure 7.20a the photograph is shown of the cross-section of a part of a bundle produced this way. These parts are sintered in an oven on a graphite substrate with a semi-cylindrical groove for various periods of time. It is assumed that the influence of gravity can be neglected due to the small size of the bundle.

The digitized shape that is used to simulate the coalescence of this bundle is plotted in figure 7.20b too. During the numerical calculations, the number of points is roughly varying around 500. The computed shape deformation at increasing time is shown in figure 7.21. The arrow in the picture at $t = 0.015$ indicates the place of a touching between two boundaries which results in a stop of the calculations since this problem cannot be handled yet.

In figure 7.22 the shape at $t = 0.006$ is compared with the experimentally obtained



(a) Bundle after pre-baking



(b) The initial numerical geometry

Figure 7.20 A cross-section of an arbitrary bundle of glass fibres after pre-baking (a) and the geometry used for the numerical simulation (b).

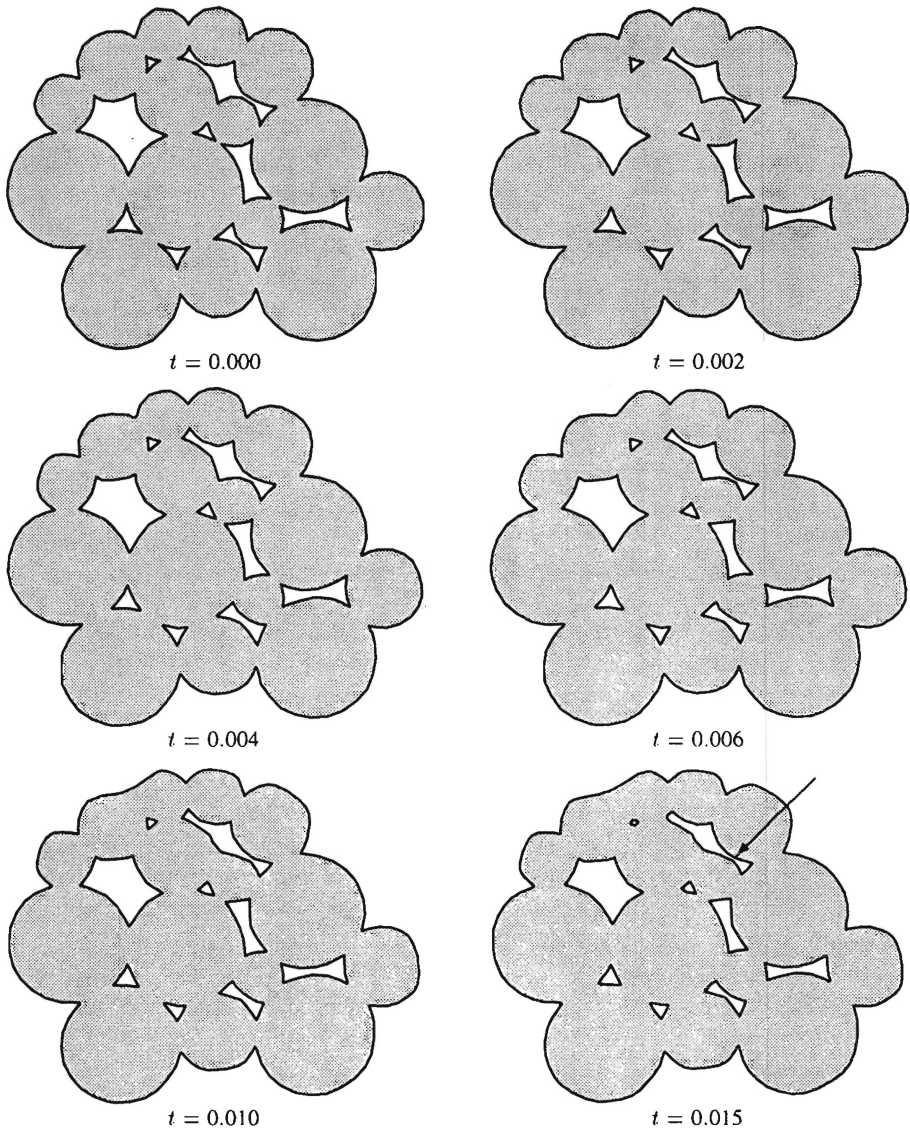
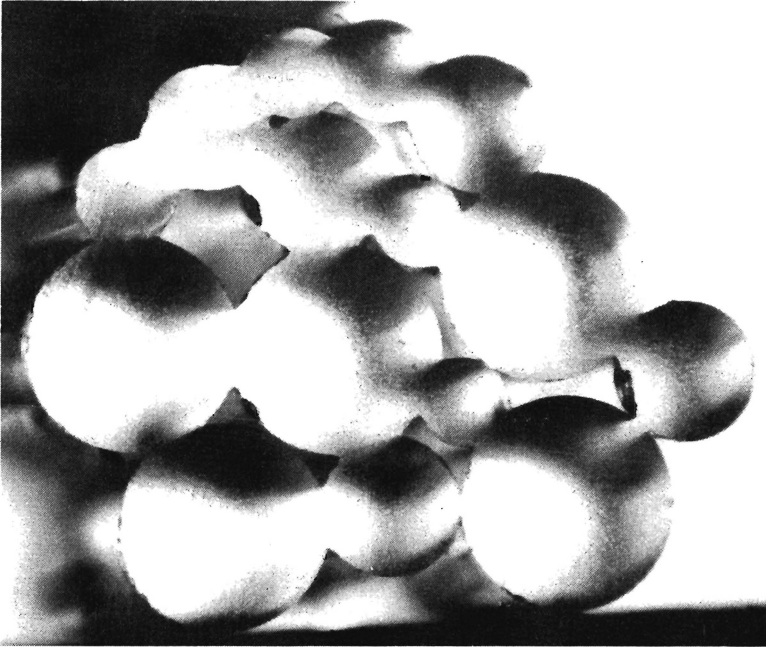
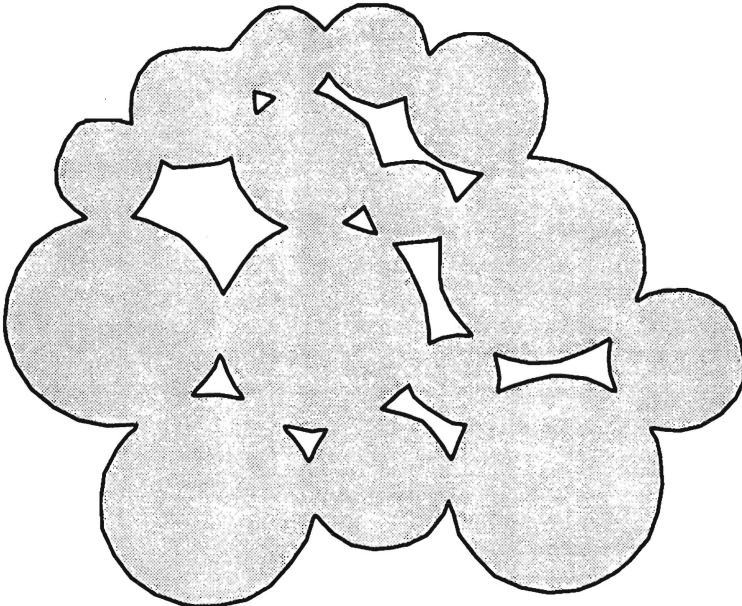


Figure 7.21 The computed coalescence of the fibre bundle at subsequent times.

cross-section of the fibre bundle after being sintered for a certain period of time. As can be observed from this figure, some of the neck regions and contact radii differ. The numerically obtained neck regions are curved sharper compared to the neck regions found experimentally. There are a number of reasons that may be responsible for these differences which should be investigated further. From a numerical point of view we mention the error in both the neck curvature and the contact radius of the initial digitized shape which might influence the computations. Therefore, it may be better to use the



(a) Bundle after sintering



(b) The calculated geometry at $t = 0.006$

Figure 7.22 The comparison between the experimentally and numerically obtained shapes shows that a number of the calculated neck regions are curved more sharply.

exact analytical solutions for obtaining the boundary of the neck regions. Another possibility is that this is a resolution problem, i.e. we should use a spline approximation for the shape. From an experimental point of view we mention the temperature sensitivity of the viscosity and the effect of the atmosphere on the surface tension (De With and Corbijn [113]). A more important problem is that the fibres of the bundle might not lie exactly parallel to each other after the pre-baking or that the rate of contact between the fibres differs in the parallel direction.

7.4 CONCLUSION

The examples we show in the previous sections illustrate that with the method presented, we are able to simulate all kinds of two-dimensional multiply connected domains. The main limitation in these simulations are formed by the computer resources; also we cannot yet deal with cases where boundaries touch during a simulation.

The comparison between analytic expressions that predict the densification rate of a certain sintering domain and the numerical results, demonstrate the applicability of these expressions for domains with both uniform sized and distributed pores. However, in the case of non-uniform pores, these models fail. This is due to the fast shrinkage of the largest pores within such a domain. The coalescence of regular and equal sized cylindrical packings can be described by the unit model of two equal cylinders. In the case of an irregular cylindrical packing the coalescence process is influenced by rearrangement of the cylinders.

It is obvious, that some experimental verification has to be performed to justify the model presented. Starting in two-dimensions, such experiments should be utilized by considering the sintering of a packing of well-controlled glass fibres that will be compared with the numerical simulation of that particular packing. A first attempt of such an experiment is discussed which shows a reasonable agreement between the experimental and numerical results. Again, the most important limitation seems to be the touching of boundaries during the simulations. Another justification of our numerical approach is provided by the experiments of Korwin *et al.* [57]-[58] and De With and Corbijn [113]. Korwin *et al.* performed experiments in which they considered the coalescence of two equal sized glass fibres. De With and Corbijn investigated the coalescence of a fibre on a glassy plate. The experimental results were compared with Hopper's analytical solutions which showed a good to excellent agreement.

THE SINTERING OF AXISYMMETRIC SHAPES

The numerical solution method we have presented in the previous chapters is extended to axisymmetric domains, i.e. domains formed by rotating a two-dimensional plane about a given axis. Because of this axial symmetry, a three-dimensional sintering problem can be reduced to a two-dimensional one since the motion is unknown in the axial and radial direction only. Hence the developed node redistribution algorithm and the time integration method apply for these problems too. In this chapter we briefly outline the derivation of the governing integral formulation used to simulate axial symmetric domains without inside holes in the fluid. Moreover, we discuss some numerical aspects of the solution of this integral equation by the BEM-BDF method as described earlier. Finally, these algorithms are applied to simulate some typical axial symmetric sintering geometries.

8.1 AXISYMMETRIC INTEGRAL FORMULATION

There are two approaches for deriving the governing integral formulation for axisymmetric problems based on hydrodynamic potentials of single- and double layers. Both methods are leading to the same equation. The first one is to obtain the integral equation by using the axisymmetric fundamental solution based on ring forces, cf. Brebbia *et al.* [8]. The second approach is to apply the fundamental solution derived from a point force so that a Cartesian version of the three-dimensional integral equation is obtained. Subsequently cylindrical coordinates are then substituted in this formulation. Here we will briefly summarize the latter method. More precise details of this derivation can be found for example in Lee and Leal [67], or in Becker [7] where this problem is considered as a special case of an elastostatic problem.

Let us denote a fluid region by Ω and its “smooth” surface by $\partial\Omega$. The derivation of the SDLP-formulation in the case of a three-dimensional Cartesian coordinate system is similar to the outline of section 2.2; in this specific case we obtain for a point \mathbf{x} of the

fluid,

$$c_{ij}v_j(\mathbf{x}) + \int_{\partial\Omega} q_{ij}(\mathbf{x}, \mathbf{y})v_j d\partial\Omega_y = \int_{\partial\Omega} u_{ij}(\mathbf{x}, \mathbf{y})b_j d\partial\Omega_y, \quad (8.1)$$

where i and j are varying between 1 and 3. Here the surface tension b_j is given by equation (2.11), i.e. $b_j = -\kappa n_j$; and the coefficients c_{ij} , q_{ij} and u_{ij} are equal to respectively:

$$c_{ij} = \begin{cases} \delta_{ij} & \mathbf{x} \in \Omega \\ \frac{1}{2}\delta_{ij} & \mathbf{x} \in \partial\Omega, \end{cases} \quad q_{ij}(\mathbf{x}, \mathbf{y}) = \frac{3(x_i - y_i)(x_j - y_j)(x_k - y_k)n_k}{4\pi|\mathbf{x} - \mathbf{y}|^5},$$

$$u_{ij}(\mathbf{x}, \mathbf{y}) = \frac{1}{8\pi} \left[\frac{\delta_{ij}}{|\mathbf{x} - \mathbf{y}|} + \frac{(x_i - y_i)(x_j - y_j)}{|\mathbf{x} - \mathbf{y}|^3} \right].$$

In order to obtain the integral equation for the axisymmetric case, we reformulate the representation above by employing cylindrical coordinates (r, θ, z) , i.e.

$$\mathbf{y} = (y_1, y_2, y_3)^T = (r \cos \theta, r \sin \theta, z)^T.$$

Because of the rotational symmetry, we only have to determine v_r and v_z ($v_\theta = 0$) at the intersection of the surface $\partial\Omega$ and (say) the half-space $\theta = 0$. This intersection curve will be denoted by Γ ; let therefore $\mathbf{x} = (R, 0, Z)^T \in \Gamma$. After successive substitution of cylindrical coordinates and integration along the θ -direction of equation (8.1) we obtain

$$c_{\alpha\beta}v_\beta^c + \int_\Gamma q_{\alpha\beta}^c v_\beta^c d\Gamma = \int_\Gamma u_{\alpha\beta}^c b_\beta^c d\Gamma, \quad (8.2)$$

where the superscript c stands for cylindrical and α, β are either 1 or 2; hence $\mathbf{v}^c = (v_1^c, v_2^c)^T = (v_r, v_z)^T$, etc. Moreover, the coefficients $q_{\alpha\beta}^c$ and $u_{\alpha\beta}^c$ depend on complete elliptic integrals of the first and second kind. After some analytical manipulation, the kernels on the right hand side of the integral equation above can be rewritten as

$$u_{\alpha\beta}^c = \frac{1}{8\pi} \int_0^{2\pi} \frac{A_{\alpha\beta}^0 + A_{\alpha\beta}^1 \cos \theta + A_{\alpha\beta}^2 \cos^2 \theta}{(a - b \cos \theta)^{\frac{3}{2}}} d\theta$$

$$= \frac{1}{2\pi\sqrt{a+b}} \left[\frac{E(k)}{a-b} \left(A_{\alpha\beta}^0 + \frac{a}{b} A_{\alpha\beta}^1 + \frac{2a^2 - b^2}{b^2} A_{\alpha\beta}^2 \right) - \frac{K(k)}{b} \left(A_{\alpha\beta}^1 + \frac{2a}{b} A_{\alpha\beta}^2 \right) \right]$$

where

$$a = r^2 + R^2 + c^2, \quad b = 2rR, \quad c = Z - z, \quad k = \sqrt{\frac{2b}{a+b}},$$

and the coefficients $A_{\alpha\beta}^n$ are given by

$$A_{\alpha\beta}^0 = -\frac{1}{2}\delta_{1\alpha}\delta_{1\beta}b + \delta_{1\alpha}\delta_{2\beta}cR - \delta_{2\alpha}\delta_{1\beta}cR + (a + c^2)\delta_{2\alpha}\delta_{2\beta},$$

$$A_{\alpha\beta}^1 = (2a - c^2)\delta_{1\alpha}\delta_{1\beta} - \delta_{1\alpha}\delta_{2\beta}cR + \delta_{2\alpha}\delta_{1\beta}cR - \delta_{2\alpha}\delta_{2\beta}b,$$

$$A_{\alpha\beta}^2 = -\frac{3}{2}\delta_{1\alpha}\delta_{1\beta}b.$$

Here $K(k)$, $E(k)$ are the complete elliptic integrals of the first and second kind respectively, defined by (recalling equation (3.7))

$$K(k) = \int_0^{\frac{\pi}{2}} \frac{d\varphi}{\sqrt{1 - k^2 \sin^2 \varphi}}, \quad E(k) = \int_0^{\frac{\pi}{2}} \sqrt{1 - k^2 \sin^2 \varphi} d\varphi.$$

The kernels on the left hand side of equation (8.2) are represented by

$$\begin{aligned} q_{\alpha\beta}^c &= \frac{3}{4\pi} \int_0^{2\pi} \frac{B_{\alpha\beta}^0 + B_{\alpha\beta}^1 \cos \theta + B_{\alpha\beta}^2 \cos^2 \theta + B_{\alpha\beta}^3 \cos^3 \theta}{(a - b \cos \theta)^{\frac{5}{2}}} d\theta \\ &= \frac{1}{\pi(a^2 - b^2)\sqrt{a+b}} \left[K(k) \left(-B_{\alpha\beta}^0 - \frac{a}{b} B_{\alpha\beta}^1 + \frac{2a^2 - 3b^2}{b^2} B_{\alpha\beta}^2 \right. \right. \\ &\quad \left. \left. + \frac{a(8a^2 - 9b^2)}{b^3} B_{\alpha\beta}^3 \right) + \frac{E(k)}{a-b} \left(4aB_{\alpha\beta}^0 + \frac{a^2 + 3b^2}{b} B_{\alpha\beta}^1 \right. \right. \\ &\quad \left. \left. + \frac{2a(3b^2 - a^2)}{b^2} B_{\alpha\beta}^2 - \frac{8a^4 - 15a^2b^2 + 3b^4}{b^3} B_{\alpha\beta}^3 \right) \right], \end{aligned}$$

where the coefficients $B_{\alpha\beta}^n$ are equal to

$$\begin{aligned} B_{\alpha\beta}^0 &= -\frac{1}{2} \delta_{1\alpha} \delta_{1\beta} db + \delta_{1\alpha} \delta_{2\beta} Rdc - \delta_{2\alpha} \delta_{1\beta} rdc + \delta_{2\alpha} \delta_{2\beta} dc^2, \\ B_{\alpha\beta}^1 &= (de + B_{11}^3) \delta_{1\alpha} \delta_{1\beta} + (R^2 n_r - rd) \delta_{1\alpha} \delta_{2\beta} c + (d - rn_r) \delta_{2\alpha} \delta_{1\beta} Rc + \delta_{2\alpha} \delta_{2\beta} Rc^2 n_r, \\ B_{\alpha\beta}^2 &= (en_r - rd) \delta_{1\alpha} \delta_{1\beta} R - \frac{1}{2} \delta_{1\alpha} \delta_{2\beta} bcn_r + \delta_{2\alpha} \delta_{1\beta} R^2 cn_r, \\ B_{\alpha\beta}^3 &= -\frac{1}{2} \delta_{1\alpha} \delta_{1\beta} bRn_r, \end{aligned}$$

and $d = -rn_r + cn_z$, $e = R^2 + r^2$. We remark that if the point \mathbf{x} is lying at the z -axis, i.e. $R = 0$, the integrals become very simple since then $b = 0$ too, we obtain

$$\begin{aligned} u_{\alpha\beta}^c &= \frac{1}{8\pi a^{\frac{1}{2}}} \int_0^{2\pi} A_{\alpha\beta}^0 + A_{\alpha\beta}^1 \cos \theta + A_{\alpha\beta}^2 \cos^2 \theta d\theta = \frac{1}{8a^{\frac{1}{2}}} [2A_{\alpha\beta}^0 + A_{\alpha\beta}^2], \\ q_{\alpha\beta}^c &= \frac{3}{4\pi a^{\frac{1}{2}}} \int_0^{2\pi} B_{\alpha\beta}^0 + B_{\alpha\beta}^1 \cos \theta + B_{\alpha\beta}^2 \cos^2 \theta + B_{\alpha\beta}^3 \cos^3 \theta d\theta = \frac{3}{\pi a^{\frac{1}{2}}} [2B_{\alpha\beta}^0 + B_{\alpha\beta}^2]. \end{aligned} \quad (8.3)$$

The integral representation (8.2) possesses one degree of freedom only: a translation in the z -direction, say $\varphi^c = (0, 1)^T$. Again, there are two methods to make this integral formulation uniquely solvable for a fixed domain. One is to perform this by adding one additional variable representing this translation freedom and requiring the fluid to be stationary at a point of the z -axis, i.e. include one extra integral constraint. The other method is to "deflate" the double layer integral operator with respect to this freedom as

was also used in the two-dimensional case. We prefer the latter approach since then no additional variable is required. After deflating equation (8.2) we obtain

$$c_{\alpha\beta}v_{\beta}^c(\mathbf{x}^c) + \int_{\Gamma} q_{\alpha\beta}^c v_{\beta}^c d\Gamma + \varphi_{\alpha}^c(\mathbf{x}^c) \int_{\Gamma} \varphi_{\beta}^c v_{\beta}^c r d\Gamma = \int_{\Gamma} u_{\alpha\beta}^c b_{\beta}^c d\Gamma. \quad (8.4)$$

This integral representation is used in the remainder of this chapter.

8.2 NUMERICAL SOLUTION

The numerical implementation of the axisymmetric integral equation (8.4) is very similar to the two-dimensional case, cf. section 4.2; we actually have two unknowns v_r, v_z on a boundary curve. Because of this, the mesh redistribution, which is shown to be a very important item during the simulation of a particular shape, can be performed by applying the algorithms developed for the two-dimensional case, cf. section 4.4. However, the time integration has to be modified slightly, and of course, the assembling of the system of equations as well. Therefore, we will highlight some details of this numerical solution in this subsection.

The application of the BEM to equation (8.4) is performed by substituting linear or quadratic element-wise truncated polynomial approximations for the boundary curve, velocity and surface tension respectively, into the discretized form of (8.4). Varying the point \mathbf{x}^c in this formulation over all the collocation points, results in the following square full rank system of linear algebraic equations, that is denoted by

$$\mathcal{H}(\mathbf{x}^c) \mathbf{v}^c = \mathcal{G}(\mathbf{x}^c) \mathbf{b}^c(\mathbf{x}^c). \quad (8.5)$$

Here \mathbf{v}^c , \mathbf{b}^c and \mathbf{x}^c are vectors that consist of the velocity, surface tension and nodal boundary coordinates respectively of all successive collocation points in the r - and z -direction. \mathcal{H} and \mathcal{G} denote the matrices obtained by element-wise integration of equation (8.4). The elliptic integrals that occur in the coefficients can be approximated by using either standard routines or a series representation. When the element integrals become singular, there are basically two approaches for computing them.

The first, quite commonly used method, is to express the elliptic integrals by a series expansion in terms of a logarithmic singularity, cf. Byrd and Friedman [13]. After substituting those expansions into the singular integrals, these integrals become of the same type as they occur in the two-dimensional case; so they are approximated by applying a logarithmic Gaussian quadrature formula.

The second approach is to apply the so-called Telles' transformation [101]. The goal of this method is to cancel the singularity by employing a transformation such that the Jacobian of this particular transformation is equal to zero at the singular point. In the case of linear elements a quadrature polynomial transformation can be constructed and in the case of quadratic elements a polynomial of degree three is used. Thereafter, the transformed integral can be computed using an ordinary Gaussian quadrature formula. Another interesting property of this transformation is that many of the Gauss points are distributed near the singularity. Here, we have chosen for the latter method.

When the point \mathbf{x}^c is a point on the z -axis ($R = 0$) the elliptic integrals that occur in the coefficients disappear: the integrals become very simple as is shown by equation (8.3). In the case of linear elements, it is even possible to compute the latter element integrals analytically when they become singular.

Another feature in which the axisymmetric implementation differs from the two-dimensional case is that the coefficient matrix $c_{\alpha\beta}$ cannot be computed using rigid-body motions in the radial direction. Again there are two approaches to obtain the (2×2) diagonal matrices of the system of equations. The first method is to apply analytical expressions for the coefficients $c_{\alpha\beta}$, cf. Brebbia and Dominguez [9]. The second approach, which is applied here and that is extensively outlined in Becker [7], consists of two parts: the first step is using rigid-body motions in the z -direction so that the diagonal matrix coefficients that apply in this particular direction are obtained, i.e.

$$\mathcal{H}_{\alpha z} = - \sum_{\substack{\beta=1 \\ \beta \neq \alpha}}^N \mathcal{H}_{\beta z}$$

The second step, the computation of the remaining diagonal coefficients which apply in the r -direction, is performed by employing a plane stress condition from which the velocity and tension can be computed that is valid for any arbitrary shaped region. In this particular case, we use the following solution

$$\begin{cases} \dot{\mathbf{v}}^c = (\dot{v}_r, \dot{v}_z)^T = (\frac{1}{6}\dot{r}, -\frac{1}{3}\dot{z})^T \\ \dot{\mathbf{b}}^c = (\dot{b}_r, \dot{b}_z)^T = (n_r, 0)^T, \end{cases}$$

and the remaining unknown diagonal elements follow from

$$\mathcal{H}_{\alpha r} \dot{v}_r = -\mathcal{H}_{\alpha z} \dot{v}_z - \sum_{\substack{\beta=1 \\ \beta \neq \alpha}}^N (\mathcal{H}_{\beta r} \dot{v}_r + \mathcal{H}_{\beta z} \dot{v}_z) + \sum_{\beta=1}^N (\mathcal{G}_{\beta r} \dot{b}_r + \mathcal{H}_{\beta z} \dot{b}_z).$$

Hence we obtain

$$\mathcal{H}_{\alpha r} = \frac{1}{r} \left[2\mathcal{H}_{\alpha z} z - \sum_{\substack{\beta=1 \\ \beta \neq \alpha}}^N (\mathcal{H}_{\beta r} r - 2\mathcal{H}_{\beta z} z) + 6 \sum_{\beta=1}^N \mathcal{G}_{\beta r} n_r \right].$$

Remark that the equation above does not apply when the point is situated on the z -axis since r then becomes zero. However, this is not that bad since the radial velocity on this axis has to be zero, so we can leave the corresponding rows and columns out of the algebraic system of equations.

The next point of concern is the computation of the surface tension vector \mathbf{b}^c , i.e. the calculation of the principal surface curvature and the outer normal. Like in the two-dimensional case, a local method is used to determine the principal curvature at the discretization points on the boundary surface Γ . For example in the linear case, this curvature at a particular collocation point is approximated by fitting a quadratic polynomial through that particular point and its neighbours; say the parametric form

$(r(s), z(s))^T$ applies with $-1 \leq s \leq 1$. Then for the approximate principal curvature at this specific point ($s = 0$) on the curve Γ we obtain

$$\kappa_m = \frac{r'z'' - r''z'}{((r')^2 + (z')^2)^{\frac{3}{2}}} + \frac{z'}{r\sqrt{(r')^2 + (z')^2}} \Big|_{s=0} \quad (8.6)$$

and for the outer normal

$$n_r = \frac{z'}{\sqrt{(r')^2 + (z')^2}} \Big|_{s=0} \quad n_z = \frac{-r'}{\sqrt{(r')^2 + (z')^2}} \Big|_{s=0}$$

This way we compute the surface tension at all discretization points. If a nodal point is at the symmetry axis ($r = 0$) the second term in equation (8.6) will cancel and the curvature in this particular points is approximated using the symmetry of the problem.

After solving the system of equations (8.5) for a fixed region, a time step has to be carried out. From the kinematic movement equation (2.14) for the three-dimensional case in Cartesian coordinates, it follows, after substituting cylindrical coordinates, that the motion of the material points on the boundary curve Γ can be described by

$$\frac{dr}{dt} = v_r, \quad \frac{dz}{dt} = v_z. \quad (8.7)$$

Substituting (8.7) into the algebraic equations (8.5) yields the following system of nonlinear ODEs,

$$\frac{d\mathbf{x}^c}{dt} = \mathcal{H}^{-1}(\mathbf{x}^c) \mathcal{G}(\mathbf{x}^c) \mathbf{b}^c(\mathbf{x}^c). \quad (8.8)$$

This system will be solved by applying the BDF implementation of the two-dimensional case with the similar approximation for the Jacobian of (8.8), i.e.

$$(\mathcal{J})_{2i-\alpha j} \doteq \mathcal{H}^{-1} \mathcal{G} \delta b_{i,\alpha}^c.$$

Note that here the vector $\delta b_{i,\alpha}^c$ differs from the two-dimensional case since the curvature term is different.

8.3 NUMERICAL RESULTS AND DISCUSSION

In this section we show examples of the simulation of axisymmetric sintering problems. It occurs that all fluid domains are deforming into a sphere, since that shape minimizes the outer surface that occupies a certain amount of material. The differences in evolution between two-dimensional and axisymmetric problems are discussed too.

The first example is the sintering of two equal spheres. The radius of the coalescing spheres is taken equal to 1; the initial radius of the contact circle between both spheres is set equal to 0.15. Like in the previous chapters, this contact radius of the coalescing circular surface will be denoted by r . The collocation points of the starting shape are

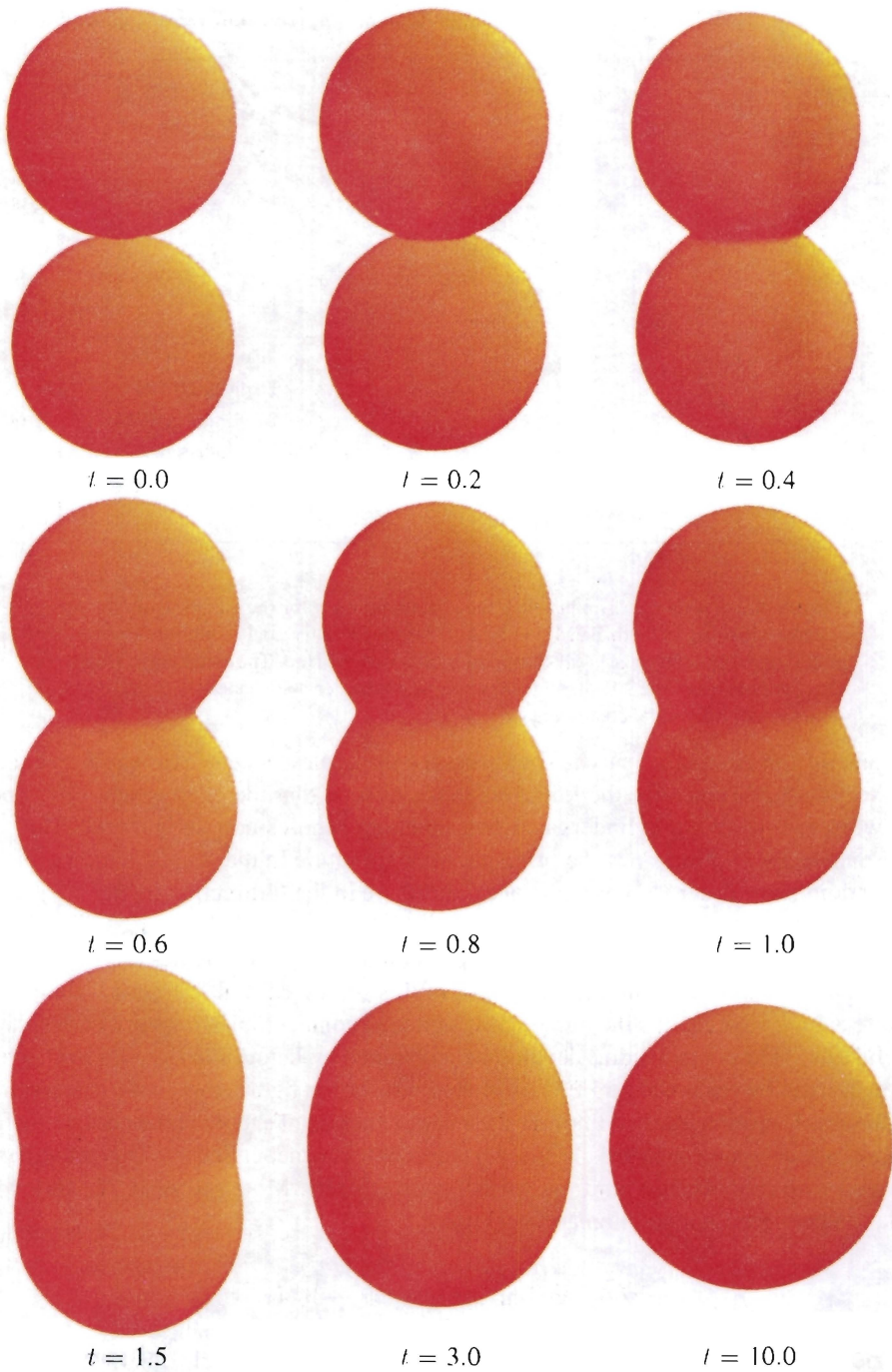


Figure 8.1 The coalescence of two equal spheres into one sphere occupying the same amount of fluid.

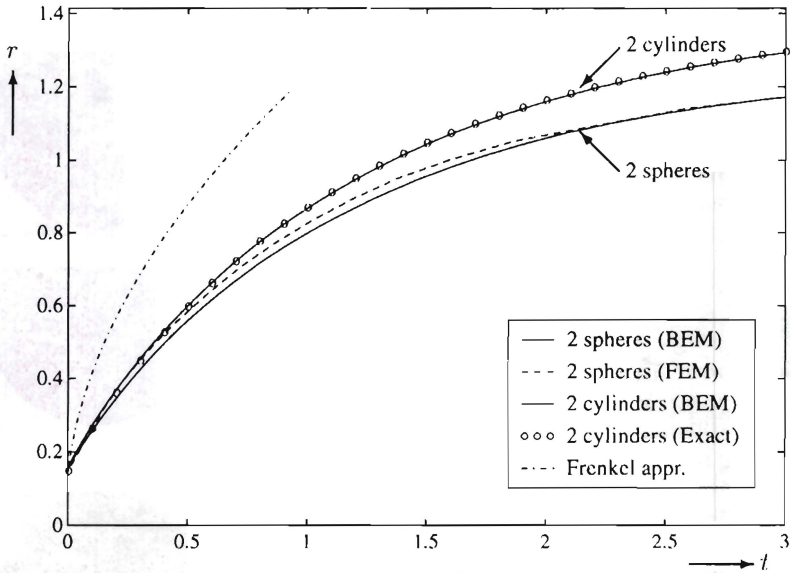


Figure 8.2 A comparison between the contact radius r for the sintering of two equal spheres obtained by both BEM and FEM. The much faster coalescing rate derived by employing the initial stage Frenkel approximation is plotted too. The matching of Hopper's exact solution and the BEM solution is also shown when the shape is considered two-dimensional (two equal coalescing cylinders).

obtained from Hopper's analytical solution for the coalescence of two equal cylinders, cf. section 3.2. Hence for the initial stage we assume that the geometrical differences between two touching cylinders and two touching spheres can be ignored. This is a reasonable assumption since the principal neck curvature in the rz -plane may assumed to be dominant (order r^{-3}) over the neck curvature in the θ -direction (order r^{-1}). Only nodal points from the first quadrant of the $\theta = 0$ plane are needed because of the double symmetry of the body. This symmetry is preserved during the calculations.

Figure 8.1 shows the simulation results of this coalescence at subsequent times t . In figure 8.2 we have plotted the numerically obtained contact radius between both spheres (solid line). The contact radius development obtained by Jagota and Dawson [48], which they derived by employing a FEM, is plotted too. In the figure, this curve is referred to as the FEM solution (dashed line). In their paper, they print a table of the contact surface between both spheres, called A , and a dimensionless time, called τ . This table has to be read with care because our time normalization differs. More precisely, the following relation between their solution and ours holds,

$$r = \sqrt{A}, \quad \text{and} \quad t = \left(\frac{3\pi}{4}\right)^{\frac{1}{3}} (\tau - \tau_0),$$

where the constant τ_0 is added to ensure the initial r to be equal to 0.15. As can be observed from figure 8.2, at later time stages the BEM and FEM solutions are matching reasonably well. During the initial time stage both solutions also match, however the

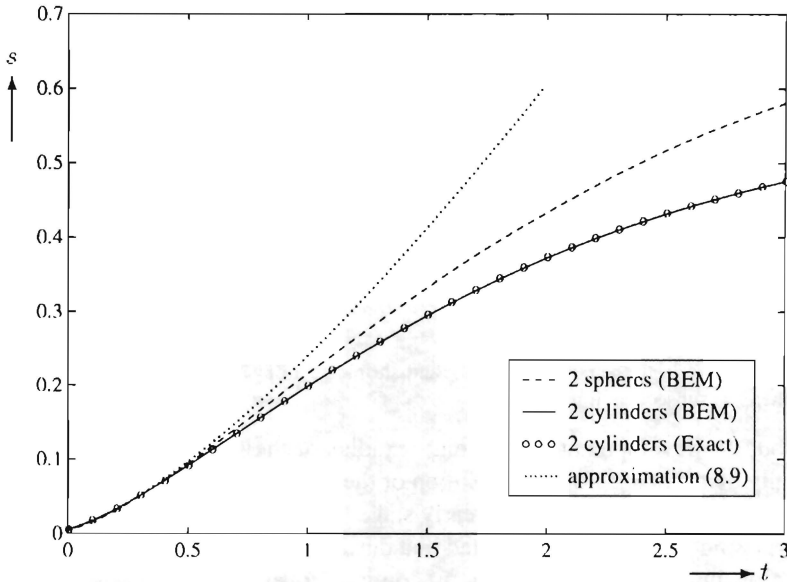


Figure 8.3 The shrinkage difference of the two equal spheres compared to both Hopper’s exact and BEM solution of two equal coalescing cylinders. Moreover, the matching of the analytic approximate shrinkage relation with the coalescing spheres shrinkage rate is shown during the early stage.

FEM solution follows the contact radius development of two coalescing cylinders a longer period of time. Hence, the FEM approach obtains a faster rate of coalescence for the period $0.25 \leq t \leq 2.0$.

In this figure we have plotted also the exact Hopper solution for the contact radius between two equal coalescing cylinders with initial radius 1 (circle marks), cf. equation (6.1) and (6.2). The BEM-solution obtained for an axisymmetric initial geometry is also shown (solid line). This solution is obtained by running our 2D-code with exactly the same program parameters for the mesh generation and the BDF time integrator as in the axisymmetric case. As can be seen from the figure, both solutions are nearly identical everywhere; this gives some validation of the correctness of the axisymmetric results.

Furthermore, in figure 8.2 we have plotted the Frenkel relation (3.44) which in the case of the considered coalescing spheres reads,

$$t_F = \frac{2}{3} (r^2 - (0.15)^2).$$

As can be seen (dashed dotted line), this relation predicts a much faster coalescence of the two spheres, even in the initial stage. Hence, we conclude that it does not make any sense to use this analytical relation anyway.

A more interesting feature is that Hopper’s solution for two coalescing cylinders is reasonably matching with the contact radius r of the two equal spheres obtained by both the FEM and BEM solution during the early stage of the coalescence. Hence during

t	r	s	t	r	s	t	r	s
0.0	0.147767	0.005648						
0.1	0.256069	0.015936	1.1	0.835476	0.239844	2.1	1.076790	0.451738
0.2	0.344573	0.031870	1.2	0.869421	0.263721	2.2	1.091422	0.469234
0.3	0.423611	0.050464	1.3	0.900912	0.287162	2.3	1.104851	0.486204
0.4	0.495164	0.070953	1.4	0.929983	0.310101	2.4	1.117181	0.502275
0.5	0.558910	0.093534	1.5	0.956720	0.332468	2.5	1.128519	0.517475
0.6	0.616099	0.117287	1.6	0.981281	0.354200	2.6	1.138930	0.531823
0.7	0.668213	0.141559	1.7	1.003816	0.375236	2.7	1.148500	0.545299
0.8	0.716292	0.166203	1.8	1.024480	0.395526	2.8	1.157276	0.558008
0.9	0.759296	0.190920	1.9	1.043433	0.415040	2.9	1.165347	0.569909
1.0	0.798940	0.215557	2.0	1.060821	0.433771	3.0	1.172759	0.581064

Table 8.1 Both the contact radius r and shrinkage s development of two coalescing spheres at subsequent time steps.

this period, the development of the contact radius of the spheres can be approximated analytically by applying Hopper's solution or the approximate relations that we derived in section 3.2, equation (3.28). This early stage (nearly) matching of the contact radius is not surprising since we already noted that during this coalescence stage, the principal curvature of the neck in the rz -plane is dominant over the principal curvature in the θ -direction. This matching validates the use of Hopper's analytical solution for the generation of the initial axisymmetric shape.

An even more important property that can be obtained from this coalescence is shown in figure 8.3. In that plot we show the shrinkage rate s of the coalescing spheres and compare it to the shrinking of two similarly sized cylinders. From the figure we observe that the shrinkage rate of the spheres (dashed line) is approximately *linear* during a large time period. Hence our calculations support the experimentally obtained linear shrinkage behaviour of regular and equally sized spherical particle packings performed by both Kuczynski [61] and Kingery and Berg [55] (as we already mentioned in the introduction).

Another interesting feature that can be obtained from figure 8.3 is that during the initial coalescence stage, the shrinkage rate is almost identical to the shrinkage of two equal cylinders. Hence the early stage shrinkage of these spheres can easily be described analytically by employing Hopper's solution or the analytic approximation that is derived in section 3.2; indeed, substituting equation (3.20) into (3.28) yields

$$t \simeq \frac{4\pi\sqrt{s}}{6\log 2 - \log s}. \quad (8.9)$$

The dotted line in figure 8.3 represents this initial stage shrinking development. As can be seen, this relation is approximately applicable for $0 \leq t \leq 1$.

Finally, in table 8.1 we have printed the numerically obtained values of the contact radius r and the shrinkage s at subsequent time points $t = 0.0(0.1)3.0$. During this particular coalescence simulation, the error which we obtained in the change of the volume was less than 1%.

The second axisymmetric sintering geometry we consider is the coalescence of

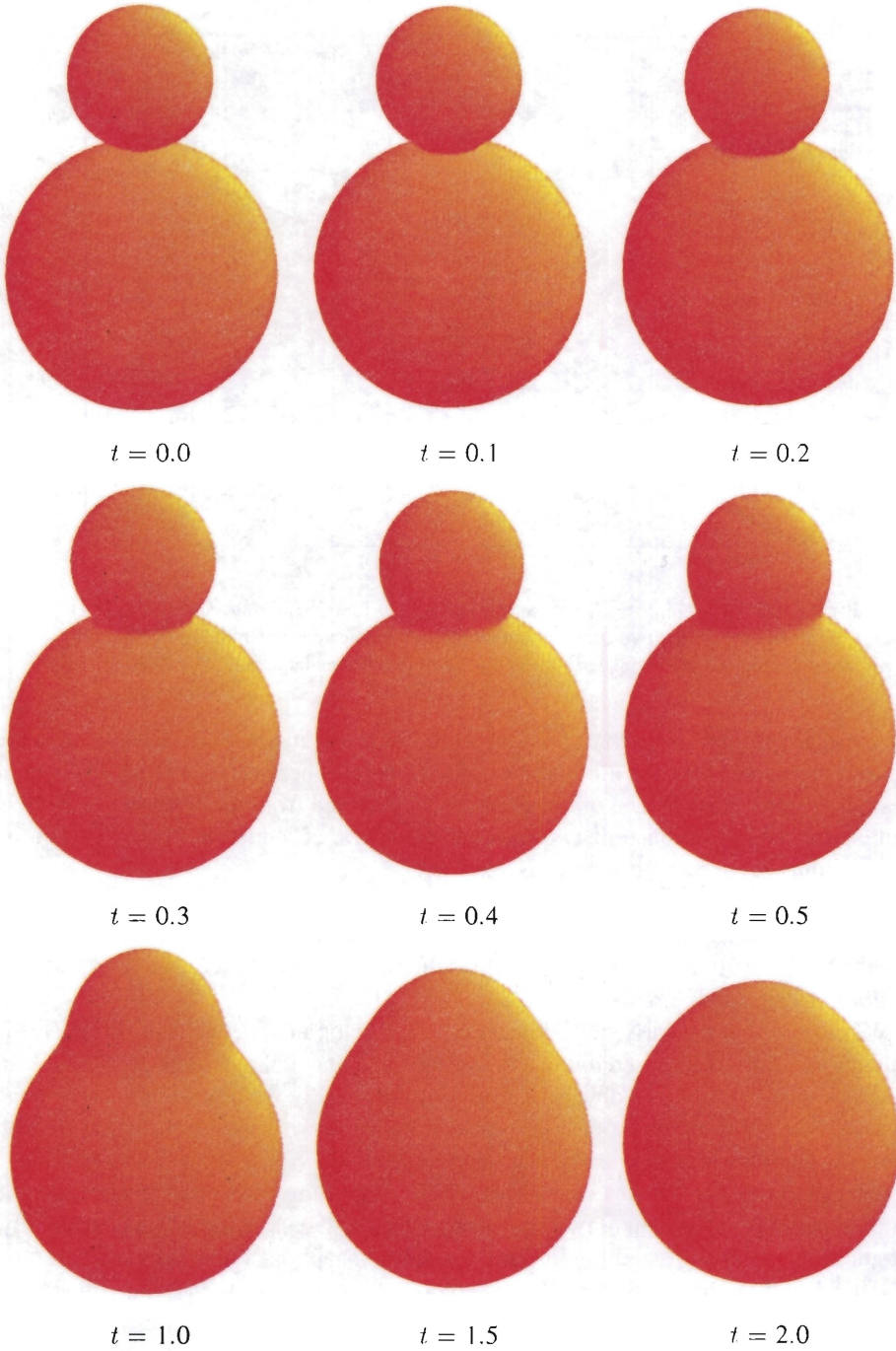


Figure 8.4 The coalescence of a sphere with initial radius 0.5 on a sphere with radius 1. The smaller sphere is gradually "eaten up" by the larger one. This phenomenon is usually referred to as *Ostwald ripening*.

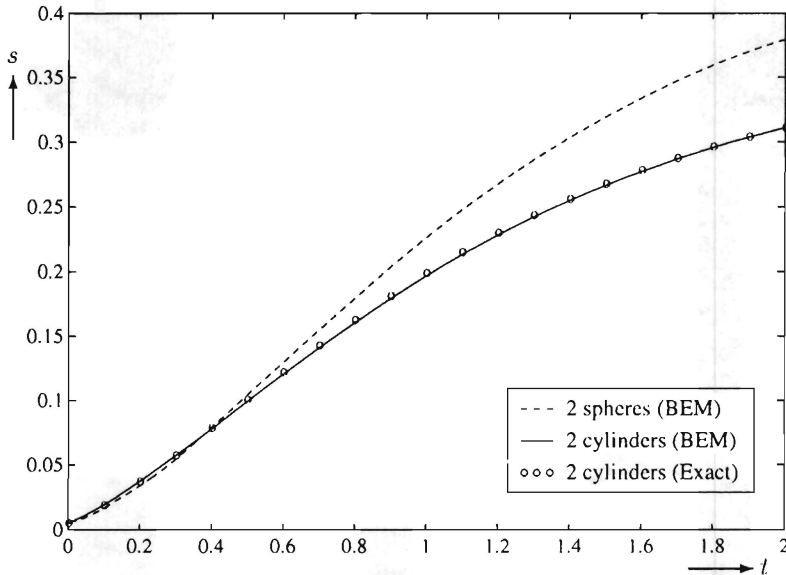


Figure 8.5 The comparison between the shrinkage s for the sintering of the two unequal spheres and the similar two-dimensional problem shows again a matching during the early stage. Moreover, this shrinkage is behaving linearly during a large period of time.

two unequal spheres. Note that this shape rotational symmetry only in contrast to the previous problem. Here, the initial radius of the largest sphere is taken equal to 1 and of the smaller sphere to 0.5. The initial geometry is obtained from Richardson's analytical solution for the coalescence of two unequal cylinders, cf. equation (3.9). The initial contact radius between both spheres is taken 0.12.

The shape evolution is shown in figure 8.4. As can be observed from these pictures the smaller sphere is gradually vanishing into the larger one. This phenomenon of growth of large particles at the expense of smaller ones is usually referred to as *Ostwald ripening* in sintering literature (cf. Mulder *et al.*[71]).

We observe that the early stage contact radius development between those spheres is behaving similar as compared to the two-dimensional unequal cylinders problem. Also the shrinkage rate of both problems is matching reasonably well during the early stage as can be seen from figure 8.5. Moreover, this figure shows that the shrinking of both spheres is evolving almost linearly as a function in time.

Next, we consider the sintering of two equal rings upon each other to compare the contact surface development of two coalescing rings, spheres and cylinders respectively. In figure 8.6 we have plotted the initial shape. This shape is obtained by a translation equal to 3.0 in the r -direction of the Hopper solution for two equal cylinders as considered in the first problem of this section. Hence the initial radius of these rings is equal to 1 and the width of the annular contact surface equals 0.30 (i.e. $2r$).

The further deformation of the geometry is also plotted in figure 8.6. Moreover, a cross-section of the shape evolution at subsequent time steps of 0.1 is shown in figure

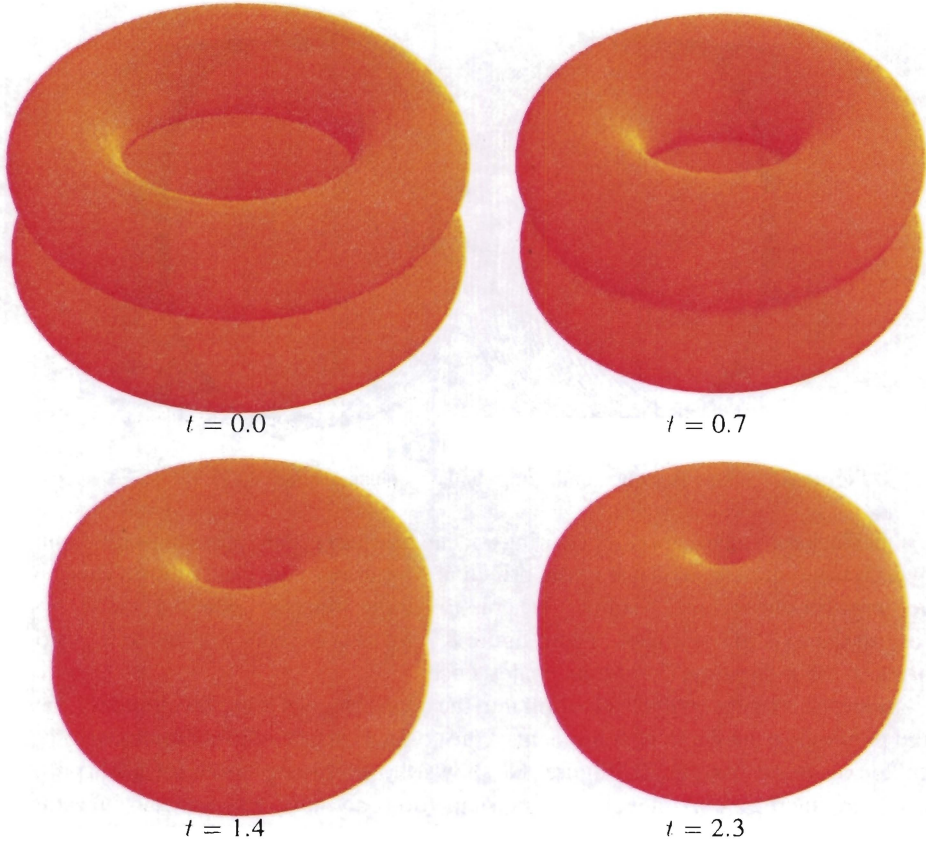


Figure 8.6 The coalescence of two ring-shaped viscous fluids which leads to a touching of the surface at the symmetry axis.

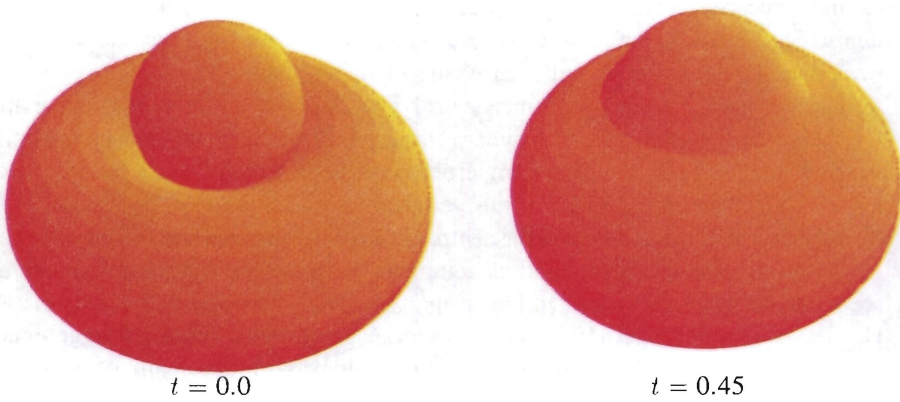


Figure 8.9 The coalescence of a sphere on a ring-shaped viscous fluid to study asymmetric neck growth.

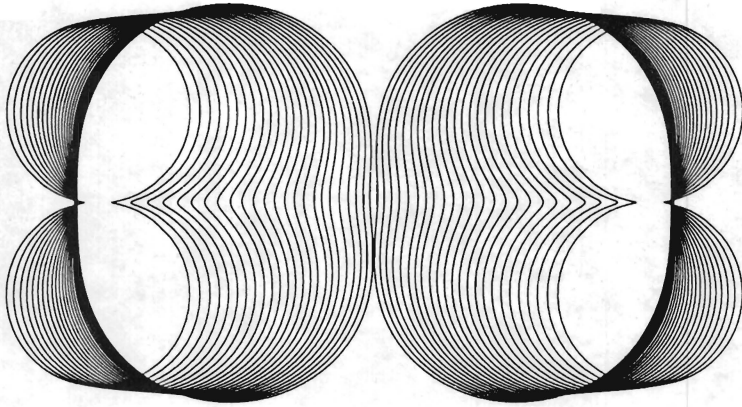


Figure 8.7 A cross-section of the rings in the rz -plane, $t = 0.0(0.1)2.3$.

8.7. Besides the coalescence of both rings, it can be observed that the rings are shrinking towards the symmetry axis due to the principal curvature in the θ -direction. This causes problems for our code as it is not (yet) able to handle situations where a boundary gets close to the axis of symmetry. From figure 8.7 we also observe that both rings do not shrink in the z -direction during the coalescence.

Since the starting geometry is similar to the coalescing spheres and cylinders considered previously, the width development of the contact surface of these three coalescence problems can be compared. Figure 8.8 shows those developments for each problem when time increases. Although the ring shape does not have a symmetric curvature at both sides of the annular contact surface, we see that the coalescence proceeds almost identical to the cylinder problem during the early stage. Moreover, the coalescence rate of the two spheres is behaving roughly the same during this stage too. At later time stages, the coalescence rate of the rings develops much faster compared to both other problems. This is due to the principal curvature in the θ -direction, since that curvature becomes dominant over the principal curvature in the rz -plane.

Another geometry to study asymmetric neck growth is the sintering of a sphere onto a ring. This is a straightforward axisymmetric generalization of the two-dimensional sintering of three cylinders with an angle between the centres of those cylinders, cf. section 7.1. The interesting aspect of this geometry is that if the initially chosen angle between the centre of the sphere and the centre circle of the ring is small, an internal hole can occur during sintering. This hole development also depends on the initial contact surface width between the sphere and the ring.

The first picture of figure 8.9 shows the initial shape of such a system. The geometry is viewed from above. In this particular case, the angle between the centre of the sphere and the ring centre line is taken equal to 100° when considered a cross-section in the rz -plane. From this picture, it is clear that when the angle is large, no internal holes during sintering will occur, since the larger the angle between sphere and ring, the deeper

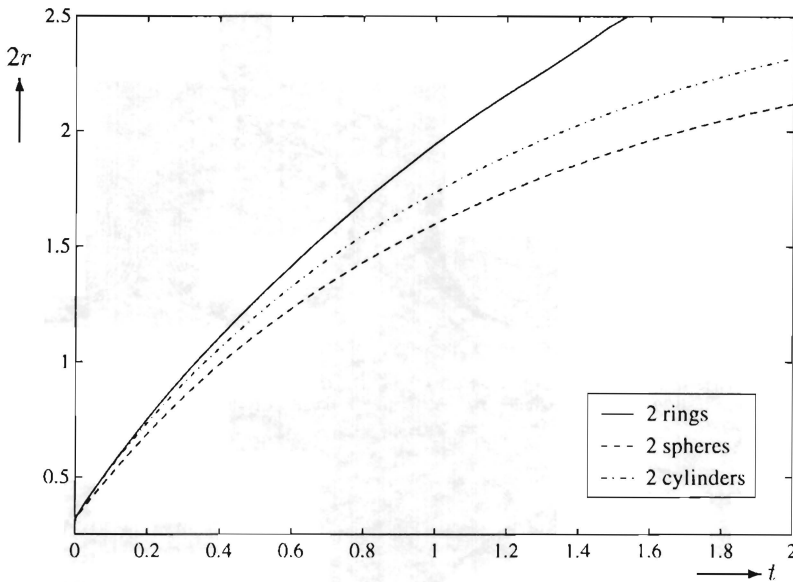


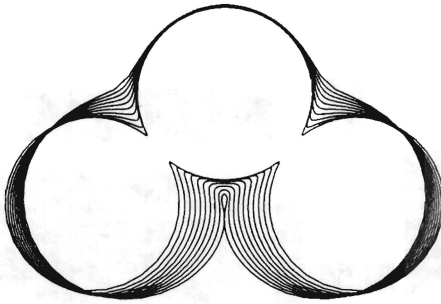
Figure 8.8 The matching of the width of the contact surface ($2r$) of the two equal coalescing rings, spheres and cylinders during the initial stage.

the sphere is initially placed inside the ring. Note, that for different angles we obtain different ring sizes. The initial radius of both the sphere and the ring is set equal to 0.5, and the contact surface is again obtained by applying Hopper's analytical solution for two equal spheres; here the contact radius is taken equal to 0.1, thus the contact surface width is equal to 0.2.

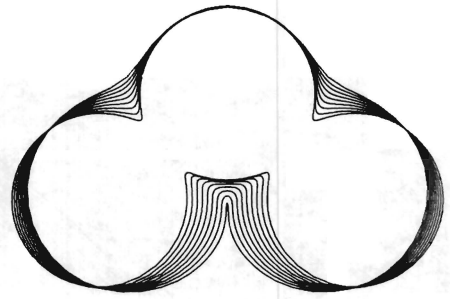
The other picture of figure 8.9 is taken at time $t = 0.45$. At that moment, the inside part of the ring is nearly touching the symmetry axis: an internal hole is formed. In order to obtain a more detailed view of this hole formation, we consider figure 8.10. Here, the evolution of the cross-section of the shape in the rz -plane is plotted at subsequent time steps. Figure 8.10^a is showing the sintering of the above described geometry at times $t = 0.0(0.05)0.45$. At the final time step a hole occurs: the remaining inner parts of the ring are nearly touching the symmetry axis.

Furthermore, we will discuss the differences in the evolution when some characteristics of the shape are slightly changed. In figure 8.10^b we have plotted the evolution of the same geometry, but now the initial contact surface width is taken two times larger, i.e. 0.4. As can be seen, no internal hole will develop since the boundary is almost completely touching the symmetry axis: a line contact occurs.

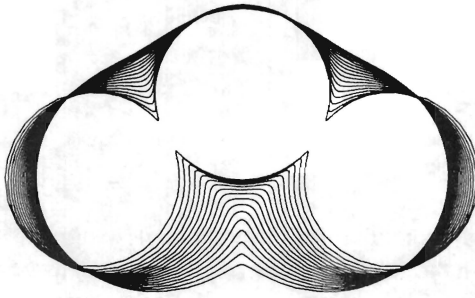
Figure 8.10^c shows the effect of an increase of the initial angle between the sphere and ring. The angle is set equal to 120° and the contact surface width is again 0.2. The curves refer to values of time $t = 0.0(0.05)0.8$. When comparing this simulation to the results of figure 8.10^a we observe that no internal hole is found. Now, the development of a cusp at this particular part is the only effect. This plot also shows that the cusp smooths out as time increases. It appears that the cusp is smoother if the initial contact



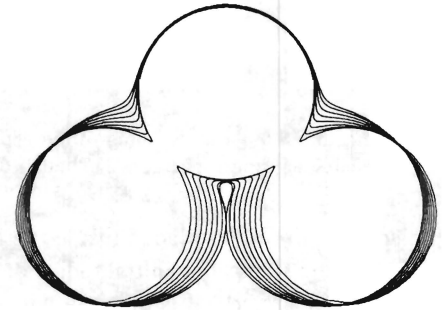
a. The initial angle is 100° and the contact surface width is equal to 0.20. The curves refer to $t = 0.0(0.05)0.45$.



b. The initial angle is 100° and the contact surface width is equal to 0.40. The curves refer to $t = 0.0(0.05)0.4$.



c. The initial angle is 120° and the contact surface width is equal to 0.20. The curves refer to $t = 0.0(0.05)0.8$.



d. The initial angle is 90° and the contact surface width is equal to 0.20. The curves refer to $t = 0.0(0.05)0.3$ and $t = 0.338$.

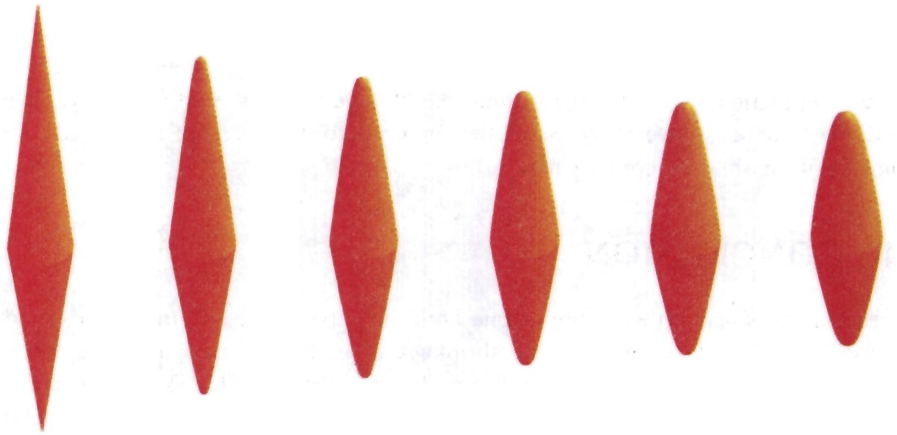
Figure 8.10 A cross-section of the coalescing sphere and ring in the rz -plane during sintering. The differences in evolution are shown when both the angle and/or the contact surface width between the sphere and ring are varied.

surface width is larger too, i.e. a similar behaviour as we found for the shape of figure 8.10^b.

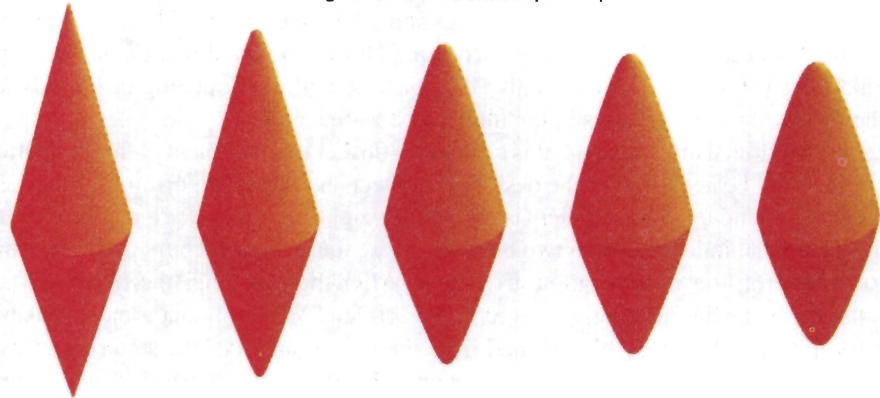
The effect of decreasing the angle between the sphere and the ring is shown in figure 8.10^d. Here, the angle is set equal to 90° . Again an internal hole is formed and this hole is larger than the one in figure 8.10^a. Hence the shape is behaving like we would expect.

If we model and simulate the geometries of figure 8.10 as two-dimensional fluids, it appears that such a hole development does not take place for all those shapes. A hole occurring only if the angle is taken much smaller, thus when the two outer cylinders are almost touching initially.

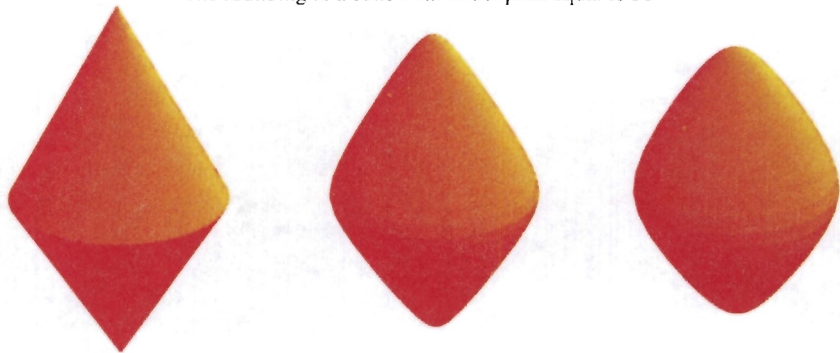
Finally, we simulate the rounding of two opposite cones that are pressed together. This is the axisymmetric extension of the sintering of rhombic fluid domains like we considered at the end of chapter 4. The initial shapes are taken equal to the two-dimensional geometries; however, they are rotated 90 degrees. Thus, the largest diagonal



$t = 0.00$ $t = 0.02$ $t = 0.04$ $t = 0.06$ $t = 0.08$ $t = 0.10$
 The rounding of a cone with initial peak equal to 15°



$t = 0.00$ $t = 0.025$ $t = 0.05$ $t = 0.075$ $t = 0.10$
 The rounding of a cone with initial peak equal to 30°



$t = 0.0$ $t = 0.1$ $t = 0.2$
 The rounding of a cone with initial peak equal to 60°

Figure 8.11 The rounding of two opposite cones that are pressed together. All the starting shapes have equal length and the initial angle of the peak is taken equal to 15, 30 and 60 degree respectively. The rounding is proceeding slower by increasing angle.

line inside those shapes is taken equal to 2 and the angle of the lines that define the sharpest corners is initially set equal to 15, 30 and 60 degrees respectively. In figure 8.11 the simulation results for these three rhombic geometries is shown. Like in the two-dimensional case, we observe that the shapes deform inside the prescribed initial geometry of the sharpest corner parts.

8.4 CONCLUSION

The examples of section 8.3 demonstrate both the capabilities and limitations of our numerical code. It is shown that the shrinkage of both two equal and two unequal spheres is proceeding at a linear rate during the initial stage. This shrinkage rate can be approximated analytically by applying the corresponding two-dimensional analytic solutions of these problems. Moreover, the rounding of sharp peaks is developing like the corresponding two-dimensional problems. Asymmetric neck growth is studied by considering the coalescence of two equal rings and a sphere on a ring. These simulations show the influence due to the principal curvature in the azimuthal direction on the shape deformation. These latter examples also demonstrate both the touching of boundaries and the formation of inner holes in the three-dimensional case.

As we mentioned in section 1.4, it is clear that a further improvement of the simulation capabilities may be achieved by the design of a detect and handle algorithm for the case of a touching boundary. This problem is not quite straightforward, since a measure has to be introduced that indicates when two boundaries are touching. Of course, this measure has to depend on the discretization error too. After the touching, the outer surface curvature of the coalescing region has to be prescribed. We think that a most sensible value for this curvature may be obtained from the unit problem of the sintering of two spheres. The initial radii of those spheres should then be chosen such that they mimic the both parts of the coalescing surface locally quite well. And of course, experimental verification has to be carried out, to justify the chosen model.

A

ANALYTICAL SOLUTION METHOD FOR MOVING STOKES FLOW

In this appendix we present the analytical solution method for the time evolution of a moving Stokes flow that is applied in chapter 3. In particular, the derivation of Hopper's evolution equation is outlined which will be performed by closely following the description of De Graaf [29]. First, we formulate the general solution of the Stokes flow for a simply connected domain in the complex plane. Further on, the kinematic equation of motion is derived which appears to be an intermediate between the Eulerian and Lagrangian approach. This kinematic relation will be substituted into the complex plane equation expressing that the surface tension is equal to the curvature in the normal direction which yields Hopper's evolution equation.

A.1 THE STOKES EQUATION IN THE COMPLEX PLANE

The Stokes equation will be constructed in the complex plane by using the representation of this equation in terms of the stream and Airy's stress functions. A more extensive outline on this representation technique can be found in England [21] and Muskhelishvili [72].

We consider a simply connected fluid domain $G \subset \mathbb{R}^2$. Moreover a particular point in G will be taken fixed during the evolution and a Cartesian (x, y) -plane is chosen so that this fixed point represents the origin of the coordinate system. The complex variable will be denoted by $z = x + iy$.

The incompressibility condition, $\text{div } \mathbf{v}$, implies the existence of a stream function $\psi(x, y)$ such that

$$v_1 = \frac{\partial \psi}{\partial y}, \quad v_2 = -\frac{\partial \psi}{\partial x}. \quad (\text{A.1})$$

From the constitutive relation for the stress tensor T and the Stokes equations it can

easily be shown that

$$(\operatorname{div} T)_i = \frac{\partial T_{i1}}{\partial x} + \frac{\partial T_{i2}}{\partial y} = 0.$$

Hence, it follows that there exists an "Airy stress function" $\phi(x, y)$ with properties

$$T_{11} = -\frac{\partial^2 \phi}{\partial y^2}; \quad T_{12} = T_{21} = \frac{\partial^2 \phi}{\partial x \partial y}; \quad T_{22} = -\frac{\partial^2 \phi}{\partial x^2}. \quad (\text{A.2})$$

Substituting the property that the pressure p is equal to

$$p = -\frac{1}{2}(T_{11} + T_{22}),$$

and equations (A.1) and (A.2) into the Stokes equation yields the Cauchy-Riemann form

$$\frac{\partial}{\partial x}(\frac{1}{2} \Delta \phi) - \frac{\partial}{\partial y}(\Delta \psi) = 0; \quad \frac{\partial}{\partial y}(\frac{1}{2} \Delta \phi) + \frac{\partial}{\partial x}(\Delta \psi) = 0.$$

This implies that $(\frac{1}{2} \Delta \phi + i \Delta \psi)$ is an analytic function on G ; hence $\Delta^2 \phi = 0$ and $\Delta^2 \psi = 0$, i.e. both the function ϕ and ψ are *biharmonic*. Because of this biharmonicity, Muskhelishvili [72] (chapter 5) shows that the following relations are satisfied,

$$\phi = 2\operatorname{Re}(\bar{z}\varphi + \chi) \quad \text{and} \quad \psi = \operatorname{Im}(\bar{z}\varphi + \chi), \quad (\text{A.3})$$

where $\varphi(z)$ and $\chi(z)$ are analytic functions of z in G and the bar denotes the complex conjugate. Note that Muskhelishvili obtains this representation for the plane theory of elasticity, hence we have to take in that relation Poisson's ratio equal to $\frac{1}{2}$. When the functions ϕ and ψ are known this establishes the functions φ and χ too.

From equations (A.1) and (A.3) we obtain that the velocity field satisfies

$$v_1 + i v_2 = -\varphi + z\bar{\varphi}' + \bar{\chi}', \quad (\text{A.4})$$

where the prime denotes the derivative with respect to the dependent (complex) variable. Note that now the functions φ and χ in equation (A.4) are uniquely defined up to a linear function $Az + B$ for a given velocity field \mathbf{v} . The tension in the normal direction in terms of the functions φ and χ becomes equal to

$$T \mathbf{n} = 2i \frac{d}{ds} (\varphi + z\bar{\varphi}' + \bar{\chi}'), \quad (\text{A.5})$$

cf. De Graaf [29]. Here s is the arc length of the boundary curve. Let α be the angle between the boundary normal and the positive x -direction, then the curvature and the outer normal can be expressed by

$$\kappa(s) = \frac{d\alpha}{ds}(s) \quad \text{and} \quad \mathbf{n} = e^{i\alpha(s)}$$

respectively. Since the tension is proportional to the curvature, it can be deduced that equation (A.5) reduces to

$$\varphi + z\bar{\varphi}' + \bar{\chi}' = \frac{1}{2}e^{i\alpha(s)} + C \quad \text{on } \partial G, \quad (\text{A.6})$$

where it is convenient to set the constant C equal to zero. Combining the above relation with equation (A.4), we derive for the boundary velocity field

$$v_1 + i v_2 = -2\varphi + \frac{1}{2}e^{i\alpha(s)} \quad \text{on } \partial G. \quad (\text{A.7})$$

Now, let $z = \Omega(\zeta, t) = \Omega(\xi + i\eta, t)$ give a conformal map of the unit disk $|\zeta| \leq 1$ onto G . Moreover, we require that $\Omega(0, t) = 0$ and $\Omega'(0, t) > 0$. The latter condition accomplishes that $\Omega(\zeta, t)$ is uniquely determined in the case that the domain G has a symmetry axis which is valid for the shapes that are considered here. The unit circle in the ζ -plane will also be denoted by $\sigma = e^{i\theta}$ which maps the boundary curve on ∂G . Note that because of the incompressibility condition the integral relation (3.1) has to be satisfied.

A.2 THE KINEMATIC RELATION

Since the domain G is moving, we require a kinematic relation to describe the motion in the ζ -plane. For the moment, we consider the mapping Ω to be in the (ξ, η) -coordinate space for which the movement equation is outlined below. We will translate the obtained equation into the complex ζ -plane afterwards.

As already mentioned, in fluid dynamics two distinct alternative kinds of describing the flow field are commonly used. The Lagrangian approach consists of labeling each material particle, say by \mathbf{X} , and the objective is to determine the trajectory \mathbf{x} of this piece of matter as a function of time, i.e. $\mathbf{x} = \mathcal{F}(\mathbf{X}, t)$ which is also illustrated in figure A.1. In the alternative *Eulerian* description, the unknown of interest is the velocity field as functions of the position in space (\mathbf{x}) and time, i.e.

$$\mathbf{v}(\mathbf{x}, t) = \dot{\mathcal{F}}(\mathcal{F}^{-1}(\mathbf{x}, t), t) \quad (\text{A.8})$$

where the dot $\dot{\cdot}$ denotes the derivative with respect to t .

For our problem, we are only interested in the determination of the shape motion of a total fluid region. Hence both previously mentioned formulations are not directly suitable. Because of this, we apply the so-called *pseudo Lagrangian* description (De Graaf [29]), i.e. at each time a fixed domain in the ζ -space is mapped by a function $\mathbf{x} = \Omega(\zeta, t)$ on to the actual configuration space G . This is also expressed in figure A.1, where $\boldsymbol{\nu}$ denotes the velocity field in the ζ -plane. Hence

$$\begin{aligned} \boldsymbol{\nu} &= \frac{d}{dt}(\zeta(\mathbf{X}, t)) = \frac{d}{dt}(\Omega^{-1}(\mathcal{F}(\mathbf{X}, t), t)) \\ &= (\mathcal{D}\Omega^{-1})(\mathcal{F}(\mathbf{X}, t), t)\dot{\mathcal{F}}(\mathbf{X}, t) + (\dot{\Omega}^{-1})(\mathcal{F}(\mathbf{X}, t), t), \end{aligned} \quad (\text{A.9})$$

where $(\mathcal{D}\Omega^{-1})$ is the Jacobi matrix of derivatives of Ω^{-1} with respect to ξ and η . Using $(\mathcal{D}\Omega^{-1}) = (\mathcal{D}\Omega)^{-1}$, together with equation (A.8) and $\mathcal{F}(\mathbf{X}, t) = \mathbf{x} = \Omega(\zeta, t)$ yields

$$\begin{aligned} \boldsymbol{\nu} &= (\mathcal{D}\Omega)^{-1}(\Omega(\zeta, t), t)\mathbf{v}(\Omega(\zeta, t), t) + (\dot{\Omega}^{-1})(\Omega(\zeta, t), t) \\ &= (\mathcal{D}\Omega)^{-1}(\Omega(\zeta, t), t)[\mathbf{v}(\Omega(\zeta, t), t) - \dot{\Omega}(\zeta, t)]. \end{aligned} \quad (\text{A.10})$$

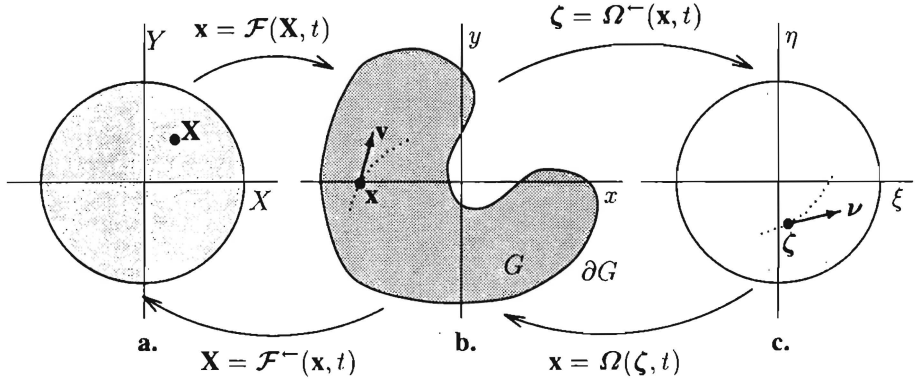


Figure A.1 The relations between the different applied spaces, i.e. figure (a) shows the particle labels in Lagrangian coordinates, (b) is the actual configuration space and (c) represents the Pseudo Lagrangian coordinate plane.

The latter equality is derived by substituting the relation

$$(\dot{\Omega}^-)(\Omega(\zeta, t), t) = -(\mathcal{D}\Omega)^{-1}(\Omega(\zeta, t), t)\dot{\Omega}(\zeta, t)$$

which in term is obtained by differentiating the identity

$$\zeta = \Omega^-(\Omega(\zeta, t), t)$$

with respect to t in a similar way as equation (A.9) is derived.

A.3 HOPPER'S EVOLUTION EQUATION

The kinematic relation (A.10) will be employed for the complex mapping function $\Omega(\zeta, t)$ with $|\zeta| \leq 1$, i.e. we have to rewrite equation (A.10) to the complex ζ -plane. Noting that in the complex plane $(\mathcal{D}\Omega) = \Omega'$, equation (A.10) reduces to

$$\dot{\zeta} = \frac{1}{\Omega'(\zeta, t)} [v_1(\Omega(\zeta, t), t) + iv_2(\Omega(\zeta, t), t) - \dot{\Omega}(\zeta, t)]. \quad (\text{A.11})$$

On the unit disk is $\zeta = \sigma = e^{i\theta}$; moreover the circular domain has to keep this form which requires that $\dot{\sigma}$ has always to be tangential towards the outer curve. Hence

$$\dot{\sigma} = iC e^{i\theta},$$

where C is a real valued function, in particular the following equation is satisfied,

$$\text{Re } \dot{\sigma} e^{-i\theta} = \text{Re } \frac{\dot{\sigma}}{\sigma} = 0.$$

Substituting this parameterization into equation (A.7) and put $\tilde{\varphi}(\sigma, t) = \varphi(\Omega(\sigma, t), t)$ this leads to

$$v_1(\Omega(\sigma, t), t) + iv_2(\Omega(\sigma, t), t) = -2\tilde{\varphi}(\sigma, t) + \frac{\sigma\Omega'(\sigma, t)}{2|\Omega'(\sigma, t)|}.$$

Applying the above relation in equation (A.11) yields

$$\frac{2\tilde{\varphi}(\sigma, t) + \dot{\Omega}(\sigma, t)}{\sigma\Omega'(\sigma, t)} = \frac{1}{2|\Omega'(\sigma, t)|} - \frac{\dot{\sigma}}{\sigma}. \tag{A.12}$$

We observe that the two terms on the right hand side of equation (A.12) are the real and imaginary parts respectively of an analytic function restricted on the boundary of the unit disk. This function will be denoted by \mathcal{F} which is analytic on the unit disk and is uniquely defined by

$$\operatorname{Re} \mathcal{F}(\sigma, t) = \frac{1}{2|\Omega'(\sigma, t)|} \quad \text{and} \quad \operatorname{Im} \mathcal{F}(0, t) = 0.$$

A specific representation for \mathcal{F} in terms of a Taylor series is deduced by De Graaf [29], which reads

$$\mathcal{F}(\zeta, t) = \alpha_0 + 2 \sum_{n=1}^{\infty} \alpha_n \zeta^n,$$

where the coefficients α_n are obtained from the representation

$$\frac{1}{2} |\Omega'(\zeta, t) \Omega'(\bar{\zeta}^{-1}, t)|^{-1} = \sum_{n=-\infty}^{\infty} \alpha_n \zeta^n.$$

Another representation for \mathcal{F} in terms of an integral can be found in the papers of Hopper [42] and Richardson [89]. Applying the definition of \mathcal{F} in equation (A.12) yields

$$2\tilde{\varphi}(\sigma, t) = \sigma\Omega'(\sigma, t)\mathcal{F}(\sigma, t) - \dot{\Omega}(\sigma, t) \tag{A.13}$$

In order to deduce Hopper's evolution equation for the mapping Ω , we substitute $z = \Omega(\sigma, t)$ and $\tilde{\chi}(\sigma, t) = \chi(\Omega(\sigma, t), t)$ in equation (A.6) which leads to

$$\overline{\Omega'(\sigma, t)}\tilde{\varphi}(\sigma, t) + \Omega(\sigma, t)\overline{\tilde{\varphi}'(\sigma, t)} + \overline{\tilde{\chi}'(\sigma, t)} = \frac{1}{2}\sigma|\Omega'(\sigma, t)|.$$

In this relation we eliminate $\tilde{\varphi}$ by employing equation (A.13) and its derivative, i.e.

$$\begin{aligned} -\sigma\overline{\Omega'(\sigma, t)}\Omega'(\sigma, t)\left(\mathcal{F}(\sigma, t) - \frac{1}{|\Omega'(\sigma, t)|}\right) - \Omega\left(\overline{\sigma\Omega'(\sigma, t)\mathcal{F}(\sigma, t)}\right)' \\ + \frac{d}{dt}\left(\Omega(\sigma, t)\overline{\Omega'(\sigma, t)}\right) = \overline{2\tilde{\chi}'(\sigma, t)}. \end{aligned}$$

Taking the complex conjugate of the above equation and noting that

$$\mathcal{F}(\sigma, t) - \frac{1}{|\Omega'(\sigma, t)|} = -\overline{\mathcal{F}(\sigma, t)},$$

we derive

$$\bar{\sigma}\Omega'(\sigma, t)\overline{\Omega'(\sigma, t)}\mathcal{F}(\sigma, t) - \overline{\Omega(\sigma, t)}(\sigma\Omega'(\sigma, t)\mathcal{F}(\sigma, t))' + \frac{d}{dt}(\overline{\Omega(\sigma, t)}\Omega'(\sigma, t)) = 2\hat{\chi}'(\sigma, t).$$

From

$$\frac{d}{d\sigma}(\overline{\Omega(\sigma, t)}) = -\frac{\overline{\Omega'(\sigma, t)}}{\sigma^2} \quad \text{and} \quad \bar{\sigma} = \frac{1}{\sigma},$$

we arrive at Hopper's evolution equation

$$-\frac{d}{d\sigma}(\sigma\overline{\Omega(\sigma, t)}\Omega'(\sigma, t)\mathcal{F}(\sigma, t)) + \frac{d}{dt}(\overline{\Omega(\sigma, t)}\Omega'(\sigma, t)) = 2\hat{\chi}'(\sigma, t). \quad (\text{A.14})$$

Finally, we will demonstrate the usage of the latter equation to obtain a set of ODEs that describe the evolution of a particular mapping. Therefore we consider the polynomial maps, conjectured by Hopper [42], of the form

$$\Omega(\sigma, t) = \sigma \sum_{n=1}^N \frac{b_n(t)}{1 - a_n(t)\sigma}, \quad (\text{A.15})$$

where $|a_n(t)| < 1$. Note that a particular mapping function of this set is applied to obtain the coalescence of two cylinders. Moreover, the conjugate is equal to

$$\overline{\Omega}(\sigma, t) = \sum_{n=1}^N \frac{\bar{b}_n}{\sigma - \bar{a}_n}, \quad (\text{A.16})$$

since $\bar{\sigma}\sigma = 1$. The analytic continuation of equation (A.14) onto the unit disk is simply found by replacing σ by ζ and requiring $|\zeta| \leq 1$, i.e. equation (A.14) can be equivalently written as

$$\begin{aligned} \overline{\Omega(\zeta, t)} \left[\left(1 + \zeta \frac{\Omega''(\zeta, t)}{\Omega'(\zeta, t)} \right) \mathcal{F}(\zeta, t) + \zeta \mathcal{F}'(\zeta, t) - \frac{\dot{\Omega}'(\zeta, t)}{\Omega'(\zeta, t)} \right] \\ + \zeta \overline{\Omega'(\zeta, t)} \mathcal{F}(\zeta, t) - \overline{\Omega(\zeta, t)} = -\frac{2\hat{\chi}'(\zeta, t)}{\Omega'(\zeta, t)}. \end{aligned} \quad (\text{A.17})$$

From the analytic continuation of equations (A.15) and (A.16), we observe that the factors of equation (A.17) which do not involve conjugate terms are analytic throughout the domain. Hence these terms do not cause any trouble for the requirement that the left hand side of equation (A.17) has to be analytic in the unit disk. Substituting equations (A.15) and (A.16) with $\sigma = \zeta$ and

$$\overline{\Omega}'(\zeta, t) = -\sum_{n=1}^N \frac{\bar{b}_n}{(\zeta - \bar{a}_n)^2}; \quad \overline{\Omega}(\zeta, t) = \sum_{n=1}^N \left(\frac{\bar{b}_n}{\zeta - \bar{a}_n} + \frac{\bar{b}_n \bar{a}_n}{(\zeta - \bar{a}_n)^2} \right),$$

into equation (A.17) yields

$$\begin{aligned} \sum_{n=1}^N \frac{1}{\zeta - \bar{a}_n} \left(\bar{b}_n \left[\left(1 + \zeta \frac{\Omega''(\zeta, t)}{\Omega'(\zeta, t)} \right) \mathcal{F}(\zeta, t) + \zeta \mathcal{F}'(\zeta, t) - \frac{\dot{\Omega}'(\zeta, t)}{\Omega'(\zeta, t)} \right] - \bar{b}_n \right) \\ - \sum_{n=1}^N \frac{(\zeta \mathcal{F}(\zeta, t) + \bar{a}_n) \bar{b}_n}{(\zeta - \bar{a}_n)^2} = \text{analytic on } |\zeta| \leq 1. \end{aligned} \quad (\text{A.18})$$

In order to fulfill the analyticity property of the equation above, the first and second order poles in $\zeta = \bar{a}_n$ have to vanish. This is accomplished by a Taylor expansion of equation (A.18) around these poles. For the second order poles this leads to

$$\frac{\dot{a}_n}{a_n} = -\overline{\mathcal{F}(\bar{a}_n, t)}, \quad (\text{A.19})$$

and for the first order terms with substitution of equation (A.19) yields

$$\frac{\dot{b}_n}{b_n} = -\frac{\overline{\Omega}''(\bar{a}_n, t)\dot{a}_n + \overline{\Omega}'(\bar{a}_n, t)}{\overline{\Omega}'(\bar{a}_n, t)}. \quad (\text{A.20})$$

Hence the real and imaginary parts of equations (A.19) and (A.20) leads to 4N coupled ODEs for the 4N unknowns.

BIBLIOGRAPHY

- [1] M. ABRAMOWITZ AND I.A. STEGUN, *Handbook of Mathematical Functions*. Dover Publications, New York, 1964.
- [2] L.K. ANTANOVSKII, Creeping thermocapillary motion of a two-dimensional deformable bubble: existence theorem and numerical simulation, *Eur. J. Mech., B/Fluids* **11**, 741–758, 1992.
- [3] L.K. ANTANOVSKII, Boundary Integral Equations for Contact Problems of Plane Quasi-Steady Viscous Flows, *Euro. J. Appl. Math.* **4**, 175–188, 1993.
- [4] R. ARIS, *Vectors, tensors, and the basic equations of fluid mechanics*. Prentice-Hall, Englewood Cliffs NY., 1962.
- [5] D.N. ARNOLD AND W.L. WENDLAND, On the Asymptotic Convergence of Collocation Methods, *Math. Comp.* **41**, 349–381, 1983.
- [6] G.K. BATCHELOR, *An Introduction to Fluid Dynamics*. Cambridge University Press, Cambridge, 1967.
- [7] A.A. BECKER, *The Boundary Element Method in Engineering*. McGraw-Hill Book Company, London, 1992.
- [8] C.A. BREBBIA, J.C.F. TELLES AND L.C. WROBEL, *Boundary Element Techniques*. Springer-Verlag, Berlin, 1984.
- [9] C.A. BREBBIA AND J. DOMINGUEZ, *Boundary Elements: An Introductory Course*. Computational Mechanics Publications, Southampton, 1989.
- [10] K.E. BRENAN, S.L. CAMPBELL AND L.R. PETZOLD, *Numerical Solution of Initial-Value Problems in Differential-Algebraic Equations*. North-Holland Publishing Company, Amsterdam, 1989.

- [11] C.J. BRINKER, Overview of sol-gel processing films, in *Proc. Conf. on The Global Business and Technical Outlook for High Performance Inorganic Thin Film Coatings*, Gorham Advanced Materials, Ipswich, 1990.
- [12] C.J. BRINKER AND G.W. SCHERER, *Sol-gel science : the physics and chemistry of sol-gel processing*. Academic Press, London, 1990.
- [13] P.E. BYRD AND M.D. FRIEDMAN, *Handbook of Elliptic Integrals for Engineers and Scientists*. Springer-Verlag, Berlin, 1971.
- [14] J.J.S.P. CABRAL, L.C. WROBEL AND C.A. BREBBIA, A BEM Formulation Using B-Splines:I- Uniform Blending Functions, *Engng. Analysis* **7**, 136–144, 1990.
- [15] J.J.S.P. CABRAL, L.C. WROBEL AND C.A. BREBBIA, A BEM Formulation Using B-Splines:II- Multiple Knots and Non-Uniform Blending Functions, *Engng. Analysis* **8**, 51–55, 1991.
- [16] B.K. CHI AND L.G. LEAL, A Theoretical Study of the Motion of a Viscous Drop Toward a Fluid Interface at Low Reynolds Number, *J. Fluid Mech.* **201**, 123–146, 1989.
- [17] M.J. COOKER, D.H. PEREGRINE, C. VIDAL AND J.W. DOLD, The Interaction Between a Solitary Wave and a Submerged Semicircular Cylinder, *J. Fluid Mech.* **215**, 1–22, 1990.
- [18] G.J. COSGROVE, J.A. STROZIER AND L.L. SEIGLE, An approximate analytical model for the late-stage sintering of an array of rods by viscous flow, *J. Appl. Phys.* **47**, 1258–1264, 1976.
- [19] A. CRAIEVICH, M.A. AEGERTER, D.I. DOS SANTOS, T. WOIGNIER AND J. ZARZYCKI, A SAXS Study of Silica Aerogels, *J. Non-Cryst. Solids* **86**, 394–406, 1986.
- [20] D.G. DRITSCHEL, Contour Surgery: A Topological Reconnection Scheme for Extended Integrations Using Contour Dynamics, *J. Comput. Phys.* **77**, 240–266, 1988.
- [21] A.H. ENGLAND, *Complex variable methods in elasticity*. Wiley-Interscience, London, 1971.
- [22] H.E. EXNER AND G. PETZOW, Shrinkage and Rearrangement During Sintering of Glass Spheres, in *Proc. Conf. on Material Science Research, Vol. 10 Sintering and Catalysis*, edited by G.C. Kuczynski, Plenum Press, New York, pp. 279–293, 1975.
- [23] H.E. EXNER, *Grundlagen von Sintervorgängen*. Gebrüder Borntraeger, Berlin-Stuttgart, 1978. In German.

- [24] J.M. FLORYAN AND H. RASMUSSEN, Numerical Methods for Viscous Flows with Moving Boundaries, *Appl. Mech. Rev.* **42**, 12, 323–341, 1989.
- [25] J. FRENKEL, Viscous Flow of Crystalline Bodies Under the Action of Surface Tension, *J. Phys. USSR* **9**, 385–391, 1945.
- [26] J. FRICKE, Aerogels, *Scient. Am.* **258**, 5, 68–73, 1988.
- [27] C.W. GEAR, *Numerical Initial Value Problems in Ordinary Differential Equations*. Prentice-Hall, Englewood Cliffs NY., 1971.
- [28] A.S. GELLER, S.H. LEE AND L.G. LEAL, The Creeping Motion of a Spherical Particle Normal to a Deformable Interface, *J. Fluid Mech.* **169**, 27–69, 1986.
- [29] J. DE GRAAF, Mathematical Addenda to Hopper's Model of Plane Stokes Flow Driven by Capillarity on a Free Surface, in *Proc. Conf. on Modern Mathematical Physics*, edited by G.F. Helminck, 1992.
- [30] I.S. GRADSHTEYN AND I.M. RYZHIK, *Table of Integrals, Series, and Products*. Academic Press, New York, 1980. transl. A. Jeffrey, Corrected and Enlarged Edition.
- [31] S.T. GRILLI, J. SKOURUP AND I.A. SVENDSEN, An Efficient Boundary Element Method for Nonlinear Water Waves, *Engng. Analysis* **6**, 2, 97–107, 1989.
- [32] C. HAACK, P. GRAVERT AND V. SCHLEGEL, The Modelling of Extreme Gravity Waves: An Approach towards a Numerical Wave Channel, in *Proc. Conf. on Computational Modelling of Free and Moving Boundary Problems, Vol.1 Fluid Flow*, edited by L.C. Wrobel and C.A. Brebbia, Computational Mechanics Publications, Southampton, pp. 91–104, 1991.
- [33] J. HAANTJES, *Inleiding tot de differentiaalmeetkunde*. Noordhoff, Groningen, 1954. In Dutch.
- [34] W. HACKBUSCH, *Integralgleichungen: Theorie and Numerik*. Teubner, Stuttgart, 1989. In German.
- [35] J. HAPPEL AND H. BRENNER, *Low Reynolds number hydrodynamics*. Prentice-Hall, Englewood Cliffs NJ., 1965.
- [36] F. HARTMANN, Computing the C-matrix in non-smooth boundary points, in *Proc. Conf. on New Developments in Boundary Element Methods*, edited by C.A. Brebbia, CML publications, Southampton, pp. 367–379, 1980.
- [37] N.A.J. HELMES, Application of the Finite Element Method for a Two-Dimensional Sintering Problem, Master's thesis, Eindhoven University of Technology, 1992. In Dutch.

- [38] H.C. HINDMARSH, LSODE and LSODI, two new initial value ordinary differential equation solvers, *ACM-Signum Newsletter* **15**, 4, 1980.
- [39] H.C. HINDMARSH, ODEPACK, A systematized collection of ODE solvers, in *Proc. Conf. on Scientific Computing*, edited by R.S. Stepleman and et al., North-Holland Publishing Company, Amsterdam, pp. 55–64, 1983.
- [40] H.C. HINDMARSH, Detecting Stability Barriers in BDF Solvers, in *Proc. Conf. on Computational ordinary differential equations*, edited by J.R. Cash and I. Gladwell, Clarendon Press, Oxford, pp. 87–96, 1992.
- [41] R.W. HOPPER, Coalescence of two equal cylinders - Exact results for creeping viscous plane flow driven by capillarity, *J. Am. Ceram. Soc.* **67**, 262–264, 1984.
- [42] R.W. HOPPER, Plane Stokes Flow Driven by Capillarity on a Free Surface, *J. Fluid Mech.* **213**, 349–375, 1990.
- [43] R.W. HOPPER, Plane Stokes Flow Driven by Capillarity on a Free Surface, 2: Further Developments, *J. Fluid Mech.* **230**, 355–364, 1991.
- [44] R.W. HOPPER, Stokes Flow of a Cylinder and Half-Space Driven by Capillarity, *J. Fluid Mech.* **243**, 171–181, 1992.
- [45] P. HRMA AND C.E. CARTER, Capillarity-Induced Spheroidization of nearly Spherical Amorphous Bodies by Viscous Flow, *J. Non-Cryst. Solids* **63**, 391–412, 1984.
- [46] G.C. HSIAO, P. KOPP AND W.L. WENDLAND, Some applications of a Galerkin-collocation method for boundary integral equations of the first kind, *Math. Meth. in the Appl. Sci.* **6**, 280–325, 1984.
- [47] D.B. INGHAM AND M.A. KELMANSON, *Boundary Integral Equation Analyses of Singular, Potential and Biharmonic Problems*. Springer-Verlag, Berlin, 1984.
- [48] A. JAGOTA AND P.R. DAWSON, Micromechanical Modeling of Powder Compacts-I. Unit Problems for Sintering and Traction-Induced Deformation, *Acta. Metall.* **36**, 2551–2561, 1988.
- [49] A. JAGOTA AND P.R. DAWSON, Micromechanical Modeling of Powder Compacts-II. Truss Formulation of Discrete Packings, *Acta. Metall.* **36**, 2563–2573, 1988.
- [50] A. JAGOTA AND P.R. DAWSON, Simulation of the Viscous Sintering of Two Particles, *J. Am. Ceram. Soc.* **73**, 173–177, 1990.
- [51] P.F. JAMES, The Gel to Glass Transition: Chemical and Microstructural Evolution, *J. Non-Cryst. Solids* **100**, 93–114, 1988.
- [52] M.A. JAWSON AND G.T. SYMM, *Integral Equation Methods in Potential Theory and Elastostatics*. Butterworth-Heinemann, Boston, 1991.

- [53] S.J. KARRILA, Y.O. FUENTES AND S. KIM, Parallel Computational Strategies for Hydrodynamic Interactions between Rigid Particles of Arbitrary Shape in a Viscous Fluid, *J. Rheology* **33**, 913–947, 1989.
- [54] S. KIM AND S.J. KARRILA, *Microhydrodynamics: Principles and Selected Applications*. Academic Press, London, 1977.
- [55] W.D. KINGERY AND M. BERG, Study of the Initial Stages of Sintering by Viscous Flow, Evaporation-Condensation, and Self-Diffusion, *J. Appl. Phys.* **26**, 1205–1212, 1955.
- [56] L.C. KLEIN (ED.), *Sol-gel technology for thin films, fibers, preforms, electronics, and speciality shapes*. Noyes, Park Ridge, 1988.
- [57] D.M. KORWIN, S.R. LANGE, W.C. EATON, I. JOSEPH AND L.D. PYE, A Study of the Sintering Behavior of Glass in Two Geometric Configurations, in *Proc. Conf. on 16th Intl. Congress on Glass*, 1992. published as a special issue of *Boletin de la Sociedad Espanola de Ceramica y Vidrio*.
- [58] D.M. KORWIN, W.C. EATON AND L.D. PYE, A Study of the Sintering Behavior of Equal Diameter Soda-Lime-Silica Glass Fibres, *J. Am. Ceram. Soc.*, 1993. (Submitted).
- [59] R. KRESS, *Linear Integral Equations*. Springer-Verlag, Berlin, 1989.
- [60] E. KREYSZIG, *Introductory functional analysis with applications*. Wiley, London, 1978.
- [61] G.C. KUCZYNSKI, Study of the Sintering of Glass, *J. Appl. Phys.* **20**, 1160–1163, 1949.
- [62] H.K. KUIKEN, Viscous Sintering: the Surface-Tension-Driven Flow of a Liquid Form under the Influence of Curvature Gradients at its Surface, *J. Fluid Mech.* **214**, 503–515, 1990.
- [63] H.K. KUIKEN, Deforming Surfaces and Viscous Sintering, in *Proc. Conf. on The Mathematics and the Computation of Deforming Surfaces Cambridge U.K.*, edited by J.C.R. Hunt, Oxford University Press, Oxford, 1992.
- [64] O.A. LADYZHENSKAYA, *The Mathematical Theory of Viscous Incompressible Flow*. Gordon and Beach, New York-London, 1963.
- [65] D. LASSEUX, *Caractérisations expérimentale, analytique et numérique d'un film dynamique lors du drainage d'un capillaire*, PhD thesis, University of Bordeaux, 1990. In French.
- [66] S.H. LEE, R.S. CHADWICK AND L.G. LEAL, Motion of a Sphere in the Presence of a Plane Interface. Part 1. An Approximate Solution by Generalization of the Method of Lorentz, *J. Fluid Mech.* **93**, 705–726, 1979.

- [67] S.H. LEE AND L.G. LEAL, The Motion of a Sphere in the Presence of a Deformable Interface. Part 2: Numerical study of the translation of a sphere normal to an interface, *J. Colloid Interface Sci.* **87**, 81–106, 1982.
- [68] M.S. LONGUET-HIGGINS AND E.D. COKELET, The Deformation of Steep Surface Waves on Water - I. A Numerical Method of Computation, *Proc. R. Soc. Lond.* **A350**, 1–26, 1976.
- [69] H.A. LORENTZ, Eene Algemeene Stelling omtrent de Beweging eener Vloeistof met Wrijving en eenige daaruit afgeleide Gevolgen, *Versl. Acad. Wetensch. Amsterdam* **5**, 168–175, 1896. Translation can be found in *Collected Papers* **4**, 7-14, Martinus Nijhoff, The Hague, (1937).
- [70] J.K. MACKENZIE AND R. SHUTTLEWORTH, A Phenomenological Theory of Sintering, *Proc. Phys. Soc. Lond.* **62**, 833–852, 1949.
- [71] C.A.M. MULDER, J.G. VAN LIEROP AND G. FRENS, Densification of SiO₂-Xerogels to glass by Ostwald ripening, *J. Non-Cryst. Solids* **82**, 92–96, 1986.
- [72] N.I. MUSKHELISHVILI, *Singular integral equations: boundary problems to function theory and their application to mathematical physics*. Noordhoff, Groningen, 1953.
- [73] N. NIELSEN, *Theorie des Integrallogarithmus*. B.G. Teubner, Leipzig, 1906. In German.
- [74] K. NISHITANI, Y. HASEGAWO AND M. HIGASHIKATO, Non-Linearity of Shrinkage in the Rate Equation of Initial-Stage Sintering for Viscous Flow, *J. Ceram. Soc. Japan* **91**, 483–486, 1983. In Japanese.
- [75] F. ORGAZ, Gel to Glass Conversion: Densification Kinetics and Controlling Mechanisms, *J. Non-Cryst. Solids* **100**, 115–141, 1988.
- [76] A. PAUL, *Chemistry of Glasses, second edition*. Chapman and Hall, London, 1990. 2nd ed.
- [77] H. POWER AND G. MIRANDA, Second Kind Integral Equation Formulation of Stokes' Flow Past a Particle of Arbitrary Shape, *SIAM J. Appl. Math.* **47**, 689–698, 1987.
- [78] C. POZRIKIDIS, The Flow of a Liquid Film along a Periodic Wall, *J. Fluid Mech.* **188**, 275–300, 1988.
- [79] C. POZRIKIDIS, The Deformation of a Liquid Drop Moving Normal to a Plane Wall, *J. Fluid Mech.* **215**, 331–363, 1990.
- [80] C. POZRIKIDIS, The Axisymmetric Deformation of a Red Blood Cell in a Uniaxial Straining Stokes flow, *J. Fluid Mech.* **216**, 231–254, 1990.

- [81] C. POZRIKIDIS AND S.T. THORODDSEN, The Deformation of a Liquid Film Flowing down an Inclined Plane Wall over a Small Particle Arrested on the Wall, *Phys. Fluids A* **3**, 2546–2558, 1991.
- [82] C. POZRIKIDIS, *Boundary Integral and Singularity Methods for Linearized Viscous Flow*. Cambridge University Press, Cambridge, 1992.
- [83] C. POZRIKIDIS, The Buoyancy-Driven Motion of a Train of Viscous Drops within a Cylindrical Tube, *J. Fluid Mech.* **237**, 627–648, 1992.
- [84] C. POZRIKIDIS, On the Transient Motion of ordered Suspensions of Liquid Drops, *J. Fluid Mech.* **246**, 301–320, 1993.
- [85] G. PROKERT, Analytical and numerical aspects of models for the motion of a viscous capillary liquid drop, Master's thesis, Dresden University of Technology, June 1993.
- [86] J.M. RALLISON AND A. ACRIVOS, A Numerical Study of the Deformation and Burst of a Viscous drop in an Extensional Flow, *J. Fluid Mech.* **89**, 191–200, 1978.
- [87] D. RAMSDEN AND G. HOLLOWAY, Timestepping Lagrangian Particles in Two Dimensional Eulerian Flow Fields, *J. Comput. Phys.* **94**, 101–116, 1992.
- [88] J.S. REED, *Introduction to the principles of ceramic processing*. Wiley-Interscience, Chichester, 1988.
- [89] S. RICHARDSON, Two-dimensional slow viscous flows with time-dependent free boundaries driven by surface tension, *Euro. J. App. Math.* **3**, 193–207, 1992.
- [90] J.W. ROSS, *Computer simulation of sintering kinetics*, PhD thesis, University of Toronto, 1980.
- [91] J.W. ROSS, W.A. MILLER AND G.C. WEATHERLY, Dynamic Computer Simulation of Viscous Flow Sintering Kinetics, *J. Appl. Phys.* **52**, 3884–3888, 1981.
- [92] G.W. SCHERER, Sintering of Low-Density Glasses: I, Theory, *J. Am. Ceram. Soc.* **60**, 236–239, 1977.
- [93] G.W. SCHERER, Viscous Sintering of a Bimodal Pore-Size Distribution, *J. Am. Ceram. Soc.* **67**, 709–715, 1984.
- [94] G.W. SCHERER AND T. GARINO, Viscous Sintering on a Rigid Substrate, *J. Am. Ceram. Soc.* **68**, 216–220, 1985.
- [95] G.W. SCHERER, Geometric Model for Sintering of Cylinders and Spheres, Technical report, Dupont Central Research and Development, 1992.

- [96] A.J. SHALER AND J. WULFF, Mechanism of Sintering, *Ind. Engng. Chem.* **40**, 838–842, 1948.
- [97] S. SŌMIYA AND Y. MORIYOSHI (EDS.), *Sintering Key Papers*. Elsevier Applied Science, London, 1990.
- [98] J.A.W. VAN DE SPEK, Inverse Formulations for Viscous Sintering Problems, Master's thesis, Eindhoven University of Technology, 1990. In Dutch.
- [99] A.H. STROUD AND D. SECREST, *Gaussian Quadrature Formulas*. Prentice-Hall, Englewood Cliffs NJ., 1966.
- [100] J. TANZOSH, M. MANGA AND H.A. STONE, Boundary Integral Methods for Viscous Free-Boundary Problems: Deformation of Single and Multiple Fluid-Fluid Interfaces, in *Proc. Conf. on Boundary Element Technology VII*, edited by C.A. Brebbia and M.S. Ingber, Computational Mechanics Publications, Southampton, pp. 19–39, 1992.
- [101] J.C.F. TELLES, A Self-adaptive coordinate Transformation for Efficient Numerical Evaluation of General Boundary Element Integrals, *Int. J. Num. Meth. in Engng.* **24**, 959–973, 1989.
- [102] G.A.L. VAN DE VORST AND R.M.M. MATTHEIJ, Implementing the Boundary Element Method for 2-D Viscous Sintering, in *Proc. Conf. on Computational Modelling of Free and Moving Boundary Problems, Vol. 1 Fluid Flow*, edited by L.C. Wrobel and C.A. Brebbia, Computational Mechanics Publications, Southampton, pp. 341–355, 1991.
- [103] G.A.L. VAN DE VORST, R.M.M. MATTHEIJ AND H.K. KUIKEN, Boundary Element Solution for Two-Dimensional Viscous Sintering, *J. Comput. Phys.* **100**, 50–63, 1992.
- [104] G.A.L. VAN DE VORST AND R.M.M. MATTHEIJ, A BDF-BEM Scheme for Modelling Viscous Sintering, in *Proc. Conf. on Boundary Element Technology VII*, edited by C.A. Brebbia and M.S. Ingber, Computational Mechanics Publications, Southampton, pp. 59–74, 1992.
- [105] G.A.L. VAN DE VORST AND R.M.M. MATTHEIJ, Numerical Analysis of a 2-D Viscous Sintering Problem with Non Smooth Boundaries, *Computing* **49**, 239–263, 1992.
- [106] G.A.L. VAN DE VORST, A BEM solution for the Simulation of Axisymmetric Viscous Sintering, in *Proc. Conf. on Computational Modelling of Free and Moving Boundary Problems II*, edited by L.C. Wrobel and C.A. Brebbia, Computational Mechanics Publications, Southampton, pp. 123–130, 1993.

- [107] G.A.L. VAN DE VORST, Integral Method for a Two-Dimensional Stokes Flow with Shrinking Holes Applied to Viscous Sintering, *J. Fluid Mech.* **257**, 667–689, 1993.
- [108] J.R. WALDRAM, *The theory of thermodynamics*. Cambridge University Press, Cambridge, 1985.
- [109] J. WEIDMANN, *Linear Operators in Hilbert Spaces*. Springer-Verlag, New York, 1980.
- [110] S. WEINBAUM, P. GANATOS AND Z.Y. YAN, Numerical multipole and Boundary Integral Equation Techniques in Stokes Flow, *Annu. Rev. Fluid Mech.* **22**, 275–316, 1990.
- [111] J.H. WILKINSON, *The Algebraic Eigenvalue problem*. Clarendon Press, Oxford, 1965.
- [112] G. DE WITH, Meso-modelling: a proposed attempt to obtain an industrially applicable sintering theory, in *Proc. Conf. on Modelling of sintering processes*, 1990. Lecture at the 71 WE Heraeus Seminar.
- [113] G. DE WITH AND A.J. CORBIJN, Fiber-on-Plate Experiments: Relaxation and Surface Tension, *J. Appl. Phys.*, 1993. (Submitted).
- [114] G. DE WITH AND A.J. CORBIJN, Morphological Relaxation of Glass Surfaces, *J. Appl. Phys.*, 1993. (Submitted).
- [115] G.K. YOUNGREN AND A. ACRIVOS, Stokes Flow past a Particle of Arbitrary Shape: A Numerical Method of Solution, *J. Fluid Mech.* **69**, 377–403, 1975.

INDEX

- Adjoint
 - operator, 29
 - adjoint system, 26
- Aerogel, 5
- Airy stress function, 156
- Backward Differences Formulae
 - (BDF method), 15, 86
- Basis functions, 62
- Biharmonic, 156
- Body force, 22
- Boundary Element Method
 - (BEM), 10, 59, 64
- Cauchy principal value, 28
- Characteristic curves, 24
- Closed pores model, 8, 111
- Coalescence
 - cylinder on a half space, 43, 48
 - two equal cylinders,
 - analytical, 41, 44
 - numerical, 78, 96
 - two equal rings, 148
 - two equal spheres, 142
 - two unequal cylinders,
 - analytical, 42
 - numerical, 80
 - two unequal spheres, 148
 - sphere on ring, 150
- Coatings, 5
- Collocation method, 60
- Complete elliptic integral
 - of the first kind, 42, 139
 - of the second kind, 139
- Conformal map, 40
- Contact radius, 104
- Continuity equation, 20
- Corrector, 93
- Creeping flow, 21
- Curvature
 - approximation, 68
 - axisymmetric, 142
 - definition, 22
 - density, 71
 - equidistribution, 71
 - oscillations, 68
 - principal, 22
- Cusp, 68
 - detection, 77
 - discretization, 74
- Cylindrical coordinates, 138
- Cylindrical packings, 119
- Deflation, 14
 - two-dimensional, 32
 - axisymmetric, 140
- Deformation
 - energy, 84

- tensor, 20
- Density
 - bulk, 112
 - skeletal, 112
- Diagonal coefficients
 - two-dimensional, 66
 - axisymmetric, 141
- Dirac delta function, 26
- Double layer
 - operator, 29
 - potential, 28
- Einstein summation convention, 22
- Elements
 - linear, 64
 - quadratic, 64
 - singular, 65
- Energy balance, 7, 23
- Equidistribution condition, 72
- Eulerian viewpoint, 12, 24, 157
- Finite Element Method (FEM), 10
- Forward Euler method, 24
- Fredholm alternative, 30
- Fredholm integral equation
 - of the first kind, 28
 - of the second kind, 11, 27,
 - approximation, 59
- Free surface energy, 21
- Frenkel
 - model, 7
 - equation, 53, 55, 145
- Froude number, 21
- Fundamental solution, 26
- Galerkin's method, 62
- Gaussian quadrature, 65
 - logarithmic, 66
- Gibbs free energy, 21
- Green's formulae, 26
- Incompressibility condition, 20
- Inner product, 29
- Jacobian:
 - approximation, 92
 - matrix, 83
 - of element, 65
- Kinematic
 - constraint, 12, 23
 - viscosity, 24
- Kronecker delta, 20
- Lagrangian polynomials, 64
- Lagrangian viewpoint, 13, 24, 157
- Liquid-phase sintering, 1
- Logarithmic integral, 46
- LSODE, 86, 93
 - order selection, 94
 - stepsize selection, 94
- Lyapunov surface, 26
- Mesh
 - redistribution, 71
 - verification, 75
- Meso-cell, 6
- Mixed Eulerian-Lagrangian viewpoint,
 - 13
- Monoliths, 2
- MS-model, 7, 111, 112
- Navier-Stokes equation, 20
- Neck
 - curvature, 44, 104
 - neck radius, 44
- Newtonian fluid, 20
- Nordsieck representation, 93
- Open pores model, 8, 112
- Ostwald ripening, 142
- Polygon, 64
- Predictor, 94
- Projection
 - method, 60
 - operator, 32
- Pseudo Lagrangian description, 40, 157
- Quasi-static, 23
- Redistribution parameters, 71

- Relative shrinkage, 45
- Reynolds number, 21
- Rhombic geometries, 82
- Rigid-body motions, 30, 66

- Scherer's model, 8, 113
- Scherer–Garino equation, 113
- SDLP–formulation, 11,28
- Self-adjoint, 29
- Single layer
 - operator, 29
 - potential, 28
- Sink point, 34
- Sol-gel technique, 3
- Solenoidal, 20
- Solid-state sintering, 1
- Source point, 34
- Spatial discretization error, 69
- Spectral radius, 83
- Step-length, 71
- Stiffness, 83
- Stokes equation, 21
- Stokeslet, 11, 26
- Stream function, 155
- Stress tensor, 20
- Surface tension prediction, 56

- Tangent circle models, 7,54
- Time discretization error, 69

- Van der Waals forces, 16, 56
- Viscous sintering, 2

- Weakly singular, 29, 60
- Wielandt's deflation, 32

- Xerogel, 4

SUMMARY

The objective of this thesis is to develop reliable methods to predict the deformation of a liquid region driven by surface tension. This research is motivated by the need to obtain a better understanding of the process of viscous sintering. Sintering is a technique in which a granular compact (e.g. of metals, ionic crystals or glasses), consisting of many particles, is heated to such a high temperature that sufficient mobility is present to release the excess free energy of the surface of the compact, thereby joining the particles together. As a result, the cohesion of the compact increases with time. There is a number of physical principles which can be held responsible for the sintering phenomena. Here the only interest is the case of sintering when the material transport can be modelled as a viscous volume flow, which is valid for amorphous materials e.g. glasses. Then, this phenomenon is called *viscous sintering* and it appears in the production of high-quality glasses by means of what is known as the sol-gel technique. A deterministic description of the microscopic flow within an actual sintering gel is very complicated because of its stochastic nature. Thus, scientists studying sintering phenomena have long been interested in the behaviour of simple systems, for instance the coalescing of two spheres, or the sintering of a sphere onto a flat surface. These studies can give a better insight in the phenomenological theory for macroscopic systems.

In this thesis, the mathematical model of viscous sintering will be outlined. It appears that this process can be described by the Stokes equations with surface tension proportional to the curvature in the normal direction. The motion of the boundary is described by using the Lagrangian description of the boundary velocity field, i.e. the material boundary points are being followed. Special attention is given to some recently obtained analytical solutions for the unit problems as the coalescence of two cylinders and a cylinder on a half space. From these rather complicated solutions simple approximations are derived for both the coalescence rate and the curvature at the coalescing surface. These approximations can be applied to determine experimentally the surface tension of a particular glass at a certain temperature.

However, the main part of this thesis describes the numerical solution of the viscous

sintering problem, in order to simulate two-dimensional and axisymmetric geometries. This numerical simulation is carried out by solving the governing Stokes equations for a fixed domain through a Boundary Element Method (BEM). Therefore, the problem has to be reformulated as a system of integral equations. Special care has to be taken for making those equations uniquely solvable. Moreover, the formulation has to be modified to incorporate shrinking holes inside the fluid domain, i.e. to solve multiply connected regions. From the implemented BEM a system of linear algebraic equations is derived which describe the boundary velocity at a fixed time. In order to determine the geometry at a next time level, the Lagrangian representation of the boundary velocity field is substituted into the system of algebraic equations. This results in a system of non-linear Ordinary Differential Equations (ODEs). It appears that, depending on the geometrical shape, this system is *stiff*. Because of this stiffness, the ODEs are numerically integrated by employing a sophisticated time integrator: a variable step, variable order Backward Differences Formulae (BDF) method, i.e. an implicit multistep method.

Furthermore, it is shown that this moving boundary problem is ill-conditioned when the boundary curvature is large (at cusps). A numerical consequence of this ill-conditioning is that special care has to be taken for distributing and redistributing the nodal points at those boundary parts. Therefore, an algorithm is developed for a fairly optimal node redistribution based on equidistributing the curvature of the boundary. Besides the special treatment for cusp regions so that the curvature is qualitatively preserved after the redistribution to avoid (numerical) oscillations in the computed velocity field, the number and position of the collocation points are taken nearly optimal, this in order to minimize the computational costs per time step.

Finally, the numerical solution method is extended to axisymmetric domains, i.e. domains formed by rotating a two-dimensional plane about a given axis. Because of this axial symmetry, such a three-dimensional sintering problem can be reduced to a two-dimensional one so that the developed node redistribution algorithm and the time integration method apply to these problems also.

For this problem a number of Fortran routines have been implemented which are used to demonstrate the sintering of various arbitrarily shaped simply and multiply connected domains. The obtained simulations are compared to some exact analytical solvable problems and show an excellent match. A few analytical densification models are compared with the results obtained by the simulation of two-dimensional shapes with holes inside. From this comparison, quantitative insights are obtained about the applicability of those models. It appears that these models fail considerably when a geometry with non-uniformly sized holes is simulated: the simulations show that the relatively larger holes are shrinking considerably faster compared to the smaller ones. Furthermore, the sintering of some cylindrical packings is considered. The latter simulations will provide a justification for the use of *unit problems* in the theory of sintering to describe the behaviour of an regular and equally sized particle packing. One of the results obtained using the axisymmetric implementation shows that the initial stage of the coalescing rate of two spheres can quite well be approximated analytically by the solution of the corresponding two-dimensional problems.

SAMENVATTING

Het doel van dit proefschrift is de ontwikkeling van betrouwbare methoden die de vorming van een vloeistofgebied, onder invloed van de oppervlaktetenspanning, kunnen voorspellen. Dit onderzoek komt voort uit de wens het viskeus sinterproces theoretisch beter te begrijpen. Sinteren is een techniek waarbij een poedercompact (dat kan bestaan uit zowel metaal-, zout- of glas-deeltjes) tot een zo hoge temperatuur verhit wordt dat de deeltjes aan elkaar smelten. Als gevolg hiervan zal de cohesie van zo'n deeltjes compact toenemen. De drijvende kracht achter dit proces is de oppervlakte energie die een poedercompact in overmaat bezit t.o.v. een vast lichaam. Er zijn een aantal fysische processen die verantwoordelijk kunnen zijn voor het sinterverschijnsel. In dit proefschrift zal alleen het geval worden beschouwd waarbij het sinterproces gemodelleerd kan worden als een viskeuze volume stroming. Dit laatste geldt in het bijzonder voor amorfe materialen zoals glas. Men spreekt dan ook wel van *viskeus sinteren* en dit proces komt o.a. voor tijdens de productie van hoogwaardige glazen die met behulp van de zogenaamde sol-gel techniek worden vervaardigd. Een precieze beschrijving van de microscopische vloeistofstroming in zo'n gel tijdens het sinteren is erg moeilijk door de stochastische structuur van de gel. Daarom hebben onderzoekers op het gebied van sinteren zich lang geïnteresseerd in het gedrag van zeer simpele systemen; hierbij kan worden gedacht aan het samensmelten van twee bollen of een bol op een plaat. Dit soort onderzoek verschaft inzicht in de fenomenologische theorie voor macroscopische systemen.

In dit proefschrift wordt eerst het mathematisch model voor het viskeus sinteren afgeleid. Het proces blijkt te kunnen worden beschreven door de Stokes vergelijkingen waarbij de spanning op de rand evenredig is met de kromming in de richting loodrecht op het oppervlak. De beweging van de rand is gemodelleerd door gebruik te maken van de Lagrangiaanse beschrijving van het randsnelheidsveld. Dit houdt in dat de baan van de randpunten wordt gevolgd door deze punten op te vatten als materieële deeltjes. Enige aandacht wordt verder geschonken aan enkele recentelijk gevonden analytische oplossingen voor bepaalde eenheidsproblemen, i.e. het samensmelten van twee cilin-

ders en van een cilinder op een plaat. Van deze nogal ingewikkelde oplossingen zijn simpele benaderingen afgeleid voor zowel de samensmeltingssnelheid als de evolutie van de randkromming ter plaatse van het samensmeltingsoppervlak. Verder kunnen de analytische oplossingen of hun benaderingen worden gebruikt om experimenteel de oppervlakte spanning van glas bij niet al te hoge temperaturen te bepalen.

Het grootste gedeelte van dit proefschrift beschrijft echter de numerieke oplossing van het viskeus sinterproces en wel voor zowel 2-dimensionale als axisymmetrische gebieden. Deze numerieke methodiek bestaat allereerst uit het oplossen van de Stokes vergelijkingen voor een vast gebied met behulp van een randelementen methode (BEM). Hiervoor dient het probleem geformuleerd te worden als een stelsel van integraal vergelijkingen. Speciale aandacht wordt geschonken aan het eenduidig maken van deze formulering. Verder dienen deze vergelijkingen aangepast te worden om het krimpen van holten in het vloeistofgebied te kunnen beschrijven, ten einde ook meervoudig samenhangende gebieden te kunnen oplossen. De BEM-methodiek resulteert in een stelsel lineaire algebraïsche vergelijkingen die het snelheidsveld van de rand geeft op een vast tijdstip. Om de geometrie op een volgend tijdstip te bepalen wordt de Lagrangiaanse representatie van het snelheidsveld in dit algebraïsch stelsel gesubstitueerd. Hierdoor wordt een stelsel niet-lineaire gewone differentiaal vergelijking verkregen. Afhankelijk van de geometrische vorm van het vloeistofgebied blijkt dit stelsel *stijf* te zijn. Daarom wordt dit stelsel gewone differentiaal vergelijkingen opgelost met een variabele stap/variabele orde terugwaartse differentie methode (BDF), i.e. een impliciete meerstapsmethode.

Daarna wordt aangetoond dat dit bewegende randenprobleem slecht geconditioneerd is als de kromming van het oppervlak op bepaalde gebieden zeer groot is; dit is in het bijzonder het geval bij scherpe hoeken. Een numeriek gevolg van dit slecht geconditioneerd zijn is dat de distributie en herdistributie van discretisatiepunten met grote zorgvuldigheid dient te geschieden voor dit soort randen omdat er anders numerieke oscillaties in het te berekenen snelheidsveld zouden kunnen optreden. Daarom is er een speciaal algoritme ontworpen om een goede puntendistributie te verkrijgen. Dit algoritme is gebaseerd op het equidistribueren van de kromming over de randelementen. Naast het op een speciale manier behandelen van gebieden met grote kromming zodat deze kromming lokaal kwalitatief behouden blijft, heeft dit algoritme nog een tweede doel: het aantal discretisatie punten en hun positie wordt zo optimaal mogelijk gekozen, dit om de rekenkosten per tijdstap te minimaliseren.

Tenslotte is de numerieke oplosmethode uitgebreid tot axisymmetrische gebieden, dwz. gebieden die verkregen worden door een 2-dimensionaal vlak te roteren rond een gegeven as. Gebruik makende van deze axiale symmetrie kan zo'n 3-dimensionaal sinterprobleem worden vereenvoudigd tot een 2-dimensionaal probleem. Aldus kunnen de ontwikkelde puntendistributie algoritme en de tijdsintegratie methode ook eenvoudig voor dit type probleem worden gebruikt.

De hierboven beschreven methodieken zijn geïmplementeerd in Fortran en deze worden gedemonstreerd voor een aantal enkel- en meervoudig samenhangende gebieden. De verkregen simulatieresultaten zijn vergeleken met enkele, exact analytisch oplosbare, problemen en tonen een uitstekende overeenkomst. Verder zijn een paar analytische

verdichtingsmodellen vergeleken met de resultaten verkregen door het simuleren van gebieden met interne holten. Van deze resultaten wordt kwantitatief inzicht verkregen met betrekking tot de toepasbaarheid van deze verdichtingsmodellen. Het blijkt dat deze modellen een forse afwijking te zien geven wanneer een gebied met niet-uniform grote holten wordt beschouwd: de simulaties laten dan zien dat de relatief grotere holten sneller krimpen in vergelijking tot de kleinere holten. Daarnaast wordt het sinteren van enkele cilindrische pakkingen beschouwd. Deze simulaties geven een rechtvaardiging voor het gebruik van eenheidsproblemen in de sintertheorie om het gedrag te beschrijven van regelmatig en gelijkvormige deeltjes pakkingen. Een van de resultaten verkregen m.b.v. de axisymmetrische implementatie is dat het samensmelten van twee bollen redelijk goed analytisch benaderd kan worden door de oplossingen van de overeenkomstige 2-dimensionale problemen.

CURRICULUM VITAE

Alfred van de Vorst werd geboren op 23 januari 1965 te Steensel. Van 1977 tot en met 1982 volgde hij met succes HAVO onderwijs aan het Rythovius College in Eersel. Hierna bezocht hij op dezelfde scholen gemeenschap de laatste twee jaren van het VWO onderwijs, dat hij voltooide in 1984.

In september 1984 begon hij met de studie Wiskunde aan de Technische Universiteit Eindhoven (TUE) die werd afgerond in juni 1989. Het afstudeerwerk werd tussen oktober 1988 en juni 1989 uitgevoerd bij het Philips Center voor Manufacturing Technology (CFT) bij de groep Mathematical Software te Eindhoven, onder begeleiding van Dr.ir. J.K.M. Jansen (TUE), Drs. J.B.M. Melissen en Ir. J.C.H. van Gerwen (beiden Philips). Dit werk resulteerde in een voorstudie van een numeriek pakket dat de warmteontwikkeling in een metaal simuleert waarbij de verhitting veroorzaakt wordt door elektrische wervel stromen in dat metaal, die opgewekt zijn door een hoogfrequent magnetisch veld.

Van eind 1989 tot en met december 1993 was hij als Onderzoeker in Opleiding (OIO) in dienst van de vakgroep toegepaste analyse van de faculteit Wiskunde en Informatica aan de TUE. Onder begeleiding van Prof.dr. R.M.M. Mattheij en Prof.dr.ir. H.K. Kuiken verrichte hij onderzoek ten behoeve van het STW-project *modelleren en numeriek simuleren van systemen voor het viskeuze sinteren*. Dit werk resulteerde in een simulatie programma, een aantal wetenschappelijke artikelen en verscheidene conferentiebijdragen. De belangrijkste resultaten van dit onderzoek zijn samengevat in dit proefschrift.

STELLINGEN

behorende bij het proefschrift

MODELLING AND NUMERICAL SIMULATION OF VISCOUS SINTERING

door G.A.L. van de Vorst

1. Met behulp van “simpele” eenheidsmodellen is het mogelijk om het viskeus sintergedrag te beschrijven van regelmatig gestapelde pakkingen van gelijke deeltjes.

Hoofdstuk 7 van dit proefschrift.

2. De vraag die Hopper stelt in [2], i.e. *kan de connectiviteit veranderen van een enkelvoudig samenhangend gebied van een viskeuze kruipvloeistof gedreven door de oppervlakte spanning*, moet met ja worden beantwoord.

Hoofdstuk 7 en 8 van dit proefschrift.

3. Het is een toevalligheid dat Frenkel’s model [1] van twee samensmeltende viskeuze bollen een lineair krimpgedrag in de tijd voorspelt.
4. Zij (ψ_n) een rij vectoren in een separabele Hilbertruimte \mathcal{H} . Dan is (ψ_n) een *frame* d.e.s.d. als er een surjectieve lineaire begrensde afbeelding \mathcal{A} van ℓ_2 op \mathcal{H} bestaat zodat $\mathcal{A}\delta_m = \psi_m$ waarbij δ_m een orthonormale basis is in ℓ_2 .
5. Bij een vensterfunctie $w(t)$ en grondfrequentie ω_0 wordt de Short Time Fourier Transform (STFT) van een functie $f(t)$ gedefinieerd door

$$\int_{-\infty}^{\infty} f(t) \overline{w_{m,n}(t)} dt \quad (m, n \in \mathbb{Z}),$$

waarbij $w_{m,n}(t) = e^{im\omega_0 t} w(t - nt_0)$ en t_0 een translatie parameter is in het tijddomein. In geval dat $\omega_0 = 2\pi$, $t_0 = \frac{1}{2}$ en $w(t)$ een $(2k)$ -de orde B-spline met drager $[0,1]$ en knooppunten in $0, \frac{1}{2k}, \frac{1}{k}, \dots, 1$, vormen de functies $w_{m,n}$ een frame van de ruimte $L_2(\mathbb{R})$. Voor het conditiegetal c_k van het frame, i.e. de verhouding van de frame bounds, geldt

$$c_k \sim 0.0362703 \cdot (5.12718)^k \quad (k \rightarrow \infty).$$

6. Het voorspellen van instabiel gedrag van periodiek aangestoten rotordynamica systemen met niet-lineaire lagermodellen door middel van het bepalen van de stabiliteit van het model, gelineariseerd rond de statische oplossing is alleen geldig voor systemen met een kleine dynamische belasting.

Zie Van de Vorst [5]

7. De veronderstelling van Styles [4] en Qiu *et al.* [3] dat de tussenlaagkoppeling van een niet-magnetische laag tussen twee magnetische lagen alleen af zou hangen van de interface tussen de niet-magnetische en magnetische laag is niet juist.

Zie Van de Vorst [6].

8. De (semi)-particuliere onderzoekscentra hoeven op het gebied van de contractresearch geen concurrentie te vrezen van die universitaire instellingen waar een mentaliteit van vrijblijvendheid heerst.
9. De recentelijke oprichting van een mestcentrale die de meststroom reguleert tussen producenten, transporteurs en afnemers is een goede stap tot het oplossen van het mestprobleem in Brabant.
10. Met het oog op de razendsnelle ontwikkeling op het gebied van de computer hardware van o.a. werkstations is merkentrouw uit den boze.
11. Het bezoeken van congressen en het leggen van (buitenlandse) contacten dient een belangrijk onderdeel te vormen van elk AIO programma en zou daarom extra gestimuleerd moeten worden.
12. Sinds de opkomst van de compact disk zijn de *gouden ouden* niet meer zoals ze geweest zijn.
13. Een verkeerslicht is per definitie overbodig als er zich geen opstoppingen voordoen bij uitschakeling.
14. Als de huidige programmering van RTL V echt massaal door hoger opgeleiden zou worden bekeken, dan zouden er nog vele honderden miljoenen gulden extra in het onderwijs moeten worden gepompt.

Referenties

- [1] J. FRENKEL, Viscous Flow of Crystalline Bodies Under the Action of Surface Tension, *J. Phys. USSR* **9**, 385–391, 1945.
- [2] R.W. HOPPER, Plane Stokes Flow Driven by Capillarity on a Free Surface, *J. Fluid Mech.* **213**, 349–375, 1990.
- [3] Z.Q. QIU, J. ANDERSON AND S.D. BADER, Oscillatory interlayer magnetic coupling of wedged Co/Cu/Co sandwiches grown on Cu(100) by molecular beam epitaxy, *Phys. Rev. B* **46**, 8659–8662, 1992.
- [4] M. STYLES, Exchange coupling in magnetic heterostructures, *Phys. Rev. B* **48**, 7238–7258, 1993.
- [5] E.L.B. VAN DE VORST, R.H.B. FEY, J. BOS AND D.H. VAN CAMPEN, Long-term Behaviour of Rotordynamic Systems with Nonlinear Bearing Supports

under Periodic Excitation, *1st European Nonlinear Oscillations Conference*,
Technical University Hamburg-Harburg, Germany.

- [6] M.T.H. VAN DE VORST, The Effect of the Magnetic Layer on the Interlayer Exchange Coupling, Master's thesis, Eindhoven University of Technology, December 1993.